Characterization and Quantification of Metallic Interconnect Degradation in Solid Oxide Fuel Cell Stacks

Von der Fakultät Energie-, Verfahrens- und Biotechnik der Universität Stuttgart zur
Erlangung der Würde eines Doktor-Ingenieurs (Dr.-Ing.)
genehmigte Abhandlung

Vorgelegt von
Markus Linder
aus Winterthur

Hauptberichter: Prof. Dr. rer. nat. K. Andreas Friedrich
Mitberichter: Prof. Dr. rer. nat. Siegfried Schmauder

Tag der mündlichen Prüfung: 25. Oktober 2016

Institut für Thermodynamik und Wärmetechnik der Universität Stuttgart

2016

"If we do not develop technologies today,
we will not be able to meet the requirements of tomorrow."

<div align="right">Markus Lehner, 2014</div>

Contents

Contents

Abstract

Stationary solid oxide fuel cell (SOFC) applications typically have targeted lifetimes of more than $40\,000\,\mathrm{h}$ with a tolerable power degradation of less than $1\,\%$ per $1000\,\mathrm{h}$. To achieve these requirements powerful methods and strategies to characterize and quantify SOFC stack degradation are needed. The objective of this work was the investigation and prediction of SOFC stack degradation based on in-situ measurements and post-test analyses. These results were combined with the findings from dedicated laboratory experiments for the investigation of single degradation effects combined with computer models to develop strategies to predict and subsequently reduce SOFC stack degradation.

This requires the development of a model for the reliable quantification and thorough interpretation of the degradation behavior of SOFC stacks under real, non-ideal conditions. The model extracts the time-dependent internal stack resistances from current-voltage data. As major advantage over assessing stack degradation simply from the slopes of current-voltage curves, these internal resistances can be directly compared with the sum of the resistances of different stack components as obtained from dedicated laboratory degradation experiments.

Due to recent progress in improving the oxidation re-reduction (redox) stability of electrolyte supported SOFCs, the main contribution to the power degradation of stacks operated of more than $10\,000\,\mathrm{h}$ is induced by the ohmic losses caused by the time-dependent and continuously formation of oxide scales on the metallic interconnects (MICs). Moreover, the oxide scale growth rate and the extrinsic electrical conductivity of the formed semi conductive Cr_2O_3 is influenced by various parameters such as scale morphology, temperature, gas atmospheres, impurities, reactive elements and interaction with adjacent components. For this reason oxide scale growth on chromium (CFY) and ferritic (Crofer) based alloys were investigated by scanning electron microscopy (SEM) including samples from SOFC stacks manufactured by the Hexis AG[1], which were operated for up to $40\,000\,\mathrm{h}$. Comparison of the measured increase in ohmic resistance with mean scale growth rates obtained from SEM cross section images revealed a non-trivial, non-linear relation-

---

[1] www.hexis.com

Abstract

ship. To understand the correlation between scale evolution and resulting ohmic losses, 2D finite element (FE) simulations of electrical current distributions were performed for a large number of scale morphologies. Oxide scale morphologies favor non-homogeneous electrical current distributions, where the main current flows over rather few "bridges", i. e. local spots with relatively thin oxide scales. Combining electrical conductivity and SEM measurements with FE simulations revealed two further advantages: it allows a more reliable extrapolation of MIC degradation and it provides a new method to assess the effective electrical conductivity of thermally grown Cr_2O_3 scales under stack operation.

On the anode side the degradation behavior of oxide scales is even more complex. For example, Ni particles released during thermal redox cycles from adjacent Ni containing components might be interspersed into the oxide scale. To study the influence of this interaction Cr_2O_3 pellets admixed with different amounts of Ni (up to $20\,vol.\%$) were produced. The electrical conductivity was investigated in-situ in reducing forming gas ($95\,\%\ N_2$; $5\,\%\ H_2$) atmosphere and air at $850\,°C$. Furthermore microstructure and crystal structure are studied at different time steps with SEM and X-ray diffraction (XRD), respectively. Based on the applied methods it can be confirmed that during oxidation in air Ni forms a $NiCr_2O_4$ spinel phase. Exposure again in a reducing environment leads to an instantaneous decomposition of this spinel phase, which in turn leads to a fine dispersion of reduced Ni particles. This rearrangement of Ni by spinel decomposition improves the electrical conductivity of the Cr_2O_3-pellets.

In conclusion, this work established new methods and models to more reliably assess of SOFC stack-degradation based on current-voltage data, which allow extracting internal stack resistances for direct comparisons with dedicated laboratory experiments of single degradation phenomena. The focus of attention is on the quantification and understanding of the complex degradation behavior of metallic interconnects (as major contribution to the overall SOFC stack degradation) caused by oxide scale growth under reducing and oxidizing conditions.

Zusammenfassung

Stationäre Anwendungen von Festoxidbrennstoffzellen (SOFCs) müssen eine minimale Lebensdauer von über 40 000 h bei einer tolerierbaren Degradation von weniger als 1 % pro 1000 h aufweisen. Um diese Anforderungen zu erfüllen, werden geeignete Methoden und Strategien benötigt, um die Degradation von SOFC-Stapel zu charakterisieren und zu quantifizieren. Das Ziel dieser Arbeit ist die Untersuchung und Vorhersage der SOFC-Stapeldegradation basierend auf in-situ-Messungen und Posttest-Analysen. Diese Resultate wurden systematisch mit den Ergebnissen aus spezifischen Laborexperimenten zur Untersuchung von einzelnen Degradationseffekten verglichen. In Kombination mit Computermodellen können Strategien für die Vorhersage und Verminderung der SOFC-Stapeldegradation entwickelt werden.

Dazu wurde ein Modell entwickelt, das eine zuverlässige Quantifizierung und Interpretation der Degradation im SOFC-Stapel unter realen Betriebsbedingungen erlaubt. Das entwickelte Modell extrahiert den Innenwiderstand der Zelle basierend auf Strom-Spannungskennlinien. Der zentrale Vorteil der Quantifizierung der Degradation basierend auf der Steigung von Strom-Spannungskennlinien ist, dass die ermittelten Innenwiderstände direkt mit der Summe der einzelnen Widerstände aus den gesonderten Laborexperimenten verglichen und interpretiert werden können.

Fortschritte in der Zellentwicklung, insbesondere in der Verträglichkeit von den im Betrieb oft unvermeidlichen Wechseln zwischen oxidierender und reduzierender Atmosphäre (Redoxzyklen), führen dazu, dass die zeitabhängige Cr_2O_3-Bildung an den metallischen Interkonnektoren (MIC) nach mehr als 10 000 Betriebsstunden wesentlich zur Degradation im Brennstoffzellenstapel beiträgt. Ausserdem sind das Oxidwachstum und die extrinsische Leitfähigkeit des halbleitenden Cr_2O_3 von verschiedenen Parametern wie der Morphologie der Oxidschicht, Temperatur, Gasatmosphären, Verunreinigungen, Reaktivelemente und Wechselwirkungen zwischen angrenzenden Komponenten beeinflusst. Aus diesem Grund wurde das Oxidschichtwachstum an MIC-Proben aus chrom- (CFY) und eisenbasierten (Crofer) Legierungen mit Hilfe der Rasterelektronenmikroskopie (REM) un-

Zusammenfassung

tersucht. Darin eingeschlossen waren auch Proben aus SOFC-Stapeln von der Hexis AG[1], ein Hersteller von Brennstoffzellenheizgeräten, die bis zu 40 000 h getestet wurden. Verglichen mit der Zunahme des ohmschen Widerstandes, zeigt das Oxidschichtwachstum basierend auf REM-Querschnittsbildern eine nicht triviale, nicht lineare Abhängigkeit. Um diesen Zusammenhang zu verstehen, wurden 2D Finite-Elemente-Simulationen (FE) basierend auf einer grossen Anzahl von REM-Daten durchgeführt. Die Ergebnisse zeigen, dass die Verteilung des elektrischen Stromes durch die Oxidschicht stark von deren Morphologie geprägt ist. Das heisst, ein Grossteil der Strompfade verläuft bevorzugt über einzelne „Brücken" an den dünnsten Stellen in der Oxidschicht. Die Kombination der Quantifizierung der Oxidschicht mit der FE-Simulation von ohmschen Widerständen basierend auf REM-Daten hat weitere Vorteile. Zum einen erlaubt diese Methode eine genauere Vorhersage der MIC-Degradation, und zum anderen kann dadurch die effektive elektrische Leitfähigkeit der thermisch gewachsenen Cr_2O_3-Schicht bestimmt werden.

Das Degradationsverhalten auf der Anodenseite des MICs ist komplexer, da zum Beispiel die Cr_2O_3-Schicht Nickelpartikel enthalten kann, die bei Redoxzyklen von angrenzenden Komponenten gelöst und anschliessend in der Oxidschicht abgelagert werden. Um den Einfluss solcher eingelagerter Partikel auf die elektrische Leitfähigkeit zu untersuchen, wurden Cr_2O_3-Pellets mit Ni-Anteilen von bis zu 20 vol.% hergestellt. Die elektrische Leitfähigkeit der Pellets wurde unter reduzierender Atmosphäre (95 % N_2; 5 % H_2) und in Luft bei 850 °C gemessen. Mit den eingesetzten Methoden konnte nachgewiesen werden, dass sich während der Oxidation in Luft $NiCr_2O_4$-Spinellphasen gebildet hatten. Erneutes Auslagern in reduzierender Atmosphäre führte zu einer unmittelbaren Zersetzung der Spinellphase mit einer einhergehenden Verfeinerung des Nickels. Diese Umverteilung durch die Spinellzersetzung führt zu einer verbesserten elektrischen Leitfähigkeit in den Cr_2O_3-Pellets.

Diese Arbeit liefert neue Methoden und Modelle für eine zuverlässigere Bewertung der SOFC-Stapeldegradation basierend auf Strom-Spannungskennlinien. Dieses Vorgehen ermöglicht die Extrahierung des Innenwiderstandes des Stapels und den direkten Vergleich mit den spezifischen Laborexperimenten für die Untersuchung der einzelnen Degradationsphänomene. Dabei steht der Fokus auf der Quantifizierung und dem Verständnis des komplexen Degradationsverhaltens von metallischen Interkonnektoren, welche durch das Oxidschichtwachstum in reduzierender und oxidierender Atmosphäre den Hauptbestandteil der gesamten SOFC-Stapeldegradation bilden.

---

[1]   www.hexis.com

Abbreviations

$0, 1, 2D$	zero-, one-, two-dimensional
0	standard conditions
A	anode
AFC	alkaline fuel cell
AFM	atomic force microscopy
an	anode
APU	auxiliary power unit
ASR	area specific resistance
ASC	anode supported cell
BIB	broad ion beam
BSE	back-scattered electron detector
ca	cathode
C	cathode
CFY	interconnect material (Cr5FeY)
CGO	gadolinium-doped ceria
CHP	combined heat and power
con	contact
CPOx	catalytic partial oxidation
Crofer	interconnect material (Fe22Cr)
CSC	cathode supported cell
CTE	thermal expansion coefficient
EDX	energy dispersive X-ray spectroscopy
EIS	electrochemical impedance spectroscopy
el	electrolyte
el.	electric
f	formation
ESC	electrolyte supported cell
FE	finite element

Abbreviations

FEM	finite element modeling
fm	modified fuel composition
fo	fuel oversupply
FU	fuel utilization
fu	fuel under supply
HHV	higher heat value
in.	input
l	local
L	load
LHV	lower heat value
LSM	lanthanum strontium manganite
M	morphology
MCFC	molten carbonate fuel cell
MIC	metallic interconnect
MSC	metal supported cell
N	Nernst
OCV	open circuit voltage
ohm	ohmic
PAFC	phosphoric acid fuel cell
PEMFC	proton exchange membrane fuel cell
RE	reactive element
redox	reduction-oxidation
RU	repeat unit
RU-C	repeat unit cascade
RU-Σ	repeat unit extracted from models
S	simulated
ScSZ	ZrO_2 stabilized with Sc_2O_3
SEM	scanning electron microscopy
SOEC	solid oxide electrolyzer cells
SOFC	solid oxide fuel cell
tot	total
TPB	triple phase boundary
(V,I)	voltage-current
XRD	X-ray diffraction
YSZ	yttria stabilized zirconia

Symbols and constants

symbol	unit	label
a	-	thermodynamic activity
A	-	positive constant
ASR	$\Omega\,\mathrm{m}^2$	area specific resistance
$\mathrm{ASR_{an}}$	$\Omega\,\mathrm{m}^2$	ASR anode
$\mathrm{ASR_{ca}}$	$\Omega\,\mathrm{m}^2$	ASR cathode
$\mathrm{ASR_{con}}$	$\Omega\,\mathrm{m}^2$	ASR cathode
$\mathrm{ASR_{el}}$	$\Omega\,\mathrm{m}^2$	ASR electrolyte
$\mathrm{ASR_{M}}$	$\Omega\,\mathrm{m}^2$	ASR that considers the M-factor
$\mathrm{ASR_{MIC}}$	$\Omega\,\mathrm{m}^2$	ASR interconnect
$\mathrm{ASR_{ohm}}$	$\Omega\,\mathrm{m}^2$	ASR ohmic
$\mathrm{ASR_{RU}}$	$\Omega\,\mathrm{m}^2$	repeat unit ASR
$\mathrm{ASR_{RU\text{-}C}}$	$\Omega\,\mathrm{m}^2$	repeat unit ASR for one cascade element
$\mathrm{ASR_{tot}}$	$\Omega\,\mathrm{m}^2$	total ASR for one cascade element
$\mathrm{ASR_{tot\text{-}C}}$	$\Omega\,\mathrm{m}^2$	total ASR for one cascade element
$\mathrm{ASR_{S}}$	$\Omega\,\mathrm{m}^2$	simulated ASR
$\mathrm{ASR_{RU\text{-}\Sigma}}$	$\Omega\,\mathrm{m}^2$	total ASR from degradation model
B	-	fitting parameter
b_0	$\Omega\,\mathrm{m}^2$	additional offset
c	variable§	constant in various degradation models
C	-	fitting parameter
E_A	eV	activation energy
g_f	$\mathrm{J\,mole^{-1}}$	Gibbs free energy of formation
G	-	fitting parameter
h	$\mathrm{J\,mole^{-1}}$	enthalpy
h_f	$\mathrm{J\,mole^{-1}}$	enthalpy of formation
i	-	index
I	A	current

Symbols and constants

symbol	unit	label
j	$A\,m^2$	current density
j_l	$A\,m^2$	local current density
$\vec{j}$	$A\,m^2$	current density
K	-	fitting parameter
k_e	$m\,s^{-n}$	exponential growth constant
k_M	-	fitting parameter
k_p	$m\,s^{-2}$	parabolic growth constant
m	-	fitting parameter
M	-	morphology factor
n	-	exponent
n	-	number of elements
$\dot{n}_{l_{O^{2-}}}$	$mole\,s^{-1}$	O^{2-} flux density
P	W	power
p	Pa / bar	partial pressure
r	m	radius (metallic bridge)
r_{50}	m	50 vol.% quantile
R	Ω	ohmic resistance
R	m	Radius (simulation domain)
s_f	$J\,mole^{-1}\,K^{-1}$	entropy of formation
S	-	fitting parameter
t	s or h	time
T	°C or K	temperature
T_C	K	cold reservoir temperature
U	V	voltage
U_0	V	open circuit voltage (Nernst potential)
U_L	V	load/terminal voltage
U_N	V	Nernst potential
U_{RU}	V	RU voltage (internal loss)
x	m	spacing
x	m	oxide scale thickness
$\bar{x}$	m	mean/averaged oxide scale thickness
X	-	mole fraction
z	-	number of transfered electrons
Z	$\Omega\,m^2$	Impedance

symbol	unit	label
Z'	$\Omega\,\text{m}^2$	real part
Z''	$\Omega\,\text{m}^2$	imaginary part
α	-	chemical species
γ	-	stoichiometrich coefficient
η	-	efficiency
η_C	-	Carnot efficiency
λ	-	stoichiometric ratio
σ	$\text{S}\,\text{m}^{-1}$	electrical conductivity
$\bar{\sigma}$	$\text{S}\,\text{m}^{-1}$	mean/averaged electrical conductivity
σ_eff	$\text{S}\,\text{m}^{-1}$	electrical conductivity (experimentally determined)
σ_i	$\text{S}\,\text{m}^{-1}$	ionic conductivity
$\sigma_{\text{i}\infty}$	$\text{S}\,\text{m}^{-1}$	ionic conductivity for $t \to \infty$
τ	-	positive constant
ϕ	$^\circ$	phase shift
Φ	V	electric potential
ω	Hz	excitation frequency

constant	dimension and unit		label
e	$1.602\,176\,6208\,10^{-19}\text{C}$		elementary charge
F	$96\,485.3365$	$\text{C}\,\text{mol}^{-1}$	Faraday constant
k_B	$1.380\,6488\,10^{-23}$	$\text{J}\,\text{K}^{-1}$	Boltzmann constant
R	$8.314\,4598$	$\text{J}\,\text{mol}^{-1}\,\text{K}^{-1}$	universal gas constant

<div align="right">

Chapter **1**

</div>

Introduction

Increasing awareness of greenhouse gas emissions and the associated impacts of global warming demands a change in the electrical power supply in Europe. In addition the accident in Fukushima Daiichi in 2011 and the unanswered questions regarding a permanent nuclear waste repository induced trend-setting political debates on nuclear power exit strategies. Germany decided to shutdown all nuclear power plants until 2020 [1]. Also, Switzerland and Belgium intend to shut down their power plants, although without a clearly defined schedule [1, 2]. To ensure the security of electrical power supply with less nuclear power plants sustainable alternatives are required. Still, an improved energy efficiency on consumer and producer side seems indispensable.

Energy supplies based on renewable energies are doubtless the most desirable answer to the above mentioned challenges. However well-engineered technologies such as wind turbines, photovoltaic and solar thermal power systems, which are economically competitive electrical power generators [3], have in common that their driving forces such as wind and solar radiation fluctuate naturally. Furthermore overcapacities cannot be simply stored in the electrical grid to compensate these fluctuations. One approach to solve this problem is known as Power-to-Gas. This concept aims at converting any surplus electrical energy to a chemical energy carrier (e. g. methane (CH_4)), which can be stored straightforward in the already available infrastructure such as caverns and the natural gas grid. The chemical energy can be re-converted to electrical power on demand by suitable devices [4]. A potential configuration of the Power-to-Gas concept is schematically illustrated in Fig. 1.1.

Fuel cells are able to convert chemical energy directly into electrical current. Furthermore, in contrast to combustion engines, the electrical efficiency of fuel cells is not fundamentally limited by the Carnot efficiency [6]. Higher electrical efficiency implies
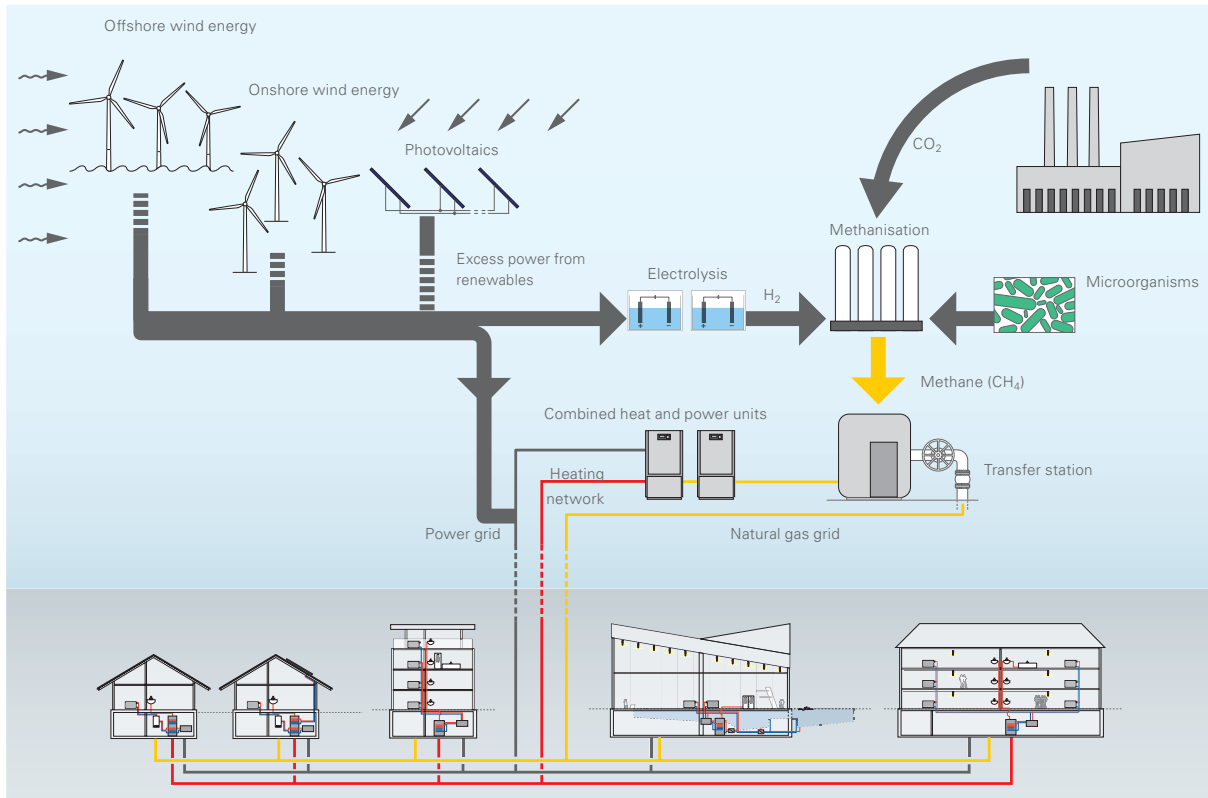
Fig. 1.1 Schematic illustration of a possible configuration of the Power-to-Gas concept. Reprinted with permission from [5].

lower demand of fuel and consequently lower emission of greenhouse gases. This characteristic might be crucial for the Power-to-Gas concept. The Solid oxide fuel cell (SOFC) is one fuel cell type that provides a high tolerance toward fuel variations, which makes them attractive for usage with hydrocarbons, e. g. from the natural gas grid. Therefore SOFCs are suitable for decentralized electrical power generation that can also reduce transmission losses e. g. by up to 7 % in Switzerland [7]. Furthermore, SOFC based combined heat and power (CHP) systems can reach overall efficiencies above 90 % [8].

The electrolysis systems for the conversion of electrical power to the chemical energy carrier must be considered and developed similarly in the comprehensive Power-to-Gas concept. However, the conceptional setup and the used materials are very similar to those of fuel cell systems. Therefore methodological approaches from SOFC research can be widely adapted to the solid oxide electrolyser cell (SOEC) technology.

One of the main focuses in present SOFC and/or SOEC research and commercialization is the reliability of stack operation and the increase of durability. For stationary SOFC applications, an average electrical power degradation below 1 % per 1000 h of stack operation over a lifetime of 40 000 h is required [9–13].

The aim of this work is to characterize and quantify the degradation in SOFC stacks. For that objective, a model-based approach to extract repeat unit resistances (ASR_{RU}) from experimental current voltage data was developed. Such a procedure provides more detailed information about the real operating behavior of stationary SOFC systems running in the field on pre-reformed natural gas from the local grid. This includes, among others, identification and quantification of leakage effects and fluctuation in the fuel composition. This approach allows in addition a comparison between stack degradation and degradation for single components as obtained under well defined laboratory conditions in respect to make lifetime and durability predictions more robust.

Recent progress in SOFC durability, particularly in the anode redox stabilities [14, 15], has shifted research towards the ohmic losses caused by oxide scales (Cr_2O_3) growing on metallic interconnects (MICs) [16, 17]. As a consequence of the continuously growing oxide scale the ohmic resistance of the MICs increases, since oxides have a significant lower electrical conductivity than the metallic base material. The net conductivity through an oxide scale layer is determined by the scale thickness, the morphology of the layer and the extrinsic (bulk) conductivity of the oxide. The extrinsic conductivity itself is known to depend on various parameters altering the defect structure like the scale formation temperature, the surrounding gas atmosphere and incorporated impurities.

In this work, the increase in the oxide scale thickness is quantified based on more than 1000 scanning electron microscopy (SEM) images and related to corresponding electrical conductivity measurements. This information is then used to establish quantitative relationships between the oxide growth and the ohmic loss over up to $40\,000\,h$ in MIC operation. However oxide scale thickness and the area specific resistance (ASR) do not exhibit a linear relation. To explain the observed non-linear relationship finite element (FE) simulations based on SEM images are performed. This method provides additional insight about the extrinsic electrical conductivity of thermal grown Cr_2O_3 scale. Combining modeling and experimental data delivers a more profound understanding of the complex degradation processes, reduces time consuming prototyping and testing activities and provides a sufficient breakdown of the involved degradation mechanism. The oxide scale on the anode side of the MIC, where Ni from adjacent components can interact with the Cr_2O_3, is further investigated by model experiments. For this purpose Cr_2O_3 pellets mixed with different amounts of nickel were prepared. The electrical conductivities of these Ni containing pellets, exposed to different atmospheres, were measured during more than $2000\,h$. To allow more thorough interpretations the obtained electrical conductivity data were complemented by SEM imaging, X-ray diffraction (XRD) and atomic force

microscopy (AFM) data.

This work is structured as follows. An overview of different fuel cell types and their potential field of application, fuel reforming methods and most relevant in-situ characterization techniques are presented in chapter 2. Chapter 3 introduces the Hexis stack concept in more details, since in this thesis the experimental work is mostly related to Hexis SOFC stacks and the corresponding materials and gives an overview of the components involved in the overall stack degradation. The model based approach that allows the quantification of degradation for the entire repeat unit based on current voltage data is introduced in chapter 4. The interconnect degradation as the main objective of this thesis is extensively discussed in chapter 5. This chapter also includes a comprehensive investigation of interactions between Cr_2O_3 and Ni under reducing and oxidizing conditions. Finally, chapter 6 summarizes this thesis and provides an outlook for further interesting work task in the scope of SOFC research.

The findings of chapter 4 and 5 are reproduced from four peer reviewed scientific publications, which were submitted in the frame of this thesis. A detailed list of publication and conference contributions is given on page 189.

Fuel cell fundamentals

This chapter presents an overview of fuel cell fundamentals and technically relevant fuel cell types including a more specific introduction to the SOFC operation principle. Fuel reforming and fuel cell characterization are introduced in sections 2.4 and 2.5, respectively. Both are crucial for a reliable interpretation of stack degradation and accurate separation of single sources as described in the subsequent chapters.

2.1 Fuel cell thermodynamics

The operating principle of fuel cells to convert chemical energy into electrical power is based on redox reactions. Thereby the oxidation reaction (i. e. the loss of electrons) and the reduction reactions (i. e. the gain of electrons) are separated in space by an ionic conductor (i. e. the electrolyte). During cell operation the ions move across the electrolyte whereas the electrons provide electrical energy to the connected device [18]. Therefore, a chemical energy carrier is continuously supplied and converted by the oxidant into electrical energy and heat. The majority of fuel cells are supplied with hydrogen and oxygen is used as oxidant. The global reaction for the hydrogen-oxygen conversion is defined as

$$H_2 + {}^1\!/_2\, O_2 \longrightarrow H_2O. \tag{2.1}$$

This net reaction is also identical to hydrogen conversion whereas reduction and oxidation takes place at the same space. In fuel cells the spatially separated reduction and oxidation reactions and the associated external electrons transport can be technically used.

Assuming that internal ohmic losses are negligible the maximum efficiency for a given fuel depends on the temperature as well as on the enthalpy and entropy changes of the

global cell reaction. The enthalpy change can be determined based on

$$\Delta h_{\mathrm{f}} = \sum_{\alpha} \gamma_{\alpha}\, h_{\alpha} \tag{2.2}$$

where γ_{α} denotes the stoichiometric coefficient for an involved chemical component α, which is determined by the chemical reaction equation for the fuel conversion [19]. Since by convention stoichiometric coefficients for reactants are negative and for products are positive the enthalpy change can be calculated for the hydrogen-oxygen conversion as given in Eq. (2.1), by

$$\begin{aligned}
\Delta h_{\mathrm{f}} &= \gamma_{\mathrm{H_2}}\, h_{\mathrm{H_2}} + \gamma_{\mathrm{O_2}}\, h_{\mathrm{O_2}} + \gamma_{\mathrm{H_2O}}\, h_{\mathrm{H_2O}} \\
&= -1\, h_{\mathrm{H_2}} - {}^{1\!}/_{2}\, h_{\mathrm{O_2}} + 1\, h_{\mathrm{H_2O}}.
\end{aligned} \tag{2.3}$$

The formation enthalpy for the elements in their most stable state such as H_2 and O_2 is zero under standard conditions i.e. at $T_0 = 298.15\,\mathrm{K}$ and at $p_0 = 1\,\mathrm{bar}$. As a consequence, for the formation of water under standard conditions, Eq. (2.3) can be simplified to [19, 20]

$$\Delta h_{\mathrm{f}} = h_{\mathrm{H_2O}}^{0} = -285.83\,\mathrm{kJ\,mol^{-1}}. \tag{2.4}$$

Note that this value for Δh_{f} assumes water in the liquid state and therefore is the higher heating value (HHV). However, this chemical energy can not be completely converted into usable electrical work. Rather the first and second laws of thermodynamics state that the Gibbs free energy defined as

$$\Delta g_{\mathrm{f}} = \Delta h_{\mathrm{f}} - T\,\Delta s_{\mathrm{f}} \tag{2.5}$$

sets the magnitude of useful electrical work. Consequently, the entropy change times the absolute temperature T has to be subtracted from the formation enthalpy. The entropy change can be determined analog to the formation enthalpy from

$$\Delta s_{\mathrm{f}} = \sum_{\alpha} \gamma_{\alpha}\, s_{\alpha} \tag{2.6}$$

and for hydrogen-oxygen conversion results in [19, 20]

$$\Delta s_{\mathrm{f}} = s_{\mathrm{H_2O}}^{0} = -163.31\,\mathrm{J\,mol^{-1}\,K^{-1}}. \tag{2.7}$$

Hence the Gibbs free energy for the formation of water under standard conditions yields

$$\Delta g_{\mathrm{f}} = (-285.83 + 48.69)\,\mathrm{kJ\,mol^{-1}} = -237.14\,\mathrm{kJ\,mol^{-1}}. \tag{2.8}$$
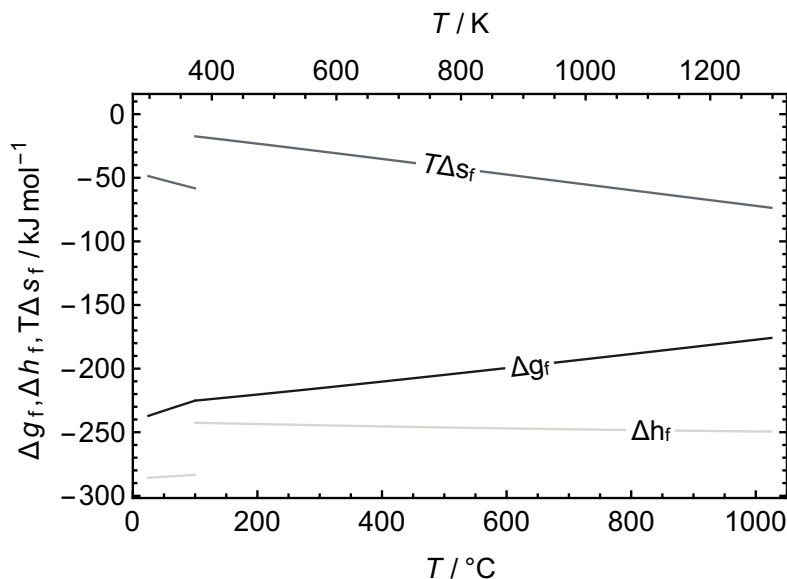
Fig. 2.1 Gibbs free energy, enthalpy of formation and the entropy change times temperature for the hydrogen-oxygen conversion as a function of temperature.

Fuel cells are commonly not operated at standard condition temperatures, thus Fig. 2.1 shows the Gibbs free energy, the enthalpy of formation and the entropy change times temperature for the hydrogen-oxygen conversion as a function of temperature. The step at $100\,°C$ for Δh_f and $T\,\Delta s_f$ is related to the water phase transformation from liquid to gaseous.

The theoretical efficiency of a fuel cell can be obtained from the ratio between the Gibbs free energy, which gives the maximum extractable electrical work and the formation enthalpy, which gives the produced heat by complete combustion. Hence the fuel cell efficiency can be calculated by

$$\eta = \frac{\Delta g_f}{\Delta h_f}. \tag{2.9}$$

For the hydrogen-oxygen conversion under standard conditions the electrical efficiency based on Eq. (2.1) is $82.96\,\%$. However, as shown in Fig. 2.2 this value decreases with increasing temperature. The efficiency limit for the methane-oxygen conversion determined in an analog manner is even higher with a maximum value of $91.86\,\%$. Note that the efficiency for methane-oxygen conversion shows a much smaller decrease with temperature compared with the hydrogen-oxygen conversion. Note that for both conversions the plotted efficiency is based on the reversible HHV, i. e. for water as product at $T > 100\,°C$ the gas phase formation enthalpy is considered. In addition, the diagram shows the Carnot
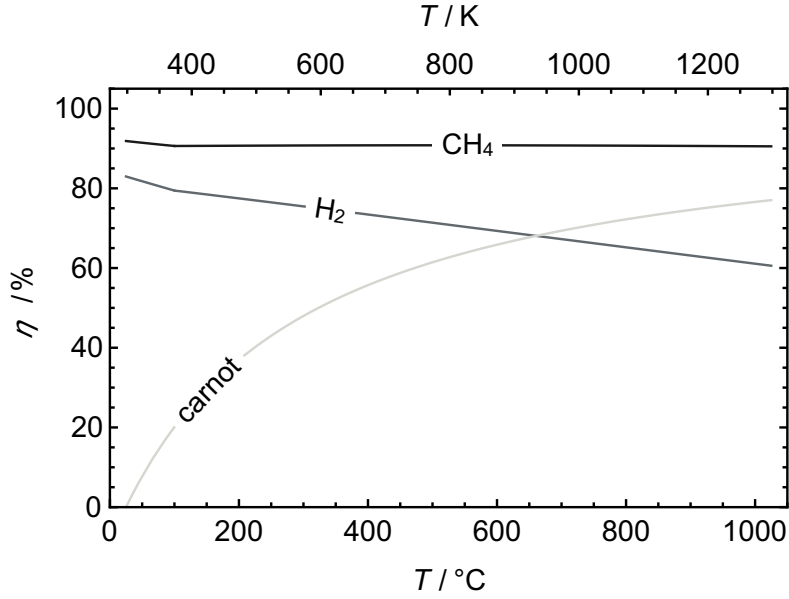
Fig. 2.2 Theoretical reversible efficiency for the hydrogen-oxygen and methane conversion related to higher heating values compared to the ideal efficiency of internal combustion engines based on the Carnot cycle.

cycle efficiency

$$\eta_C = 1 - \frac{T}{T_C} \tag{2.10}$$

using $T_C = 298.15\,\mathrm{K}$ as the lower process temperature. This illustrates the comparatively higher potential of fuel cells compared to internal combustion engines in particular in the temperature range below $650\,°C$.

The open circuit voltage of an electrochemical cell can be calculated by [19, 21]

$$E = -\frac{\Delta g_f}{z\,F} \tag{2.11}$$

where z is the number of electrons transfered per cycle and F is the Faraday constant. Since fuel cells usually are operated at atmospheric pressure, i.e. partial pressure corresponds to the reference pressure, the equation for the entropy change can be simplified to [19]

$$\Delta s_f = \Delta s_f^0(T) + R\ln\left(\frac{\prod X_{\mathrm{reactants}}^{\gamma_\alpha}}{\prod X_{\mathrm{products}}^{\gamma_\alpha}}\right) \tag{2.12}$$

where R is the universal gas constant, X the mole fraction of the species α and γ the corresponding stoichiometric coefficient. Inserting Eq. (2.12) into Eq. (2.5) and the result
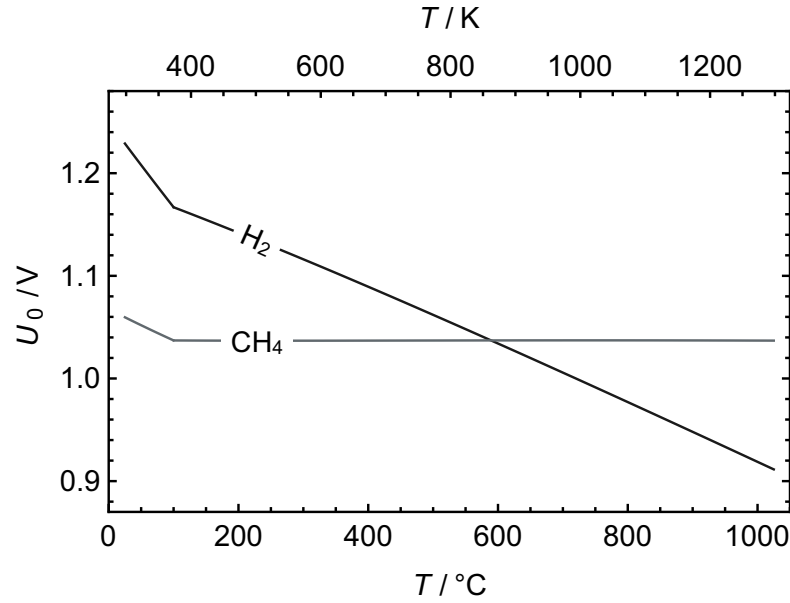
Fig. 2.3 Reversible Nernst potential for the hydrogen-oxygen and methane conversion as function of temperature.

in Eq. (2.11) yields to the Nernst equation [19, 22]

$$U_0 = \frac{\left|\Delta g_{\mathrm{f}}^0(T)\right|}{z\,F} + \frac{R\,T}{z\,F}\ln\left(\frac{\prod X_{\mathrm{reactants}}^{\gamma_\alpha}}{\prod X_{\mathrm{products}}^{\gamma_\alpha}}\right). \tag{2.13}$$

Adapting the Nernst equation to the hydrogen-oxygen conversion as given in Eq. (2.1) delivers [19]

$$U_0 = \frac{\left|\Delta g_{\mathrm{f}}^0(T)\right|}{2\,F} + \frac{R\,T}{2\,F}\ln\left(\frac{X_{\mathrm{H_2}}\sqrt{X_{\mathrm{O_2}}}}{X_{\mathrm{H_2O}}}\right). \tag{2.14}$$

Fig. 2.3 shows the reversible Nernst potential as function of temperature for both hydrogen-oxygen and methane conversion. In reality, the reversible fuel cell efficiency is reduced during operation i.e. at currents greater zero, by various influencing factors such as fuel and false air leakages, ohmic and polarization losses. Further details about SOFC specific losses are given in chapter 3 and summarized in Table 3.2.

2.2 Major fuel cell types

Fuel cells are typically divided into five major types, which are primarily distinguished by the electrolyte material [22, 23] and, as a consequence, the relevant ionic charge carrier. The cells are used for different applications and operated at characteristic temperatures

Table 2.1 Overview of different fuel cell types with applied materials and typical operation temperatures [22, 23].

cell type	electrolyte	carrier	operating temperature	catalyst	cell components	fuel compatibility	application examples
PEMFC	polymer membrane	H^+	80 °C	Platinum	carbon based	H_2, methanol	mobile applications and μCHP
PAFC	liquid H_3PO_4	H^+	200 °C	Platinum	carbon based	H_2	large CHP
AFC	liquid KOH	OH^-	60–220 °C	Platinum	carbon based	H_2	space vehicles
MCFC	molten carbonate	CO_3^{2-}	650 °C	Nickel	stainless based	H_2, CH_4	medium and large CHP
SOFC	ceramic	O^{2-}	600–1000 °C	Perovskites, Nickel	ceramic based	H_2, CH_4, CO	all size CHP, APU

[22, 23]. Table 2.1 summarizes the different fuel cell types with their corresponding key features.

The proton exchange membrane fuel cell (PEMFC) is probably the best known fuel cell type since a high power density, a low operating temperature and excellent dynamic characteristics makes it the preferred cell type for car manufactures [22, 24]. PEMFC are also used for stationary applications (e. g. as emergency power generator) and are also proposed for portable applications such as cell phones and notebooks [24]. The phosphoric acid fuel cell (PAFC) was the first fuel cell type available commercially [23]. PAFCs are typically used for CHP applications up to 200 kW [6, 23]. PAFC can be operated with reformed fossil fuels and air [25]. The alkaline fuel cell (AFC) provides high electrical efficiencies of up to 70 % [25]. A major challenge remains the catalyst intolerance toward impurities such as carbon oxides and the need of air and fuel purification [6, 23, 25]. However, AFC application fields include submarines and space missions. The molten carbonate fuel cell (MCFC) is a high temperature fuel cell, which uses a carbonate salt mixture as electrolyte [25]. Due to the high operating temperature high reaction rates can be reached by Ni-based catalyst [23, 25]. MCFC are currently in use for coal-based and natural gas power plants [25]. The solid oxide fuel cell (SOFC) is a high temperature fuel cell with a ceramic electrolyte [25, 26]. The high operating temperature allows the use of various fuels and internal reforming, without the need of noble metals for the electrodes [23]. SOFCs are primarily designed for stationary applications such as CHP. Due to
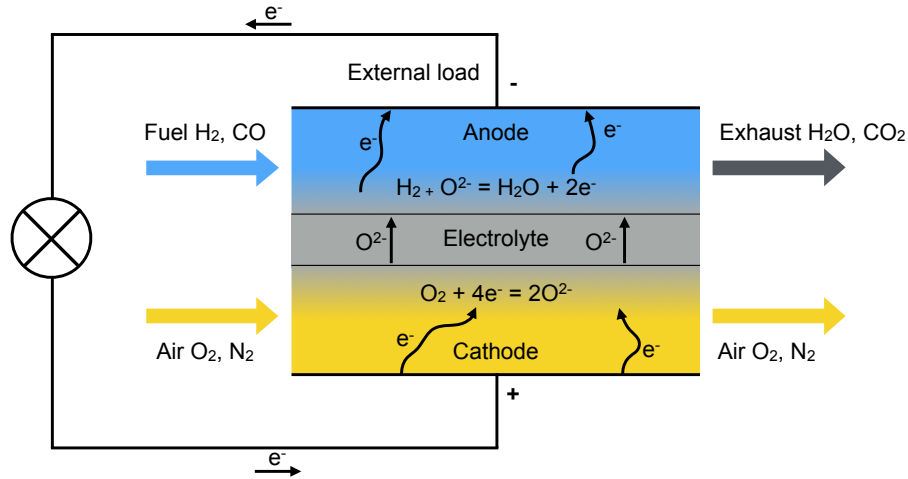
Fig. 2.4 Illustration of electrochemical processes in an SOFC with external load.

the fuel tolerance to various hydrocarbon fuels such as diesel SOFCs are also suitable as vehicle onboard auxiliary power units (APUs) [27].

2.3 Solid oxide fuel cell functionality, design and types

The global electrochemical reactions of an SOFC are shown in Fig. 2.4. The convertible fuel components are basically hydrogen and carbon monoxide. On the anode of the electrolyte, H_2 and eventually CO is oxidized according to the overall reactions

$$H_2 + O^{2-} \longrightarrow H_2O + 2\,e^- \tag{2.15}$$

$$CO + O^{2-} \longrightarrow CO_2 + 2\,e^-. \tag{2.16}$$

The released electrons are conducted through the external load. CO can also react with H_2O according to the water gas shift reaction,

$$CO + H_2O \longrightarrow H_2 + CO_2. \tag{2.17}$$

On the cathode side of the electrolyte, oxygen is ionized by the electrons returning from the external load,

$$O_2 + 4\,e^- \longrightarrow 2\,O^{2-}. \tag{2.18}$$

At typical SOFC operating temperatures between 550 °C and 1000 °C the electrolyte, usually made of yttria-stabilized zirconia (YSZ) or scandia stabilized zirconia (ScSZ), becomes an ion conductor. The oxygen ions move from the cathode side to the anode side driven
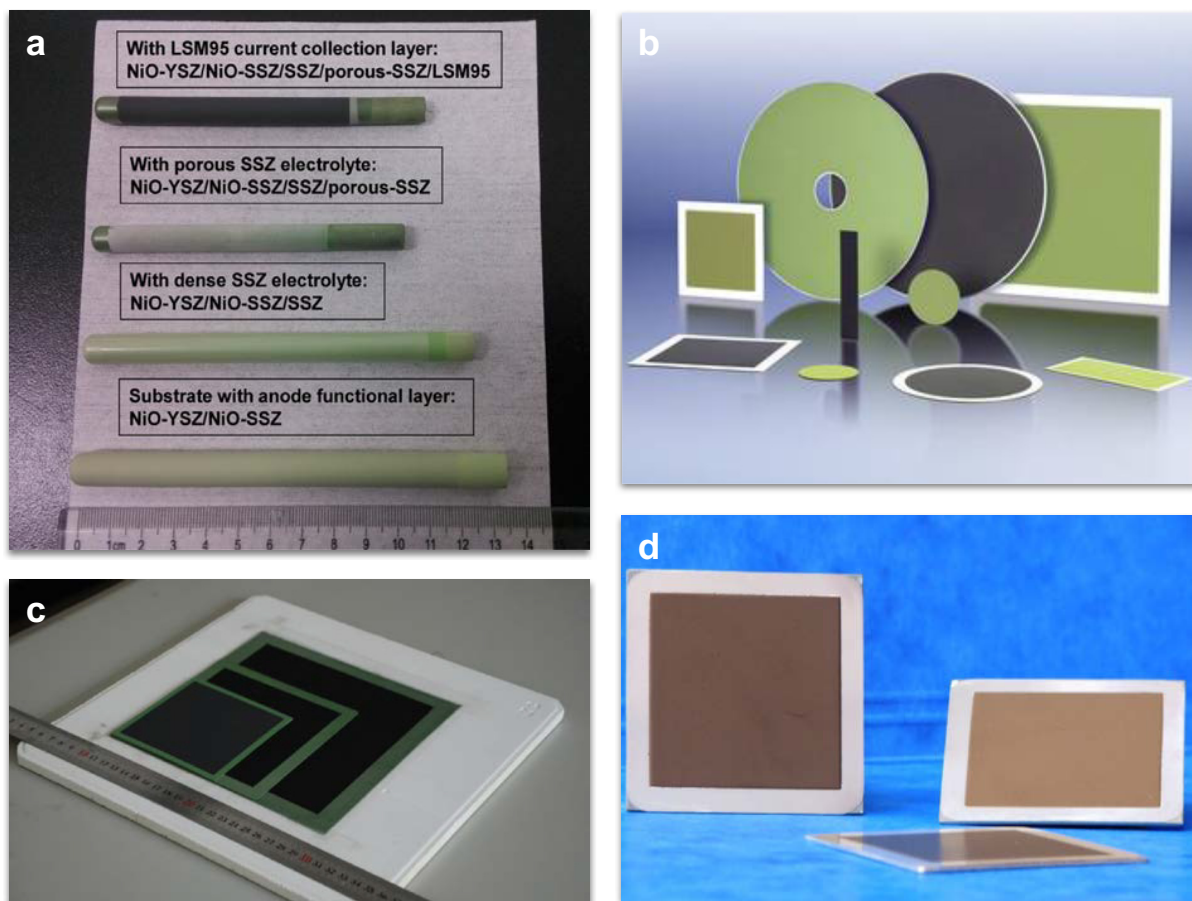
Fig. 2.5 Examples of different SOFC types: a) Cathode supported tubular SOFCs at different fabrication steps, reprinted with permission from [31]. b) Electrolyte supported SOFCs, reprinted with permission from [32]. c) Anode supported SOFCs, reprinted with permission from [33]. d) Metallic supported SOFCs, reprinted with permission from [34].

by the electrochemical potential across the electrolyte. Note that the elementary kinetics and the corresponding reaction pathways in SOFCs are more complex than shown here (see e. g. [28]).

SOFCs are designed and developed for different applications and power classes. According to that there is a variety of different SOFC designs, which can be subdivided into tubular and planar cells. Some examples of tubular and planar SOFCs are shown in Fig. 2.5. Tubular SOFCs were established by Siemens Westinghouse and other manufactures [23, 26]. The main design advantage of these tubular cells is that the sealing between oxidant and fuel does not have to be located in the hot zone [23, 26, 29]. Issues with high temperature sealing materials are not relevant for tubular SOFCs. Furthermore tubular cells provide a high resistivity against thermal cycles [26, 29]. However, the relatively long electrical current pathways lead to internal ohmic losses and therefore to smaller

current densities compared to the planar SOFC design [26, 29, 30]. Another advantage of the planar cell design is the possibility for a simple serial connection by bipolar plates and interconnects, respectively, within stacks. Probably one of the most crucial factor for the development planar cells is the perspective of applying low-coast fabrication methods e. g. tape casting and screen printing, during cell manufacturing process [23, 26, 30]. The main drawback of the planar cell design is that the sealings between fuel and air channels, which are located in the hot zone in most designs require sophisticated materials [23, 29]. Note that the Hexis stack is, in contrast, a design without the need of additional sealing material.

A further categorization of SOFCs is done by the supporting layer:

- anode supported cell (ASC)

- cathode supported cell (CSC)

- metal supported cell (MSC)

- electrolyte supported cell (ESC)

Fig. 2.5 shows representative images for these cell types. The supporting layer provides the mechanical stability during manufacturing, assembling and operation. The advantage of the ASC, CSC and MSC is the lower ohmic resistance achieved by an electrolyte thickness of less than $20\,\mu$m compared to a typical ESC with electrolyte thicker than $100\,\mu$m [9, 35, 36]. This is even more relevant for SOFCs operated at low temperature as their ionic conductivity is thermally activated. The main advantage of the ESC compared to the other cell types is the improved redox stability, which is an essential feature as start-stop procedure and irregular shutdowns occur inevitably in the field [26]. Despite these advantages, most researchers and manufacturers focus on ASCs [35, 37]. Typical examples for CSC are tubular cells. In the past few years the MSCs have attracted the interest of the SOFC community as an alternative cell concept [38–40]. Some characteristic advantages of MSCs are low material costs, manufacturing benefits and mechanical ruggedness during operation where the latter make them suitable for mobile application [38, 39]. MSCs indicate improved redox and thermal cycle stability compared to the brittle ceramic or cermet supports in ASCs, CSCs and ESCs [38, 39]. A potential issue for the MCSs is the formation of oxide scales on the metallic support [38]. On MSCs such scales are even more problematic than on ESCs (to which this work is dedicated), as not only the electrical performance but also the mechanical strength of the cells is severely affected. Furthermore, oxide scale formation is also induced during cathode sintering at high temperature and oxidizing atmosphere [41].
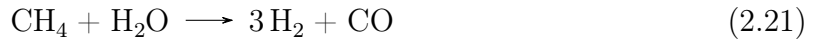
2.4 Fuel reforming

One of the main advantage of SOFCs is their ability to operate on a wide spectrum of fuels, however, a reforming of hydrocarbons to electrochemically convertible H_2 and CO is required. This can be done in an external reforming unit upstream of the cell stack, or within the cell's anode channels itself. However, such a so called internal reforming, is more difficult to control. Hydrocarbon pyrolysis can lead to soot formation, but a carbon deposition on the electrochemically active sites of the electrodes has to be avoided. Global reaction for carbon formation during methane reforming is given by:

$$CH_4 \longrightarrow C + 2\,H_2 \tag{2.19}$$

and for higher hydrocarbons [26]

$$C_xH_{2x+2} \longrightarrow xC + (x+1)\,H_2. \tag{2.20}$$
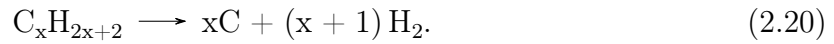
Soot formation can be suppressed by adding steam to the fuel supporting the following global reaction:

$$CH_4 + H_2O \longrightarrow 3\,H_2 + CO \tag{2.21}$$

and for higher hydrocarbons [26]

$$C_xH_{2x+2} + xH_2O \longrightarrow (2\,x+1)\,H_2 + xCO. \tag{2.22}$$
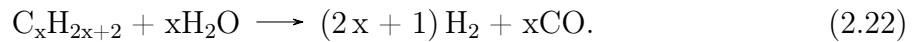
The water formed during the fuel oxidation according to Eq. (2.15) supports the steam reforming reactions, Eqs. (2.21) and (2.22). Another issue of internal reforming is the endothermicity of the steam reforming process, which leads to local heat sinks [26]. As a consequence, temperature gradients may occur on the cell leading to mechanical stress and possibly cracks [26, 42]. Due to these challenges with internal reforming SOFC system manufacturers often favor an external reforming process. The three main reforming concepts used in SOFC applications are presented next: steam reforming, catalytic partial oxidation and autothermal reforming.

2.4.1 Steam reforming

The stoichiometric steam reforming process for methane is shown in Eq. (2.21). To avoid soot formation the steam to carbon ratio is adjusted to values over 2 [26]. Taking into

account the water-shift reaction (Eq. (2.17)) the following global methane conversion may occur for a steam to carbon ratio of 3:

$$CH_4 + 3\,H_2O \longrightarrow 4\,H_2 + CO_2 + H_2O. \tag{2.23}$$

Heat must be supplied to this endothermic reaction which requires a sophisticated SOFC thermal management system. Yet another difficulty of steam reforming in μCHP applications is the required water supply. For an autonomous operation water can be rehashed from the exhaust condensate but a purification system is required then [43].

2.4.2 Catalytically partial oxidation reforming

During catalytically partial oxidation (CPOx) reforming the hydrocarbon fuel is partially oxidized to hydrogen and carbon monoxide. This conversion is achieved by controlling the carbon to oxygen ratio also known as the air-fuel ratio lambda. The stoichiometric oxidation defines the lambda value of 1 (e. g. 2 mole O_2 per mole CH_4). For methane an ideal CPOx is achieved at $\lambda = 0.25$:

$$CH_4 + {}^1\!/_2\,O_2 \longrightarrow 2\,H_2 + CO. \tag{2.24}$$
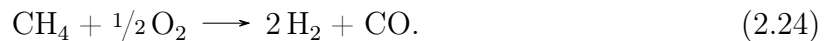
However, real CPOx processes operate slightly above this lambda. Also, a sufficient reforming temperature is required to prevent soot formation. The soot formation tendency during CPOx reforming can be investigated by thermodynamic equilibrium calculations. Fig. 2.6 visualizes the soot formation tendency depending on the process temperature and lambda for natural gas with a methane content of about 90 % as provided from the local grid in Winterthur, Switzerland [44]. The contour plot visualizes the fraction of soot $X_{C(s)}$ formed per mole of natural gas. For the given natural gas composition, the reformer temperature must be above 750 °C with a $\lambda > 0.26$ in order to avoid soot carbon deposition on the reformer and the cell catalysts. However, an increasing lambda decrease the fuel cell efficiency as H_2 and CO are oxidized by excess O_2 and are not available for electrochemical conversion anymore. Therefore, controlling the CPOx lambda is crucial in SOFC systems, and varying natural gas compositions in field applications pose an additional challenge. However, starting the SOFC without providing steam or water is a key advantage of CPOx over steam reforming [26].
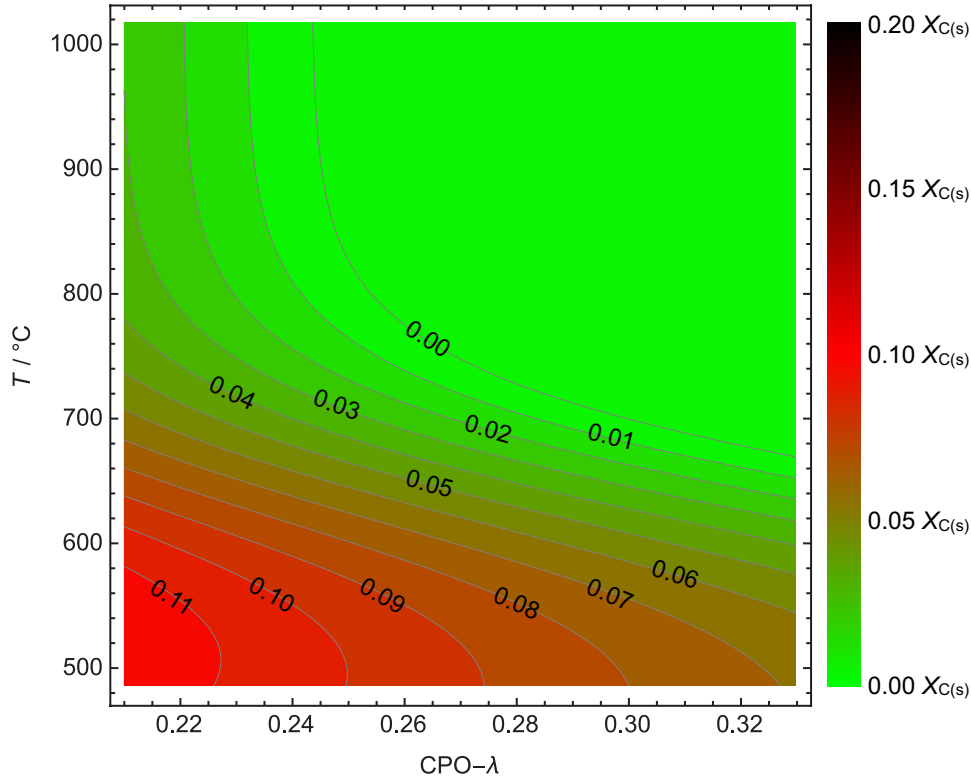
Fig. 2.6 Soot formation region for natural gas from the local grid with a CH_4 content of $90\,\%$ [44] as a function of temperature and CPOx λ at ambient pressure based on thermodynamic equilibrium calculation.

2.4.3 Autothermal reforming

The autothermal reforming simplifies the thermal management by combining the exothermic CPOx and the endothermic steam reforming. The heat released by the CPOx reactions is directly consumed by the steam reforming reactions. Combining Eqs. (2.21) and (2.24) yields to [22]

$$C_xH_y + zH_2O + (x - \tfrac{1}{2}z)O_2 \longrightarrow (z + \tfrac{1}{2}y)H_2 + xCO_2. \qquad (2.25)$$
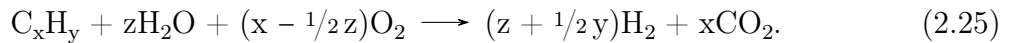
However, this strategy requires a proper control system to adjust the endothermic and exothermic processes especially during start-up and load point variation.

2.5 Fuel cell characterization

Fuel cell characterization is important to quantify their efficiency and their degradation for benchmarks and technological improvement. It is also important to consider
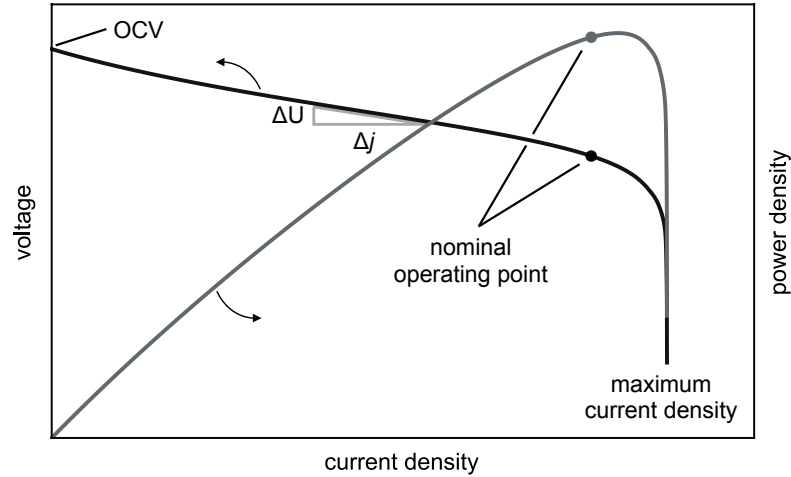
Fig. 2.7 Schematic illustration of (V,I)-characteristic and power density.

conditions such as temperature, load point, fuel type, fuel amount, applied materials and stack design. The most common in-situ electrical characterization techniques are the current-voltage (V,I) measurements and the electrochemical impedance spectroscopy (EIS).

2.5.1 Current voltage characteristic

Fuel cells are generally characterized by the electrical operating parameters current, voltage and/or power [8, 44–48]. Variations in the additional parameters i. e. temperature, fuel composition and available fuel amount are leading to alterations of the (V,I)-characteristic [22]. Fig. 2.7 shows a schematic illustration of a (V,I)-curve and the corresponding power density. The main parameters extracted from (V,I)-curves are open circuit voltages (OCV) and overall area specific resistances (ASR$_{tot}$) [46, 49]. Deviations between the measured and theoretical OCVs (based on the nominal anode and cathode gas compositions) can be related to unusual fuel reformer operation or fuel leakages. A measure for ASR$_{tot}$ can be determined based on the slop of the (V,I)-characteristic

$$\text{ASR}(j_0) = \left| \frac{\mathrm{d}U}{\mathrm{d}j}(j_0) \right|. \tag{2.26}$$

ASR(j$_0$) has units of $\Omega\,\text{m}^2$, which originates from the current density j in $\text{A}\,\text{m}^{-2}$. ASR(j$_0$) is denoted as ASR$_{tot}$ since experimentally (V,I)-data necessarily includes all losses for a given operating point that can be asocciated to an overal ohmic resistance. The time dependent ASR$_{tot}$ evolution is an indicator for cell and stack degradation, respectively.

Deviation and changes in the maximal current density are related to variation in the available fuel amount and gas composition.

2.5.2 Electrochemical impedance spectroscopy

The electrochemical impedance spectroscopy is one of the most often used diagnostic techniques in the scope of electrochemistry [22, 50]. This technique allows in-situ measurements and provides a more accurate interpretation of electrochemical fuel cell behavior compared to (V,I)-measurement. The different electrochemical processes and the charge separation at material transitions/interfaces exhibit characteristic time constant. As a result the impedance spectra enables the separation of ohmic, polarization and gas concentration losses from the overall resistance ASR_{tot} [37]. This separation is essential in order to understand the efficiency degradation from a phenomenological viewpoint.

Fig. 2.8 illustrates an EIS measurement with galvanostatic sinusoidal excitation around a given load point and the corresponding voltage response. The impedance $Z(\omega)$, defined as

$$Z(\omega) = \frac{U(\omega)}{I(\omega)}, \tag{2.27}$$

depends on the given load point and the excitation frequency. Capacitive behavior is usually associated with an accumulation of charge carriers, e. g. at interfaces where charge transfer happens [22]. As a consequence a phase shift ϕ between the excitation and the response occurs. The frequency-dependent phase shift due to the fuel cell processes is determined. This is illustrated in Fig. 2.9a for a single load point. The impedance $|Z|$
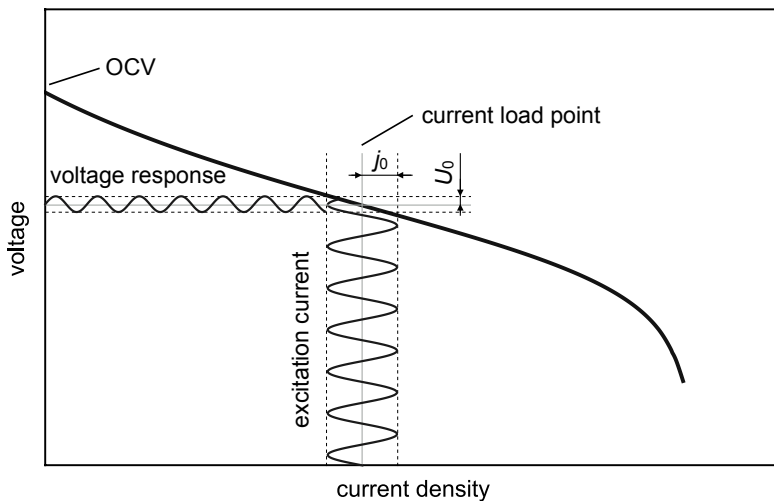
Fig. 2.8 Schematic illustration of EIS measurement with galvanostatic sinusoidal excitation with its associated voltage response for a given load point.
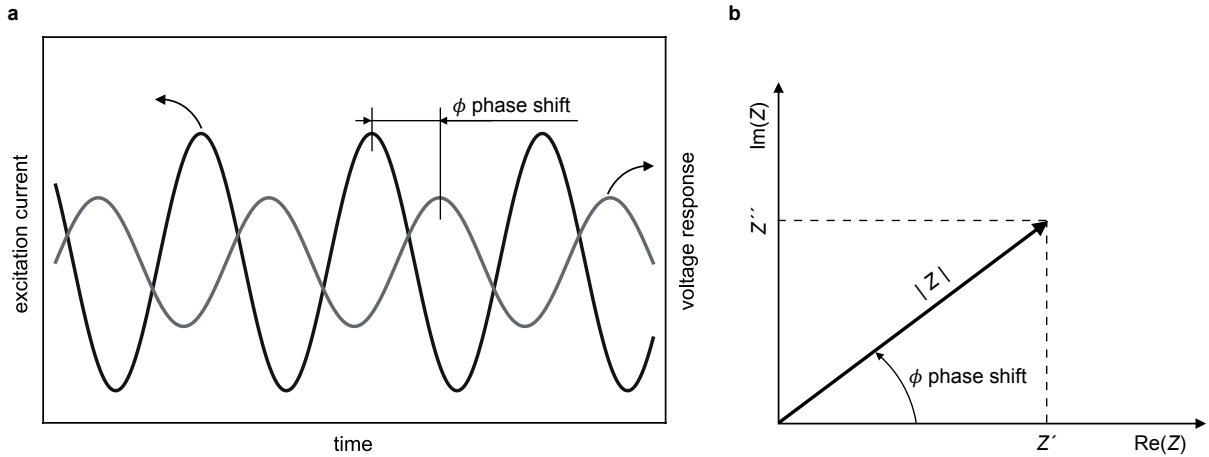
Fig. 2.9 a) Phase shift during EIS measurement between excitation current and voltage response. b) Vector diagram of the impedance.

can be transformed into the complex plane by

$$\mathrm{Re}(Z) \equiv Z' = |Z|\cos(\phi) \tag{2.28}$$

and

$$\mathrm{Im}(Z) \equiv Z'' = |Z|\sin(\phi) \tag{2.29}$$

as shown in Fig. 2.9b [50]. If now the excitation frequency is varied, typically by several orders of magnitude from mHz up to MHz, the impedance can finally be plotted in a Nyquist-plot as shown in Fig. 2.10. Different process can be separated by partly overlapping semi circles in the Nyquist plot. In this example the three processes labeled as I, II and III are related to activation polarization. Thereby the characteristic peak
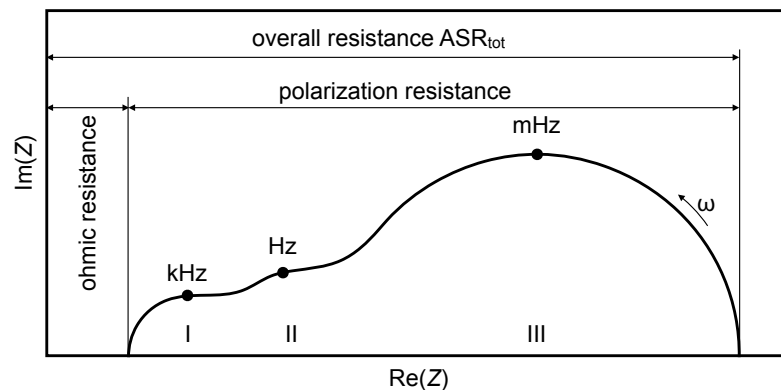
Fig. 2.10 Schematic impedance spectrum shown as a Nyquist plot with characteristic peak frequencies and separation of different resistances.

19

frequencies are indicated by small dots on top of the three semi circles. In this example, firstly, the low frequency process III in SOFCs operated with natural gas is interpreted as gas concentration impedance. The processes I and II can be assigned to anode and cathode polarization. The ohmic resistance can be read from the axis intercept in the high frequency region (MHz). The overall resistance ASR_{tot} can be extracted from the low frequency (mHz) axis intercept [37]. In general, the interpretation of EIS is difficult and requires a lot of experience and knowledge about the fuel cell layout and the applied materials. More details on the interpretation of EIS-data are given in chapter 4.

Hexis SOFC system and degradation

This chapter provides an overview of the Hexis SOFC system, since all experimental and theoretical work in this thesis is, if not noted otherwise, related to this stack and the materials used therein, respectively.

3.1 Hexis Galileo 1000 N system

Fig. 3.1 shows the Hexis Galileo 1000 N system, a SOFC based stand-alone μCHP system, which consists of the fuel cell stack and the balance of plant components as well as an additional condensing burner. The Galileo 1000 N is designed to cover the required full heat demand and the averaged annually electrical energy demand in single-family homes, which is about 5000 kWh electricity per year [52]. The system is operated with natural gas and allows an overall thermal and electrical efficiency of more than 95 % referred to lower

Fig. 3.1 Hexis Galileo 1000 N stand-alone μCHP system for single-family homes. Reprinted with permission from [51].

Table 3.1 Excerpt of technicals specification for the Hexis Galileo 1000 N [8, 51].

electrical output	1	kW (AC,net)
thermal output	1.8–2.5	kW
electrical efficiency	35	% (LHV)
overall efficiency	95–109	% (LHV)
fuel	natural gas, biogas	
fuel reformation	CPOx	
additional condensing burner	20	kW
noise (1 m in front of the system)	30	dBA
dimensions (width / depth / height)	620 / 580 / 1640	mm
weight	170	kg
certification	C€	

heat value (LHV) [8, 51, 52]. An excerpt of the most relevant technical specifications of Galileo 1000 N is given in Table 3.1.

Fig. 3.2 shows a schematic illustration of the Hexis SOFC based μCHP system with a nominal electrical power output of 1 kW AC. The system is fueled by natural gas, which is first mixed with the required amount of air for CPOx reforming (see section 2.4.2 for more details) at the hot module inflow. The mixture rich in H_2 and CO is then supplied to the fuel cell stack. An additional air stream provides the required oxygen to the cathodes and ensures the temperature control for the stack. The exhaust heat is transferred to the domestic heat circuit. The Hexis system also incorporates a DC/AC inverter to supply electricity to the grid.
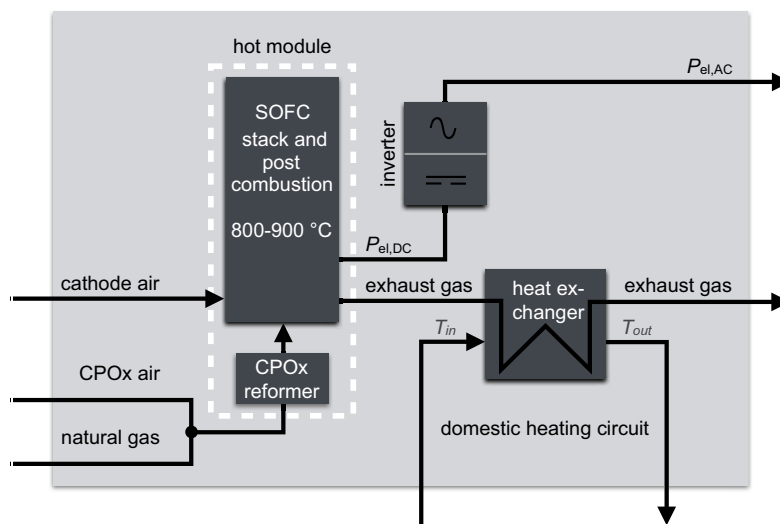
Fig. 3.2 Schematic illustration of the Hexis SOFC based μCHP for decentralized feed- and heat exchanger for domestic heat supply consisting of SOFC stack, CPOx reformer and electrical inverter.
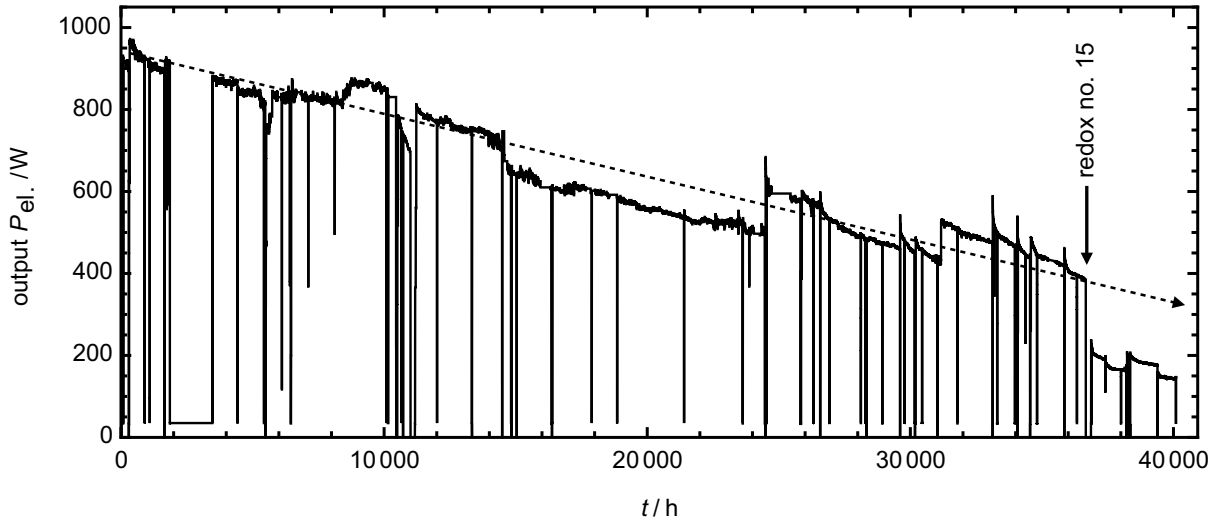
Fig. 3.3 Electrical power output obtained from a Hexis Galileo 1000 N system for more than 40 000 h. The system was operated at 900 °C with natural gas from the local grid in Winterthur, Switzerland. Hexis stack technology of 2007 was used. The electrical power degradation is indicated by the dashed line and is about 1.6 % per 1000 h till 37 000 h. At start, he electrical efficiency was 28 % DC and 24 % AC net [8].

Hexis Galileo 1000 N was launched in autumn 2013 into a pilot market. Before then more than 200 Galileo 1000 N systems have been installed and tested in demonstration projects in Germany and in the german-speaking part of Switzerland. Based on these field test experiences Hexis research and development activities focused on improvements regarding durability and long-term stability of the SOFC stacks as well as on the overall efficiency of the μCHP system [8]. Electrical power output data from a long-term Galileo 1000 N system test operated at 900 °C with CPOx reformed natural gas from the local grid in the Hexis laboratory in Winterthur is shown in Fig. 3.3. The test was started in 2007 and finished after the required minimal stack life time of 40 000 h in 2012. The overall power degradation was about 1.6 % per 1000 h till 37 000 h stack operation. Then redox cycle number 15 led to a sudden power drop resulting in total failure. Note that the applied cell and stack technology for this system date back to 2007. However, Fig. 3.4 shows the electrical power output of a Galileo 1000 N system with the latest cell and stack technology (as of 2015). In this test only a small degradation of about 0.5 % per 1000 h operation can be observed within the first 11 000 h. After this point in time the degradation was partially compensated by a slight increase of the natural gas input [52]. The resistance against thermal and redox cycles could be also significantly improved with the latest cell technology. Fig. 3.5 shows the electrical power output evolution during numerous on/off cycles, power modulations and inverter disruption within 5500 h of operation. The
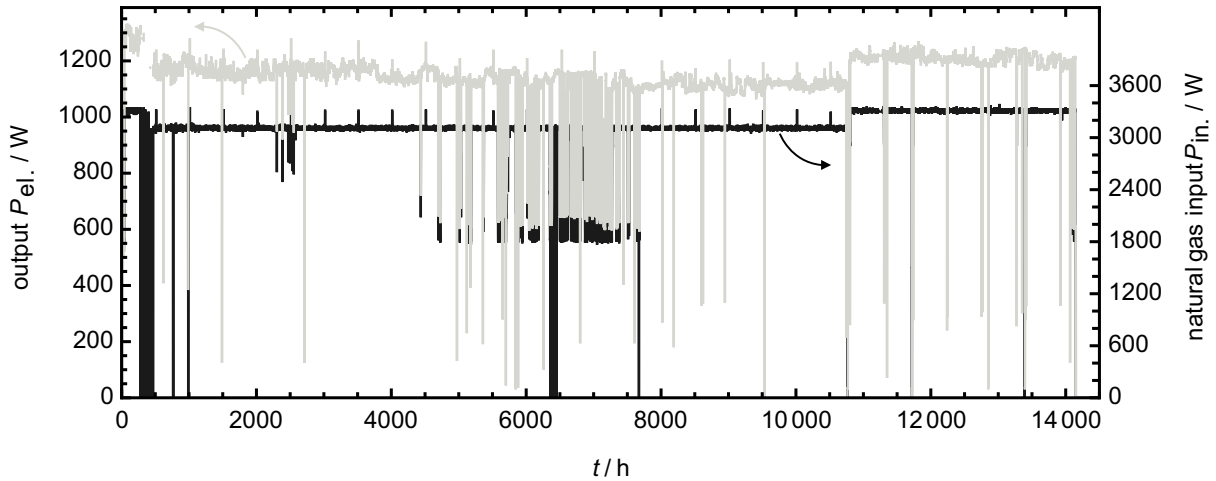
Fig. 3.4 Electrical power output of a Galileo 1000 N operated for more than 14 000 h in Albstadt-Ebingen, Germany. The average electrical power degradation (gray) between 1000 and 11 000 h is about 0.6 W per 1000 h, which corresponds to $0.5\,\%\,\text{kh}^{-1}$. The slight increase of gas input (black) after 11 000 h partially compensates the stack degradation [52].
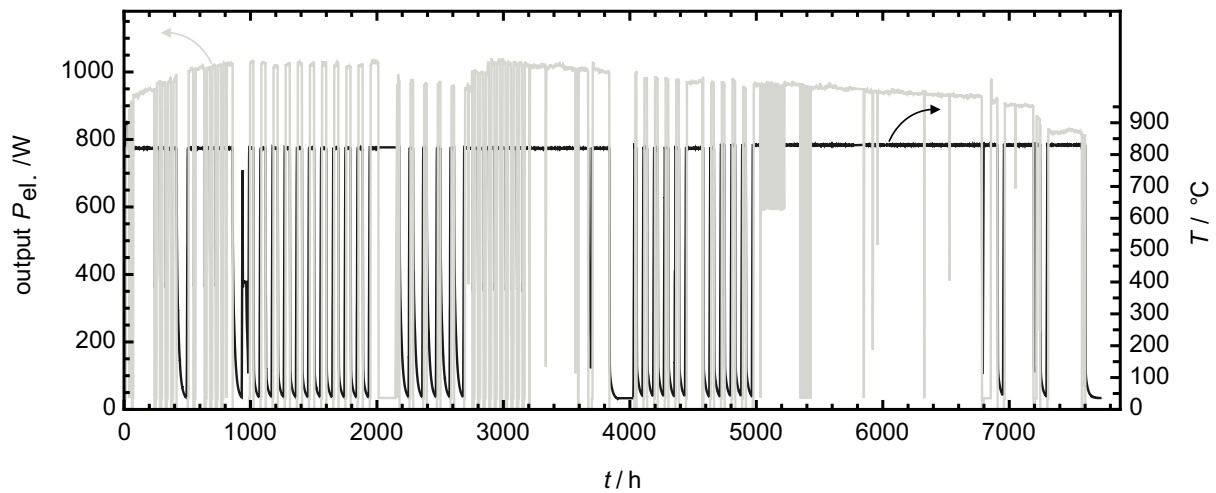

Fig. 3.5 Electrical power output (gray) and stack temperature (black) of a Galileo 1000 N system during cycling test, including 50 on/off cycles, 20 inverter disruptions and 20 power modulations. Power degradation differs not significantly compared to the long-term test e. g. as shwon in Fig. 3.4 [53].

observed electrical power degradation during these demanding stack operations does not significantly differ from degradation under normal operation conditions.

3.2 Hexis stack concept

Since a single fuel cell does not provide enough power for technically relevant applications several cells are stacked and thereby connected in series. The stack concepts are specific, i.e. most manufactures have their proprietary design. This is related to the fact that fuel cell systems and the integrated stacks are developed for different applications and power classes. The cell design might differ by the flow field on the anode and the cathode side, the gas sealing concept, the manifold connections, the thermal management and the post combustion concept [26]. Most cells are nowadays of rectangular shape, the disk-shaped planar cell used by Hexis is less common. The resulting cylindrical stack is shown in Fig. 3.6. The Hexis cell with an active area of $100\,cm^2$ as well as the metallic interconnects (MICs) have a center hole to provide the fuel to the anode. The anode flow pattern is radial, i.e. from the center hole to the outer stack surface. Air is provided to the cathode channels by four centripetal inlets. The air gets redirected at the stack center and leaves the stack radially. As a consequence, most of the cell area is operated in a co-flow regime. In the Hexis stack design, the post combustion of unutilized fuel takes place adjacent to the stack, labeled as afterburner in Fig. 3.6. The released heat in the post combustion zone simplifies the thermal stack management [8, 12], i.e stack temperature is widely constant and independent of the stack operating point. The system
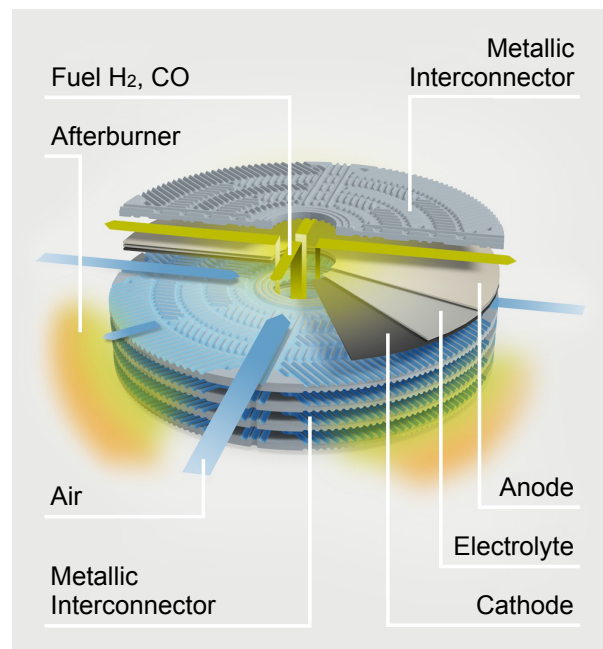

Fig. 3.6 Hexis SOFC stack concept with electrolyte supported disk-shaped planar cells. Reprinted with permission from [51].
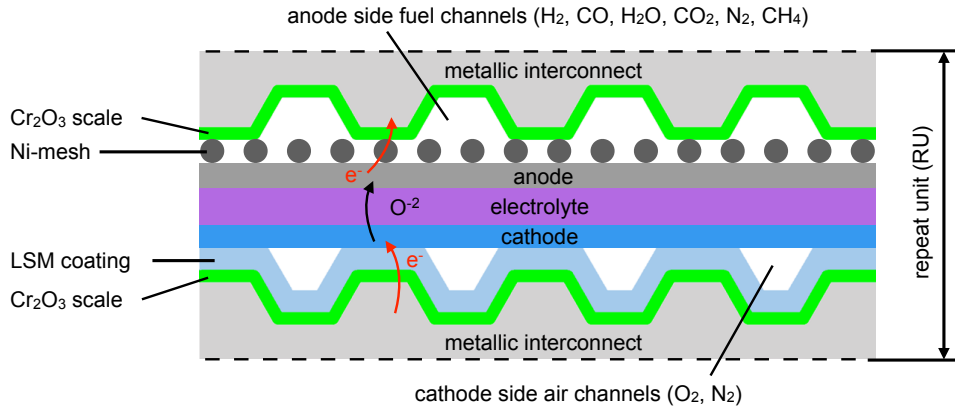
anode side fuel channels (H₂, CO, H₂O, CO₂, N₂, CH₄)

metallic interconnect

Cr₂O₃ scale
Ni-mesh

anode

O⁻² electrolyte

cathode

LSM coating
Cr₂O₃ scale

metallic interconnect

repeat unit (RU)

cathode side air channels (O₂, N₂)

Fig. 3.7 Schematic illustration of a single repeat unit cross section within the Hexis fuel cell stack.

is nominally operated at $850\,°C$ with a cell current density of about $300\,\mathrm{mA\,cm^{-2}}$ [12]. The cells are fueled by $0.04\,\mathrm{g\,h^{-1}\,cm^{-2}}$ (related to the active cell area) CPOx reformed natural gas [8, 12].

Fig. 3.7 schematically shows the cross section of the Hexis repeat unit (RU). A RU includes, from the bottom to the top: cathode side interconnect, Cr_2O_3 oxide layer formed on the interconnect exposed to the cathode atmosphere, lanthanum strontium manganite (LSM) coating to avoid cathode poisoning, the cathode, the electrolyte, the anode, a Ni-mesh that acts as current collector, Cr_2O_3 scale formed on the MIC on the anode side and anode side interconnect.

A fully assembled stack of the Hexis Galileo 1000 N μCHP system consisting of 60 RUs is shown in Fig. 3.8a. The CPOx reforming catalyst is integrated into the bottom area of the unit. Fig. 3.8b shows a five cell short stack test bench on which each cell's voltage and temperature can be measured individually. Also, isothermal conditions are assured by an external heating system. This is important for a reliable cell and RU characterization. The current voltage and the electrochemical impedance spectroscopy measurements presented in this thesis are performed on such short stacks, typically.

3.3 Degradation behavior of Hexis SOFC stack

The long-term stability of SOFC materials is one of the major issues for a successful commercialization of this technology [46]. Degradation phenomena are related to microstructural changes in both electrodes and the electrolyte, deactivation and poisoning of catalytically active areas e. g. by chromium poisoning or carbon deposition, the formation of electrically low conductive oxides scales on the MICs and increasing contact losses
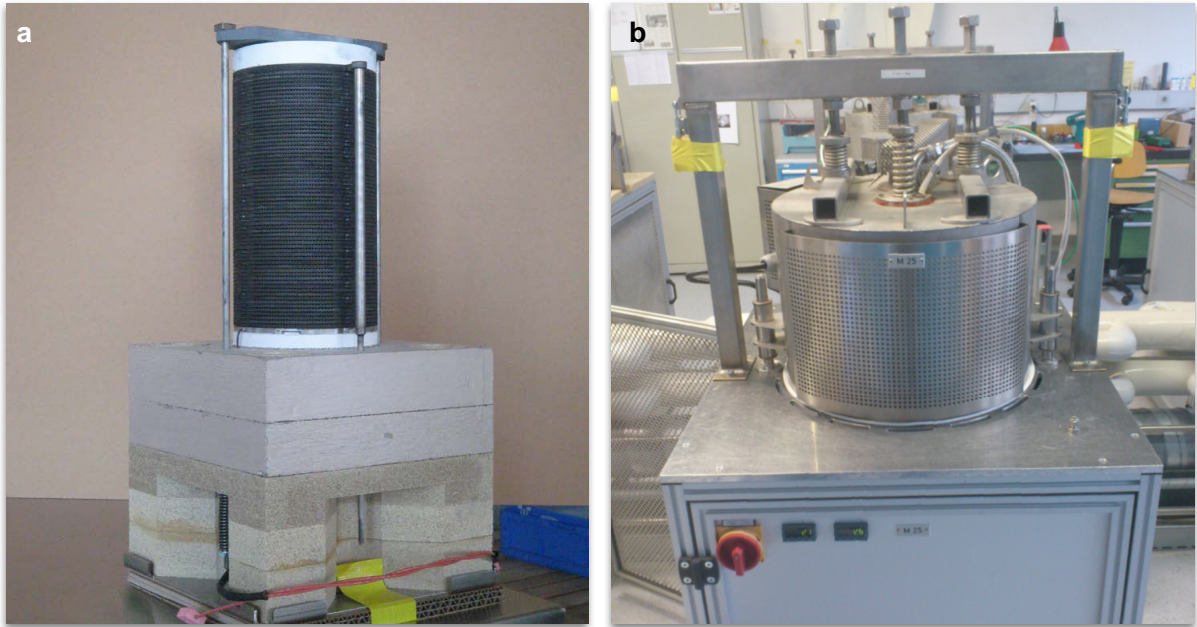
Fig. 3.8 a) Hexis Galileo 1000 N stack with 60 cells. b) 5 cell test bench as used in the Hexis laboratory for cell and stack characterization. Reprinted with permission from [54].

between various RU components [46, 55]. These degradation phenomena take place on individual time scales and are in addition affected by the operational management, which includes various number of parameters, e. g.:

- operation time e. g. for a required life time of more than $40\,000\,h$

- operation temperature and temperature distribution within the stack

- number and instants of time of redox cycles

- number and instants of time of thermo cycles

- number and instants of time of thermo-redox cycles, i. e. thermo-and redox-cycle simultaneously

- varying fuel composition, which is relevant for stack operation with natural gas from the local grid

The stack and RU degradation, respectively, is quantified by the $\mathrm{ASR_{RU}}$ increase, which can be separated into a number of different contributors,

$$\mathrm{ASR_{RU-\Sigma}}(t) = \mathrm{ASR_{MIC}}(t) + \mathrm{ASR_{con}}(t) + \mathrm{ASR_{el}}(t) + \mathrm{ASR_{an}}(t) + \mathrm{ASR_{ca}}(t) \tag{3.1}$$

Table 3.2 Overview of different ASR contributors with the corresponding degradation mechanisms with respect to the Hexis SOFC stack.

ASR	type	deg. law	major deg. mech.	obtained by	ASR[*] predicted by model at $t =$				thesis section
					0 h	5000 h	10 000 h	40 000 h	
ASR_{MIC}	ohmic	$k_e\, t^n, n \geqslant 0.5$	Cr_2O_3 formation	el. con. measurement	$0^{[‡]}$	$135^{[‡]}$	$210^{[‡]}$	$524^{[‡]}$	5
ASR_{con}	ohmic	c	mechanical issues[†]	el. con. measurement	0–100	0–100	0–100	0–100	3.3.3
ASR_{el}	ohmic	$\sigma_{i\infty} + A_1\, e^{-\frac{t}{\tau_1}} + A_2\, e^{-\frac{t}{\tau_2}} - c\, t$	microstructure	ionic con. measurement	$130^{[‡]}$	$215^{[‡]}$	$217^{[‡]}$	$217^{[‡]}$	3.3.2
ASR_{an}	pol.	$c\, t$	microstructure	EIS	$100^{[§]}$	$115^{[§]}$	$130^{[§]}$	$220^{[§]}$	3.3.1
ASR_{ca}	pol.	$c\, t$	microstructure	EIS					
ASR_{gas}	pol.	c	no degradation	EIS or model	$450^{[¶]}$	$450^{[¶]}$	$450^{[¶]}$	$450^{[¶]}$	4

[*] ASR in $m\Omega\, cm^2$

[‡] difficult to define

[†] for MICs operated at 900 °C

[‡] for electrolytes with a thickness of 160 μm at 900 °C

[§] total for anode and cathode at 900 °C since the electrode processes cannot be clearly separated

[¶] For Hexis stack operated at 900 °C with $0.04\, g\, h^{-1}\, cm^{-2}$ CPOx reformed natural gas. Note that, ASR_{gas} is influenced only by gas composition and fuel amount and not by the different components and materials used in the stack. As a consequence ASR_{gas} is constant over the entire stack operation time.

where $ASR_{MIC}(t)$ is the ohmic resistance of the interconnect which increases due to the growing Cr_2O_3 scale on the metallic interconnect, $ASR_{con}(t)$ the contact resistance, $ASR_{el}(t)$ the electrolyte resistance and $ASR_{an}(t)$ as well as $ASR_{ca}(t)$ the electrode resistances. Table 3.2 summarizes the ASR contributors with their corresponding degradation behavior and mechanisms with respect to the Hexis stack.

The separation of single degradation effects is relevant for further development of fuel cells and stacks. This quantification can be done either based on laboratory experiments such as heat exposure and conductivity measurements to investigate single degradation effects, see section 5.2, or based on stack experiments operated in the lab or field. The result extracted from the single laboratory experiments provides fundamental information for the interpretation of stack degradation where the classification of the single effects is often difficult even with EIS characterization. The following subsection gives a brief overview of relevant mechanisms and time dependent quantification in the Hexis stack.

3.3.1 Electrodes

Electrode resistances can be readily identified in impedance spectra, but a separation between anodic and cathodic resistances is difficult. Anode degradation is due to three mechanisms in the state of the art Ni/YSZ and Ni/CGO anodes [57]: First, the cat-
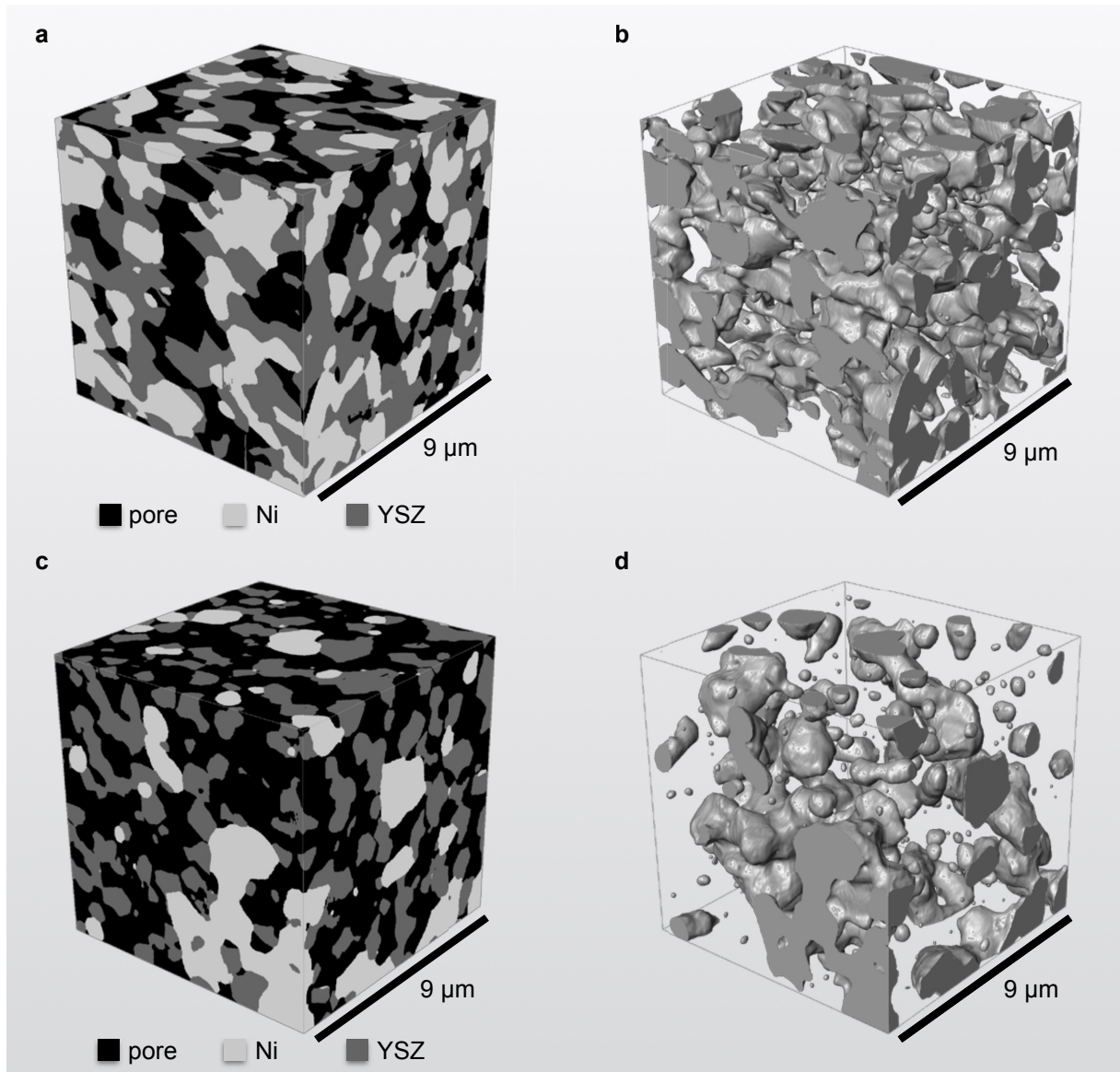
Fig. 3.9 a) 3D data of Ni/YSZ anode as manufactured with well connected Ni phase and b) corresponding Ni phase. c) Microstructure of the same anode type after 8 redox cycles at 850 °C, which indicates Ni redistribution. d) The isolated phase visualize the increasingly disconnection of the electrical conductive Ni matrix [56].

alytically active nickel surface decreases due to particle growth at elevated temperatures. Also, electric pathways can be locally disconnected by this Ni coarsening, which consequently leads to an increase of the ohmic resistance. Such a Ni coarsening is illustrated in Fig. 3.9. Secondly, catalyst deactivation by carbon deposition or poisoning by sulfur and other fuel impurities. Thirdly, mechanical issues originate from residual stresses caused by as mismatch of the coefficients of thermal expansion (CTE) between anode and adjacent

components. Such a mismatch can lead to cracks and delamination in the anode.

Most cathodes are manganese-based with lanthanum and strontium (LSM). LSM is further mixed with yttria stabilized zirconia (YSZ) to ensure the ion conductivity towards the electrolyte [57]. The most relevant cathode degradation effect originates from chromium poisoning. Released chromium species from oxide scales can lead to measurable cathode degradation caused by Cr adsorption and deposition on the electrochemical active sites [58, 59]. Further degradation mechanism that leads to triple phase boundary reduction, electrical and/or ionic conductivity decrease includes: microstructure coarsening, material decomposition, chemical interaction with adjacent electrolyte and delamination at the electrolyte interface [57]. Cathode degradation might be reinforced by inadequate operating condition, which includes very low oxygen pressures, e. g. by air depletion at cathode side, and high overpotentials at elevated fuel utilization. Note, the intrinsic degradation of LSM cathodes provides only a minor contribution to the overall long-term stack degradation [57].

The electrodes degradation is characterized based on EIS-data from Hexis short stacks without detailed investigation and study of degradation mechanism. Specifically, the experimental data, which includes data sets for up to 20 000 h stack operation are described by a regression line based on a least square fit. Such a procedure is sufficient in the context of overall stack degradation for the Hexis system where electrodes degradation are comparable small and thus the deviations from a linear behavior.

3.3.2 Electrolyte

Enabling the oxygen ion transport is the main function of the electrolyte. At the same time, the electrolyte must ensure gas separation between anode and cathode and act as an electrical isolator between the electrodes [36, 60]. The electrolyte must be stable in both oxidizing and reducing atmospheres, compatible with electrode materials in terms of CTE values and low reactivity and sufficient mechanical strength [40]. A common electrolyte material for ESCs is ZrO_2 stabilized with Sc_2O_3 (ScSZ) [61–63]. The ionic conductivity originates from oxygen vacancies, which are introduced by dopant into the ZrO_2 lattice [40, 62]. For ScSZ the conducting mechanism can be described by Kröger-Vink notation:

$$Sc_2O_3 \;=\; 2\,Sc'_{Zr} + 3\,O_O + V_O^{\bullet\bullet} \tag{3.2}$$

The formation and migration of oxygen vacancies is thermally activated i. e. the ionic conductivity increases with temperatures.
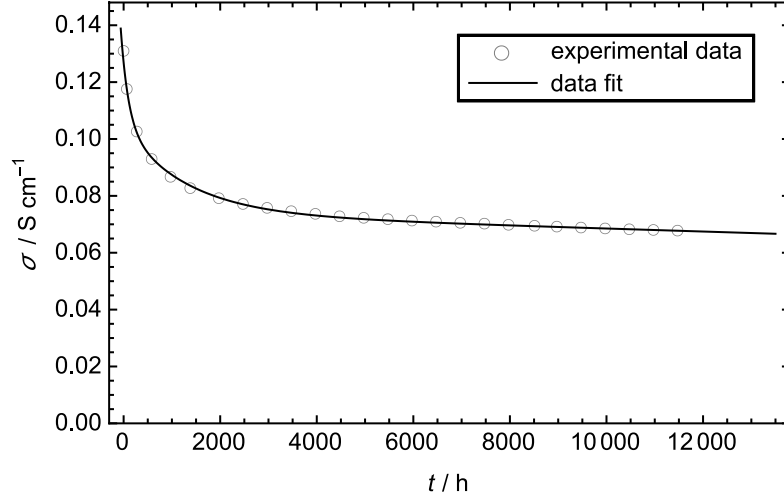
Fig. 3.10 Ionic conductivity data for 6ScSZ obtained from a four-point measurement carried at 850 °C in the Hexis lab [63]. The curve describes the experimental data based on Eq. (3.4).

The initially high ionic conductivity of ScSZ decreases rapidly within the first few hundred hours [62]. The mechanism behind this phenomena is currently under discussion, commonly proposed are phase transformations from the tetragonal phase to the cubic phase and vacancy trapping whereas charge carriers are immobilized [40, 63].

Fig. 3.10 shows the decrease of the ionic conductivity at 850 °C. A sharp initial drop is followed by a steady decline after about 4000 h. The electrolyte degradation is dominated by a broad alteration of overall conductivity for bulk and grain boundaries effects, which occurs with different time rates [63]. Suzuki et al. [64] described this behavior as follows:

$$\sigma_i = \sigma_{i\infty} + A_1 \; e^{-\frac{t}{\tau_1}} + A_2 \; e^{-\frac{t}{\tau_2}} \tag{3.3}$$

Where $\sigma_{i\infty}$ is the ionic conductivity after the initial drop, A and τ are positive constants and the subscription 1 and 2 are used to distinguish the bulk and grain boundary process. Since the experimental data show an ongoing linear decrease an additional term has been added,

$$\sigma_i = \sigma_{i\infty} + A_1 \; e^{-\frac{t}{\tau_1}} + A_2 \; e^{-\frac{t}{\tau_2}} - c \; t \tag{3.4}$$

where c is an additional fitting parameter. Based on the experimental data it can be concluded the electrolyte provides a significant contribution to the overall degradation within the first 4000 h for ESCs.

31
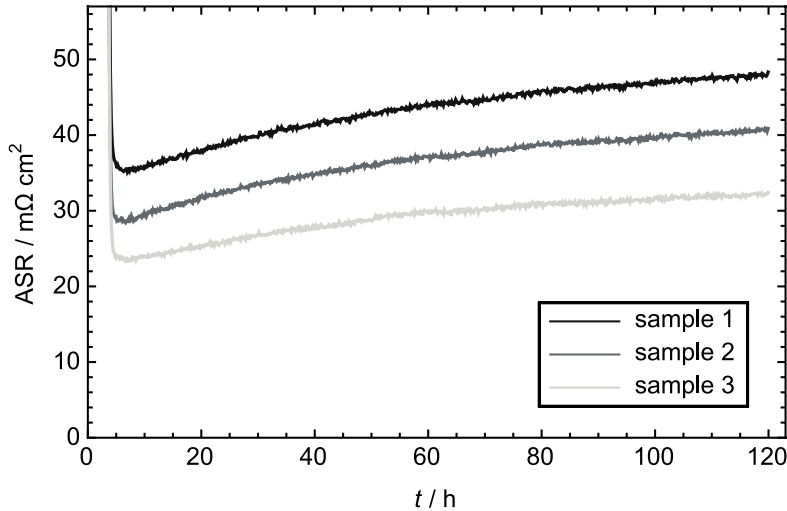
Fig. 3.11 ASR data for LSM coated CFY interconnect samples exposed to air at 850 °C. The electrical connection was realized with Pt plates. The excessive ASR decrease within the first 8 h is related to the heat up phase [67].

3.3.3 Contacts

For reliable SOFC stack operation satisfying contacts between adjacent components are essential [65]. However, the contact theme often gain insufficient attention, moreover ohmic contact losses are difficult to separate apart from other ohmic resistances such as electrolyte and formed oxide layers on MICs. Even EIS does not enable the classification of ohmic resistances. Authentic references about the contact losses can be extracted from conductivity experiments e. g. from heat exposed MIC samples. In such experiments the contacting is usually realized with platinum plates to avoid oxide scale formation on their surface at given test condition, which would provide an additional ohmic resistance. Examples of experimental ASR data trends from LSM coated CFY samples are shown in Fig. 3.11. These data shows a large scatter in the initial conductivity, which result in a permanent offset between the different samples. This behavior indicates imperfect contacts between the Pt plates and the MIC samples [66]. To improve the electrical connection between interconnect and adjacent components a contact slurry can be applied additionally, which minimizes the variance of the initial conductivity values too.

An exact time-dependent characterization of the contact resistances is extremely difficult since there are several parameters that influence the electrical connection. These include the applied contact slurry, which often shows an increasing electrical conductivity within the first period of time [68–70]. This behavior is related to some sintering effects that take place at high temperature while organic binder is released. Furthermore some

often unavoidable thermal and thermal-redox cycles can lead to a partly disconnection of the conducting phases due to mechanical stress because of deviating CTE values between adjacent materials [66].

3.3.4 Metallic interconnect

Metallic interconnect degradation is basically related to the continuous formation of oxide scales. Oxide scale formation takes place under both oxidizing conditions on the cathode and reducing conditions on the anode. Oxide scale growth is often described by Wagner's parabolic law [71]. However, in the course of this work the oxide scale thickness is proposed to follow the more general function

$$x = k_{\mathrm{e}}\, t^{n}, \tag{3.5}$$

were k_{e} is an rate constant and n an exponent that might differ significantly from 0.5. This relation more accuraltely describes the often reduced growth rates especially at exposure times longer than several hundred of hours. In contrast to Wagner's parabolic law the exponent n is usually < 0.5. These findings are described in detail in chapter 5.1.

Chapter 4

Model-based degradation and fuel distribution quantification

For commercially available stationary SOFC applications a lifetime of at least $40\,000\,\mathrm{h}$ with a power degradation lower than $1\,\%$ per $1000\,\mathrm{h}$ are required [9, 11–13, 72]. To meet these goals the performance of SOFC stacks needs to be monitored during operation and the obtained results need to be properly interpreted [73].

Stack performance data can be used to identify operation errors and irregularities such as changes in the fuel supply. Performance data are often extrapolated over time to make predictions regarding the stack life-time. However, to get the maximum benefit from stack performance data combined experimental and theoretical methods have to be applied.

Performance losses are generally characterized by monitoring an operation parameter such as current, voltage or power or by current-voltage data analysis at different time steps [8, 44–48]. The main parameters extracted from (V,I)-curves are open circuit voltages and overall area specific resistances (ASR_{tot}) of an individual or all repeat unit(s) [46, 49]. Ideally the ASR_{tot} obtained from (V,I)-data of the stack can be correlated with partial resistances of local degradation phenomena, that are most suitably studied in button cell or other laboratory experiments. However, the ASR_{tot} is affected by fuel gas effects which make comparisons with partial resistances difficult. In addition, these fuel gas effects show fluctuations resulting from fuel leakages, unequal fuel distribution between the different repeat units within the stack and unavoidable variations in the fuel composition provided by the natural gas from the local grid [44]. As a result, experimental (V,I)-data from SOFC stacks operated e. g. with natural gas from the local grid often shows significant scatter. Variations in the observed degradation data can happen from one stack to another and within a single stack from one RU to another [49, 74]. Deviations between the measured

and theoretical OCVs can be caused, for example, by unusual fuel reformer operation or fuel leakages that affect the anode and/or cathode gas composition by direct oxidation of a certain amount of fuel and air upstream to the RU [49, 75, 76]. In addition, deviations in the (V,I)-characteristic can be related to the overall amount of fuel available [49]. This can be affected by unequal fuel distribution between the different repeat units of a single stack e. g. by manufacturing and assembling tolerances. It can also be caused by fuel leakages [60, 77] (e. g. by cracks and sealing points) and by sensor malfunctions such as drifts in the output of upstream located thermal mass flow controllers [78]. Furthermore, the overall temperature level and the temperature distribution over the stack both can vary and therefore cause additional scatter in observed stack performances. This is because temperature influences the cell potential, but also ohmic and polarization losses [42, 79]. Note however that recent advances in the thermal management of SOFC stacks led to well controllable and rather homogeneous stack temperatures [76, 80]. Fuel gas effects are often the main cause for deviations from normal stack behavior for the Hexis SOFC stack. The separation of fuel gas effects from the "true", internal resistance of a stack repeat unit ($ASR_{RU} \neq ASR_{tot}$) can be accomplished by electrochemical impedance spectroscopy (EIS) shown in section 4.1 [49, 81, 82]. However, EIS measurements are generally not available for SOFC stacks running in the field. There is, hence, a need for extracting internal stack repeat unit resistances from commonly available, time-dependent (V,I)-data, to accurately predict and interpret the performance of SOFC stacks under real conditions (using e. g. natural gas as fuel).

A method for extracting ASR_{RU} from (V,I)-data has already been published by Linder et al. [44]. There a 0D thermodynamic equilibrium model assuming a uniform distribution of fuel and air over the entire RU to calculate ASR_{gas} for hydrocarbon containing fuels is used [83]. If this 0D-approach is applied to fuel cells with an active cell area of several square centimeters, e. g. $100\,cm^2$, the calculated gas concentration resistance ASR_{gas} is significantly overestimated. Such a deviation is obvious, since the fuel composition and oxygen partial pressure variations along the gas channels between corresponding inlet and outlet is not considered in a 0D-approach.

In this chapter a model-based approach to extract repeat unit resistances ASR_{RU} from experimental (V,I)-data without using any fitting parameters is proposed. The model separates internal ohmic and polarization losses from fuel gas concentration effects and takes into account different types of fuel leakages and possible fluctuations in the fuel gas composition from the grid. The comparison of time dependent ASR_{RU} evolution during stack operation with averaged ASR trends obtained from single experiments under labo-

ratory conditions has a number of applications. It allows one to verify if the degradation phenomena observed in single experiments under laboratory conditions can explain the degradation behavior within stacks using the same components. The model enables furthermore to extract local species concentration in the flow channels as well as local current densities and potentials for a given fuel utilization (FU).

4.1 Conceptual approach

Depending on the cell and stack design, ASR_{RU} includes the contributions of the different RU layers and their mutual interfaces as shown in Fig. 3.7. For Hexis stacks based on electrolyte-supported cells including metallic interconnects, the main contributions comprise ohmic losses (ASR_{ohm}) from the electrolyte (ASR_{el}), contact resistances (ASR_{con}) and oxide layers formed on metallic interconnect as well as ohmic and polarization losses from the electrodes (ASR_{an}, ASR_{ca}).

Electrochemical impedance spectroscopy enables to separate internal repeat unit resistances ASR_{RU} from gas concentration losses (ASR_{gas}) since the overall resistance is defined as follow:

$$ASR_{tot} = ASR_{RU} + ASR_{gas}. \tag{4.1}$$

Fig. 4.1 shows impedance data for one repeat unit in a Hexis 5-cell short stack operated at 900 °C with CPOx reformed natural gas. The mass flux of natural gas was varied between 0.02 and 0.06 g h^{-1} cm^{-2}. Fig. 4.1a presents the EIS-data in a Nyquist plot whereas each spectrum was measured at about 50 % FU. Variations of the fuel amount basically affects the gas concentration arc in the low frequency region (< 0.5 Hz) on the right whereby this arc is scaled-down with increasing fuel amount. For a large surplus of fuel, typically delivered in button cell experiments, the gas concentration arc disappears since gas concentration losses are inverse proportional to the fuel feed [37, 83, 84]. Furthermore fuel variations have a negligible impact on the electrode resistances ASR_{an} and ASR_{ca} compared to the overall resistance ASR_{tot}. This behavior is also representative for other stacks with different cell types at OCV [79, 85, 86].

The internal resistance ASR_{RU} extracted from EIS-data consist of the ohmic resistances ASR_{ohm}, at the high frequency intercept in the Nyquist plot (Fig. 4.1a), and the electrode losses ASR_{an} and ASR_{ca} represented by the two smaller not fully formed arcs in the frequency range > 0.5 Hz. Effects of the fuel amount variations are also shown in Fig. 4.1b whereby Im(Z)-part is plotted against the frequency. Variations related to electrodes processes are identifiable in the frequency range > 0.5 Hz.
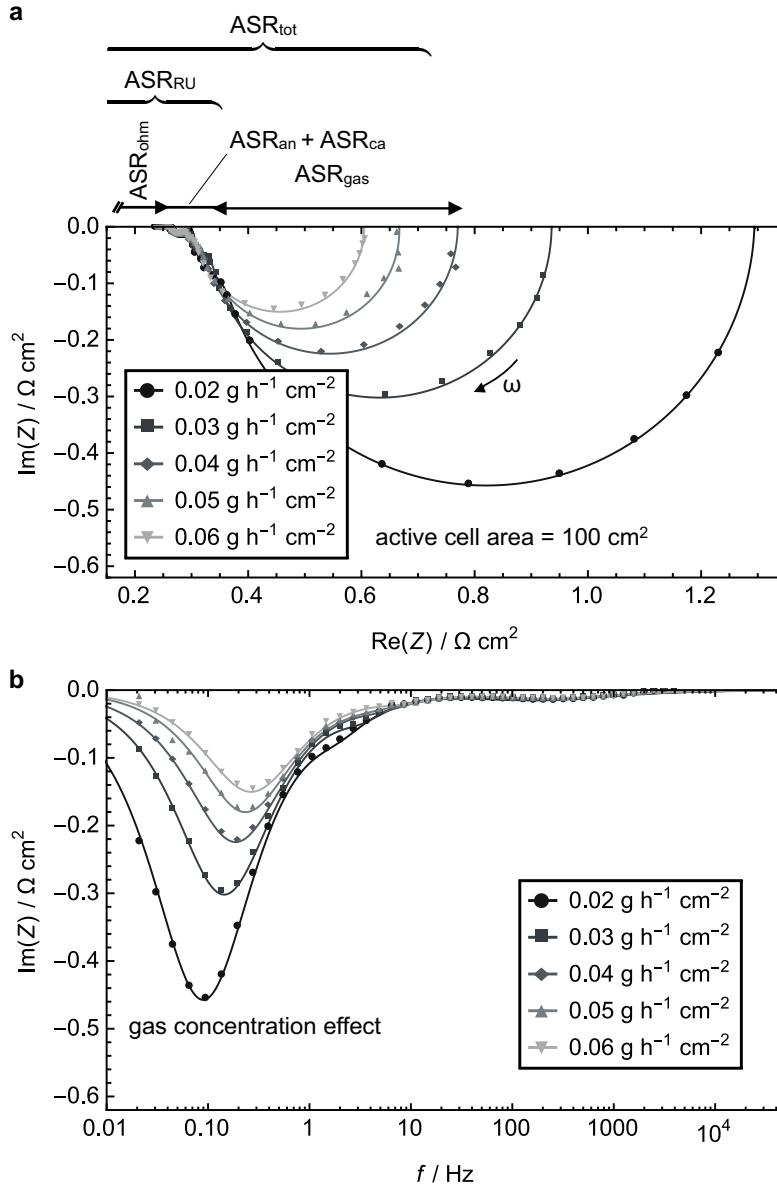
Fig. 4.1 EIS data from a Hexis cell ($100\,cm^2$) operated in a short stack at $900\,°C$ with CPOx reformed natural gas with a CH_4 content of $90\,\%$ [44] for varying fuel amounts at $\approx 50\,\%$ FU and corresponding cathode air flow i.e. $61\,mA\,cm^{-2}$ at $1\,g\,h^{-1}\,cm^{-2}$ cathode air flow, $121\,mA\,cm^{-2}$ at $1.5\,g\,h^{-1}\,cm^{-2}$, $171\,mA\,cm^{-2}$ at $2\,g\,h^{-1}\,cm^{-2}$, $221\,mA\,cm^{-2}$ at $2.5\,g\,h^{-1}\,cm^{-2}$ and $251\,mA\,cm^{-2}$ at $3\,g\,h^{-1}\,cm^{-2}$. a) Nyquist diagram including the interpretation of the different resistances. b) Corresponding $Im(Z)$-part plotted against frequency.

Reliable separation and quantification of fuel gas concentration effects from internal resistances (ASR_{RU}) based on experimental (V,I)-data are the main purposes of this section. Since the further discussion is about fuel leakages and uneven fuel distributions over the stack it is important to define the term "nominal fuel supply" as the ideal case.
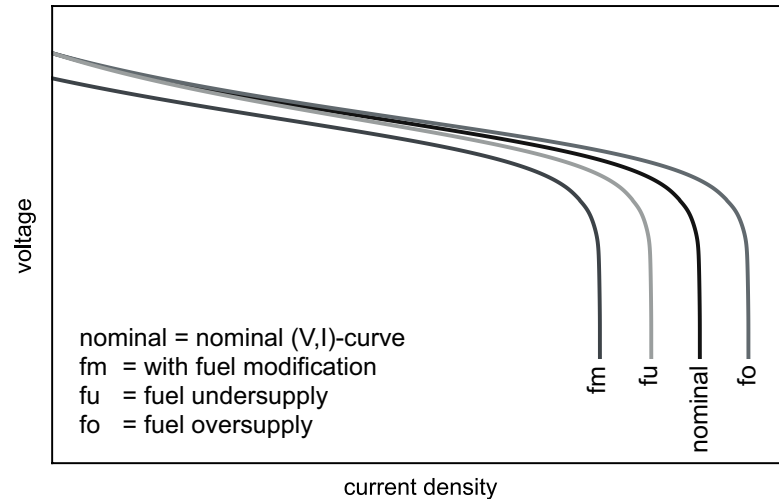
Fig. 4.2 Schematic illustration of (V,I)-curves with typical influences of fuel amount variation (fu or fo) and changes in fuel composition (denoted as fm). Further explanations about the meaning of nominal, fu, fo and fm are given in section 4.1.

The nominal fuel supply corresponds to the preset amount of fuel entering each RU. However, in reality a specific RU will most probably be fed with an amount of fuel that differs somewhat from the nominal one. In any case, the nominal fuel implies the absence of the following unwanted effects:

i) leakages effecting the upstream fuel composition by a partially direct oxidation of fuel caused by air leaking from the air to the fuel supply denoted by fm

ii) fuel oversupply caused by uneven fuel distribution within the stack or/and by positive deviations in the overall fuel caused by malfunctions of the flow controllers denoted by fo

iii) fuel undersupply caused by fuel leakages, uneven fuel distribution within the stack or/and by negative deviations in the overall fuel caused by malfunctions of the flow controllers denoted by fu.

Note that fo and fu defined in ii) and iii) can be related to one or several of the listed effects, i. e. they can occur simultaneously.

The impact of fuel variations on the (V,I)-behavior is schematically illustrated in Fig. 4.2. The curve denoted as nominal represents a nominal (V,I)-curve as defined above. fo and fu represent an increase and a decrease with respect to the nominal fuel amount, respectively. As a result the maximum current density is shifting to the right and vice versa. Consequently the slopes of the corresponding (V,I)-curves change as well. That

implies that an increased fuel amount decreases the slope of the resulting (V,I)-curves and consequently the overall ASR (ASR_{tot}) and vice versa, see Fig. 4.1a. Note that in this work ASR_{tot} is defined by the local derivative $|dV/dj|$ [46]. Leakages might also influence the anodic fuel composition and the cathodic oxygen partial pressure by direct oxidation of fuel upstream to the cells. The impact of such leakages on (V,I)-curves is illustrated in Fig. 4.2 (labeled fm, fuel modification). Direct fuel oxidation upstream to the cell reduces the Nernst potential and thus the OCV. Since direct fuel oxidation reduces the available fuel amount the maximum current is decreased too. Note that direct fuel oxidation upstream to the cells does not affect the slopes of the corresponding (V,I)-characteristics. However, direct fuel oxidation shifts the (V,I)-curves to the left resulting in lower voltages and a lower maximum current density, for further details see Linder et al. [44]. Generally, a combination of these effects occurs in fuel cell stacks. For example, if the available fuel amount at the inlet of a single RU is higher than the nominal value fo and simultaneously the fuel composition is influenced by upstream leakages fm the maximum current density might just stay constant. However, in such a case the OCV is still decreased below its nominal value. This shows that for an accurate interpretation of experimental (V,I)-data both the OCV and the maximum current need to be taken into account. As fuel compositions affects the ASR_{tot}, it is obvious that such variations lead to unfavorable scatter with respect to the overall repeat unit resistance. This further complicates the interpretation of (V,I)-data. Therefore concepts are needed to separate fuel gas effects (ASR_{gas}) from the "true" internal RU resistance (ASR_{RU}) in order to correctly interpret the (V,I)-data and the total resistance (ASR_{tot}).

4.2 Model

4.2.1 Local equilibrium cascade model

Fig. 4.1 shows the variation of EIS-spectra from a single cell within a stack upon changes in gas amount at $\approx 50\%$ FU. The two main regions that can be correlated with ASR_{RU} and ASR_{gas} are discussed separately below.

Fig. 4.1 shows that the ASR_{RU} undergoes only very small changes compared to the total resistance ASR_{tot}. This indicates that the ASR_{RU} does not vary (e.g. as a model assumption) as a function of the available fuel amount and gas concentration, respectively. In principle, ASR_{RU} varies with temperature since it depends on electrode polarization resistance, electrolyte and oxide scales conductivities, which have a temperature

dependency themselves [42, 79, 87, 88]. However, for the Hexis stack design including metallic interconnects with high thermal conductivities in the range of 24–94 W m^{-1} K^{-1} [89, 90] the heat transfer between the stack and the post combustion zones [8] is very efficient. Consequently the temperature is rather uniform and thus ASR$_{RU}$ is nearly constant over the entire cell/MIC (e. g. fuel inlet or adjacent to post combustion zone). A constant ASR$_{RU}$ also indicates the absence of gas transport limitations within the electrodes, which is typical for design with electrolyte supported cells. The polarization losses can thus be considered as linearly dependent on electrical current (ohmic law), which are not significantly affected by the local anode- and cathode gas compositions. Overall, the ASR$_{RU}$ becomes nearly independent from the load point i. e. fuel utilization. Furthermore, in the RU-model it is justified to assume uniform voltage distribution over the entire current-collector due to the high electrical conductivity in these components [89–92]. Hence an externally applied voltage U_L holds for the entire repeat unit.

Fig. 4.1 document that changes in fuel amount and composition basically affect the ASR$_{tot}$ and not the ASR$_{RU}$. Such a behavior derived from EIS data has been observed as well for other electrolyte supported cells [85] and for SOFC stacks with anode supported cells [79, 81]. Due to the ongoing fuel utilization the gas composition varies within the cell and along gas channels, respectively. To capture the fuel consumption along a repeat unit more realistically, a spatial discretization of the RU by subdividing it into an arbitrary number of compartments that are connected to each other is made. Such a scenario is shown in Fig. 4.3a. Each compartment has a fuel gas composition that is assumed to be in thermodynamic equilibrium taking into account the water gas shift reaction. This is justified by the high operation temperatures and the catalytic active Ni present at anode side [93]. The local voltage of each compartment can then be calculated from the Nernst equation

$$U_N = \frac{k_B\,T}{4\,e} \ln\left(\frac{p_{O_2}^C}{p_{O_2}^A}\right) \tag{4.2}$$

for a given composition of anode and cathode gases within a single cascade element. In Eq. (4.2), k_B is the Bolzmann constant, T the absolute temperature, e the elementary charge and p_{O_2} the oxygen partial pressure on the cathode (C) and anode (A) side, respectively [94].

The fuel composition in the first compartment at the anode inlet corresponds to the reformed natural gas in thermodynamic equilibrium at a given cell temperature and relevant pressure. In this work, the thermodynamic equilibrium is determined with the open-source software package Cantera [95]. Details about the natural gas composition
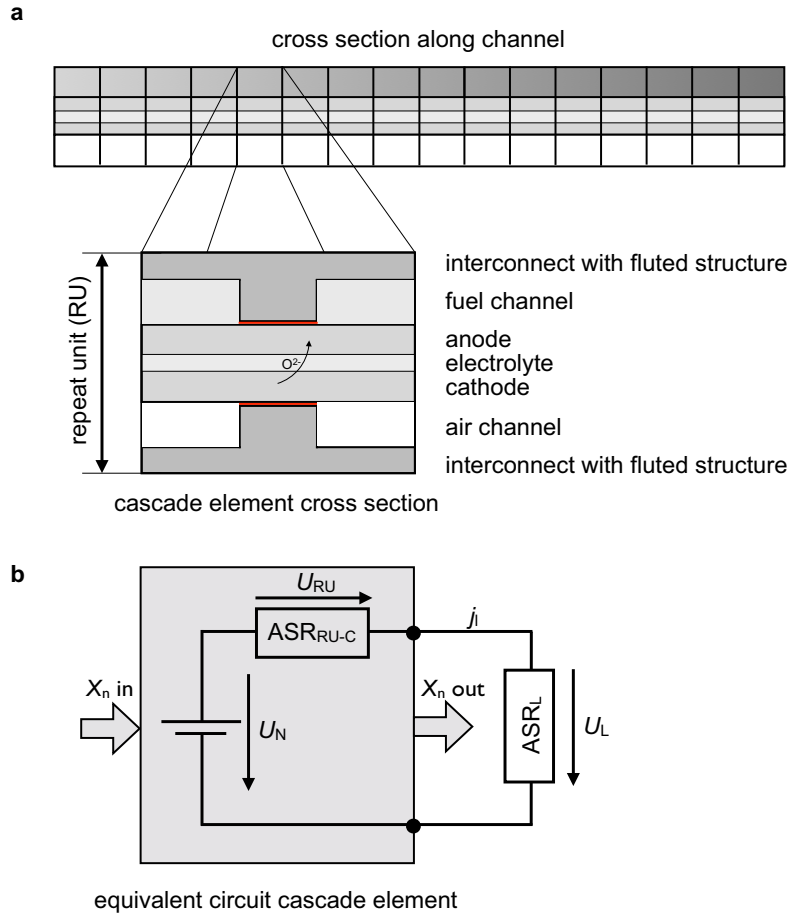
a

cross section along channel

repeat unit (RU)

interconnect with fluted structure
fuel channel
anode
electrolyte
cathode
air channel
interconnect with fluted structure

cascade element cross section

b

U_{RU}

ASR$_{RU-C}$

j_l

X_n in

X_n out

ASR$_L$

U_N

U_L

equivalent circuit cascade element

Fig. 4.3 a) Schematic illustration of the model based on cascade elements along the flow channels of a SOFC stack repeat unit. The enlargement shows the cross section of the RU for a single cascade element. An electrical equivalent circuit for a single cascade element is shown in b). X_n denotes the specific molar fractions for the fuel gas composition at the inlet and outlet, respectively.

are given by gas chromatography or from the local gas suppliers. Air is supplied to the cathode side. With the above made assumptions, the current-voltage behavior of each compartment can be represented by the equivalent circuit as shown in Fig. 4.3b. Since the externally applied terminal voltage U_L is constant over the whole repeat unit the local repeat unit voltage drop is obtained as the difference between the local Nernst voltage and the external voltage, i. e.

$$U_{RU} = U_N - U_L. \tag{4.3}$$

The local current density j_l then follows as the ratio of the repeat unit voltage and the

assumed repeat unit resistance $\text{ASR}_{\text{RU-C}}$ in the cascade model, i.e.

$$j_\text{l} = \frac{U_\text{RU}}{\text{ASR}_{\text{RU-C}}}.$$ (4.4)

The term $\text{ASR}_{\text{RU-C}}$ is specifically used to denominate ASR_{RU} values that are determined by the cascade model based on experimental (V,I)-data. Knowing the local current density the corresponding O^{2-} flux density $\dot{n}_{\text{l}_{\text{O}^{2-}}}$ across the electrolyte can be calculated by Faraday's law

$$\dot{n}_{\text{l}_{\text{O}^{2-}}} = \frac{j_\text{l}}{2\,F}$$ (4.5)

whereas F is the Faraday constant. A new gas composition originates from the O^{2-} transport across the electrolyte, which leads to a changed thermodynamic equilibrium state. This process also results in a new thermodynamic equilibrium for the water-gas shift reaction and the steam reforming of the remaining hydro-carbonates (e.g. CH_4, C_2H_6, C_3H_8) [44]. The resulting gas concentrations are used to determine U_N in the following downstream element based on Eq. (4.2). The O_2 consumption on the cathode side known from Eq. (4.5) is likewise considered in the calculation. This procedure is sequentially repeated from inlet to outlet for all n cascade elements. Finally, the averaged cell current-density j is obtained as the sum over all local current-densities divided by the number of cascade elements n

$$j = \frac{\sum\limits_{i=1}^{n} j_{\text{l}_i}}{n}.$$ (4.6)

The modeled (V,I)-characteristic is finally obtained from the given load U_L and the resulting global current density j at each load point.

Since $\text{ASR}_{\text{RU-C}}$ is initially unknown, it is obtained from fitting the model to (V,I)-data. This is performed using the method of least squares to minimize the error between the cascade model and the experimental data.

The cascade model takes the real fuel composition and fuel amount at the inlet as input. However, because of fuel leakages and changes in the natural gas composition when provided from the grid both are generally unknown but can be assessed by comparing the nominal values for the OCV and maximum current with the real ones obtained from (V,I)-data.
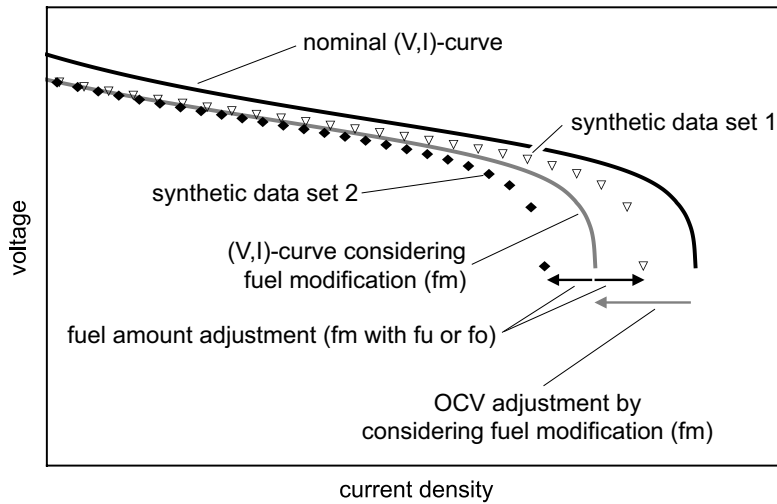
Fig. 4.4 Illustration of the influence of fuel leakages for two types of (V,I)-data. The black curve represents the nominal (V,I)-curve. The gray curve represents the modeled (V,I)-curve including only fuel leakage effects i. e. without any additional fuel amount deviation. The symbols schematically illustrate two different types of experimental data, which include fuel leakages that affect the fuel composition upstream to the cell. The triangles illustrate experimental data with a fuel oversupply and the diamonds with a fuel under supply, respectively.

4.2.2 Accounting for fuel leakages and compositional variations

Fuel leakages reduce the total amount of available fuel or alter the fuel composition. These gas effects may lead to a reduction of the OCV, see Eq. (4.2). Uneven fuel distribution between the different repeat units within a stack affects the fuel amount available for a certain RU. The influences on (V,I)-data by fuel leakages and uneven fuel distribution are illustrated in Fig. 4.4 with synthetic data to give a qualitative description of this effects. This Figure also includes two sets of synthetic data which exhibit the same OCV but different maximum currents and therefore different total resistances ASR_{tot}. Their OCV is reduced, when compared with the nominal (V,I)-characteristic shown as the black curve. This indicates the presence of leakages that alter the fuel composition (fm) at the inlet with respect to the nominal inlet composition. This kind of leakage is usually related to false air upstream to the cell that necessarily leads to a partial oxidation of fuel at relevant SOFC stack temperatures. In the model such partial oxidation leads to a new (V,I)-characteristic with a reduced OCV that corresponds to the experimental OCV. Further details are given by Linder et al. [44]. The resulting (V,I)-curve is illustrated by the gray line in Fig. 4.4. This modeled curves still differs from the synthetic data sets with respect to their maximum currents j_{max}. Set 1 exhibits a higher j_{max}-value than the model and set 2 a smaller one. This means synthetic (V,I)-data represented by set 1

gets a higher than nominal net fuel amount (fo) with leakages (fm) and vice versa for synthetic data represented by set 2. Hence the modeled (V,I)-curve (gray curve) needs to be adjusted with respect to the fuel amount available at the cell inlet by matching the j-values of the provided synthetic data. The available amount of fuel is determined from present j-values at the characteristic bend at high FUs. It must be emphasized that in these experiments the fuel utilization is generally limited to $95\,\%$ in order to avoid Ni oxidation [96]. This limits the range of experimental (V,I)-data.

The voltage drop at fuel utilizations close to $100\,\%$ is more pronounced in the derivative $\mathrm{d}V/\mathrm{d}j$ of (V,I)-data (see e.g. Fig. 4.6). Building a simple difference quotient based on the experimental data is often insufficient due to the unavoidable signal noise during the measurement. Therefore a fit function

$$\mathrm{ASR_{RU-C}}\ j = -K + \frac{\ln\left(\frac{j-B}{C-j}\right)}{G},\ C \le j \le B \tag{4.7}$$

with four degrees of freedom is used to describe the experimental data where $C = j$ represents the asymptotic limit at the left side, $B = j$ the increment between the left and right side asymptotes and G the gradient at the inflection position $K = j$. To improve the fit quality an additional symmetry factor S is included

$$\mathrm{ASR_{RU-C}}\ j = K - \frac{\ln\left(\frac{\left(\frac{B-C}{B-j}\right)^S - 1}{S}\right)}{G},\ C \le j \le B. \tag{4.8}$$

whereby the resulting parameters from the experimental data description by Eq. (4.7) are required to find reasonable parameters for Eq. (4.8) with five degrees of freedom. An example of fitted experimental data with both function is shown in Fig. 4.5.

The experimental (V,I)-data and the modeled (V,I)-data are described by the functions given in Eq. (4.7) and Eq. (4.8), respectively, to determine the effectively available fuel amount on each RU. The fuel amount fitting is an iterative procedure based on least square where the derivative of the modeled (V,I)-characteristic is fitted to the derivative of the experimental (V,I)-data. Fig. 4.6 illustrates the derivatives of the modeled (V,I)-characteristics considering fm adaptation and the adjusted fuel (fu). Thereby the latter one shows a good agreement with the experimental data. To find a robust solution only a defined section between the maximum in the derivative of experimental (V,I)-data and a predefined value at high current densities is used during this fitting procedure.
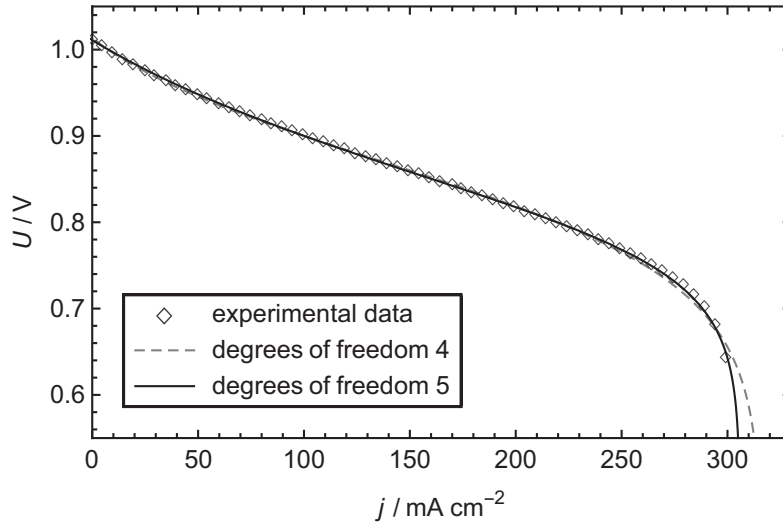
Fig. 4.5 Experimental (V,I)-data after $200\,\mathrm{h}$ stack operation at $900\,°\mathrm{C}$ with $0.04\,\mathrm{g\,h^{-1}\,cm^{-2}}$ CPOx reformed natural gas from the local grid with a CH_4 content of $90\,\%$ [44] and $2\,\mathrm{g\,h^{-1}\,cm^{-2}}$ air on cathode side, described by the fit functions with four and five degrees of freedom, Eqs. (4.7) and (4.8), respectively.
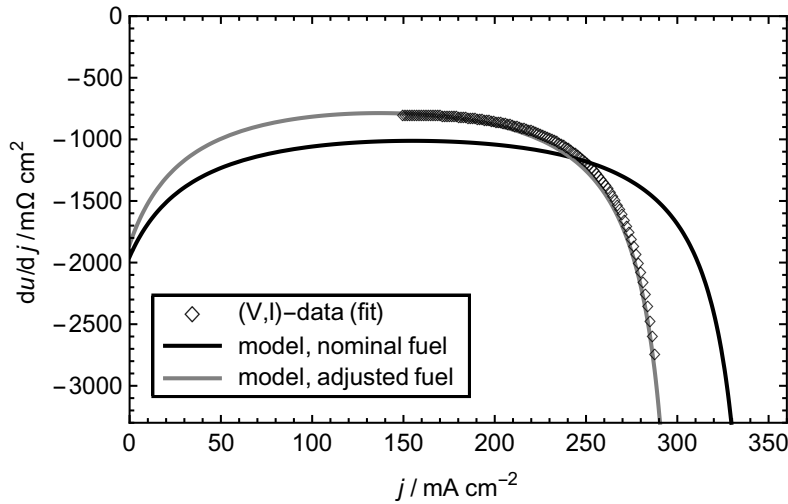
Fig. 4.6 Illustration of the fuel fit. The black diamonds represent the derivative of the fitted experimental data and the curves represent the derivative of the modeled (V,I)-data for different fuel amounts after fm adjustment. The black curve represent the derivative of modeled (V,I)-curve for the nominal fuel amount adjusted by fm and the gray curve for a fitted fuel amount i. e. adjusted by fm and fu. Experimental (V,I)-data are obtained from a short stack operated at $900\,°\mathrm{C}$ with $0.04\,\mathrm{g\,h^{-1}\,cm^{-2}}$ CPOx reformed natural gas from the local grid with a CH_4 content of $90\,\%$ [44] and $2\,\mathrm{g\,h^{-1}\,cm^{-2}}$ air on cathode side.

4.2.3 Model process

To evaluate the internal resistance and the effective fuel amount for a single cell the different subroutines as described above are combined in a global routine. The overall procedure is illustrated in the flowchart in Fig. 4.7. This procedure can be repeated at different time steps to extract a time-depend ASR_{RU-C} to study RU degradation based on (V,I)-data.

4.2.4 Degradation model

A degradation model is introduced in Eq. (3.1), which describes time dependent behavior of single ASR_{RU} components. The sum of these different RU resistances can be compared with ASR_{RU-C} determined from experimental data with the cascade model. If the differ-
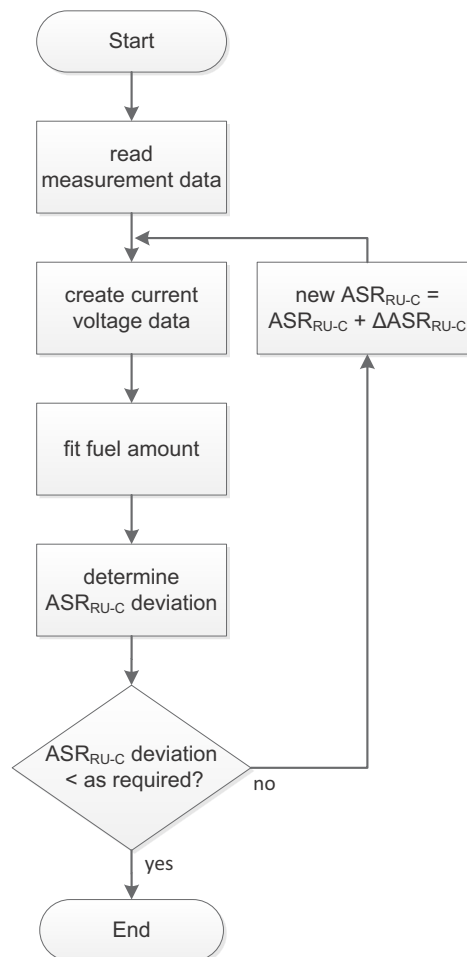
Fig. 4.7 Illustration of the overall cascade model procedure to determine ASR_{RU-C} based on experimental (V,I)-data.

ence between $\text{ASR}_{\text{RU}-\Sigma}(t)$ and $\text{ASR}_{\text{RU-C}}$ turns to zero it can be concluded that the stack behaves as expected based on the degradation model.

4.3 Experiments for model validation

The experimental work is done with electrolyte supported SOFCs in the planar Hexis design arranged in an open stack with a direct post combustion. These experiments are realized in short stacks consisting of five standard cells with an active cell area of $100\,\text{cm}^2$. The stacks are running with catalytic partial oxidized (CPOx) natural gas from the local grid. The nominal gas flux is defined as $0.04\,\text{g}\,\text{h}^{-1}\,\text{cm}^{-2}$. The stack temperature is set between 850 and $900\,°\text{C}$.

4.3.1 (V,I)-characteristics

The drawing for the (V,I)-characteristics starts at OCV. Thereafter the current from the external load is increased in $0.5\,\text{A}$ steps. At each point a dwell of $120\,\text{s}$ is predefined to ensure steady state conditions before logging the resulting cell potential. This procedure is repeated until the abort criterion $< 0.6\,\text{V}$ is reached for one cell in the short stack. Gas fluxes and temperatures are constant during the (V,I)-measurement. (V,I)-characteristics are measured for each single cell within the short stack.

4.3.2 EIS measurement

EIS measurement is realized with a Zahner IM6(ex) in combination with Zahner PP240 potentiostat. The measurements are done with an external load at $15\,\text{A}$ ($150\,\text{mA}\,\text{cm}^{-2}$), which corresponds approximately to $50\,\%$ FU with an amplitude of $1\,\text{A}$. The frequency domain is defined between $50\,\text{kHz}$ and $20\,\text{mHz}$. Deviations from these standard measurement parameters are explicitly mentioned in this section.

4.3.3 Gas chromatography

The natural gas composition from the local grid in Winterthur (Switzerland) is analyzed half-hourly to ensure that the relevant gas data for the model based analysis are available. The gas composition is determined with an Agilent Varian CP-4900 gas chromatograph.

4.4 Results and Discussion

In this section a detailed model validation focusing on the accuracy of determined $ASR_{RU\text{-}C}$ data and fuel amounts is presented at the beginning. Then comparison of results from experiments and from degradation models for the single stack components and their potential to detect deviations from the averaged stack behavior will be discussed. The possibility to extract local RU conditions that are relevant for further degradation studies is introduced as an additional cascade model feature at the end of this section.

4.4.1 Model validation

The hypothesis that ASR_{RU} is independent of the fuel amount is validated by the EIS-data shown in Fig. 4.1a for a single cell. This figure shows that no significant changes in the polarization arcs can be observed even for an extraordinary large fuel amount variation between 0.02 and $0.06\,\mathrm{g\,h^{-1}\,cm^{-2}}$.

To further validate the cascade model, its (V,I)-behavior is compared with experimental (V,I)-data from one cell obtained from a Hexis short stack operated at $850\,°\mathrm{C}$ and fueled with CPOx reformed natural gas. Fig. 4.8 shows ASR_{tot} and ASR_{RU} data plotted against current density extracted from EIS, experimental and modeled (V,I)-data, respectively. ASR_{RU} extracted from the EIS-data are illustrated by the diamonds for the different
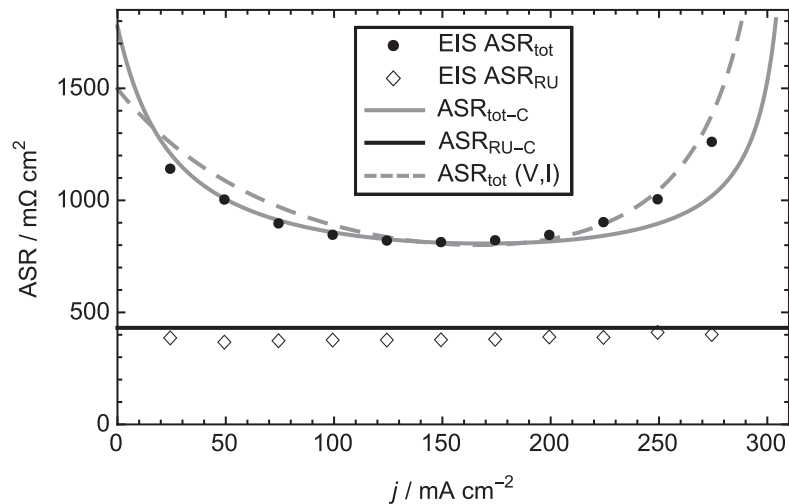
Fig. 4.8 Comparison of ASR values extracted from EIS measurements (dots and diamonds) at corresponding load points with experimental (dashed line) and modeled (solid lines) (V,I)-data, respectively. The model predictions take into account fm and fu, see section 4.1. The cell was operated at $850\,°\mathrm{C}$ with $0.04\,\mathrm{g\,h^{-1}\,cm^{-2}}$ CPOx reformed natural gas from the local grid with a CH_4 content of $90\,\%$ [44] and $2\,\mathrm{g\,h^{-1}\,cm^{-2}}$ air on cathode side.
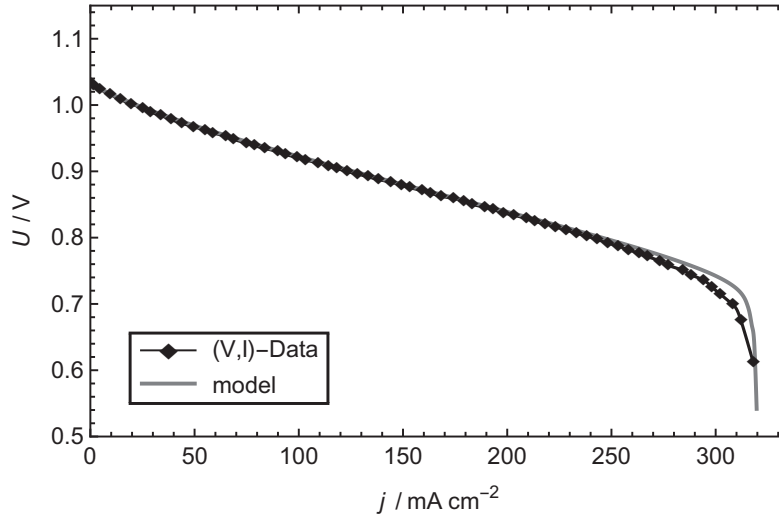
Fig. 4.9 Comparison between experimental (V,I)-data ($850\,°C$, $0.04\,\mathrm{g\,h^{-1}\,cm^{-2}}$ CPOx reformed natural gas from the local grid with a CH_4 content of $90\,\%$ [44] and $2\,\mathrm{g\,h^{-1}\,cm^{-2}}$ air on cathode side) with (V,I)-data from cascade model fit. The cascade model considers leakages (fm) and fuel amount deviations (fu).

current densities. The scatter of these data is small and shows a horizontal behavior, which confirms that ASR_{RU} can be considered as being constant and can, therefore, be modeled independently from load variations in the cascade model. $ASR_{RU\text{-}C}$ is represented by the black line at $432\,\mathrm{m\Omega\,cm^2}$, which show a good agreement with the relevant EIS data. The dots illustrate the ASR_{tot} as provided by the EIS data. The dashed curve show the ASR_{tot} trend based on the derivative $|dV/dj|$ of measured (V,I)-data. $ASR_{tot\text{-}C}$ behavior resulting from the cascade model is shown by the gray curve. Fig. 4.8 illustrates that the cascade model agrees well with the data for current-densities up to $250\,\mathrm{mA\,cm^{-2}}$. However, for higher current-densities the agreement becomes rather poor. Apparently, this mismatch does not affect the ability of the cascade model to accurately predict $ASR_{RU\text{-}C}$. Experimental (V,I)-data from the same cell are shown in Fig. 4.9 by the symbols. The gray curve represents the (V,I)-curve as fitted by the cascade model. This curve is only visible for current densities $> 250\,\mathrm{mA\,cm^{-2}}$ due to the good agreement with the experimental data.

ASR trends extracted from the (V,I)-data and EIS measurements are compared in Fig. 4.10 to verify consistency. The data at the top in Fig. 4.10a show the $ASR_{tot\text{-}C}$ evolution during stack operation for a short stack operated at $850\,°C$ with CPOx reformed natural gas extracted from (V,I)-data. The $ASR_{RU\text{-}C}$ trends are shown in the middle. Fig. 4.10b show as well ASR_{tot} and ASR_{RU} trends from the same stack derived from EIS measurement. In general the (V,I)- and EIS-data agree well with each other, which con-
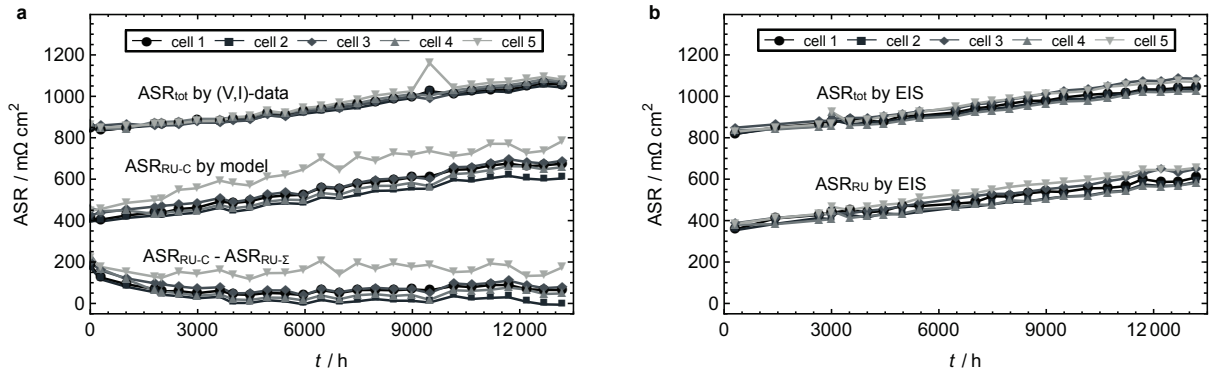
Fig. 4.10 a) Degradation behavior extracted from (V,I)-data of a Hexis short stack operated at 900 °C with $0.04\,\mathrm{g\,h^{-1}\,cm^{-2}}$ CPOx reformed natural gas from the local grid with a CH_4 content between 88 % and 90 % [44] and $2\,\mathrm{g\,h^{-1}\,cm^{-2}}$ air on cathode side. The top family of curves represents the total ASR increase for each cell. The middle ones represent the increase of $ASR_{RU\text{-}C}$ determined by the cascade model. The curves at the bottom represent the difference between ASR_{RU} from the cascade model and from the degradation model (cf. section 4.2.4). b) ASR_{tot} and ASR_{RU} trends extracted from EIS measurements.

firms the reliability and accuracy of the cascade model. Except for repeat unit number 5 in Fig. 4.10a where $ASR_{RU\text{-}C}$ is clearly higher compared to the corresponding trend extracted from EIS. This behavior is related to a none uniform fuel distribution within the stack where cell number 5 is oversupplied. This instability lead to a reduction of gas concentration losses and consequently of ASR_{tot}. In this specific case $ASR_{RU\text{-}C}$ is additionally overestimated by the cascade model, which is using the characteristic bend at high FU to determine the effective available fuel amount (cf. Fig. 4.6). This feature in (V,I)-data is missing here, hence the effective fuel amount is overestimated. Nevertheless, the cascade model provides a reliable indication that repeat unit 5 is oversupplied as confirmed by the corresponding Nyquist plots and by the ASR_{RU} trend in Fig. 4.10b. Furthermore it could be shown for other examples that a performance rating for single cells based on (V,I)-data can lead to a misinterpretation. This is due to non-uniform fuel supply within SOFC stacks, which can have a strong influence on each repeat unit and consequently on the corresponding effective operating behavior.

The capability of the cascade model to predict the true fuel amount feed to a specific repeat unit is documented in the following section. As shown in Fig. 4.11, the gas concentration impedance extracted from the spectra shown in Fig. 4.1 follows a linear correlation with the inverse of the corresponding fuel amount. Furthermore the regression line has only a marginal offset from the origin. Hence, the experimental data show a good agreement with the theoretical behavior, where the gas concentration resistance must be zero for an infinite fuel amount [84, 85, 97]. This relation is used to determine the
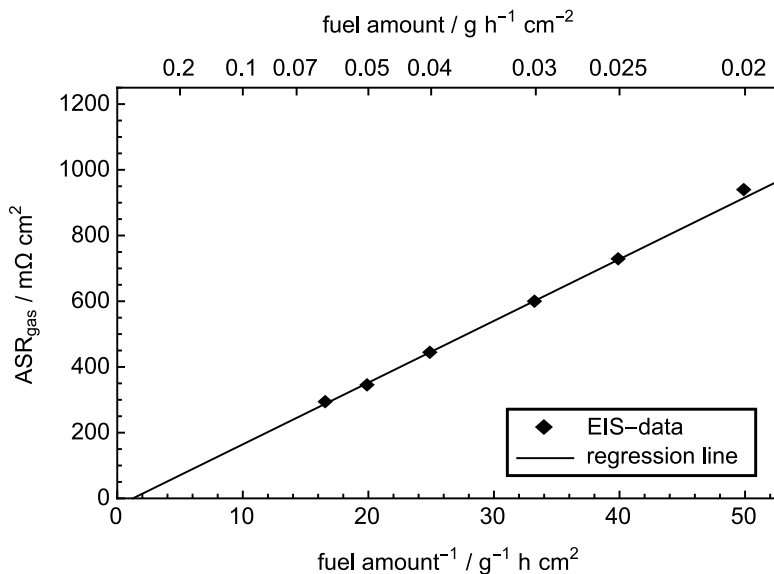
Fig. 4.11 ASRgas extracted from EIS-data, as a function of the inverse fuel amount. All data points are measured at 50 % FU. Details about operating conditions are given in Fig. 4.1.

fuel distribution over the various repeat units of a Hexis short stack based on EIS data. A detailed comparison between fuel deviation based on EIS data and extracted by the cascade model is shown in Fig. 4.12 for two cases. In one case (Fig. 4.12c) the deviation is below 3 %. In another case (Fig. 4.12d) the fuel amounts deviate from the nominal value by up to 10 %. Both fuel amounts determined by the cascade model are confirmed by changes of the gas concentration impedance data as shown in Fig. 4.12a, 4.12b and in the corresponding bars in 4.12c and 4.12d, respectively. However, the deviation between these two stacks is not related to a faulty design, but rather to production tolerances, assembling issues or leakages. Note, the high frequency intercept that corresponds to the ohmic resistance in the Nyquist plots (Fig. 4.12a and 4.12b) are shifted for each cell to the same point. The aim of this adjustment is to illustrate more clearly the variation in the size of the gas concentration arcs in the low frequency region, which are affected by the available fuel amount.

As described above reliable quantification of the fuel feed per RU depends on the quality of the available (V,I)-data. Crucial for a good fuel amount fit is the characteristic bend of the (V,I)-curve at high FUs. This has been confirmed by comparison of predictions by the cascade model with EIS-data. This characteristic bend is usually more pronounced for cells that exhibit a fuel undersupply. Detecting fuel undersupply is crucial for secure stack operation. This is because it can lead to harmfully high FUs resulting in excessive anode degradation e. g. by NiO formation and resulting microstructure changes [96, 98].
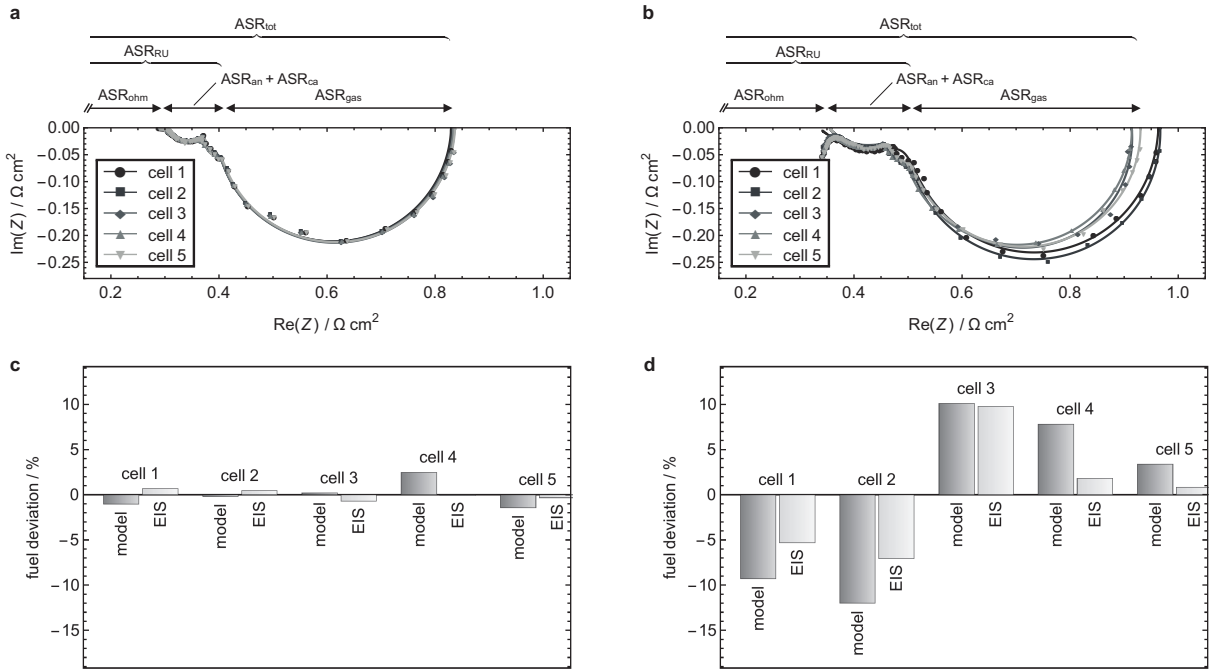
Fig. 4.12 a) EIS spectra with small fuel variation extracted from a short stack operated at 850 °C with CPOx reformed natural gas after 1120 h. b) EIS spectra measured in a short stack at 900 °C after 9600 h stack operation with CPOx reformed natural gas. c) Standardized fuel deviation determined by the cascade model compared to the corresponding EIS data shown in a). d) Standardized fuel deviation determined by the cascade model and by EIS for b). Fuel feed irregularities indicated either by EIS or by the cascade model reproduce the trend with a good agreement.

In contrast, fuel oversupply does not affect degradation but decreases the overall electrical efficiency.

4.4.2 Comparison of experimental data with degradation model

The cascade and degradation models enable the comparison between internal resistances under stack operation ($\text{ASR}_{\text{RU-C}}$) and the sum of the resistances of individual stack components ($\text{ASR}_{\text{RU-}\Sigma}(t)$) obtained either from single laboratory experiments or from averaged experimental stack analysis (cf. section 4.2.4). If all local degradation phenomena within a stack can be described by $\text{ASR}_{\text{RU-}\Sigma}(t)$ then the difference to the extracted $\text{ASR}_{\text{RU-C}}$ should consequently turn to zero. The ASR trends at the bottom of Fig. 4.10a represent the residual by subtracting $\text{ASR}_{\text{RU-}\Sigma}(t)$ based on single degradation effects (degradation model), from the repeat unit resistance $\text{ASR}_{\text{RU-C}}$ calculated by cascade model based on experimental (V,I)-data. The widely horizontal ASR trends around zero features that the applied degradation models includes all relevant degradation losses. The
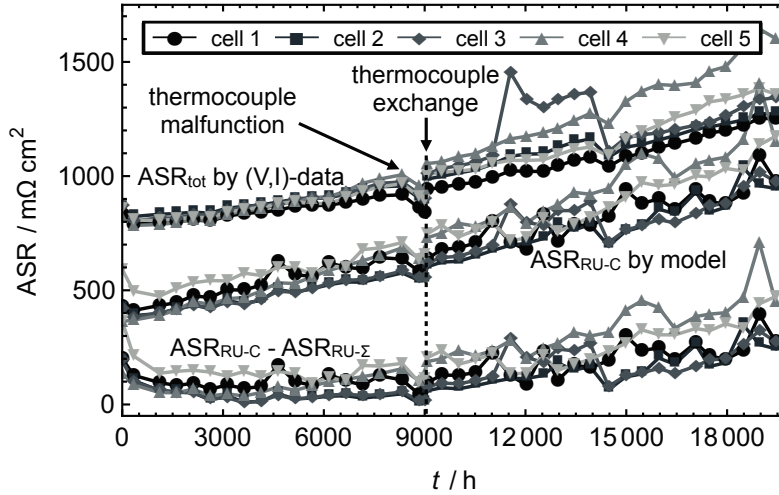
Fig. 4.13 ASR trends from a short stack operated with $0.04\,\mathrm{g\,h^{-1}\,cm^{-2}}$ CPOx reformed natural gas from the local grid with CH_4 contents between $88\,\%$ and $93\,\%$ and [44] and $2\,\mathrm{g\,h^{-1}\,cm^{-2}}$ air on cathode side at $900\,\mathrm{°C}$. Irregularities at ca. $9000\,\mathrm{h}$ represent an enhanced degradation due to instable temperature control. The top family of curves represents the ASR_{tot} increase for each cell. The middle set of the curves represent the increase of the ASR_{RU-C} determined by the cascade model. The curves at the bottom represent the remaining deviation between ASR_{RU-C} from cascade model and $ASR_{RU-\Sigma}$ from degradation model (cf. section 4.2.4).

above discussed overestimation of ASR_{RU-C} in Fig. 4.10a for cell number 5 is consequently still present since $ASR_{RU-\Sigma}(t)$ does not implicitly include a fuel amount misinterpretation. However, within the first $3000\,\mathrm{h}$ some phenomenas take place that are not taken into account properly by $ASR_{RU-\Sigma}(t)$. This can be associated with reverse effects between contact resistance, by settling phenomena, coating and interfering oxide formation effects on the MIC within this initial period influencing the electrical conductivity [68–70, 99–105].

Fig. 4.13 shows the ASR evolutions for another stack that was operated at $900\,\mathrm{°C}$ with CPOx reformed natural gas. The residual curves at the bottom line ($ASR_{RU-C}-ASR_{RU-\Sigma}$) show also the decreasing trend within the first $3000\,\mathrm{h}$ that turns into the expected horizontal behavior close to zero. After $8000\,\mathrm{h}$ the ASR curves show an irregular and pronounced decrease. This irregularity is related to a thermocouple drift. Thermodynamic calculations show that the temperature increase must be in the range of $100\,\mathrm{°C}$, since the OCV was reduced by $30\,\mathrm{mV}$ within $1000\,\mathrm{h}$. After the thermocouple replacement at $t \approx 9000\,\mathrm{h}$ the residual trends at the bottom line show a clearly recognizable increase which is not captured by the applied degradation model $ASR_{RU-\Sigma}(t)$. It is believed that the stack temperature excursion to around $1000\,\mathrm{°C}$ has induced an excessive and irreversible degradation. This example illustrates that model based analysis of (V,I)-data in combination

with a degradation model ($ASR_{RU-\Sigma}(t)$) can help to identify unexpected degradation phenomena. Such a identification can be applied in real time. Thus, some corrective action for safe stack operation to avoid overheating can be taken immediately.

In addition, the modeling approach allows one to analyze the effect of variations of the fuel composition on the ASR [44]. Besides that, there are additional malfunctions of SOFC stacks, which probably could be identified by the degradation model. Specifically, carbon deposition [106] and sulfur poisoning, which both affect the triple phase boundary (TPB) activity and hence the electrical performance. For example, for SOFC systems operated with natural gas, the cascade model predicts that sulfur poisoning caused by the end of life of the upstream desulfurizer causes a decrease of the fuel amount by about 33 % for CPOx reformed natural gas. This is related to sulfur absorption on the Ni sites, which are then no longer available for the water gas shift reaction [107].

4.4.3 Further model features

For the entire series of connected elements, the cascade model enables to extract information about local species concentration, current density and Nernst potential. Local species concentrations for each cascade element were determined by Eq. (4.5) and the corresponding thermodynamic equilibria. The local current density for each cascade element follows from Eq. (4.4) and Eq. (4.2) provides the local Nernst potential. The graphs in Fig. 4.14 on the left side (4.14a, 4.14c, 4.14e) represent the local current density j_l and the Nernst potential U_N, respectively as function of cell radius r at different FUs. The underlying planar disc cell design is shown in Fig. 4.15. The curves for the local Nernst potential have a constant slope at low FU, but show changes in slope at high FU. The local Nernst potential starts independently of the load point (FU) at the OCV. This behavior is expected since at the channel inlet ($r = 2\,cm$) the gas composition is not altered by any fuel consumption. Regardless of the effective fuel utilization the Nernst potential U_N is decreasing along the fuel channels towards external load potential U_L at the channel outlet ($r = 6\,cm$). This behavior is related to the ohmic law and it is characteristic for the applied equivalent circuit in the cascade model, as shown in Fig. 4.3b. The local current density j_l also shows a decreasing behavior along the fuel channel, which correlates to the local Nernst potential. This is expected since, according to the ohmic law, the local current density must be proportional to U_l for a constant ASR_{RU} as provided by the cascade model.

Figs. 4.14b, 4.14d and 4.14f on the right side show the local molar fractions for the anode gas at different FUs along the fuel channels. These molar fractions result from
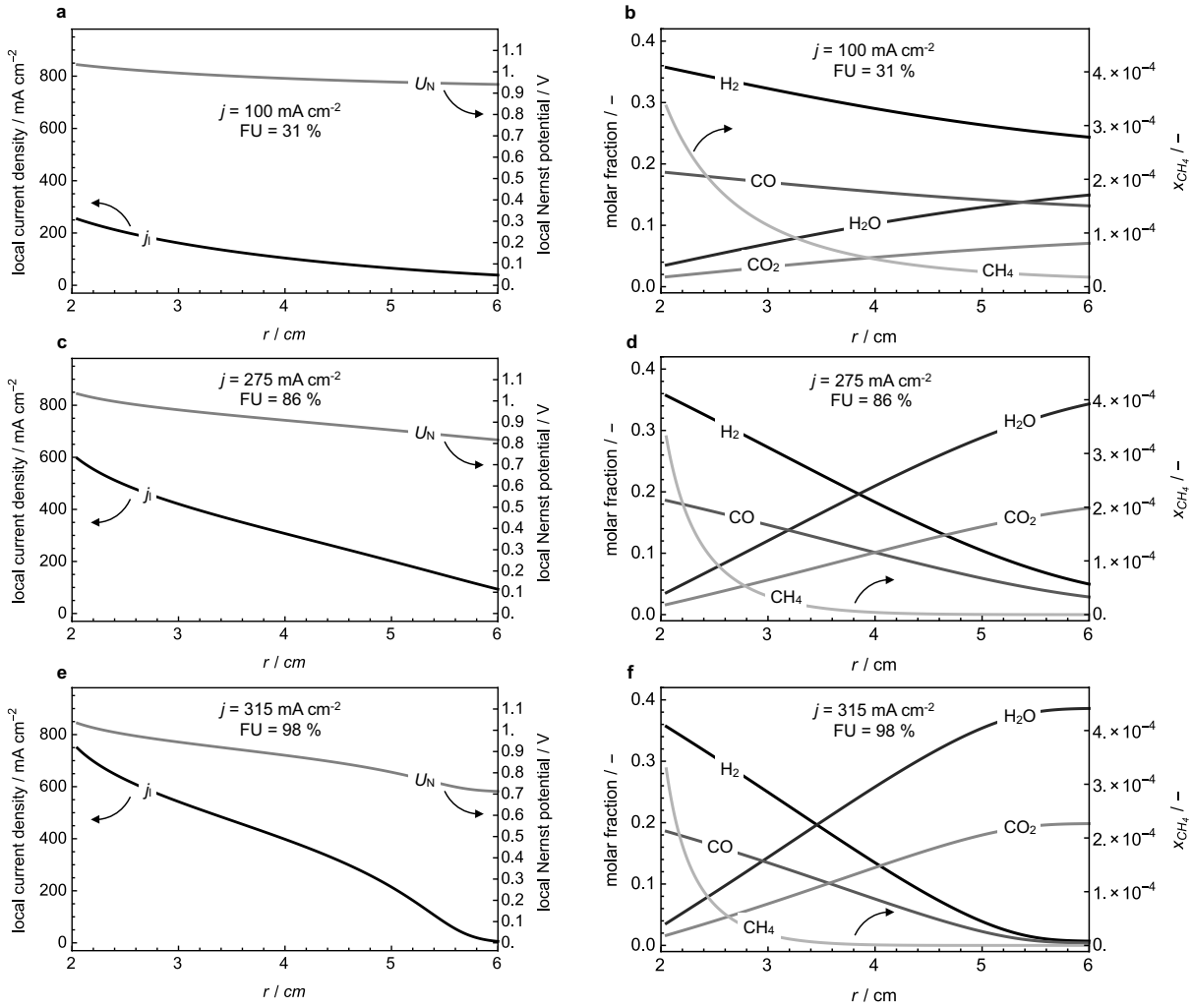
Fig. 4.14 Graphs a), c) and e) represent the local current (j_l) and Nernst potential (U_N), respectively as function of cell radius (r) for different FUs with $0.04\,\mathrm{g\,h^{-1}\,cm^{-2}}$ CPOx reformed natural gas from local grid with a CH_4 content of 90 % [44] and $2\,\mathrm{g\,h^{-1}\,cm^{-2}}$ air on cathode side at 850 °C. The local gas concentrations at the corresponding FUs are illustrated in b), d) and f).

the thermodynamic equilibrium calculation based on the O^{2-} transport across the electrolyte (cf. Eq. (4.5)). The inlet fuel mixture is identical for all fuel utilizations, which is consistent to the Nernst potential at the channel inlet (cf. Figs. 4.14a, 4.14c and 4.14e). The concentration of reagents (CH_4, H_2 and CO) decreases gradually along the channel. This decrease is obviously more pronounced at higher FU (cf. Figs 4.14d and 4.14f). The products (H_2O, CO_2) correlate to the fuel oxidation and hence increase along the flow channel.

Transport limitation by diffusion along and orthogonal to the gas channels are neglected in the introduced cascade model. Nonetheless comparisons of the results from the cascade
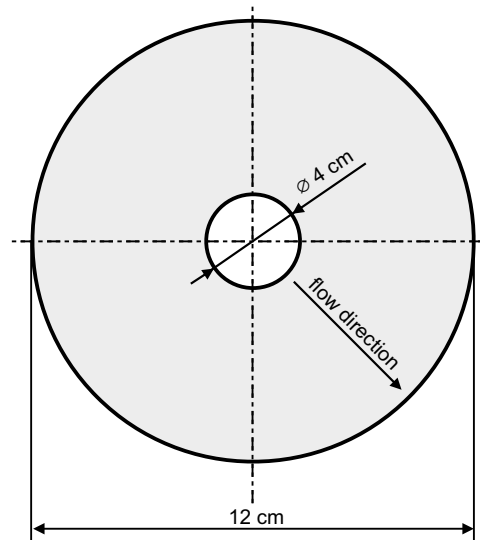
Fig. 4.15 Schematic illustration of a planar disk shaped cell design. Further details are given in [8].

model (cf. Fig. 4.14) with data available in literature based on different model types show a good qualitative agreement [108–111].

The option to extract information about the local conditions that vary with FU as illustrated in Fig. 4.14 provides useful references to study the degradation behavior of different components under accurate conditions [103, 112–114].

4.5 Conclusions

The introduced cascade model takes into account stack effects like leakages and nonuniform fuel distribution that are often related to manufacturing tolerances and varieties in the natural gas composition. Considering these effects is relevant for further stack improvement since degradation characterization based on an overall ASR trend can lead to misinterpretation.

Stack characterization with EIS is doubtless the favored method since the available information in impedance spectra can be separated into single loss constituents. However the required infrastructure for EIS analysis is expensive and not everywhere available e. g. for stacks running in the field. The introduced cascade model is able to quantify ASR_{RU-C} based on experimental (V,I)-data accurately. This is confirmed by comparison of ASR_{RU-C} trends extracted by the cascade model with those from EIS data. Hence the introduced model has the potential to provide additional information from SOFC stacks running in the field. Further work will focus on the improvement of the quantitative fuel amount

determination in case of fuel oversupply and on the applicability of the cascade model to other stack designs and cell types operated with natural gas, e. g. anode supported cells.

Comparing stack repeat unit degradation systematically with averaged degradation behaviors of the single contributions can also help to detect unusual stack behavior (especially during early stages of the operation). Based on these results the operating conditions can be adapted in a purposeful manner, in order to reduce degradation and finally to appropriate corresponding operation measures.

Chapter 5

Metallic interconnect degradation

The interconnect in a fuel cell stack has overtake different functionalities in the stack such as providing the fuel to the anode and the air to the cathode, respectively, collect and transfer the electrical current and separate the fuel and the air [66, 115, 116]. The ideal properties for materials used in interconnects are as follow:

   i) oxidation and corrosion resistance,

  ii) high electrical conductivity,

 iii) coefficient of thermal expansion matching to cell components,

  iv) mechanical durability,

   v) low volatility of constituents,

  vi) high thermal conductivity,

 vii) chemical compatibility with adjacent materials and

viii) low material and manufacturing cost [26, 66, 116, 117].

To find a suitable material for interconnects that meet the comprehensive requirements different materials and variation of them were reviewed. Ceramic materials, such as doped lanthanum chromite $La_xSr_1 - xCrO_3$, exhibit outstanding temperature stability, However, issues like fabrication difficulties and consequently high costs makes ceramic as a interconnect material unsuitable for SOFC application outside of laboratory [116]. Conventional high temperature alloys, which usually contain Al, Si or Cr to form a desired protective scale, fulfill requirements for oxidation and corrosion resistant, as well the cost targets. Al and Si as alloying components leads to a formation of slow growing Al_2O_3

Table 5.1 Composition of investigated materials (in wt.%) [89, 90, 120, 121]. CFY is used in stack and exposure experiments. Crofer is used in exposure tests only. JS-3 composition is needed for comparison within the discussion in section 5.1.3.

	Cr	Fe	C	N	Mn	Si	Cu	Al	W	S	P	Ti	reactive elements	
													La	Y
Crofer 22 APU	20-24	Bal.†	0.03‡		0.3-0.8	0.5‡	0.5‡	0.5‡		0.02‡	0.05‡	0.03-0.2	0.04-0.2	
Crofer 22 H	20-24	Bal.†	0.03‡	0.03‡	0.3-0.8	0.1-0.6	0.5‡	0.1‡	1-3	0.006‡	0.05‡	0.02-0.2	0.04-0.2	
JS-3*	23.3	Bal.†			0.4	0.009		0.005				0.047	0.089	
CFY	Bal.b†	5												0.02–0.2

† difference to 100 wt.%
‡ maximum amount
* semi-commercial Crofer 22 APU [121, 122]

and SiO_2 scale, respectively at SOFC operating temperatures. These oxide scales provide high temperature oxidation and corrosion resistance. The main drawback of these oxide scales is there comparatively low electrical conductivity, which lead to an increase of the overall area specific resistance. Besides the low electrical conductivity, addition of Si in Ni-, Co- and Fe-based alloys, lead to embrittlement and therefore to unwanted mechanical disadvantages.

Fe- and Cr-based alloys achieve a reasonable compromise in fulfilling these multifaceted properties requirements, including a CTE similar to ceramic cell components. Such alloys are chromium formers, i.e. a semi-conductive Cr_2O_3 scale is growing upon surface oxidation, which introduce a corrosion resistance at the contact between MIC and electrode [92, 115, 116]. Hence, the main problem with Cr_2O_3 scales is the formation of a layer with low electric conductivity compared to the base-alloy, which leads to unwanted ohmic losses.

A possible strategy to reduce the formation of an oxide layer is the additions of reactive elements (RE), which lead to a change of the scale growth mechanism [99, 118]. It is assumed that outward diffusion of Cr along grain boundaries is hindered so that the slower oxygen inward diffusion becomes the dominant process in scale growth. Thereby, the oxide formation takes place at the interface between metal substrate and the oxide scale [99]. This improves scale adherence and reduces the oxidation rate [92, 99, 116, 118, 119]. In detail, the involved mechanisms yielding these improvements are however unclear [118]. The chromium-based elemental mixed oxide dispersion strengthened (ODS) composition containing 5 vol.% iron (CFY) [90] (cf. Table 5.1) is an example of such a Cr_2O_3 scale forming material. It contains small amounts of yttrium as a reactive element. The CTE of this alloy is ca. $10.4 \, 10^{-6}$ K^{-1} (around 900 °C) and fits well to electrolyte supported cells.

Crofer 22 APU (X1CrWNbTiLa22) and Crofer 22 H (X1CrWNbTiLa22) are other established SOFC MIC materials. Their compositions are given in Table 5.1. These Fe-based alloys combine surface oxidation stability with enhanced electrical conductivity for the oxide scale and a CTE matching to anode-supported cells. These alloys contain La as a reactive element. By the addition of Mn (≈ 0.5 wt.%) a $(Mn,Cr)_3O_4$ spinel layer is formed on top of the Cr_2O_3 sub layer. The electrical conductivity of $(Mn,Cr)_3O_4$ is five times higher at $900\,°C$ than Cr_2O_3 [92, 115, 116, 123–125]. Moreover, the Cr volatility of the $(Mn,Cr)_3O_4$ spinel phase is roughly three times lower compared to spinel free Cr-oxide scales such as the ones formed upon oxidation on CFY [115, 116].

In fuel cell stacks Cr_2O_3 scale exposure to water vapor containing atmospheres promotes the formation of volatile Cr species [117, 123, 126]. Under certain condition, this volatilization leads to chromium poisoning due to the accumulation of Cr within cathode layers [127, 128]. For improved properties regarding Cr evaporation, surface modifications and coatings are usually applied on the MIC [66, 116, 129, 130]. Effective coatings combine the following properties:

i) reduction of Cr diffusion from the metallic interconnect to the cathode,

ii) chemically compatibility with adjacent SOFC materials,

iii) high electric conductivity and

iv) a CTE close to the one of the MIC to avoid spallation [66, 116, 129, 130].

The aim of this chapter is to provide an overview of different aspects relevant for degradation of metallic interconnects. This includes an extensive study of oxide formation under realistic operating condition in section 5.1. There, the oxide scale growth is analyzed based on post-test samples of CFY MICs operated in SOFC stacks up to $40\,000\,h$ and heat exposed samples made of CFY and Crofer. To analyze oxide scale thicknesses and inhomogeneities a dedicated statistical image analysis method has been applied. SEM images are used to compare the structural phenomena related to MIC oxidation at different sample locations. Section 5.2 considers the discrepancy between oxide scale formation and ASR increase on the cathode side, which reveals a non-trivial, non-linear relationship. To understand the correlation between scale evolution and resulting ohmic losses, 2D finite element simulations of electrical current distributions have been performed for a large number of real oxide scale morphologies. The methods applied in section 5.2 are further used in section 5.3 for a qualitative characterization of the electrical current paths on the anode side, which is even more complex than the scale formation behavior on the cathode

side. Among other things, this is due to the rather vaguely defined interface between the Ni-mesh and the formed oxide scales. Finally in section 5.4 a comprehensive study of the interaction of Cr_2O_3 and adjacent Ni is presented. The latter can be originated from the Ni-mesh, the Ni coating of the employed MIC and Ni containing anodes. To study the influence of nickel on the electrical conductivity of grown oxide scales, pellets made of Cr_2O_3 mixed with different amounts of Ni were investigated in-situ under both reducing and oxidizing gas atmospheres at 850 °C. The formed crystals were analyzed using X-ray diffraction, whereas the resulting microstructures were quantified using SEM.

5.1 Quantification and characterization of oxide scale growth on MICs

The aim of this section is to quantify the oxide scale growth rates for metallic interconnects in stationary SOFC-CHP systems. This information is considered as a basis, which is then needed in a later sections to establish quantitative relationships between the oxide growth with the corresponding ohmic loss over the complete device lifetime. For the quantitative description of scale formation in the present section, a large amount of SEM images is analyzed and quantified by applying a simple imaging processing method. Oxide dimensions are assessed from heat-treated MIC samples as well as from post-stack test samples. The latter are extracted from fuel cell stacks operated with CPOx pre-reformed natural gas. This investigation also includes a unique set of post-endurance samples, obtained after completing and dissecting a CFY interconnect-based planar stack having reached 40 000 h of operation in a Galileo 1000 N system from Hexis [12]. The results are discussed also in comparison with the relevant literature data. It must be emphasized that a systematic correlation of oxide growth with ohmic losses is addressed in section 5.2.

5.1.1 Experimental details

Scale growth rates are determined by oxide size measurement from samples out of interconnects after stack-testing and from samples heat-treated in a furnace. During the heat treatment tests only cathode conditions are simulated. From the stack test samples, the oxide formation can be investigated for both atmospheres, cathode as well as for anode conditions which is called "dual atmosphere" test. The assessment of growth kinetics is based on time-lapse microscopy, i. e. scale dimensions are quantified with SEM and image analysis for different time steps.

The investigated interconnects have a fluted structure in order to provide the fuel to the anode and the air to the cathode, respectively. Thereby the ridge tops are basically used as contacts with the electrode in order to ensure the electron transport within a stack(ed) configuration between the repeat units. Throughout this work this top region is denoted as flat whereas the bottom of the gas channels is denoted as valley. This specific terminology for the fluted interconnect structure is also illustrated in the schematic cross section in Fig. 5.1.

Layer thickness determination

The layer dimensions of Cr_2O_3 scales are determined on the basis of SEM image analysis of sample cross sections. Therefore samples are cold mounted in epoxy resin and after hardening grinded and polished with SiC papers up to 4000 grit on a Struers TegraPol-35. SEM images are taken on a Tescan VEGA TS 5130 MM with the backscattering detector. This microscope is equipped with an INCAx-sight from Oxford Instruments for energy dispersive X-ray spectroscopy (EDX). To generate representative results up to ten SEM images are analyzed for each sample location as given in Fig. 5.1, e.g. the contacting
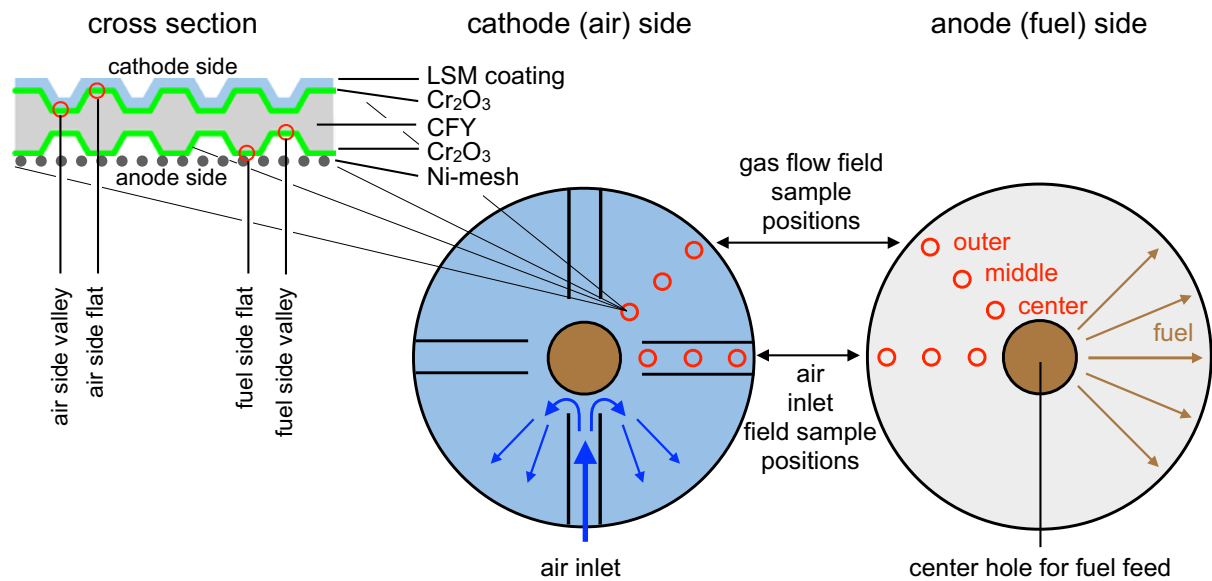
Fig. 5.1 Schematic illustration of Hexis' MIC design. The blue disk in the middle pictures the flow path on the cathode side. Each quadrant comprises an inlet channel, with air fed from the outer edge. The flow direction is deviated near the central hole to reach a co-flow regime within the main area of the cell. The right side illustrates the anode flow field where the fuel flows from the central hole (co-flow) to the outer edge. The red circles mark the locations of sample extraction. As shown on the left side, anode, cathode as well as flat and valley are analyzed for all six sample locations.
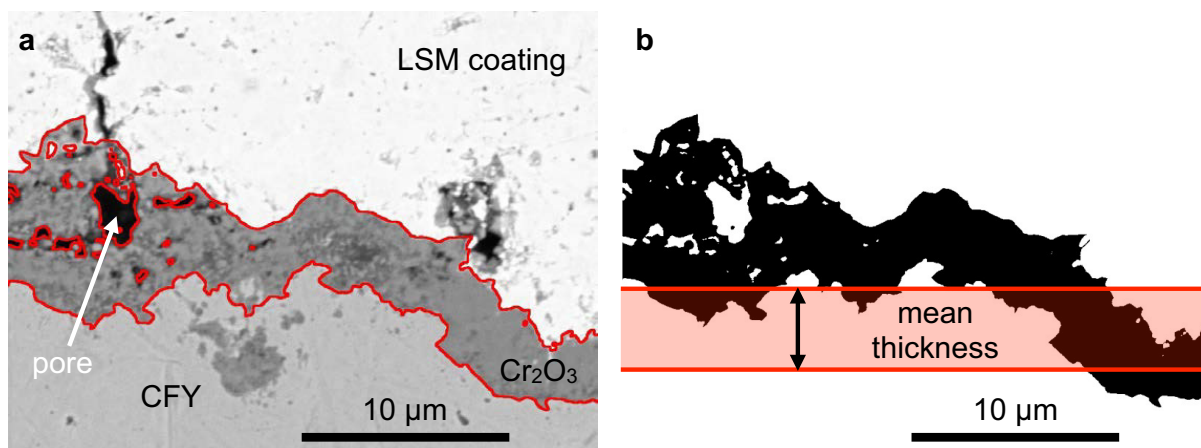
Fig. 5.2 a) SEM image of a cross section of a metallic interconnect after 2000 h exposure (850 °C in air). The perimeter of the Cr_2O_3 scale is marked by a red contour line. b) From the segmented and binarized SEM image a mean scale thickness is calculated.

flat on the anode side. The number of images that is necessary for a representative analysis varies as a function of sample location and magnification of an investigated area. For thicker layers, found at longer exposure time, the magnification can be reduced and hence a smaller number of images is required. The quantification process is illustrated in Fig. 5.2. Therefore the Cr_2O_3 layer is identified based on its gray-scale contrast. After segmentation with the Adobe Photoshop CS5 image precessing software the (black) pixels representing the Cr_2O_3 layer are counted. For each image, the mean layer thickness is then calculated by dividing the number of black pixel with the image width. This result is then multiplied by the corresponding pixel size. Counting and calculation steps are done automated with the computational tool Mathematica 8.0. Note: image orientation is always perpendicular to the MIC surface.

Heat treatment tests

In these heat treatment tests, four different materials are investigated; these are Crofer 22 APU, Crofer 22 H, CFY and LSM coated CFY. Their elemental compositions are given in Table 5.1. All compounds present a fluted-structure (Fig. 5.1) that is comparable to a MIC and ensures fuel and air distribution (valley) as well as current collection (flat) in a stack(ed) configuration. The samples are exposed to 850 °C at ambient air in a Carbolite CWF 12/13 box furnace without an additional air circulation. Heating rate is 3 °C min⁻¹. For the different time steps up to 5300 h the furnace was cooled down to remove probes at each time step for time lapse microscopy.

Observation of surface crystal formation on a heat-treated sample

A specific surface location on a uncoated CFY sample was marked in order to follow the growth of individual surface crystals at different time steps. The marked sample was exposed together with the heat treatment samples at the same time and under the same conditions. This sample was always removed from the box furnace during ordinary samples removal for the time lapse microscopy. Before the furnace at any one time was reheated the surface of this specific sample was investigated on the marked location by SEM analysis with the secondary electron detector.

Post-test stack samples

Oxide scale growth on the CFY MIC from SOFC stacks was assessed by analyzing more than 1000 SEM images from 30 samples, which were extracted from different CFY interconnects that had been operated for several thousand hours in five different stacks at 900 °C. These on the cathode side with LSM coated MICs were operated under dual atmospheres SOFC conditions. This implied the simultaneous exposure to anode fuel and cathode air environments. Testing conditions involve ambient air and pre-reformed (CPOx) natural gas (NG) from the local grid at Winterthur (Switzerland). The reformed natural gas mainly consists of N_2, H_2, CO, CH_4 and a certain amount of H_2O depending on the fuel utilization and the current load (see Fig. 4.14). Variations in the natural gas composition are ineluctable in the natural gas grid [44], especially within 40 000 h operation. Such long-term testing also inevitably involves incident as well as maintenance shut downs, leading to thermo and full redox cycles which means that the whole anode is oxidized in the sealing-less stack design. Detailed operating conditions are given in Table 5.2.

In this work, the samples from the Galileo stack were removed from the middle part. Despite of the convex temperature profile along the vertical direction it can be assumed that the samples from both short- and system stacks have experienced the same temperatures of 900 °C (Table 5.2).

Within a repeat unit the scale growth rates may vary. This is due to local variation of parameters such as temperature gradients, oxygen partial pressure (p_{O_2}), water partial pressure (p_{H_2O}) or gas flow rates. In order to quantify those variations six samples are taken from different locations of each single MIC. The positioning of the sample extraction locations within the MIC flow-field is given in Fig. 5.1.

Table 5.2 Operating conditions and test history of investigated stacks. Active cell and MIC area in this round planar stack is $100\,\text{cm}^2$.

									cell contact	
test time	stack type	fuel	reformat	redox[*]	temp.	fuel flux	air flux	load[†]	fuel side	air side
4200 h	short	NG	CPOx	2	900 °C	$0.04\,\text{g}\,\text{h}^{-1}\,\text{cm}^{-2}$	$2\,\text{g}\,\text{h}^{-1}\,\text{cm}^{-2}$	25 A	Ni-mesh	LSM[‡]
5700 h	short	NG	CPOx	0	900 °C	$0.04\,\text{g}\,\text{h}^{-1}\,\text{cm}^{-2}$	$2\,\text{g}\,\text{h}^{-1}\,\text{cm}^{-2}$	25 A	Ni-mesh	LSM[‡]
10 700 h	short	NG	CPOx	2	900 °C	$0.04\,\text{g}\,\text{h}^{-1}\,\text{cm}^{-2}$	$2\,\text{g}\,\text{h}^{-1}\,\text{cm}^{-2}$	25 A	Ni-mesh	LSM[‡]
13 200 h	short	NG	CPOx	24[§]	900 °C	$0.04\,\text{g}\,\text{h}^{-1}\,\text{cm}^{-2}$	$2\,\text{g}\,\text{h}^{-1}\,\text{cm}^{-2}$	25 A	Ni-mesh	LSM[‡]
40 000 h	Galileo	NG	CPOx	15	900 °C	$0.04\,\text{g}\,\text{h}^{-1}\,\text{cm}^{-2}$	—[¶]	0.72 V	Ni-mesh	LSM[‡]

[*] numbers of redox cycles
[†] either constant current or constant voltage
[‡] LSM coating on cathode side
[§] 20 redox cycles within the first 800 h
[¶] air flux is varying with discharged heat amount to keep the stack temperature constant (temperature controlled)

5.1.2 Results

Layer thickness determination

The size distribution for the analyzed amount of SEM images at each single sample location is investigated to ensure that the applied oxide scale size quantification gives a representative mean scale thickness. Such a distribution is shown in Fig. 5.3. The distribution in this example based on the data out of nine SEM images (flats) over each single pixel column follows a normal distribution. A similar behavior is usually observed for all sample locations. This confirms that the applied method is reliable to determine a mean oxide scale thickness based on the analyzed SEM images.

CFY interconnect oxidation under dual atmospheres exposure in stacks

In the following section a qualitative description of the main microstructural features associated with scale growth will be presented and then the local quantitative variations on the anode and cathode sides will be discussed.

Qualitative variations in the microstructure   An illustration of the main microstructural features is shown with three representative images in Figs. 5.4a to 5.4c. On Fig. 5.4a (anode side) interaction of the Cr_2O_3 scale with the Ni-mesh leads to the formation of a patchy layer, which contains metallic Ni-grains (bright) that are embedded in a Cr-oxide matrix (gray). This scale-structure is typical for the flat on the anode side (center position). Below this outer Cr-oxide layer the upper part of the MIC is transformed into a porous zone, which contains metallic grains (from the initial MIC) as well as oxides
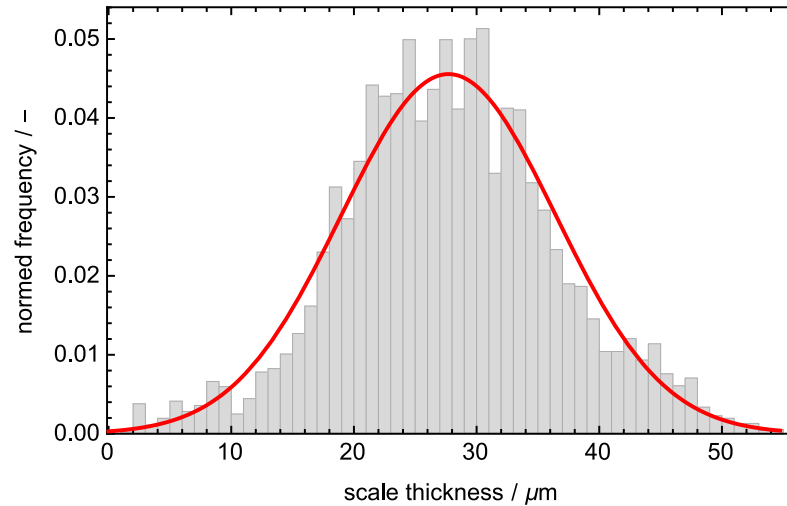
Fig. 5.3 Scale size distribution based on single pixel columns out of nine SEM images from a sample located in air inlet channel in the middle region on flat at anode side after 5700 h stack operation (cf. Fig. 5.1).

(Cr_2O_3 mainly). This layer is subsequently called "internal oxidation layer", because the oxidation is growing inwards from the initial MIC surface. Underneath the porous, internal oxidation layer an additional phase (darker than CFY, but brighter than Cr_2O_3) is observed on SEM/BSE (back-scattered electron detector) images. This phase is identified as Cr_2N by EDX spot analysis and it is a typical feature for the center position on the anode side.

Fig. 5.4b shows the valley at the outer position of the anode side. The scale is composed of a homogeneous Cr_2O_3 layer marbled with pores. In contrast to the center position,
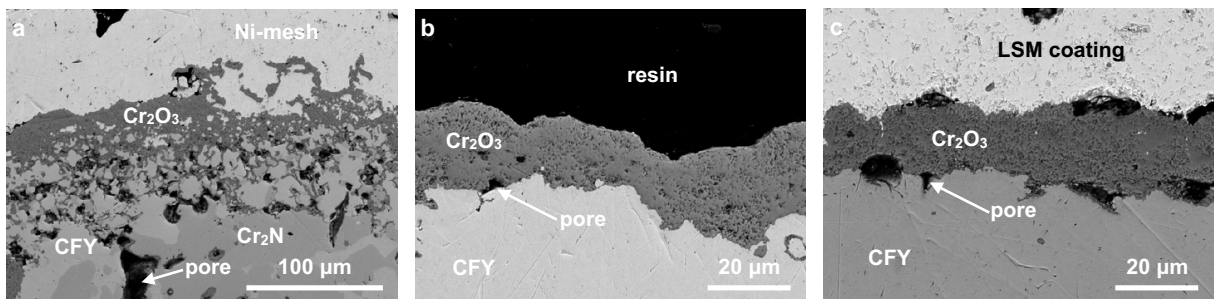
Fig. 5.4 Scale characteristics for cathode/anode | flat/valley locations after 10 700 h short-stack operation with CPOx reformed natural gas. These SEM backscattered electron images illustrate the trends for the Cr-oxide microstructures given in Table 5.3. a) Anode side, center position, flat location: strong internal oxidation, few pores within the Cr_2O_3 scale, nitride formation beneath the oxide layer and some Ni-mesh interaction. b) Anode side, outer position, valley location: pores are present within the oxide scale. c) Cathode side, middle position, flat location: pores are formed at the scale interfaces. NB: magnifications differ for sub-figures a), b) and c).

Table 5.3 Trends of oxide scale characteristics for all 24 sampling locations (Fig. 5.1) assessed for five stacks with 1000 SEM images. The specific characteristics are exemplary given in Fig. 5.4.

| | | air inlet field | | | | | | gas flow field | | | | | |
| | | flat | | | valley | | | flat | | | valley | | |
		center	middle	outer	center	middle	outer	center	middle	outer	center	middle	outer
anode	internal oxide	●	●	◐	●	●	○	●	●	◐	●	●	○
	pores only within the oxide scale	○	○	○	○	◐	●	○	○	○	○	◐	●
	Cr_2N	●	◐	○	●	◐	○	●	◐	○	●	◐	○
	Ni-mesh interaction	◐	○	○				◐	○	○			
cathode	internal oxide	○	○	○	○	○	○	○	○	○	○	○	○
	pores within the oxide scale and at the interfaces	●	●	●	●	●	●	●	●	●	●	●	●
	Cr_2N	○	○	○	○	○	○	○	○	○	○	○	○
	LSM interaction as $CrMn_2O_4$-spinel formation	●	●	●	●	●	●	●	●	●	●	●	●

○ not observed
◐ partly observed
● observed

there is no internal oxidation layer and no formation of Cr_2N at the outer position.

Fig. 5.4c is representative for the scale structure on the cathode side. A relatively homogeneous Cr_2O_3-layer is formed between MIC (bottom) and LSM layer (top). The layer contains pores whereas some of them are formed at the interfaces to the MIC and to the LSM protection layer. Furthermore the formation of $(Cr,Mn)_3O_4$ spinel was identified with SEM and EDX (see Fig. 5.12 and corresponding discussion in section 5.1.3), which appears to be typical for the oxidation of cathode MICs with an LSM protection layer (not clearly visible in Fig. 5.4c).

Based on the described observations four main structural features associated with MIC scale growth can be observed. These features, which may vary as a function of the sample location, are the following: i) the internal oxidation layer (anode side), ii) the formation of pores within the oxide layer and at its interfaces with the adjacent MIC or LSM layers, iii) the formation of Cr_2N in the MIC and iv) interactions between Cr-oxidation layer with the adjacent current collector materials (i. e. Ni-mesh on anode side, LSM on cathode side).

Based on the extensive sampling for all 12 sample locations as described in Fig. 5.1 (i. e. air inlet and gas flow fields | center, middle and outer positions | flat and valley) a systematic pattern of microstructural variations can now be characterized. These variations are summarized qualitatively in Table 5.3 and they can be described as follows:

First of all it is important to note that the scale structures on the cathode side are more homogeneous than on the anode side. On the cathode side differences are neither observed between flat and valley nor between the air inlet and gas flow fields. Hence, for

all sample locations on the cathode side the structures are similar as shown in Fig. 5.4c.

On the anode side the scale characteristics are changing as a function of the sample location. The formation of an internal oxidation layer (with pores) is typically observed at the center and middle positions. In the outer positions this layer is weak on the flats and it is completely missing on the valleys. The formation of pores is a characteristic feature at the valley of the outer positions. In contrast Cr_2N is only observed in center and middle positions. There are thus clear differences on the anode side between different radial positions (center, middle, outer) and between flat and valley. However there are no structural differences between equivalent positions in the air inlet and in the gas flow fields.

Quantitative variations in the scale thickness The focus in this paragraph is on the quantitative description of the mean scale thickness (and its evolution over time), by using the procedure illustrated in Fig. 5.2. A representative example for the extent of MIC oxidation at different sample locations and after a given operating time is shown in Fig. 5.5. This result comes from a five cell short stack that had been operated for 10 700 h at 900 °C with CPOx reformed natural gas. Mean scale thicknesses are presented for the different sampling locations. Each data point is obtained from numerous SEM images. The mean (red diamond) and median (gray line) thicknesses as well as the upper and lower quartiles present some scatter of the data in this Box-Whisker chart. Quantitative trends are however clearly identified with such a statistical representation. The anode scale thickness is higher than on the cathode side, i. e. scale growth rates are higher in the fuel compartment with lower oxygen partial pressure and presence of steam. Anode flat oxide layers are thicker than at valley locations where no covering with a Ni current-collecting material is present. The latter trend, higher oxide amounts on the flat compared to the valley, is also observed on the cathode side, although less pronounced. For both cathode and anode side, no systematic quantitative differences are evidenced between the various sample locations, neither for sampling within the air inlet region nor within the gas flow fields with respect to radial shifts. However, as shown in Table 5.3, there are some qualitative microstructual features that vary with sample locations.

Systematic quantitative differences are only found between anode and cathode as well as between flat and valley and not for the different sampling locations. All scale thickness measurements within a MIC are averaged for the following four categories: anode flat, anode valley, cathode flat and cathode valley. These results are plotted in Figs. 5.6 and 5.7 for different stack tests.
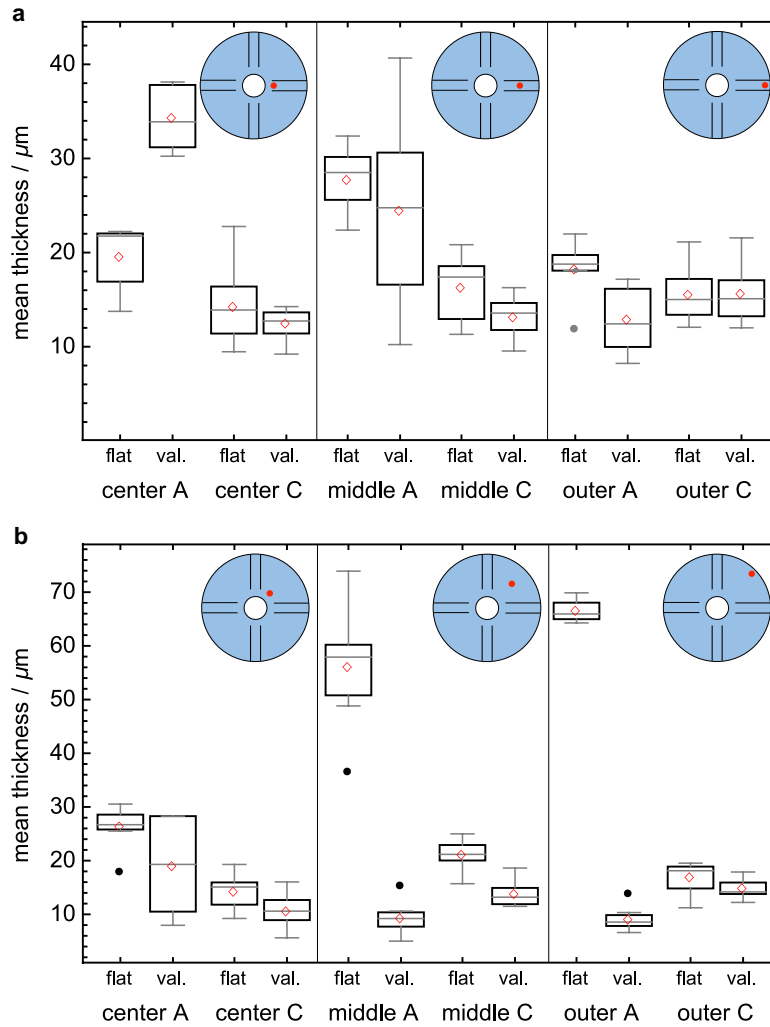
Fig. 5.5 Box-Whisker charts for the distributions of the mean scale thickness after 10 700 h operation. These samples were extracted at different locations (given in Fig. 5.1) a) in the air inlet channel and b) the gas distribution field. The denominations center, middle and outer specifies the different radial positions. A and C stand for the anode side and the cathode side, respectively.

Oxide scale growth rates during stack operation

In order to describe the scale growth rate the data from time laps microscopy was first fitted with a parabolic rate law that is based on Wagner's oxidation theory by

$$x^2 = k_\mathrm{p}\, t \tag{5.1}$$

were x is the mean scale thickness, t the operating time and k_p the parabolic rate constant. However, in most cases the parabolic rate law is unsuitable to describe chromium oxide scale growth rates especially at longer exposure time. Therefore the data was fitted with

a more generic exponential relation. For convenience Eq.(3.5) defined in chapter 3.3.4 is reproduce here

$$x = k_e \, t^n \tag{5.2}$$
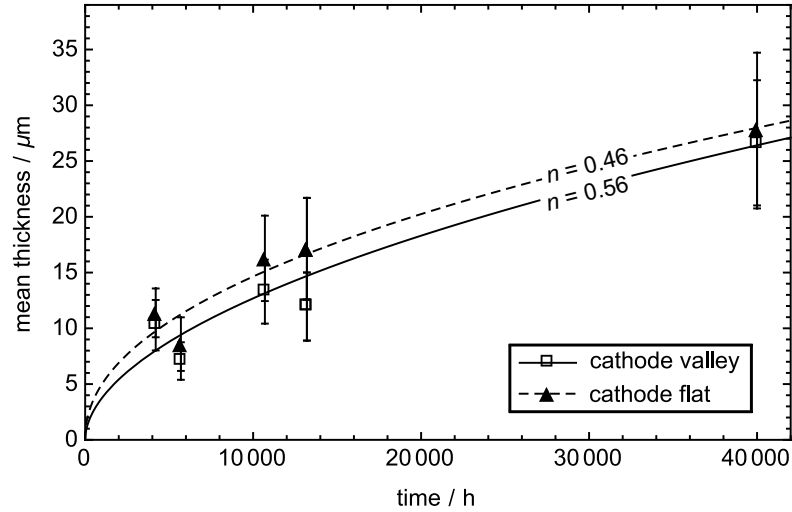
Fig. 5.6 Cathode side MIC oxidation evolution in stacks. Flat scales (closed symbols) are systematically thicker than valley oxide layers (open symbols); the difference is however small. The mean data points follow a parabolic growth law, where the exponents fitted by Eq. (5.2) are close to $n = 0.5$.
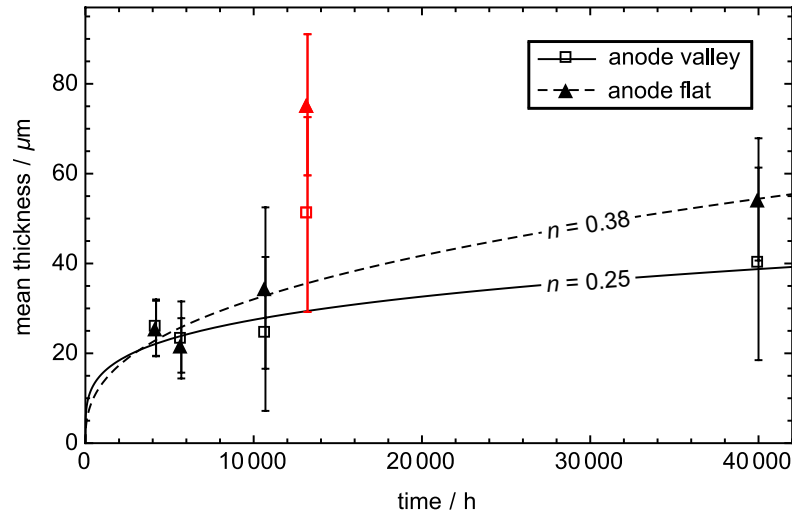
Fig. 5.7 Oxide scale growth on the anode MIC upon stack testing up to 40 000 h. Open symbols represent mean values of calculated scale thicknesses for flat regions. Closed symbols represent mean values from valley cross sections. The curves are based on data fits with Eq. (5.2) without considering the data points at 13 200 h (red marked). These samples are derived from a stack with 20 redox cycles within the first 800 h of operation. The exponents ($n = 0.38$ for flat, $n = 0.25$ for valley) indicate a non-parabolic scale growth on the anode side.

were k_e is the exponential rate constant and n the exponent. This relation better describes the often reduced growth rates at exposure times longer than several hundred hours. Such reduced growth rates are observed for alloys that contain reactive elements (RE) [131]. Thereby the reactive elements prevent outward diffusion of metal ions e. g. Cr^{3+} [99].

As shown in Fig. 5.6 the growth rate exponents for the cathode side are close to $n = 0.5$. The scale growth on the cathode side can thus be interpreted as being parabolic. In contrast the exponents describing oxidation on the anode side (Fig. 5.7) are clearly smaller (i. e. $n = 0.25$ for anode valleys and $n = 0.38$ for anode flats). However for the fits the data points at 13 200 h (red marked) are not considered on the anode side. This data are derived from five cell short stack which was operated with 20 full redox cycles during the first 800 h of operation. As a result of this operation mode the oxide scale on anode side is significantly enlarged and does obviously not match to the overall scale size development. In contrast some influence by these redox cycles during initial stage to the quantitative oxide scale formation on the cathode side is not indicated (Fig. 5.6).

When comparing absolute scale thicknesses in Figs. 5.6 (cathode side) and 5.7 (anode side) with each other it becomes apparent that the oxide layers on the anode side are thicker despite of the smaller n-values. This is attributed to a higher exponential rate constant k_e, which leads to formation of relatively thick oxide layers on the anode side during the first few hundred hours. Furthermore it is important to note that the scales on the flat are systematically thicker than on the valley. These local differences are also observed on the cathode side. However, there they are less pronounced.

Scale thickness and growth rates derived from heat treatment tests

To investigate and compare some effects of different materials and to interpret the results from stacks tests, MIC samples of four different materials were additionally exposed in ambient air up to 5300 h. The results of such model experiments are more comparable to literature data, which are usually collected in a similar way. Fig. 5.8 shows the time dependence of the mean oxide layer thicknesses (values are calculated from over 300 SEM images) for CFY, CFY coated with LSM, Crofer 22 APU and Crofer 22 H. The growth characteristics during the first 500 h are similar for all four materials. At longer exposure time (i. e. more than 2000 h) oxide thicknesses for Fe-based alloys are larger than for the Cr-based CFY. Hence different growth rates and exponents are determined for the two material types by fitting the data with Eq. (5.2). The exponent obtained for the Crofer 22 APU is equivalent to $n = 0.5$. Also Crofer 22 H with $n = 0.46$ follows an oxidation behavior close to a parabolic rate law. For the LSM coated and uncoated
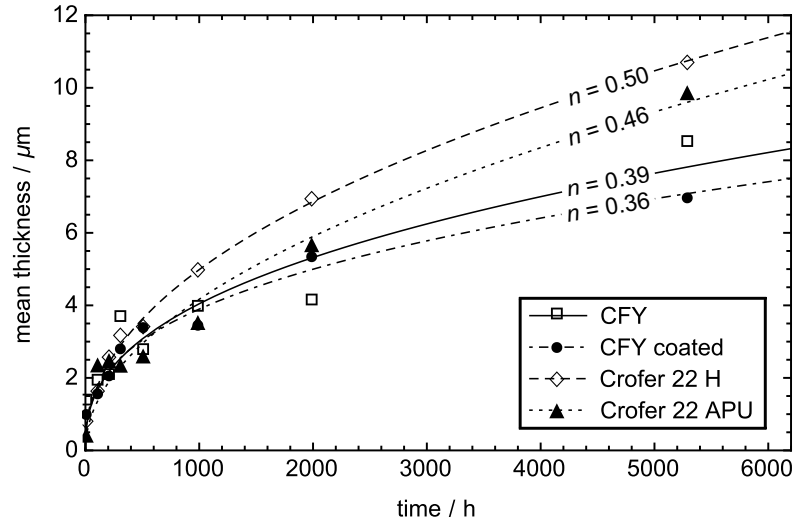
Fig. 5.8 Oxide scale growth derived from exposure tests (850 °C in air) for different MIC materials. The lines show the fitted growth rates according to Eq. (5.2). The variation of exponent n indicates different oxidation mechanism for such material configurations.

CFY the exponents are $n = 0.36$ and $n = 0.39$, respectively. In this context it should be emphasized, that the experiment in Fig. 5.8 is performed under static conditions (i.e. no airflow). As shown by Stanislowski et al. [126] in the static case equilibrium is reached between evaporation and re-precipitation (called "equilibrium vaporization") and thus, no significant influence of evaporation on the growth rate is expected. This may explain the similar scale growth rate and behavior of coated and uncoated samples.

Surface oxide formation on a heat-treated sample

To investigate the surface oxide formation on the RE containing CFY a discrete spot was analyzed for the different time steps. Fig. 5.9 show the development of surface crystals during heat exposure. The final arrangement and shapes of surface crystals are recognizable already after 10 h heat exposure. A tendency for covering the original crystals by the formation of new crystal nucleus could not be observed which means that further oxide scale growth takes place at the scale/alloy interface or somewhere within oxide scale. The quantitative assessment of surface crystal growth is given in Fig. 5.10, which points out that the initially high growth rates reduce to moderate rates after 100 h. After 2000 h, the surface crystal growth is terminated and no significant surface alterations are visible at longer exposure times.
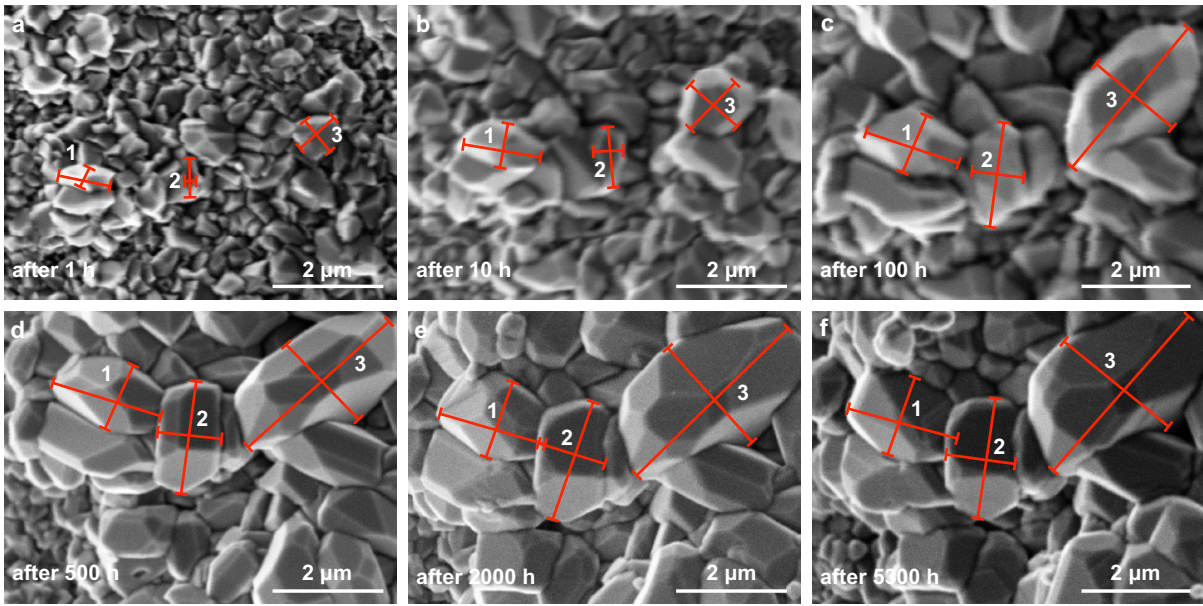
Fig. 5.9 This series of SEM images shows the qualitative chronology of crystal development on a CFY surface exposed to air at 850 °C after a) 1 h, b) 10 h, c) 100 h, d) 500 h, e) 2000 h and f) 5300 h. All images are taken from the same sample location, which is marked, to ensure that always the same spot is considered. The red bars are used to quantify the crystal growth rates (reported in Fig. 5.10).
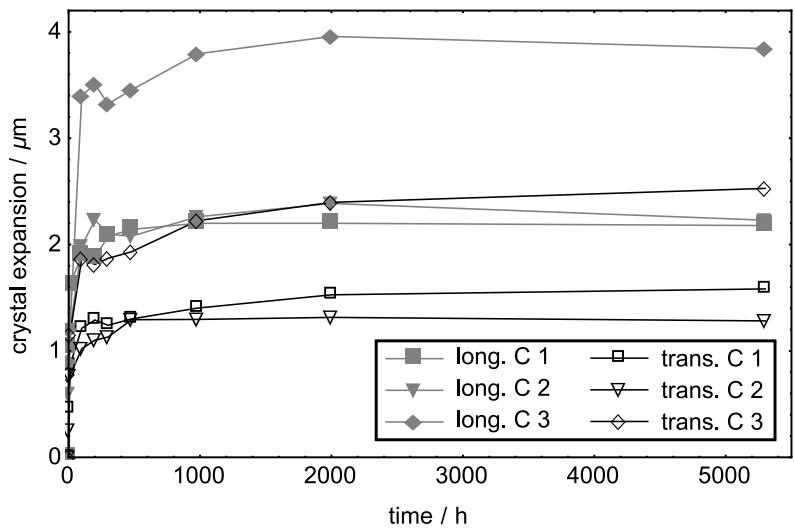
Fig. 5.10 Longitudinal and transversal growth rates for single crystals based on the surface observation presented in Fig. 5.9. This CFY sample was exposed to air at 850 °C. C1, C2 and C3 represents the individual oxide crystals.
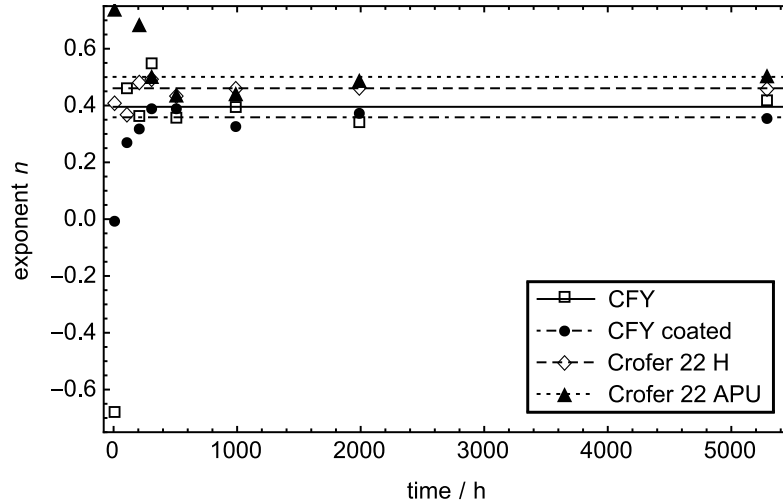
Fig. 5.11 Exponents n according to Eq. (5.2) for fixed rate constants k_e show a large scatter within the first 500 h.

5.1.3 Discussion

The comparison between Figs. 5.6 and 5.7 shows that the oxide growth rates for 40 000 h stack operation deviate from Wagner's oxidation theory. Thereby oxidation progresses faster on the anode side of the SOFC MICs. Bringing these results together with literature data should strengthen the findings. Direct comparison with growth rates from other research groups is however difficult as different test conditions, sample preparation methods and geometries as well as assessment methods are involved [10, 131–133]. The oxidation is generally estimated from weight gain measurements and sometimes correlated to scale evolution in post-test observations [133]. Even for similar test conditions, scale growth rate predictions in literature tend to be smaller up to a factor of five [133]. Therefore it is deduced that the limited time-spans over which the oxidation behavior is generally assessed, lead to a high uncertainty of results. Such investigations generally cover insufficient exposure times, typically below 500 h [124, 134]. From Fig. 5.8 it becomes apparent that the data points related to short exposure times (i. e. < 1000 h) show a significant divergency instead of defining clear trend lines. This scattered picture becomes even more evident when the n-values are determined for each single data point while keeping the rate constant k_e fixed. The corresponding results are shown in Fig. 5.11. Again, the n-values obtained for short exposure times show a large variation, whereas at exposure times > 500 h the obtained n-values are uniform. A possible explanation for this scatter may be related to the fact that the scale growth at short oxidation times is dominated by local heterogeneities (such as presence and absence of pores or variable concentrations of

reactive elements etc.) and different mechanism. In any case, the results document that the growth rates relevant for long-term prediction cannot be derived from experiments that cover only the initial oxidation period. Obviously, only after approximately 500 h (or even more) a steady state oxidation regime relevant for long-term operation is reached.

Scale growth rate description

Different mathematical functions, which deviate from Wanger's theory (Eq. (5.1)) describe the scale growth for various materials and oxidation stages. A logarithmic rate law addresses metal oxidation at low temperatures (below 300–400 ℃). Under such conditions the initially fast scale growth reaches a negligible rate due to the formation of a blocking oxide layer. In contrast, the linear rate law describes scale growth mechanisms taking place in priority at the outer scale surface. Such a linear reaction rate is independent of the consumed amount of metal or gas, which is e. g. characteristic for the initial oxidation period. The different reaction rates combine upon occurrence of diverse oxidation stages during long-term oxidation [99]; the resulting oxidation law deviates from a parabolic description [131, 135, 136]. It is also pointed out by Quadakkers et al. [115] that the description of the complex scale growth mechanism based on experimental data can only by accident be described by a parabolic rate law. A combined rate law is suggested by Kofstad [99] and corresponds to Eq. (5.2). The superimposition of changing oxidation stages with time induces a time dependence of the exponent n and the grow rate constant k_e. Fig. 5.11 therefore shows the exponent n that is determined for each data point with a fixed rate constant k_e. The resulting time evolution of exponent n illustrates data scattering for the first 500 h induced by the adjustable growth states in the initial oxidation phase.

A similar behavior was observed by monitoring the surface crystal growth on CFY (Figs. 5.9 and 5.10). The fast surface crystal formation during the first few hours of heat treatment is decelerating gradually. This observable process is widely finished after 500 h heat exposure. This observation, together with the enlarged scattering of the exponent n (Fig. 5.11), indicates the oxide scale growth during the first few hundred hours (< 500 h) to be governed by different overlaying mechanisms. Therefore it is deduced that the experimental characterization of oxidation after long-term exposure ($> 10\,000$ h) is needed to ascertain a reliable quantitative description of the growth behavior, which takes into account the oxidation mechanisms relevant for SOFC device lifetime predictions.

Scale growth influencing parameters

Both quantitative and qualitative oxidation characteristics are influenced by various SOFC design- and operating-dependent parameters, such as MIC composition (alloying elements), temperature and steam contents (both dependent on fuel utilization) as well as adjacent components (coating and contacting materials).

Oxide scale growth rate is strongly affected by the temperature. With increasing temperature the growth rate constant increases exponentially [99, 133, 137, 138]. The Box-Whisker charts (Fig. 5.5 represent only one example) show no systematic trends for the mean scale thickness in correlation with the sample positioning (i. e. air inlet and gas flow fields | center, middle and outer positions) on the MIC. This corroborates the influence of the high heat conductivity of CFY, which leads to a homogeneous temperature distribution on the MIC. The scale thickness on flat is however enlarged in comparison to the valley. This may be caused by a minimal local temperature rise due to the ohmic losses under locally high electrical current densities.

The oxygen partial pressure is also known to influence the oxidation rate. Increasing Cr_2O_3 growth is reported for reduced oxygen partial pressures down to a certain limit [132, 139] which is in general compatible with the observation of thicker scales on the anode side. Only a minor p_{O_2} reduction is observed on the cathode side, due to oxygen consumption under load. This is in agreement with constant scale thickness distributions over a cathodic MIC surface, which is also reported in literature [137, 140]. Certainly for the anode side a different behavior for the specific operation mode with extensive full redox cycling during the initial stage was observed. The data points at 13 200 h in Fig. 5.7 (red marked) do not suit to the overall trend. Obviously the scale formation on anode side was accelerated by the alternating atmospheres during this 20 full redox cycles within the first 800 h. Such an influence on oxide scale formation related to redox cycles is mentioned by Bastidas [141].

The oxygen partial pressure that is influenced by the presence of steam plays a key role on the anodic MIC oxidation; in particular the H_2O/O_2 ratio is a relevant factor. The scale growth is enhanced with increasing H_2O/O_2 ratios [112, 132, 142]. The Cr_2O_3 scale thickness on the anode side (Fig. 5.7) is clearly enlarged after 40 000 h in comparison to the cathode side (Fig. 5.6) that is exposed to a dry environment with a high oxygen partial pressure ($p_{O_2} > 10^4$ Pa). Thermodynamic calculations for the Hexis system have shown the p_{O_2} at nominal operating point under CPOx reformed natural gas to be below 10^{-14} Pa for the entire anode side. An increase up to 30 % of the steam concentration is brought by fuel utilization along the radial position within a repeat unit, i. e. dry conditions near

the center and humid atmospheres at outer cell regions. It must be emphasized that the influence of the H_2O/O_2 ratio on Cr_2O_3 growth is still debated in literature [132]. But it is also reported that H_2O content along the fuel flow path to positively influence the scale tightness and adhesion [115, 117, 132, 143].

This suggestion is strengthened by the observation of a Cr_2N phase, which is present in the central region of anodic MICs (dark gray spots in Fig. 5.4a). Obviously the permeable oxide scales enable N_2 access ($pN_2 \approx 0.4\,$bar in CPOx gas mixtures) to the CFY alloy. Nitrogen transport is suggested to occur preferably via gas transport rather than by solid state diffusion [115]. Hence gas diffusion occurs through oxide scales with insufficient tightness. Again, the gas tightness is improved in the outer region due to the increased water content. On the cathode side (Fig. 5.4c) Cr_2N formation is not observed, although the nitrogen partial pressure is two times higher in air than in CPOx reformed anode gas. The LSM coating and the Cr_2O_3 layer thus seems to act as a diffusion barrier for the N_2.

Cr_2O_3 scale growth is also affected by evaporation of volatile Cr-species, in particular of $CrO_2(OH)_2(g)$ which is formed in humid atmospheres [126, 144], according to the following reaction:

$$Cr_2O_3(s) + \tfrac{3}{2}\,O_2(g) + 2\,H_2O(g) \rightleftharpoons 2\,CrO_2(OH)_2(g) \tag{5.3}$$
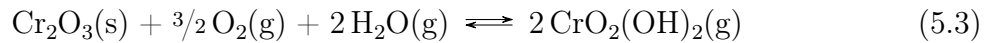
Chromium evaporation during stack operation occurs from the uncoated anodic MIC surface and also through cracks in the LSM coating on the cathode side. The anodic flat is capped with a nickel mesh, acting as a flow barrier, which reduces local flow rates and hence reduces Cr evaporation [126]. Fig. 5.7 indicates thinner oxide scales in valley locations that are exposed to the fuel/exhaust flow, which may trigger the evaporation. In contrast, on the cathode side no significant difference is observed between valley and flat (Fig. 5.6). This observation indicates that the air flow is suggested to only have a minor influence on Cr evaporation from the cathodic Cr_2O_3 scale, because it is fully covered with LSM.

Besides its Cr retaining property that consequently reduce cathode poisoning, the LSM interacts with the Cr_2O_3 scale to build a $(Mn,Cr)_3O_4$-spinel layer at their interface [145]. This effect is confirmed for different samples by EDX analysis and is illustrated in Fig. 5.12. The $(Mn,Cr)_3O_4$-spinel phase positively influences the electric resistance of the phase (by a higher conductivity) and furthermore reduces Cr evaporation [115, 146, 147]. On the one hand, literature data suggests LSM coatings to reduce MIC oxidation [10, 101], on the other hand the results from the 5300 h exposure experiment does not clearly conclude on mitigated Cr_2O_3 growth (Fig. 5.8). Although the absence of Cr_2N indicates that LSM
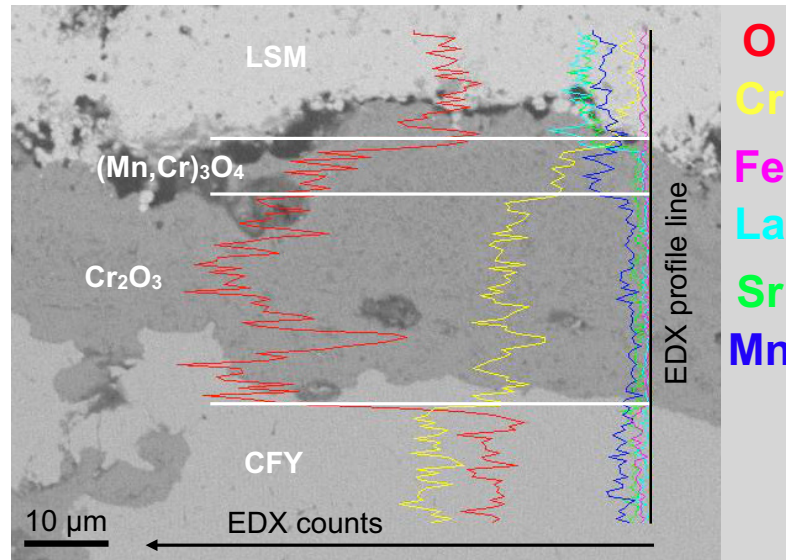
Fig. 5.12 SEM/BSE image with EDX line scan of LSM coated CFY after 40 000 h stack operation. A weak BSE contrast reveals the formation of a distinct $(Mn,Cr)_3O_4$ spinel-layer at the LSM/Cr_2O_3 interface, which is confirmed by the EDX line profile. EDX spot analysis for the spinel phase reveals the following compositions: $Cr = 23.6$ at.%, $Mn = 13.4$ at.%, $O = 63.0$ at.%.

coatings exhibit gas tightness, the coatings do not prevent from oxygen diffusion that governs MIC oxidation [148].

Solid state hydrogen transport from the anode side to the cathode side can also influence the oxide scale formation under dual atmosphere operating conditions [138, 149–151]. Such a solid state H_2 diffusion through Fe-based alloys is indicated by the formation of Fe oxide-rich nodules on cathode side on uncoated samples [138, 149, 151]. This dual atmosphere effect is decreased for alloys with increased Cr-content [150, 152] as well as for increased sample thickness [138]. Also the formation of a dense oxide scale can lead to a significant reduction of hydrogen permeability [153]. In the presented investigations the ODS interconnect material has a relatively porous structure compared to Fe-based alloys. Therefore hydrogen transport through the interconnect material cannot be excluded. However, the formation of Fe-rich nodules could not be observed on the investigated LSM coated CFY samples. These samples were operated under dual atmosphere in the SOFC stacks, but the stack experiments were not explicitly designed to detect solid state hydrogen transport and effects thereof.

The native lattice defect concentration in slow growing oxides, like Cr_2O_3, is small [154]. Oxygen diffusion is therefore believed to essentially occur along the grain boundaries and is strongly influenced by the presence of impurities. The effect of differences in impurity levels on oxidation is given by references [91, 115] by comparing the high purity JS-3 to

Crofer 22 APU (differences in composition are highlighted in Table 5.1). Such influence also explains the higher scale growth rates for Fe-based MIC with higher alloying amounts compared to the Cr-based CFY that only contains Y_2O_3 as RE. The sequences of scale growth rates derived after 5300 h of exposure (Fig. 5.8) are therefore compatible with literature data [91, 115, 122, 133].

Scale growth dependent SOFC lifetime prediction

The major goal of this section is to give reliable quantitative predictions of the oxide scale development over the prospective lifetime of SOFC systems. Such a prediction should ideally be derivable from testing times shorter than the prerequisites for stationary SOFC application to minimize experimental efforts. The various parameters influencing MIC oxidation, e. g. environments with varying temperature, flow rates, gas compositions and H_2O/O_2 ratios affect both quantitatively and qualitatively the Cr_2O_3 microstructure. This unavoidably leads to a scatter in the scale thickness data (e. g. Fig. 5.5) and consequently requires an enlarged observation prediction interval (Figs. 5.6 and 5.7) for reliable information. Moreover, scale growth is shown in Figs. 5.8 and 5.11 to be driven by different oxidation mechanisms at different oxidation periods.

To get a reference for the investigation period needed for a reliable scale growth prediction some data fits according Eq. (5.2) based on data for a shorter test period were extrapolated e. g. for the heat treatment test the fitted scale growth function based on the scale thickness data were extrapolated for the first 1000 h. It turns out that for a statistically robust extrapolation the data should covering at least a quarter of the prediction interval which includes a sufficient amount of reliable data. Naturally for such an extrapolation the different overlaying mechanism during the initial stage (< 500 h) has to be considered as well.

A direct transposition from the mean oxide scale thickness into ohmic losses needs furthermore an additional methodology. Such a method for the elaboration of ohmic resistances is presented in section 5.2. It is based on the simulation of charge transport by using the finite element technique and it will include all the relevant microstructural information (variable scale thickness, local porosity etc.), which is described in this section. Furthermore with this modeling approach also the influence of variations in temperature and prevailing oxygen partial pressures on the extrinsic electrical conductivity of the oxide layers will be taken into account (see e. g. [87]). In this way it is intend to obtain a complete picture of the relationships between (time dependent) scale thickness, microstructure, operating parameters and the resulting ohmic losses at the electrode-MIC interfaces.

5.1.4 Conclusions

In order to investigate Cr_2O_3 scale development on metallic interconnects, samples from stack tests up to 40 000 h as well as from heat treatment experiments were investigated. A systematic methodology for quantitative image analysis was applied to a large number of images from different sample locations. This approach allows to set up a database of oxide microstructures that comprises qualitative and quantitative scale characteristics for different locations in the MICs and for a period, which covers the complete required SOFC life time for stationary applications.

Qualitative observations reveal a complex but systematic pattern of scale microstructures: On the cathode side the microstructures and scale thicknesses are relatively homogeneous. However the scales on the flats are slightly thicker than in the valleys. The interaction with the LSM protection layer leads to the formation of a conductive Mn-spinel within the oxide scale. In contrast, the scale growth on the anode side is thicker than on the cathode side and also more heterogeneous. The most important features of the scale microstructures on the anode side are the following: Scales on the flat are thicker than in the valley. In the center positions the interaction of the oxide layer with the Ni-mesh is more intense than in the outer positions. In the center and middle positions there is also a pronounced formation of Cr_2N, which is absent in the outer positions. In contrast, in the outer positions the scales contain a systematically higher porosity than in the center positions. No significant difference is observed between air inlet and gas flow fields.

Quantitative results are collected for scale thicknesses and associated growth rates up to 40 000 h. In the stack tests, the scale growth on the cathode side follows more or less a parabolic behavior ($n \approx 0.5$). In contrast, the scale growth on the anode side is better described with a non-parabolic law Eq. (5.2), where the exponential values are close to $n = 0.3$. These small n-values correspond with reduced scale growth during the long-term oxidation period. However, the rate constants k_e for the anode scales are higher than for the cathode scales, which explains the larger scale thicknesses for the anode.

The quantitative results from the exposure tests are comparable with data reported in literature. However the exposure tests show that the growth rates are dependent on material type. The scale development on industrial manufactured Crofer materials is enhanced in comparison to the CFY material, which can be attributed to impurities from manufacturing. Most important, in all executed experiments a large scatter in the data points is observed at exposure times < 1000 h. Only at longer exposure times (i. e. > 1000 h) a steady state oxidation regime is reached which allows for a reliable determination of growth rates that are relevant for long-term predictions.

Overall, the observed variations of the scale microstructures, scale thicknesses and growth rates can be attributed to local variations of the influencing parameters (temperature, flow rate, p_{O_2}, p_{H_2O}). The variation of parameters in the present section is associated with the systematic sampling of different location in the MIC. In order to understand the growth mechanism the MIC scales must be considered as dynamic systems, which involve different reaction steps. Thereby, the rate determining step for scale growth may change with time. Such a complex mechanism cannot be deduced entirely with a simple curve fit and extraction of a single exponential parameter. However, if the statistical basis includes a large number of samples and if it is collected over a sufficiently long observation period (i.e. 10 000 h), then the obtained growth rate allows for a reliable prediction of scale growth for the entire SOFC lifetime (40 000 h).

Future section have to focus on the elaboration of the relationships between scale microstructure, scale thicknesses, growth rates and operating conditions with the corresponding resistances and ohmic losses at the MIC-electrode interface. For this purpose a dedicated finite element model was applied.

5.2 Prediction of ohmic resistance of MICs from oxide scale growth based on SEM data for cathode side

Oxide scale growth is in general extracted from data of weight gain change measurements or from scale thickness determinations based on SEM cross section images [124, 153, 155–158]. These quantification methods have in common that they neglect chemical composition and structural information, i.e. the oxide scale morphology and the presence of inclusions and pores. A typical SEM image of an oxide scale thermally grown on CFY at 900 °C in air together with the segmented oxide scale and its resulting average thickness is shown in Fig. 5.13. Note the strong geometric irregularity of the oxide scale, which is typical for thermally grown scales. Note also that oxide scale growth data available in the literature often covers only few testing hours [124, 155]. Scale growth data, which covers a time period > 1000 h is rarely available [103, 159]. However, the observed time span can strongly influence the reliability of rate law parameters fitted to the experimental data [99]. In contrast to Wagners equation, the modified rate law is useful to describe the long-term oxide formation (> 5000 h), which is usually a super position of different oxidation stages. These different oxidation stages are typically indicated by a time dependence of the fitted exponent n as given in Eq. (5.2) [135]. Investigations about the deviations from parabolic oxide growth usually report sub-parabolic behavior,

Fig. 5.13 a) SEM image of a metallic interconnect cross section after 10 700 h stack operation at 900 °C in air. The green perimeter marks the relevant oxide scale. b) Uniform distributed mean scale thickness (green bar) as defined from the segmented SEM image.

i. e. $n < 0.5$ (see also Fig. 5.8) [115, 124, 131, 134, 135, 160]. These deviations might be related to changes in chemical composition due to impurities, microstructure changes such as pore formation and grain size variation, diffusion and evaporation mechanism. Furthermore, the oxide formation process on MICs is influenced by the specific conditions during stack operation. As examples, both solid state hydrogen transport through the MIC from the anode to the cathode side [138, 149–151], the local electrical currents resulting from the applied electrical load [157, 158] and the presence of water vapor may influence the oxide growth behavior [138, 142].

Measuring electrical conductivities is another common method to quantify MIC degradation by extracting the ASR increase as a function of time [68, 69, 100, 150, 161, 162]. Since the oxide scale formation is considered to be the dominant effect for the observed ASR increase, both scale growth and ASR evolution are expected to show a similar time-dependent behavior. However, in contrast to the usually observed sub-parabolic growth of oxides scales, the experimental data for the ASR evolution often exhibits a growth with exponents clearly above 0.5 [163]. In order to explain the observed differences in oxide scale and ohmic resistance growth behaviors, finite element simulations are used to describe the non-trivial electrical current paths. These simulations take into account the realistic scale morphologies, by using SEM images as geometric input for the simulations. In order to obtain representative results, numerous SEM images are used for each sample and for each time step. The FE model takes the electrical conductivity of the scale as input parameter, which can be obtained by fitting to experimental ASR-data. This is important because the extrinsic conductivity of thermally grown oxide scales can differ

from the values of pure Cr_2O_3 by about two orders of magnitude [91, 164].

The aim of this section is to explain the different time evolution curves for oxide scale thickness and for the corresponding ASR-component. The objective is to provide a long-term prediction for the MIC degradation on the cathode side. The results for oxide scale formation from the previous section 5.1 is thus compared to the ASR evolution extracted from electrical conductivity data. To explain the deviations in growth behavior, the impact of oxide scale morphology is investigated using finite element simulations to calculate the current paths through the scale. Furthermore, a work flow to analyze a large amount of SEM images in a fully automated manner is presented.

5.2.1 Experimental

This subsection is structured as follows: The first three subsections summarize the experimental details for the scale thickness determination as shown in section 5.1. These results are the basis for the investigation of the coherence between the scale thickness and the ASR evolution. Experimental details about the conductivity measurements used for ASR determination are given in a further subsection. The last subsection introduces the applied modeling approach, which is used to establish a quantitative relationship between the evolution curves for ASR and for scale thickness on the cathode side.

Heat treatment tests

In the heat treatment experiments four different MIC-materials, namely LSM coated as well as uncoated CFY, Crofer 22 APU and Crofer 22 H, were investigated [89, 90, 120]. Details of the elemental composition are given in Table 5.1. All samples have a fluted structure similar to the MICs in a typical stack configuration. The investigated interconnect materials were exposed in a Carbolite CWF 12/13 box furnace to air at 850 °C without additional air circulation. The furnace was cooled down and reheated repeatedly in order to remove material samples for oxide scale thickness determination at specific time steps over a period up to 5300 h. The heating rate was adjusted to 3 °C min^{-1}.

Post-test stack samples

Post-test samples were extracted from CFY interconnects which had been operated in five different SOFC stacks for several thousand hours at about 900 °C. Hence, these interconnects were exposed to air on the cathode side and to CPOx reformed natural gas on the anode side. Also, long-term testing under real conditions involved maintenance and

incident shut downs, that lead to thermo- and redox-cycles in the considered Hexis stacks. The stacks were operated with pre-reformed (CPOx) natural gas from the local grid at Winterthur (Switzerland) with N_2, H_2, CO, CH_4 and H_2O as main components. Note however that the local fuel gas composition to which the interconnect is exposed depends on the fuel utilization, the interconnect locality and possible variations in the natural gas composition [44]. More details about sample location, MIC design and operating conditions are given section 5.1.1.

Layer thickness determination

For scale thickness determination based on cross section SEM images the samples were cold mounted in a epoxy resin. After resin hardening they were grinded and polished on a Struers TegraPol-35 with SiC paper up to 4000 grit. Contact force during polishing was 15 N. The images for the layer thickness determination were taken with a backscattering detector on a Tescan VEGA TS 5130 MM microscope equipped with an INCAx-sight detector from Oxford Instruments for energy dispersive X-ray spectroscopy.

The oxide layer was identified based on the specific threshold of the Cr_2O_3 in the SEM images. Therefore the images were segmented into two phases using Adobe Photoshop CS5 image processing software. In the segmented images one phase represents the oxide layer and the other "phase" summarizes all other components. The mean oxide scale thickness can then be determined based on the segmented phase area. These steps have been automated using the Mathematica 8.0 software package. Further details about the layer thickness determination are described in section 5.1.1.

Conductivity measurements

Long term conductivity measurements have been realized in a GERO tube furnace type SR 70-500 in air at 850 °C. No air flow was enforced during the experiment. A spring load ensured a sufficient contact force ($\approx 4\,\mathrm{N\,cm^{-2}}$) between the samples and the platinum voltage tap plates. The applied current density was $440\,\mathrm{mA\,cm^{-2}}$. Furthermore the temperature dependence of the electrical conductivity was tested at various points of time. Therefore the temperature was stepwise decreased down to 700 °C within an overall time period of less than 10 h. The temperature was then brought back to 850 °C.

The tested materials were LSM coated CFY and Crofer 22 APU (cf. Table 5.1). The samples were connected in series and they have a fluted-structure as illustrated in Fig. 5.14. The samples have an entire thickness of 3 mm with overall dimension of 19×19 mm and a known contact area. Some additional contact slurry made of LSM was applied to provide
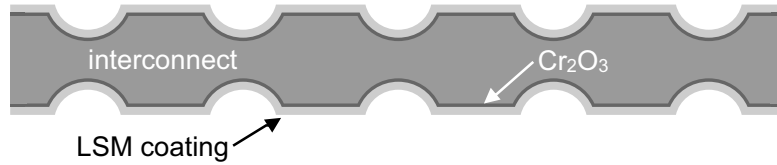
Fig. 5.14 Illustration of a cross section through a MIC-sample as used in the conductivity measurements. Exposed to air at 850 °C, a Cr_2O_3 layer (dark gray) is formed between the LSM coating (light gray phase) and the interconnect material (gray phase).

a uniform conduction between the sample and the Pt plates.

Modeling of electrical current paths

Image segmentation To investigate the influence of the oxide scale morphology on the ohmic losses of the considered MIC-samples, the corresponding SEM images are segmented into different components with different conductivities. This segmentation is performed in Mathematica 9.0 including threshold finding options and batch processing for the analysis of large numbers of SEM images. After segmentation each image contains four phases indicated by different colors that represents Cr_2O_3, LSM coating, CFY and pores. An example of such an automatically segmented image is shown in Fig. 5.15. Note: Fig. 5.13b
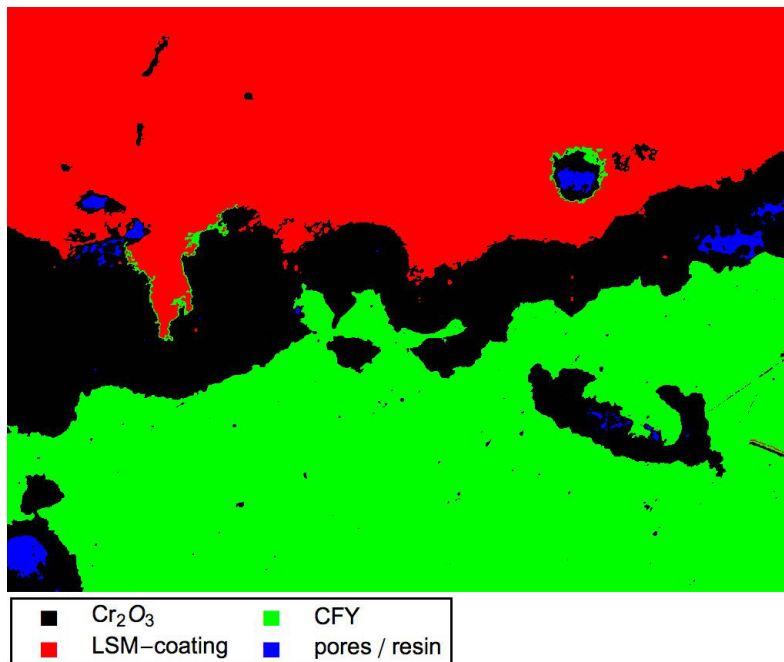
Fig. 5.15 Segmented SEM image with four phases. The original SEM image is shown above in Fig. 5.13a.

shows the same SE-image, where all features that are irrelevant for FE-analysis were removed "by hand".

FE modeling of ohmic losses The simulation process is a sequence of four different steps, which is realized by a combination of several software tools: i) The initial step is the image segmentation based on SEM image thresholds as described in section 5.2.1. ii) The next step is the mesh generation in Mathematica 9.0 that is realized based on RGB color information in the segmented image (Fig. 5.15). This information is used for the mesh generation and material allocation inside the FE-software iii) The actual FE model to perform local electrical current simulations has been implemented in the multiphysics software NM-SESES [165]. NM-SESES simulates the local electrons transport based on the ohmic law

$$\vec{j} = -\sigma \, \nabla \Phi \tag{5.4}$$

whereas $\vec{j}$ is the electrical current density in $\mathrm{A\,m^{-2}}$, σ the electrical conductivity in $\mathrm{S\,m^{-1}}$ and Φ the electric potential in V. Furthermore steady state conditions without any electron source or sinks are provided. This is ensured by the predefined charge balance.

$$\nabla \vec{j} = 0 \tag{5.5}$$

On one end of the modeling domain a fixed voltage was applied as boundary condition. On the other end, a fixed electrical current is assigned. The later one is a modified Neumann boundary condition, where the electrical potential maintains a constant value. vi) The simulation process finishes with the post processing of the obtained simulation results, which includes the illustration of the electric streamlines.

The described process loop is implemented in a Mathematica notebook and can be used for a fully automated analysis of SEM image batches.

Morphology factor The morphology factor (M-factor) is a measure for the impact of $\mathrm{Cr_2O_3}$ scale morphology on the measurable ASR value. In this work, the morphology factor is defined as the ratio between the calculated ASR based on a mean thickness of a uniform oxide layer and the "real" ASR resulting from FE simulation considering the irregular oxide scale morphology.

$$M(t) = \frac{\mathrm{ASR}_{\bar{x}}(t)}{\mathrm{ASR_S}(t)} \tag{5.6}$$

Note that the morphology factor $M(t)$ is a time depending quantity and so is the mean ASR value based on a homogeneous and continuously growing mean scale thickness defined as:

$$\text{ASR}_{\bar{x}}(t) = \frac{\bar{x}(t)}{\bar{\sigma}} \qquad (5.7)$$

Here $\bar{x}(t)$ represents the time depending mean scale thickness. Due to the presence of pores in the oxide scale an averaged electrical conductivity $\bar{\sigma}$ for the mean ASR calculation is used i.e. the electrical conductivity for the simulation is determined based on the particular amount of Cr_2O_3 and pores within the oxide scale whereas the pores are assumed as a none conducting phase ($\sigma = 0$ S m^{-1}). $\text{ASR}_\text{S}(t)$ represents the simulated ASR value, which is defined as the ratio between the voltage drop ΔU determined by the FE model and the current density j. The current density is one boundary condition in the FE model (cf. section 5.2.1):

$$\text{ASR}_\text{S}(t) = \frac{\Delta U}{j} \qquad (5.8)$$

Based on the time dependent M-factor one obtains a more accurate prediction of the ASR, which considers the morphology effect of the Cr_2O_3 scale, as follows:

$$\text{ASR}_\text{M}(t) = \frac{\bar{x}(t)}{M(t)\,\sigma} \qquad (5.9)$$

An M-factor > 1 means that the ASR value based on the simplified calculation with a mean oxide layer thickness is overestimated. Whereas an M-factor < 1 means that the same ASR value is underestimated. The M-factor is expected to be > 1, because narrow "bridges" in the scale layer tend to decrease the ASR and this effect is not captured by ASR calculations which are based on the mean scale thickness (compare Fig. 5.13 and Fig. 5.16). However this reasoning does not account for the pores that are possibly present in the oxide scale. Pores covering a wide area act as isolators and can significantly reduce the local oxide scale conductivity, especially if their orientation is parallel to the oxide layer. Such large pores are captured in the SEM images and are therefore considered in the simulation as insulating objects.

Synthetic samples Synthetic samples are generated to compare the results from SEM image analysis with the theoretical evolution of an ASR, which takes into account a morphology factor M. In thin scale layers, variation of the surface topology easily lead to formation of bridges that act as preferred current pathways. However, as the layer
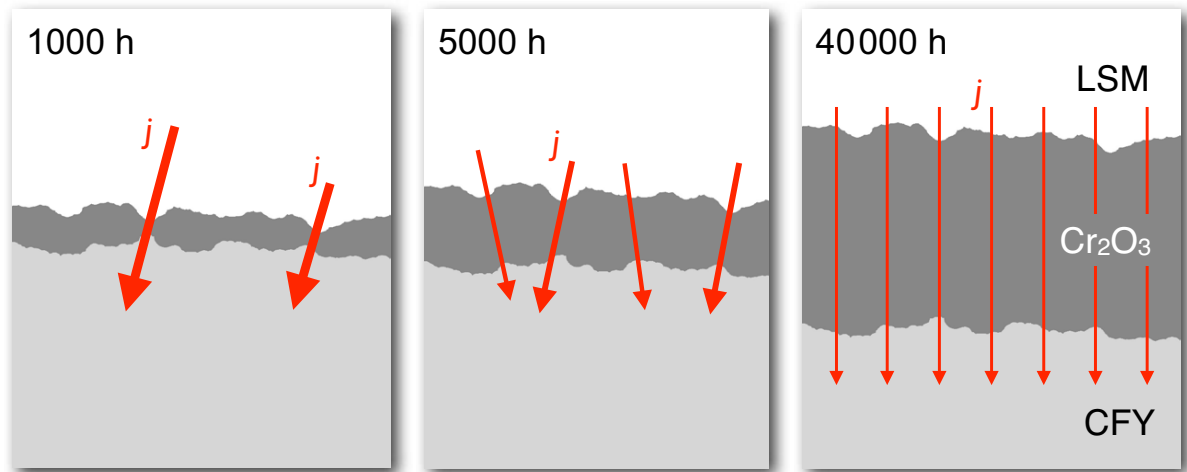
Fig. 5.16 Synthetically generated Cr_2O_3 scales at different time steps with fixed scale morphology, i.e. the surface topography (top and bottom of the scale layer) does not change with time. The mean scale thickness is derived from the oxide scale evolution based on post test samples over $40\,000$ h, cf. section 5.1. The red arrows and their width indicate the preferred electrical current paths and the corresponding current density, respectively.

thickness increases with time, the influence of irregular surface morphology will decrease. Hypothetically this behavior is considered as the main reason for changing M-factor over time. This hypothesis shall be tested with synthetic samples of controlled morphology and thickness evolution. For this purpose synthetic samples with growing scales but with constant surface topography were generated. The mean scale thickness evolution for synthetic images at the different time steps is based on the experimental data from post-test samples, cf. section 5.1 or [103]. To investigate the morphology on the resulting ASR compared to a uniform mean oxide scale the morphology need to remain unchanged as illustrated in Fig. 5.16. Such a scale thickness extension is done with the Mathematica 9.0 software package. After this enlargement process the FE modeling procedure as described above (cf. section 5.2.1) is applied.

5.2.2 Results

Conductivity measurement

Conductivity is investigated to verify if there exists a correlation between oxide layer growth and ASR evolution. In comparison to the oxide scale growth two main differences are observed in the ASR evolution curves: Firstly an offset occurs in the ASR curves (Figs. 5.17 and 5.18), which includes a sum of various resistances (e.g. conductivity and coating resistances) that cannot be straightforward separated into single components. The
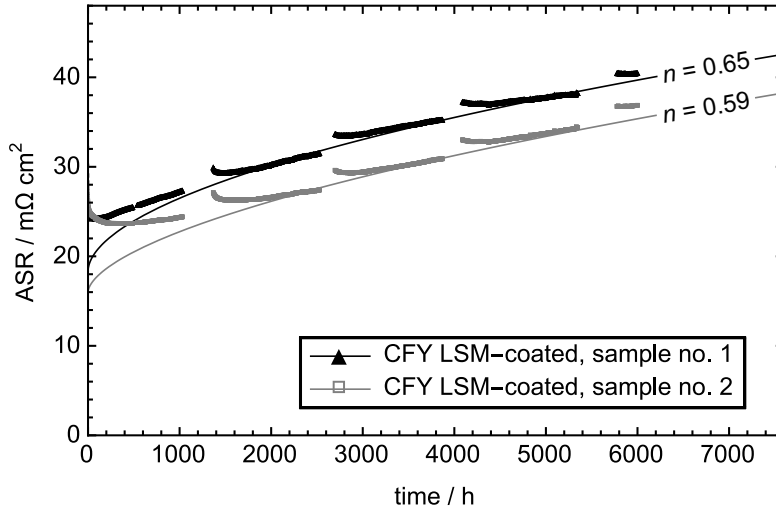
Fig. 5.17 ASR evolution for two LSM-coated CFY samples measured in air at 850 °C. Both samples show a similar trend, indicated by the comparable exponents n (cf. Eq. (5.10)).
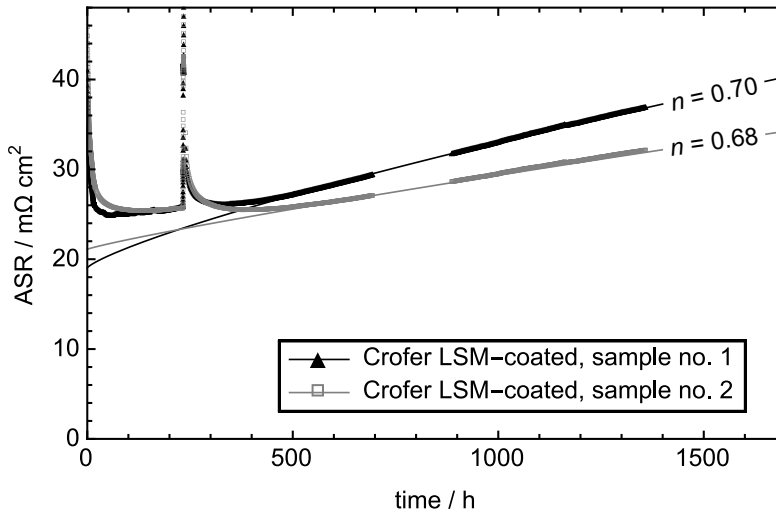
Fig. 5.18 ASR trend for Crofer 22 APU up to 1350 h exposed to air at 850 °C. Fit exponents (cf. Eq. (5.10)) are $n = 0.70$ and $n = 0.68$, respectively.

ASR trend is therefore given by a modified version of Eq. (5.2)

$$\mathrm{ASR}(t) = b_0 + k_\mathrm{e}\, t^n \tag{5.10}$$

where $\mathrm{ASR}(t)$ is the measured ASR value, b_0 the additional offset at the beginning of the test, k_e the growth constant, t the test duration and n the adjustable exponent.

Secondly, exponent n describing the ASR evolution is generally following a over-parabolic trend that is shown by n values ≥ 0.5. This behavior is observed under cathode side conditions for LSM coated CFY (Fig. 5.17) as well as for Crofer 22 APU (Fig. 5.18). In these
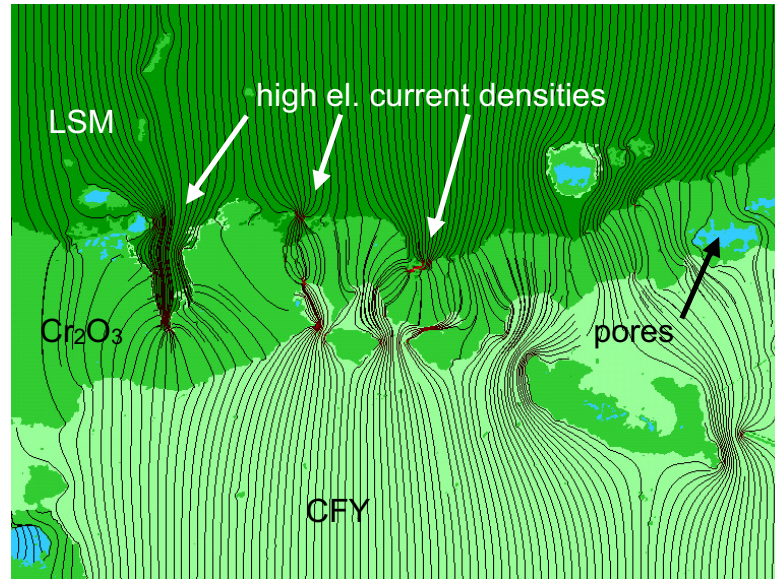
Fig. 5.19 Visualization of streamlines obtained with FE simulations, which represent preferred pathways for the electrical current. The image represents the scale layer that formed after 10 700 h stack operation. Note, the closer the lines the higher the local electrical current density. Red streamlines represent the regions with very high electrical current density. The calculated morphology factor M for this section is 1.64.

figures, periodic sharp increases of ASR are due to temperature variations to determine the activation energy of the Cr_2O_3 scale can be observed. After few 100 h the values are recovered. The missing data points between 700 h and 890 h in Fig. 5.18 are caused by a data logger failure.

During the initial phase (i. e. $\leq$ 500 h) the ASR trend is affected by sintering effects of the contact paste, resulting in an increase of the electrical conductivity and therefore deviate from Eq. (5.10).

Morphology factor evolution based on FE simulation

Fig. 5.19 shows the current density distribution based on FE simulation on a Cr_2O_3 morphology after 10 700 h stack operation. The preferred electrical current paths are represented by stream-lines. The current density is increased on locations, where the Cr_2O_3 scale is narrow. For this specific case a morphology factor of 1.64 was determined by the FE model. A morphology factor of 1.64 leads to an ASR reduction of 39 % compared to an ASR calculated based on an uniform oxide scale with an identical mean scale thickness.

A clear trend for morphology factors based on the SEM images at different time steps is not easily recognizable, as scale thickness and morphology scatters in a limited number of
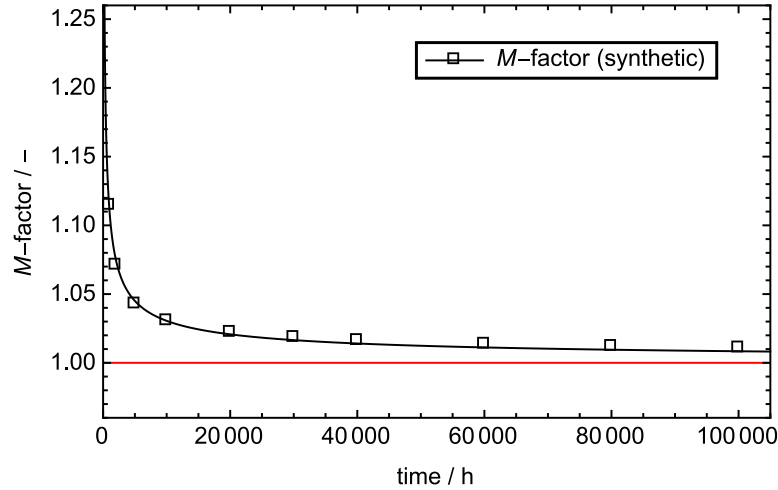
Fig. 5.20 M-factor evolution based on synthetic image data for $100\,000\,\mathrm{h}$. The fit based on Eq. (5.11) shows asymptotic convergence to the value 1 for large times. Note, squares represent discrete data points, obtained from simulations based on images similar as those in Fig. 5.16. The line represents a fit using Eq. (5.11).

samples. In a first step the time dependent evolution of the morphology factor based on synthetic data is thus investigated. In a further step the results from the heat exposure experiment will be presented.

M-factor evolution based on synthetic data   Fig. 5.20 shows M-factors based on the synthetic image data. For the initial period ($< 5000\,\mathrm{h}$) the M-factor decreases rapidly and tends to an asymptotic convergence at longer exposure times ($t > 40\,000\,\mathrm{h}$). The M-factor evolution is thus described as follows:

$$M(t) = 1 + \frac{k_\mathrm{M}}{t^m} \tag{5.11}$$

where M represents the morphology factor and t the test time. k_M and m are fitting parameters that describe how fast the function tends to 1. Eq. (5.11) can be used for the elaboration of the M-factor evolution based on experimental data, as discussed in the next session.

M-factor evolution based on heat treated LSM-coated CFY samples   Fig. 5.21 shows calculated M-factors from the heat exposure test. The analyzed cross section images were derived from time lapse microscopy covering a period of $5300\,\mathrm{h}$. The mean scale thickness evolution derived from these SEM images is shown in Fig. 5.8. Fig. 5.21 illustrates the M-factor fit (black line) based on Eq. (5.11) and M-factor data points for
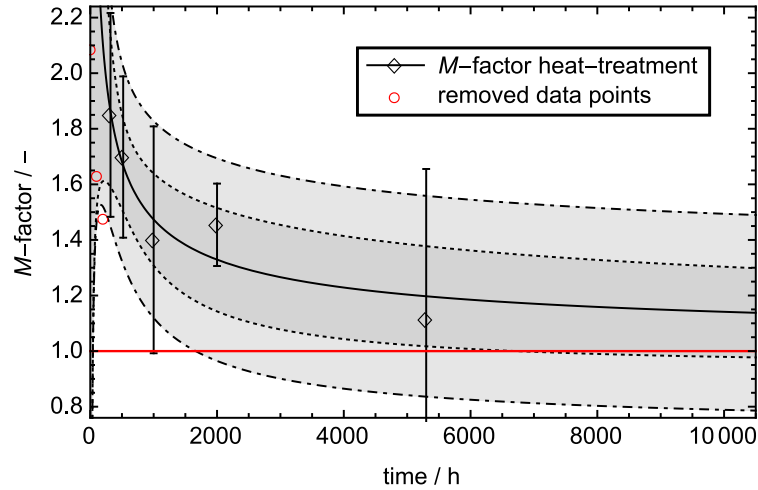
Fig. 5.21 M-factor values determined on SEM images from the heat exposure experiment. The red data points are affected by unknown short-time effects leading to scatter, and therefore they are not used in further data treatment. The gray interval between the doted curves represents the confidence interval, the light gray area inside the dot-dashed curves the prediction interval. The black line represents the fitted function (cf. Eq. (5.11), $k_M = 17.73$, $m = 0.5245$).

$t > 300$ (black diamonds). Some data points (red circles) were removed for the data fit. The gray area limited by the doted curves represents the confidence interval and the light gray area within the dot dashed curve the prediction interval. The intervals are based on a 95 % confidence level. The data shows the expected transition to an asymptotic behavior, with a strong decrease within the first hundreds ($t < 1000\,\text{h}$) of hours.

ASR determination based on scale thickness

ASR determination without M-factor adjustment Calculated ASR values based on Eq. (5.7), i. e. without considering the scale morphology influence are shown in Fig. 5.22. Different ASR curves are obtained by varying the electrical conductivity σ for the Cr_2O_3 scale. However, none of the trend lines describes the experimental data in a satisfying way. The large spread between the curves indicates that the ASR of thermal grown oxide is strongly dependent on extrinsic Cr_2O_3 properties. The data points are obtained from the electrical conductivity measurement (Fig. 5.17).

ASR determination with M-factor adjustment The calculated ASR considering the morphology influence according to Eq. (5.9) is shown in Fig. 5.23. The ASR trends (curves) are calculated for five different electrical conductivities. The large variation between these curves again indicates that the conductivity is a sensitive parameter for a reliable ASR determination for thermal grown Cr_2O_3. The diamonds represent the same
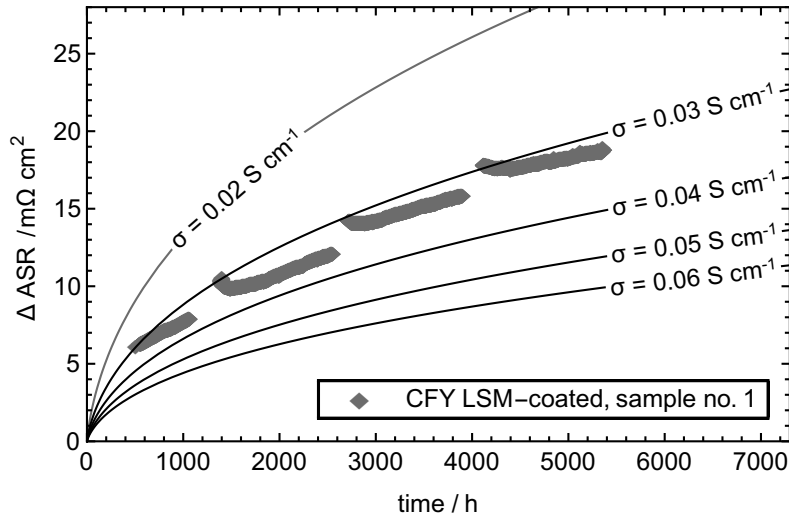
Fig. 5.22 Comparison between the measured ASR evolution and the calculated ASR (Eq. (5.7)) without considering the time dependent morphology effect (M-factor) for different Cr_2O_3 conductivity values.
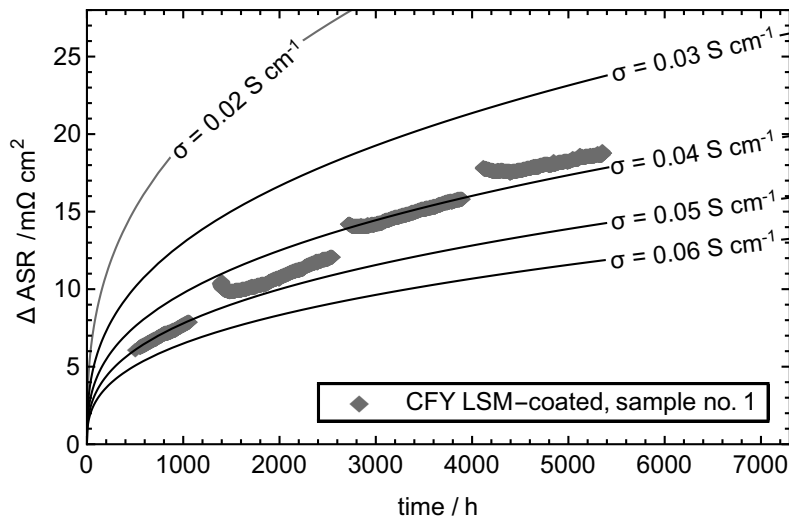
Fig. 5.23 Measured ASR trend compared to calculated ASR values taking into account the time dependent M-factor. The curves show the evolution for various Cr_2O_3 conductivity values.

experimental data as shown in Fig. 5.17. A predicted trend line based on a conductivity of $0.03\,S\,cm^{-1}$ matches well with the experimental data.

ASR determination with fitted electrical conductivity Fig. 5.24 shows a comparison between experimental and calculated ASR values either by considering the morphology influences (Eq. (5.9)) or without (Eq. (5.7)). The σ values for the plotted curves are determined via a least square fit to the measured data. Modulated ASR trend, considering
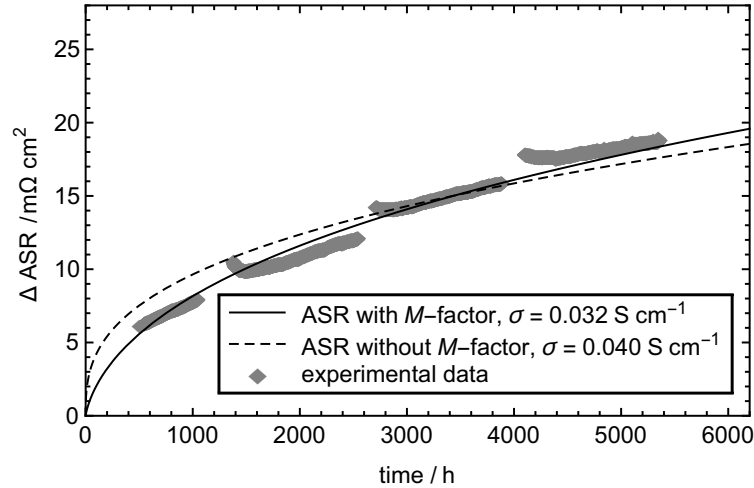
Fig. 5.24 Experimental ASR compared to a calculated ASR evolution curves with and without taking into account the time dependent M-factor function. Note that the ASR curve based on M-factor matches better with the experimental data. Cr_2O_3 σ-values are defined by a least square fitted for both curves.

the none linear time dependent morphology function $M(t)$ generates a reliable description of the MIC behavior and offers a correlation between mean oxide scale growth and ASR evolution.

5.2.3 Discussion

This section focuses on the comparison of scale growth characteristics as shown in Fig. 5.8 with the measured ASR evolutions as shown in Figs. 5.17 and 5.18. For both sets of data the same functional form was used: Eq. (5.2) for scale growth and Eq. (5.10) (with a modification to take into account the unavoidable contact resistance offset at $t = 0$) for ASR increase. A general deviation from the parabolic rate law is observed for both the oxide scale thicknesses exhibiting sub-parabolic behavior (except for Crofer 22 H) and for the ASR increase showing an over-parabolic evolution ($n > 0.5$). The observed exponents of $n < 0.5$ in case of the scale growth could in principle be explained by scale spallation [163]. However, as shown in Fig. 5.8 such a mechanism is unlikely to happen, since the LSM coated samples (where spallation is prohibited) show the most pronounced deviation from parabolic behavior indicated by the smallest exponent $n = 0.36$.

In any case it is obvious that the deviating exponents between the growth of the oxide scale thickness and the corresponding voltage drop indicate a non-trivial, non-linear relationship between these two. This behavior is not obvious and can be influenced by a variety of effects such as the scale morphology and changes in the extrinsic electrical

conductivity of the oxide scale.

Influence of scale morphology on ASR evolution

To investigate the impact of the thermally grown oxides layers on the overall resistance the method introduced in section 5.2.1, i.e. simulating electrical current paths for complex oxide scale geometries obtained from SEM images, has been applied. As it turns out the wrinkled structure of the observed Cr_2O_3 scales has a significant impact on the voltage drop. As stated earlier, the increase of the MIC resistance can be influenced by various factors. It depends on the alloy composition [69, 91, 103, 163], the applied coatings [69, 124, 166], the sample geometry as well as the manufacturing and preparation methods. Furthermore, surface treatment of the bare metal for instance by polishing or sand blasting can as well have a crucial impact on the original surface topology and finally to the scale morphology evolution. The oxide scale growth is also related to the operating conditions, which includes the temperature, number of thermo- and redox-cycles, the various atmospheres (single or dual) and the electrical load [103, 149–151, 157, 167].

To investigate the influence of oxide scale morphology on the ASR synthetic oxide layers, shown in Fig. 5.16, were used to estimate the morphology factor, defined by Eq. (5.6), as a function of time, see the results in Fig. 5.20. As expected, $M(t)$ approaches unity towards infinite oxide scale thicknesses whereas morphology influences are negligible. A function to describe the time-dependence of $M(t)$ with only two fitting parameters has been introduced in Eq. (5.11). As shown by the solid line in Fig. 5.20, Eq. (5.11) fits the calculated M values very well.

The M-factor extracted from the post test cross section SEM analysis of the heat treated samples shows the expected monotonous decrease with time, see Fig. 5.21. However the M-factors based on real oxide morphology data show a large scatter which is mainly related to the presence of pores and their position and orientation. The electrical current paths are in addition influenced by irregularities within the MIC materials, especially for the powder metallurgical manufactured CFY material where internal oxide formation plays a role cf. Table 5.3 and Fig. 5.4. That is Cr_2O_3 accumulation, which is not part of the surface oxide layer that disturbs the electrical current due to their low electrical conductivity. However, it can be assumed that the impact on the global ohmic resistance is small, since the alloy has an electrical conductivity of about 7900–8700 S cm^{-1} [90, 120] compared to ≈ 0.03 S cm^{-1} for Cr_2O_3.

Taking into account $M(t)$ clearly leads to a better fit with experimental data, see Fig. 5.24. From this results it is concluded that the oxide scale morphology has an

important impact on the corresponding ASR behavior. Specifically, it gives an explanation for the shift in the growth exponent n from sub-parabolic in case of mean scale growth to over-parabolic in case of ASR evolution. The remaining disagreement between results from modeling and the experimental data can be caused by various effects such as impurities, which are involved in the oxide formation process and which can have an impact on the electrical conductivity [164, 168, 169].

Influences on the effective electrical conductivity of oxide scales

The extrinsic electrical conductivity of oxide scales thermally grown on MIC materials during stack operation is not just a function of temperature, but is also influenced by various other factors and in addition can vary with time. Typical conductivity values range between 0.001 and $0.2\,\mathrm{S\,cm^{-1}}$ [91, 164].

For CFY MICs studied here it is likely that in particular the type of applied protection layer as well as the related formation of Mn spinels affects the oxide scale growth behavior and its extrinsic conductivity. Mn spinel formation, which for example takes place by interaction between the oxide scale and the LSM coating [145] increases the overall electrical conductivity of the oxide scale. In the previous section 5.1.3 a clearly visible Mn spinel phase on LSM coated CFY interconnects after $40\,000\,\mathrm{h}$ stack operation could be found. The Mn spinel accounted for roughly $20\,\%$ of the formed oxide scale (by volume). Since the exact amount and the evolution of this spinel phase is not quantified yet, it cannot be ruled out that the Cr_2O_3 to $(Mn,Cr)_3O_4$ ratio is time depending and consequently the averaged electrical conductivity of the overall oxide layer too. Such a behavior would imply variation of the oxygen diffusion coefficient and has to be addressed in further work.

The electrical conductivity of the oxide scale is as well influenced by the temperature, the oxygen partial pressure and deviations in the stoichiometric composition of the oxide. The latter can be due to impurities or alloying elements [88]. This behavior is caused by the fact that Cr_2O_3 is a p-type conductive material under cathode operating conditions (i.e. 600–$900\,^{\circ}\mathrm{C}$ and $p_{O_2} > 0.07\,\mathrm{bar}$) [87, 88, 168, 170]. It is generally found that the electrical conductivity of pure Cr_2O_3 is reduced with decreasing p_{O_2} [87, 88]. However, compared to temperature effects this influence is small in the typical cathode p_{O_2} range between 0.07 and $0.21\,\mathrm{bar}$ [87, 168, 169]. The LSM coating is a dense layer with low permeability, which should reduce the oxidation and chromium evaporation rates. Therefore it can be assumed that the oxygen partial pressure is decreasing inwards along the coating and oxide layers towards the alloy/scale interface. This can lead to electrical conductivity

variations along the oxide scale and consequently to changes in the ASR with increasing scale thickness.

Figs. 5.22 to 5.24 show computed ASR values obtained from Eq. (5.7) or Eq. (5.9) with slightly varied electrical conductivities. Although the ASRs show a large spread the applied electrical conductivity values for the oxide scale are in a good agreement with published data [91, 164]. These results illustrate that the ASR is very sensitive towards changes in electrical conductivity. Unfortunately the effective conductivities can vary over a large range. However, for experimental data sets where the morphology factor is established, the proposed method can now also be used to determine the effective electrical conductivity of the scale layer, as demonstrated in Fig. 5.24.

Long term investigation and prediction of scale growth and associated ASR-contribution

The proposed method includes FE simulations based on real oxide scale morphologies, which allow to predict reliably the corresponding ASR from scale growth. The results clearly document that the oxide morphology plays an important role during the first 1000 h of testing. In addition, the modeling approach considering the morphology effects also increases reliability of extrapolations over the entire stack lifetime, even if they are based only on short- to medium-term experimental ASR-data. This is important since stationary SOFC applications have to reach a minimal time of operation of 40 000 h whereas the continuous testing and improvement of MIC-materials only permit much shorter testing periods. This raises the issue how much testing time is needed to get meaningful results and even more important to make reliable predictions over the envisaged lifetime.

Investigations of the oxide scale growth and the corresponding ohmic losses often cover only few hundreds or even less testing hours [100, 124, 134, 150, 161, 167, 171]. In the previous section 5.1 it was found that the scale formation is influenced by interfering growth mechanisms during the first few hundreds of hours. After this initial stage the scale growth can be described according to Eq. (5.2) without significant variations in the exponent n. Consequently for a reliable prediction it is absolutely necessary to include data that goes beyond this hardly quantifiable initial phase (< 1000 h). Likewise it is not obvious how to extrapolate the available experimental data. This involves two issues, namely the scatter in the experimental data and the selected model to describe the data. Here, I suggest a model given by Eq. (5.9), which contains two time-dependent parameters, i. e. the growth rate of the mean oxide scale thickness and the morphology factor, which is a monotonic function decreasing to unity with time.

ASR behavior during electrical conductivity measurements

The ASR-data shown in Figs. 5.17 and 5.18 exhibit some unexpected behavior that will be clarified in the following.

Decreasing ASR trend during the initial stage In Figs. 5.17 and 5.18, the ASR decreases during the initial growth phase, i.e. for $t < 500\,\mathrm{h}$. Such a behavior is also known from the literature [68, 69, 100, 101, 150, 167] and can have various reasons. Among others, it can be associated with the increased temperature during start up and with changes in the microstructure of the oxide scale. The latter has been observed by Yang et al. [101]. However, in this specific case, this cannot be the only explanation. In another experiment, conductivity measurements of LSM slurry showed that the electrical conductivity was continuously increasing with increasing time [70]. This suggests that the initially decreasing ASR of the CFY-samples upon heat up is caused by increasing electrical conductivity of the LSM slurry. It is conceivable that this is caused by a densification of the contact paste. These changes in its microstructure can be caused by evaporation of the organic binder, relaxation upon an external mechanical load and further sintering of the contact slurry [69, 172]. Those phenomena depend on temperature, material and binder composition, layer thickness, mechanical load/force and oxygen partial pressure. Another effect that might increase the electrical conductivity is the recrystallization of the original partly amorphous LSM coating [171]. In summary, this makes the initial decrease of the ASR difficult to describe and predict.

ASR increase after temperature variations Another phenomena that can be observed from the ASR data in Figs. 5.17 and 5.18 are the steps in the ASR followed by a rather slow decrease back to the expected trend line. This can be explained as follows: for the shown data, even though the temperature was kept constant at $850\,^{\circ}\mathrm{C}$ there have been temperature variations on purpose right at the points of discontinuity to extract the associated activation energies. It turns out that these temperature variations alter the oxide scale such that its ohmic resistance gets higher as it would in a constant temperature experiment. Possible reasons for this unexpected behavior are materials segregation, impurities and defects in the oxide crystal structure. The $p_{\mathrm{O_2}}$ can be assumed as unchanged in the non-sealed tube furnace during the conductivity test. However it cannot be completely ruled out that variations of the oxygen partial pressure play a role for the observed behavior. With increasing temperature both the mobility of vacancies and the concentration are increased [87, 99]. However, it is unlikely that a thermally activated process is responsible

Table 5.4 CTE values for the different layers present in the electrical conductivity tests. They are arranged in the order as they appear in the test setup.

Material	CTE / $10^{-6}\,\mathrm{K}^{-1}$
Platinum [173, 174]	8.8–9.1
LSM slurry	—[*]
LSM coating [115, 175, 176]	12.0–12.3 , 11–14[†]
$(Cr, Mn)_3O_4$ (spinel) [177]	7–9.3
Cr_2O_3 [99, 178]	7.3–9.6
CFY [115], Crofer 22 APU [120]	9–10[†] , 12

[*] No data available, should be in the similar range as the LSM coating, especially after the binder evaporation and sintering.
[†] Based on Quadakkers et al. [115] and Refs. therein.

for the observed ASR increase after the induced temperature reduction. It is more likely that this behavior is caused by mechanical mismatches between the involved layers due to the imposed temperature variation that lead to mechanical damages at their interfaces. "Curing" these damages is a slow process that takes place over several hundreds of hours. Indeed, the used materials and the additional phases (Cr_2O_3, $(Cr,Mn)_3O_4$) formed during the oxidation process have different CTEs. Table 5.4 shows the CTE ranges for the involved materials. The interfaces between the oxide layer and the adjacent materials differ in CTE values by up to $7 \times 10^{-6}\,\mathrm{K}^{-1}$. This leads to unavoidable tensile stresses during temperature variations and can cause local spallation and interruption of the electrical connected paths, respectively [66]. However, it could be that the mechanical damage is followed by a recovery process driven by inter diffusion of different species eventually reestablishing new electrical current paths [148]. If inter diffusion plays a key role in the observed recovering process then the diffusion coefficients of Cr and O_2 within the oxide scale determine its time scale. Since the considered MIC-materials CFY and Crofer 22 APU both contain reactive elements the inward directed oxygen transport dominates the scale growth [99]. The interface between the LSM contact slurry and the Pt plate has as well a high CTE mismatch of up to $5 \times 10^{-6}\,\mathrm{K}^{-1}$. However it appears less likely that the observed ASR increase is related to the reduction at this interface because the electrical conductivities of LSM and Pt are several orders of magnitudes higher compared to the Cr_2O_3. Consequently an increase of ohmic losses due to prolonged lateral current path within these are unlikely to result in a significant increase of the ASR. This effect would only occur in cases where a very large area at the Pt/LSM interface is disconnected.

5.2.4 Conclusions

To give reliable lifetime predictions for SOFC stacks the oxide scale growth and the corresponding ohmic losses were investigated for two different metallic interconnect materials. It turns out that the oxide scale growth usually can be described with a sub-parabolic rate law, whereas the ASR shows an over-parabolic behavior. In order to understand the different rate laws in the evolution curves of ASR and scale thickness one has to consider effects of the irregular morphology of the thermally grown oxide layers.

Specifically, it was demonstrated that the oxide scale morphology is a major cause for the noticeable deviation between the oxide scale growth and corresponding ASR evolution by FE simulations of the ohmic losses taking into account the oxide scale morphology from real SEM data. The results of the FE simulations were used to define a morphology factor. The latter is defined as the ratio between the realistic voltage drop within the real scale structure and the hypothetical voltage drop of a geometrically homogeneous oxide layer with a mean oxide scale thickness, see Eq. (5.6). The calculated M-factors at different time steps confirmed that the influence of the oxide scale morphology is higher during the initial stage of the scale growth than for larger times above $10\,000\,\text{h}$. This behavior is caused by a decreasing influence of the layer morphology with increasing thickness (i.e. lower probability of "bridging"), as depicted in Fig 5.16. Furthermore, when taking into account the M-factor in ASR calculations, Eq. (5.9), this leads to values for the exponent n which are very similar to the ones obtained in rate laws from direct fitting to experimental ASR data. As a consequence it can be concluded that predictions of the degradation behavior of effective electrical power are only reliable when the scale thicknesses as well as the morphology influence are taken into account.

Furthermore, the results in Figs. 5.22 to 5.24 show that small variations in the extrinsic electrical conductivity of the thermally grown oxide scale can have a significant impact on the resulting ASR. Such variations in conductivity can be induced by intrinsic impurities and inhomogeneities of the MIC materials. Alternatively they may also originate from chemical interactions with the coating, with adjacent cell components or even with "foreign" species transported by the gas from more distant components of the stack module. Varying operating parameter such as temperature and partial pressures can as well influence the electrical conductivity of the formed oxide layer.

To further reduce the time consuming cell and stack development process it is essential to have efficient methods at hand which allow reliable prediction of the long-term behavior for the various stack components under the varying and complex SOFC operating conditions. For testing and prediction of scale growth and associated MIC degradation it

is highly recommended to consider the following points: i) The testing conditions should be as close as possible to the real stack operating conditions, which includes the dual atmospheres, the electrical current/load, the operating temperature and the materials including the applied coating. ii) The duration of testing should exceed the initial phase (> 1000 h) during which the results are often largely scattered due to different interfering oxidation mechanisms. iii) The model describing the ASR evolution has to be selected and verified carefully. It should incorporate additional experimental data such as the growth rates of mean scale thickness and the influence of scale morphology and other factors. iv) Scale thicknesses have to be quantified with suitable methods and interpreted under statistical perspectives to handle unavoidable scatter, i.e. multiple SEM images for each point in time have to be analyzed.

The next section focus on data analysis on the anode side of interconnect samples that were operated under stack conditions.

5.3 Investigation of morphology parameters on the interconnect anode side

In this section the relevant morphology parameters for the electrical current pathways on the interconnect anode side are investigated based on the methods introduced for the cathode side in section 5.2. A reliable quantification of the morphology impact on the anode side is more complex compared to the cathode side due to the hardly definable interfaces between the formed oxide scale, the Ni-mesh and the MIC, respectively. A schematic comparison between those two MIC sides is given in Fig. 5.25. Fig. 5.25a represents a typical oxide layer formed on the anode side with no well defined Cr_2O_3/Ni-mesh and Cr_2O_3/MIC interfaces. Note that often a characteristic internal oxidation zone adjacent to oxide scale is observed, cf. section 5.1.2 and Table 5.3. The Ni particles present at the anode side oxide scale might originate from various sources: i) the anode it self [179], ii) the current-collector mesh [180–182], or iii) Ni containing interconnect coatings [129, 181, 183–185]. Fig. 5.25b shows that on the LSM coated cathode side the transitions between coating/oxide scale and oxide scale/MIC are in general much better defined except for a few pores along the interfaces.

The aim of this section is to investigate the influence of the present Ni particles and their specific arrangement on the ohmic resistance. For this purpose the electric conductivity was investigated with a FE model to simulate the electrical current fluxes using real SEM image data as input. Furthermore the effect of small percolating metallic bridges
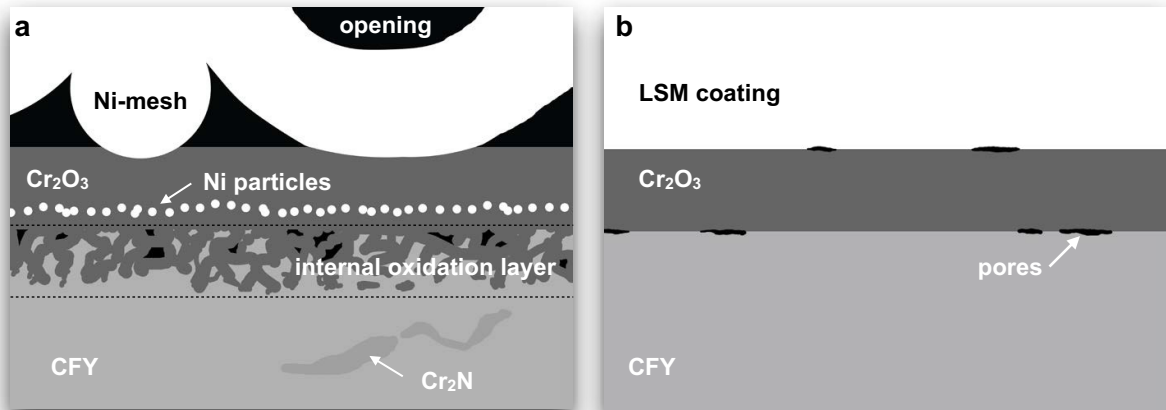
Fig. 5.25 Schematic representation of oxide scales typically formed on CFY interconnects during stack operation. a) Aanode side and b) LSM coated cathode side.

across the oxide scale as observed by Mikkelson et al. [185] or originated from spot welded Ni-meshs [186, 187] is investigated in detail. For this purpose the required frequency of occurrence and ideal spacing of such bridges are determined by FE simulations as a function of the bridge diameter and the oxide scale thickness.

5.3.1 Experimental and applied methods

FE simulations of the local electrical currents were carried out based on cross section SEM images for CFY interconnects obtained from Hexis stacks operated for several thousands hours at about 900 °C with CPOx reformed natural gas. Further details about the testing conditions, sample preparation, image processing and FE modeling are given in section 5.2.1.

Influence of Ni particles inside oxide scale

Original SEM image data were modified to investigate the influence of Ni particles within the Cr_2O_3 scale similarly to the situation shown in Fig 5.25a. For this purpose the bright spots within the oxide scale identified as Ni were manually replaced by a gray scale, which corresponds to Cr_2O_3. This modification was done with the image processing software Adobe Photoshop CS5. The modified SEM image data were then used as input to the FE-model to determine the ASR of the interconnect oxide scales as described in detail in section 5.2.1.
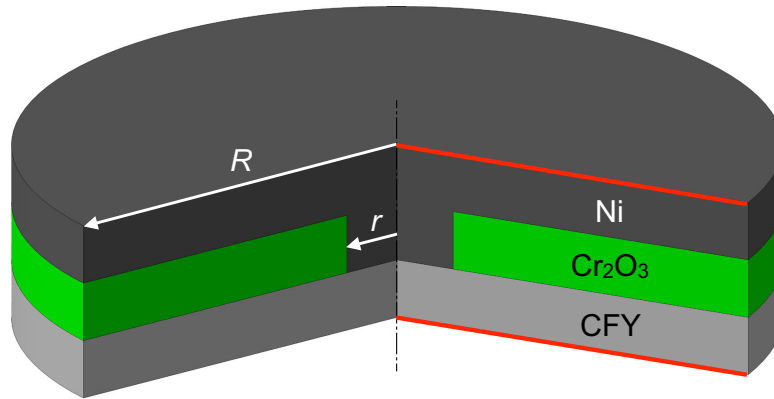
Fig. 5.26 Schematic illustration of the 2D rotation symmetric model. The red edges and the centerline, respectively indicate the locations of the applied boundary conditions.

Influence of highly conductive local bridges

The 2D FE model described in section 5.2.1 was modified to a 2D rotation symmetric model to investigate the impact of metallic bridges across the Cr_2O_3 layer. Fig. 5.26 shows the schematic setup of the model. To determine the dimension of the surrounding region for a given bridge diameter $(2\,r)$ the simulation domain was systematically enhanced i. e. radius R was continuously increased up to a size where the simulated ASR was approximately equal to the ohmic resistance of an unaffected oxide scale of identical thickness. The simulations were repeated for different bridge diameters and scale thicknesses. The electrical conductivity for the low conductive Cr_2O_3 layer was set to $\sigma = 0.02\,\mathrm{S\,cm^{-1}}$ for all calculations.

5.3.2 Results and Discussion

ASR quantification

Fig. 5.27 shows a Box-Whisker chart of ASR values determined by FE simulation based on SEM images obtained from SOFC stacks at different time steps (cf. section 5.2.1). The electrical conductivity of the Cr_2O_3 phase was set to $\sigma = 0.02\,\mathrm{S\,cm^{-1}}$. The ASR increases towards longer stack operations as expected from the mean scale thickness evolution. This behavior, as observed for the median (gray horizontal lines) and for the mean values (red diamonds), is related to the increase of the scale thicknesses as shown in Fig. 5.7. However, the outliers, marked by circles and/or the partly large whiskers, illustrate that there is a large scatter between the different positions where the SEM images were obtained from. It may thus be concluded that ten or less images for each time step would be too few
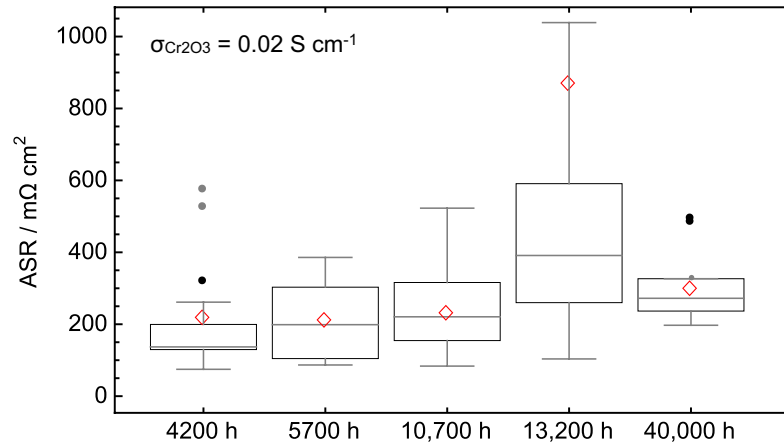
Fig. 5.27 Box-Whisker chart of simulated ASR values from post test SEM images extracted from interconnects operated in Hexis stacks at 900 °C. The ASR mean values show a comparable trend to the extracted oxide scale thickness evolution shown in section 5.2.1 on p. 69 and Fig. 5.7, respectively.

to obtain representative results for the specific morphological conditions given on the anode side (see Fig. 5.25a). Unexpected high ASRs are determined based on image data obtained after 13 200 h stack operation. This behavior is related to the enhanced scale formation during the 20 redox cycles performed within the first 800 h of stack operation and the resulting impact on the oxide scale thickness shown in Fig. 5.7.

Oxide scale morphology and Ni particles effects

The electrical conductivity of oxide scales is influenced by morphology effects and Ni particles present within the formed Cr_2O_3 phase. Fig. 5.28 outlines a couple of different cases that are relevant for further investigations. Fig. 5.28a shows a horizontal arrangement of Ni particles. For this configuration, the impact on the ohmic resistance is proportional to the Ni/Cr_2O_3 ratio, i.e. the beneficial effect of present Ni particles decreases with increasing scale thickness provided that the size and amount of the Ni particles is unchanged. Fig. 5.28b illustrates a vertical arrangement of Ni particles, which form a preferred electrical current path across the oxide scale. As consequence the ohmic resistance can be significantly reduced within a certain area. Fig. 5.28c displays a horizontal arrangement of few Ni particles basically located at the broader regions of the oxide scale. Such an arrangement of Ni particles does not significantly reduce the ohmic resistance since the electrical current primarily flows through the narrow regions within the scale as described in section 5.2. In Fig. 5.28d the morphology effect is enhanced by the arrangement of Ni particles within the already preferred electrical pathways. Fig. 5.28e shows a particular
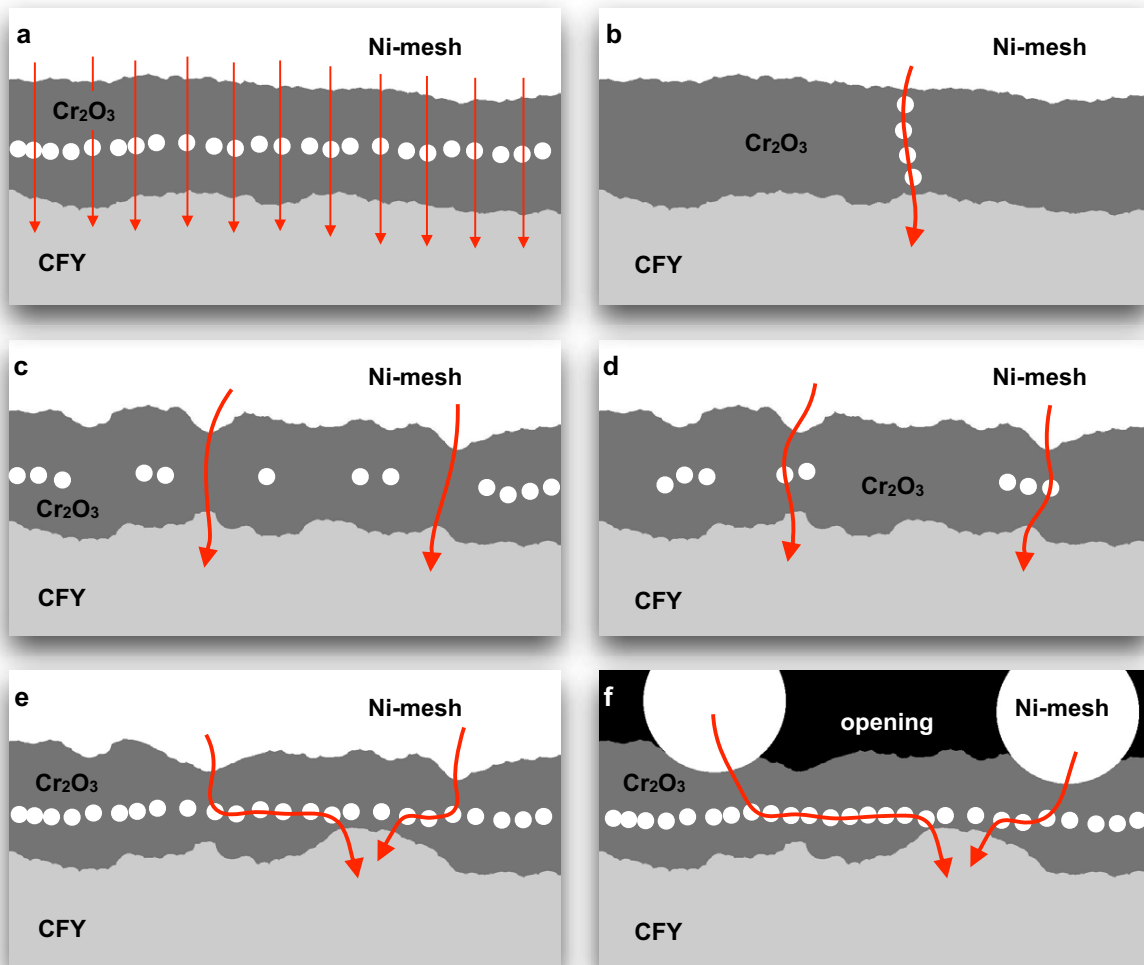
Fig. 5.28 Schematic representation of different types of relevant electrical current flux regimes for Cr_2O_3 scales containing different arrangements of Ni particles. The red arrows indicate the preferred electrical current paths.

case where the morphology effect is additionally amplified by the horizontal alignment of Ni particles. This particle arrangement provides transversal electrical current pathways, which reduce the overall ohmic resistance. This transversal conduction behavior is even more pronounced in the configuration shown in Fig. 5.28f where the electrical current originates from the cross sections of the Ni-mesh wires.

FE simulations were used to quantify the influence of Ni particles within the oxide scale based on SEM images obtained from anode side MIC cross sections after 10 700 h of stack operation. For that purpose the simulations were executed based on original and modified SEM image data and compared to each other. Figs. 5.29 and 5.30 shows the comparison between the streamlines of the electrical current pathways across the oxide scale a) for the
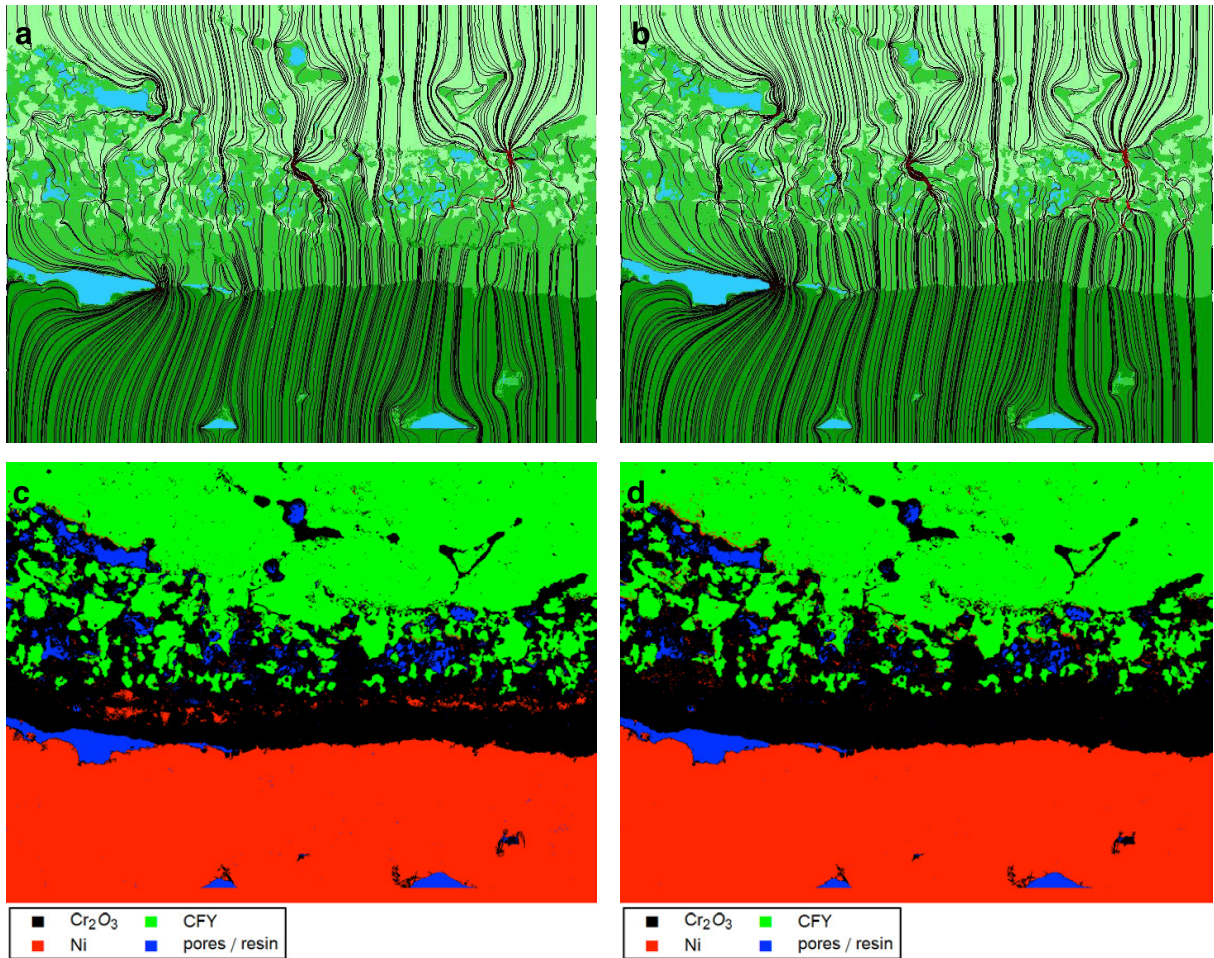
Fig. 5.29 Preferred pathways of local electrical current densities obtained from FE simulations a) after $10\,700\,h$ stack operation with CPOx reformed natural gas at $900\,°C$ with Ni particles and b) without Ni particles, i. e. the latter artificially replaced by Cr_2O_3 by image processing (SEM image label as used in Fig. 5.31 and Table 5.5: #120321). c) and d) shows the corresponding SEM image as segmented for the simulations.

original image data and b) for the modified one where Ni particles were replaced by Cr_2O_3. c) and d) shows the segmented SEM images. The Ni particles as arranged in the oxide scale in Fig. 5.29c contribute to a reduction of the ohmic resistance by about $7\,\%$ compared to the same oxide scale without the highly conductive Ni particles as shown in Fig. 5.29d. The dominating effect for this specific horizontal particle alignment in combination with the oxide scale morphology and presence of pores can be mainly attributed to the current flux regime shown in Fig. 5.28a. In this case transversal conductivity effects can be neglected. A large reduction of the ohmic resistance by Ni particles result from the FE simulation results in Fig. 5.30. In this case the metallic particles are able to reduce the ohmic resistance by up to $30\,\%$ due to the ability of enhanced transversal conductivity
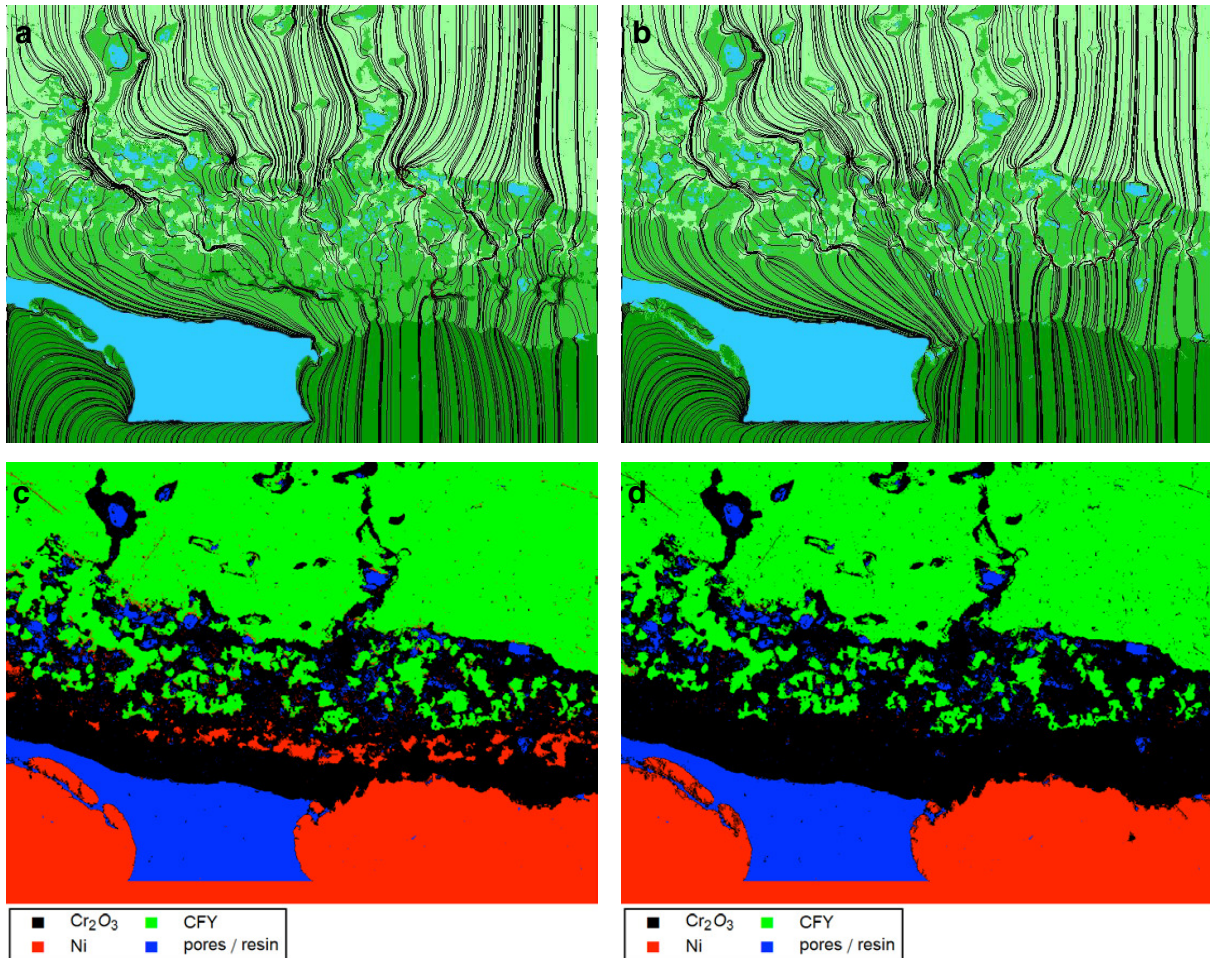
Fig. 5.30 Preferred pathways of local electrical current densities obtained from FE simulations a) after 10 700 h stack operation with CPOx reformed natural gas at 900 °C with Ni particles and b) without Ni particles, i. e. the latter artificially replaced by Cr_2O_3 by image processing (SEM image label as used in Fig. 5.31 and Table 5.5: #120359). c) and d) shows the corresponding SEM image as segmented for the simulations.

within the oxide scale as schematically illustrated in Fig. 5.28f. Further comparison of FE simulations with and without the presence of Ni particles inside oxide scales are given in Figs. A.1 to A.5 in appendix A.1.

Fig. 5.31 summarizes the ASR values obtained from the FE simulations with and without Ni particles. For the determination of these ASR values the electrical conductivity of the Cr_2O_3 phase was fixed to $\sigma = 0.02\,\mathrm{S\,cm^{-1}}$. The abscissa gives the ASR as obtained from the FE simulations. The ordinate shows the mean ASR as determined from the corresponding averaged oxide scale thicknesses as described in section 5.2.1 by Eq. (5.7). The empty symbols represent the simulated ASR values as obtained from the original SEM images. The corresponding filled symbols represent those obtained from the mod-

5.3. Investigation of morphology parameters on the interconnect anode side
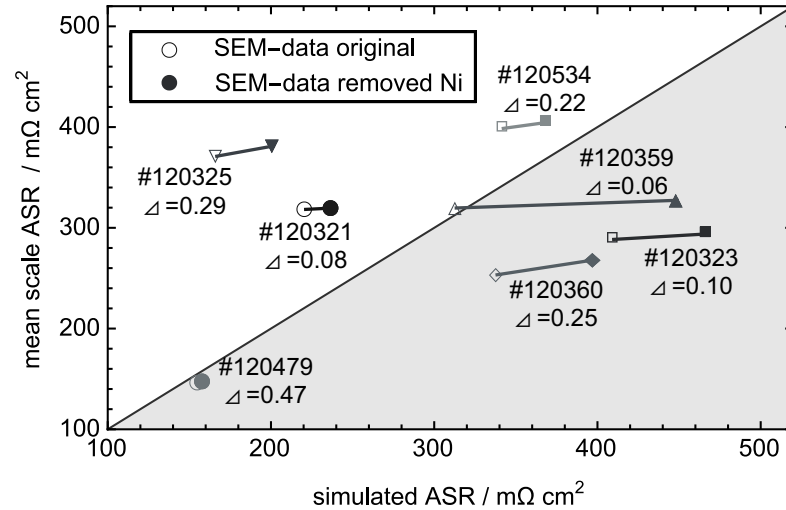
Fig. 5.31 Comparison between ASR values obtained from original SEM image data as calculated from mean scale thickness and by FE simulations, respectively, with the corresponding results for the modified image data, where Ni particles were artificially replaced with Cr_2O_3 by image processing.

ified SEM images where Ni particles were artificially replaced by Cr_2O_3. Note that the calculated mean ASR values for the oxide scales without Ni must increase as a consequence of replacing the highly conductive Ni by Cr_2O_3. The connection line between two data point serves the identify the corresponding data sets. In addition, the slopes of these connections measure the impact of Ni particles within the oxide scale. The slopes are labeled by the triangles with values between 0 and 1 below the sample identification number. The smaller the slope the grater the impact of the Ni particles within the oxide scale. In other words, if the slope is equal to 1 the influence of Ni particles is inexistent. Such a behavior occurs in the hypothetic case where the Ni particles do not influence the preferred electrical current pathways across the oxide scale at all. However, note that the impact of Ni is relevant in all cases since the resulting slopes are always smaller than 1. Note also that a classification of the different effects as shown in Fig. 5.28 is not obvious from Fig. 5.31. Instead such a classification must be extracted from the streamlines of the electrical current pathways across the oxide scale as shown in Figs. 5.29, 5.30 and A.1–A.5. In addition, for a reliable quantification, the relative increase of simulated ASRs for the images with replaced Ni particles must be considered as summarized in Table 5.5.

The diagonal in Fig. 5.31 subdivides the diagram into two parts that provide further relevant information based on the determined ASR values. Data sets above the diagonal (white area) indicate that the electrical conductivity is most probably affected by morphological effects in combination with the presence of Ni particles according to cases a–d

Table 5.5 Relative ASR increase after artificially replacing the Ni particles within the SEM images by Cr_2O_3. SEM images were obtained from CFY interconnects after $10\,700\,h$ stack operation with CPOx reformed natural gas at $900\,°C$.

image data set	ASR increase / %
#120321	7.3
#120323	13.9
#120325	20.7
#120359	43.2
#120360	17.5
#120479	1.9
#120534	7.8

in Fig. 5.28. Data points that are located below the diagonal (gray area) indicate that the ASR simply obtained from the mean scale thickness underestimates the true ASR. Such a behavior is related to dominant transversal electrical current pathways within the oxide scale as illustrated in Figs. 5.28e and 5.28f. The impact of such transversal electrical current pathways is obvious in image data set #120359 in Fig. 5.30. The corresponding streamlines illustrate the transversal electrical current pathways across the Ni particles. In the corresponding oxide layer with replaced Ni particles the preferred transversal current pathway disappeared i. e. traversal current transport must take place via the low conductive Cr_2O_3 phase. This is also verified by comparing the relative ASR increases with and without Ni particles in Table 5.5.

Impact of high conductive metallic bridges across the oxide scale

Fig. 5.32 illustrates the simulation domain of the 2D rotation symmetric model and the corresponding electrical current pathways that are visualized as streamlines. Obviously the metallic Ni bridge dominates the electrical behavior, which leads to high current densities within the metallic bridge to overcome the oxide scale. Such high electrical conductive pathways can exhibit a significant decrease of the overall ohmic losses and lead to a overall resistance that shows the behavior characteristic for metallic conduction as observed Mikkelsen et al. [185].

To quantify the impact of such a high electrically conductive path across the oxide scale a comprehensive parameter study was carried out. This includes the systematic increase of the simulation area R, the variation of the bridge diameter r and the oxide scale thickness $\bar{x}$. These parameters have an influence on the electrical current transport within the Ni layer and the CFY interconnect, respectively, to overcome the very low conductivity of the oxide scale. The ideal arrangement of such bridges corresponds to a close packing of
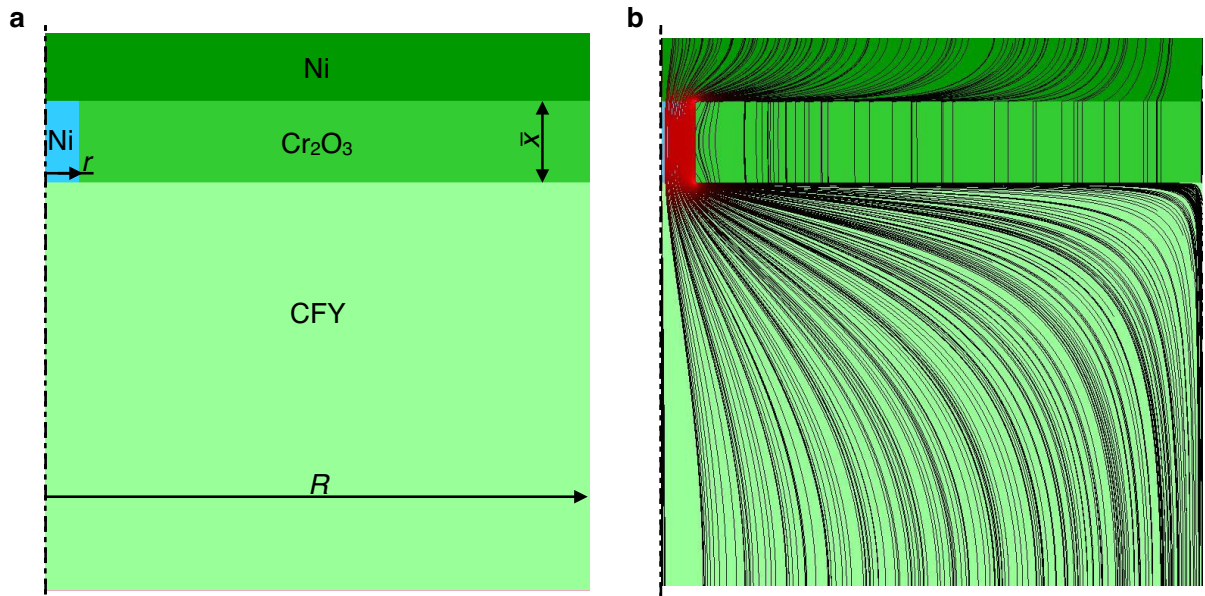
Fig. 5.32 a) 2D rotation symmetric model domain with the different materials. b) Streamlines of electrical current densities for a typical simulation run. The region where the streamlines are red exhibits high current densities.

circles as schematically illustrated in Fig. 5.33. Note that the spacing x corresponds to the simulation domain R in the 2D rotation symmetric model illustrated in Fig. 5.26. The results of these simulations are shown in Fig. 5.34, where the sub figures a) to d) represent the result for different scale thicknesses as labeled. The oxide scale thickness of $60\,\mu$m was chosen to match to the expected oxide scale thickness on the anode side of a MIC after $40\,000\,$h stack operation (cf. section 5.1 and Fig. 5.7). The curves show the percental reduction of ohmic losses in dependency of the bridge diameter and the required spacing x of such bridges. For instance for metallic bridges formed trough a spot welded Ni-mesh onto the MIC with bridge diameters of $100\,\mu$m, this arrangement would reduce the overall
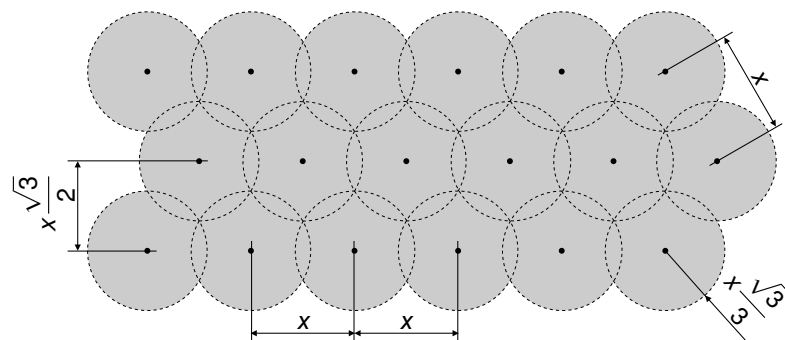
Fig. 5.33 Schematic illustration of an ideal arrangement of highly conductive bridges across an oxide scale. The black dots represent the metallic bridges.

111
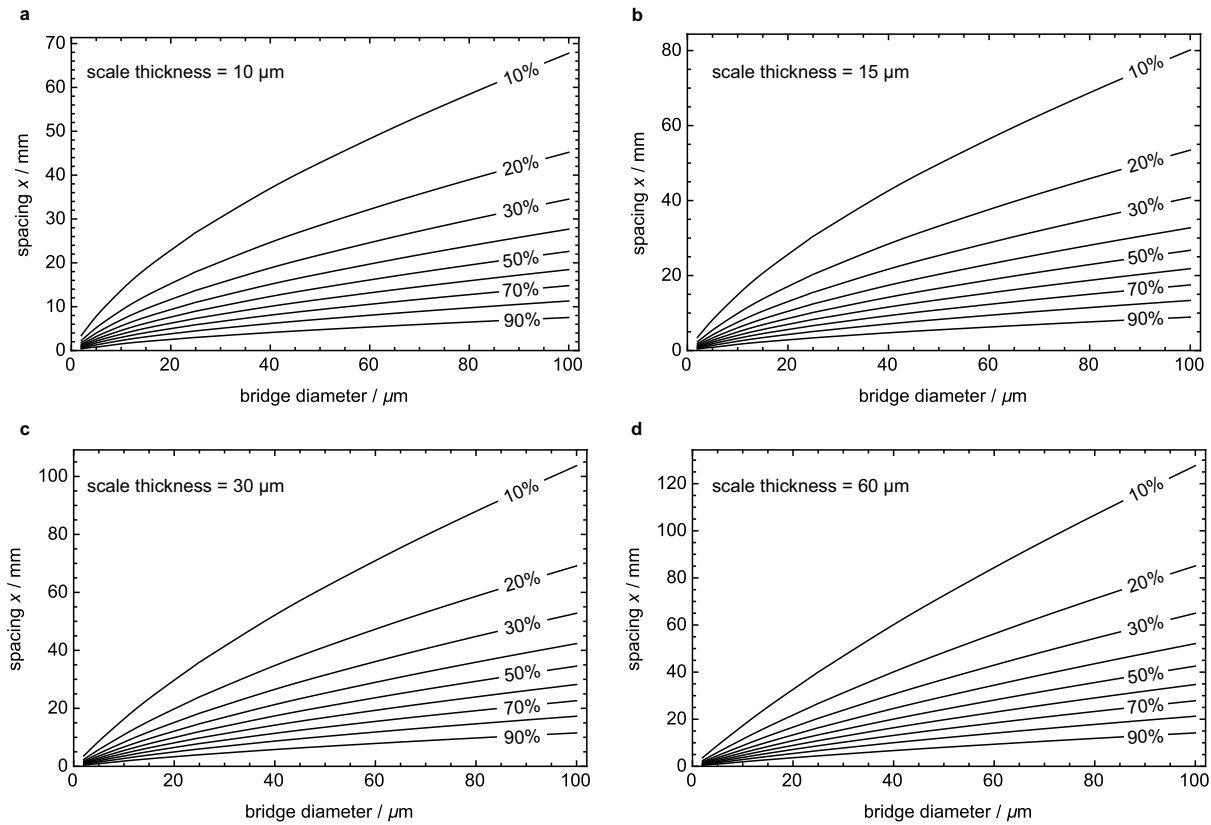
Fig. 5.34 Percental reduction of ohmic losses across the oxide scale for different scale thicknesses plotted as a function of the metallic bridge diameter against the spacing x between two metallic bridges (cf. Fig. 5.33).

ohmic losses by $50\,\%$. For oxide scales with a thickness of $60\,\mu$m it must be ensured that the distance between the single welding points is smaller than $45\,$mm as obvious from Fig. 5.34d. However, it must be emphasized that variations in the electrical conductivity, pore formation and morphology effects were not considered in these simulations.

5.3.3 Conclusion

The FE simulation results of the electrical current flow through oxide scale geometries based on anode side SEM images provide relevant information for the further understanding of interconnect degradation behavior during stack operation. The quantitative rating of the simulation results shows a large scatter that is attributed to the heterogeneity of the images obtained at different locations. The FE simulations provide a further insight into the dominant electrical current pathways across the formed oxide scales, which in turn delivers relevant information about influencing quantities such as the oxide scale morphology, Ni particles and their arrangement within the oxide scale and the transition

between the Ni-mesh and oxide scale. Therefore for a reliable interpretation of the stack degradation behavior quantitative and qualitative data must be considered likewise.

The most important finding based on the anode side SEM image data is the significance of transversal electrical conductivity pathways promoted by the presence of Ni particles. The possibility for transversal electrical current transport within an oxide scale provides an essential contribution to the ASR reduction especially for regions with an insufficient contacting e. g. Ni-mesh cavities or along pores and cracks.

Furthermore, the impact of highly electrically conductive pathways to overcome the low conduction of pure Cr_2O_3 scales was systematically investigated using FE simulations. From the comprehensive parameter variations that were performed it is possible to extract distance maps that deliver the dimensioning of metallic bridges for a significant ASR reduction. These distance maps include the required patterns and the required diameter of highly conductive bridges in relation to the oxide scale thickness. However, to validate these findings designated experimental studies would be required.

The following section treats the interaction of the formed Cr_2O_3 with Ni at relevant SOFC conditions i. e. under alternating reducing and oxidizing atmospheres.

5.4 Ohmic resistance of nickel infiltrated chromium oxide scales in solid oxide fuel cell metallic interconnects

Significant ohmic losses are caused by Cr_2O_3 scale formation on Cr containing interconnects. This degradation occurs under both oxidizing and reducing (water containing) conditions. Due to the low conductivity of Cr_2O_3 in the range of 0.001–0.2 S cm^{-1} [91, 164], the oxide layers often provide a major contribution to the overall resistance of SOFC stacks. However, the extrinsic electrical conductivity of thermally grown semi-conductive Cr_2O_3 is influenced by various parameters including temperature, impurities and variations of the gas composition with the oxygen and water partial pressures as most relevant contributions. (Note: At temperature below 1000 °C the electrical conductivity of Cr_2O_3 is dominated by impurities, which is denoted as extrinsic property [88, 91, 188–190]). In the previous sections 5.2 and 5.3 results for the ohmic losses originating from the cathode and anode side of metallic interconnects are presented. In this section, the focus will be on anodic side MIC degradation. As will be shown, the latter exhibiting greater variation in the microstructures, including possible formation of spinel phases. Additionally
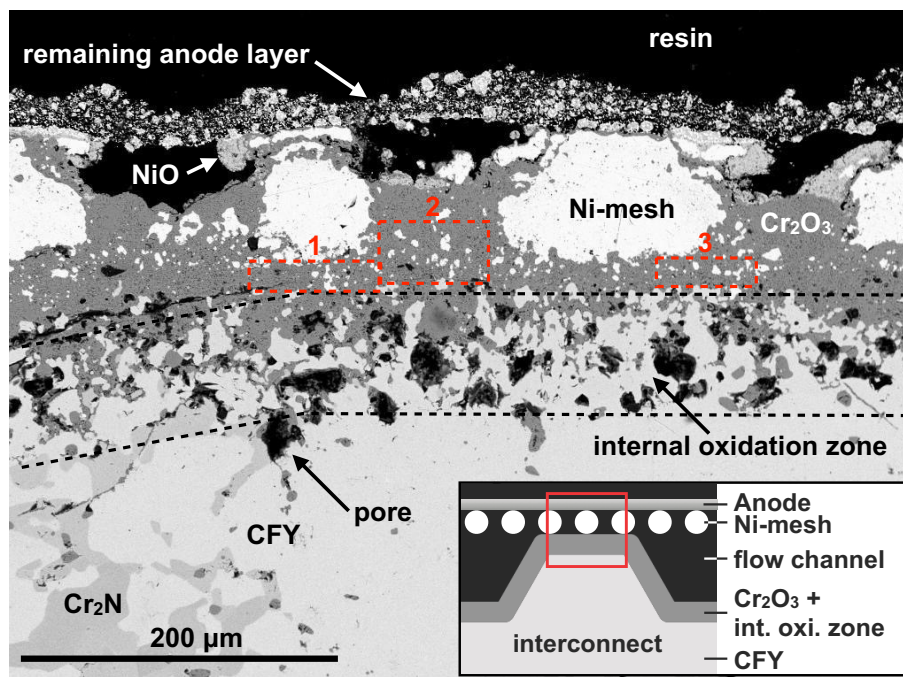
Fig. 5.35 Cross section of a CFY MIC operated in a Hexis SOFC stack under real conditions at 900 °C for 40 000 h including 15 redox cycles running on CPOx reformed natural gas [8, 103].

the extrinsic electrical conductivities may vary with changing gas composition. If Ni is present on the anode side of a SOFC stack repeat unit the formed Cr_2O_3 might interact with nickel or nickel oxide. The involved nickel might originate from different sources: the anode [179], the current-collector mesh [103, 180–182], or Ni containing interconnect coatings [129, 181, 183–185]. For a CFY interconnect [191], operated for 40 000 h in a Hexis stack at about 900 °C, Fig. 5.35 shows a typical SEM cross section. The image was taken at the top of the interconnect with a Ni-mesh and the remaining anode aside. The red rectangle in the inset illustrates schematically the SEM image location. Note the bright spots within the Cr_2O_3 matrix are identified as metallic Ni. Obviously, the Cr_2O_3 scale formed on the CFY MIC interacts with the Ni-mesh and the Ni containing anode. Note that the observed NiO represented as light gray color, was formed during shut down under partly oxidizing conditions. Dashed black lines mark the internal oxidation zone, which together with the Cr_2N formation are typical features of CFY degradation on the anode side, cf. section 5.1.2. To illustrate the magnitude of the local Ni content in a thermal grown Cr_2O_3 layer the phase content for three specific regions was additionally quantified within the red dashed rectangles in Fig. 5.35. The corresponding phase distributions are shown in Fig. 5.36. As shown the local Ni content can be rather high, i.e. more than 11 vol.%.
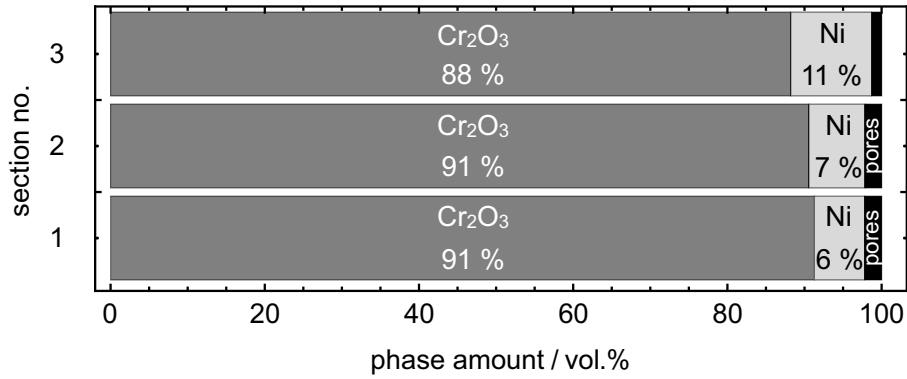
Fig. 5.36 Phase distribution within thermal grown oxide scale after 40 000 h stack operation for the specific regions marked by red dashed rectangles in Fig. 5.35.

It is obvious from Fig. 5.35 that the ohmic losses associated with oxide scales will depend in a complex way on the microstructure and the distribution of the various phases. In particular, it will depend on the presence of Ni, which has an electrical conductivity several orders of magnitude higher compared with that of Cr_2O_3 [91, 164, 192]. Therefore the motivation of this section is to improve the understanding of the Ni/Cr_2O_3 interaction typically occurring on the anode side of MICs with high chromium contents such as for CFY. Electrical conductivity measurements of MIC materials in reduced and/or oxidized gas atmospheres are indispensable to detect their overall degradation behavior. However, the obtained findings are difficult to interpret since they represent a superposition of a number of mechanisms such as oxide scale formation, segregation of reactive elements [118, 193], integration of impurities into the Cr_2O_3 lattice structure [188, 190, 194] and spinel formation by alloys. To single out the effect of Ni interaction with Cr_2O_3 were instead pellets made, which contained only Cr_2O_3, unavoidable pores and different amounts of Ni. The later one was systematically varied to take into account the observed wide range of local Ni contents in the anode side oxide scale as observed in Fig. 5.35. The electrical conductivities of these Ni containing pellets were studied in situ at different gas atmospheres including redox cycles for an overall period of more than 2000 h, i.e. under long-term conditions. In addition, the thermal activation energy was determined by temperature variations at different points in time. To allow more thorough interpretations, the obtained electrical conductivity denoted as σ_{eff} and the thermal activation energy E_A for all experimental data were complemented by microstructure, X-ray diffraction (XRD) and atomic force microscopy (AFM) data as well as information from literature.

5.4.1 Experimental details

Pellet preparation

To prepare the pellets, Cr_2O_3 powder was mixed with different amounts of nickel powder. The resulting compositions and the corresponding labels are summarized in Table 5.6. Note that the provided values for Ni content correspond to the volume fraction of solids e. g. a pellet with 10 vol.% Ni is denoted as Cr_2O_3-10. For the preparation of the Cr_2O_3-0.5 pellets nickel(II) nitrate hexahydrate (N_2NiO_6 $6H_2O$) was mixed with the Cr_2O_3 powder. The samples with a Ni content of 5 vol.% and higher were admixed with ball milled metallic Ni particles with an averaged particle size r_{50} of 5.5 μm. To ease the pellet handling after pressing few drops Terpineol were added. The powder was uniaxially pressed with 200 kN at room temperature in a steel die with 40 mm diameter to form 2 mm thick tablets. The tablets were sintered in two batches at the highest available temperatures (for the available equipment) to minimize the porosity. The first batch with the Cr_2O_3-0 pellets was sintered in air for 2 h at 1585 °C. To avoid NiO formation the second batch with the Ni containing pellets was sintered for 2 h in reducing hydrogen atmosphere at 1400 °C, i. e. just below the Ni melting point. The tested Cr_2O_3 pellets of size 10–12 mm × 35 mm after sintering were cut out of the sintered tablets. Note that one Cr_2O_3-5 pellet was broken during preparation hence resulting in two smaller samples of sizes 5–7.5 × 25 mm.

Electrical conductivity measurement

σ_{eff} was measured using a four-point probe set-up in a Gero SR 70-500 tube furnace under various atmospheres overall for more than 2000 h. To adjust the flow rates the set-up was equipped with flow controllers to overflow the samples with the desired atmosphere. The furnace was equipped with a Pt/YSZ/Pt-sensor to record the Nernst potential next to the samples. To monitor the temperature a thermocouple type K was also placed near to the samples. Since the used set-up did not provide measuring channels for all samples

Table 5.6 Ni content in Cr_2O_3 pellets and corresponding labels as used in this work. The test batch column denotes the two different conductivity measurement campaigns (cf. section 5.4.1).

matrix	Ni content / vol.%	text label	figure label	test batch #
Cr_2O_3	0.0	Cr_2O_3-0	0 % Ni	2
Cr_2O_3	0.5	Cr_2O_3-0.5	0.5 % Ni	1
Cr_2O_3	5.0	Cr_2O_3-5	5 % Ni	1
Cr_2O_3	10.0	Cr_2O_3-10	10 % Ni	1
Cr_2O_3	20.0	Cr_2O_3-20	20 % Ni	2
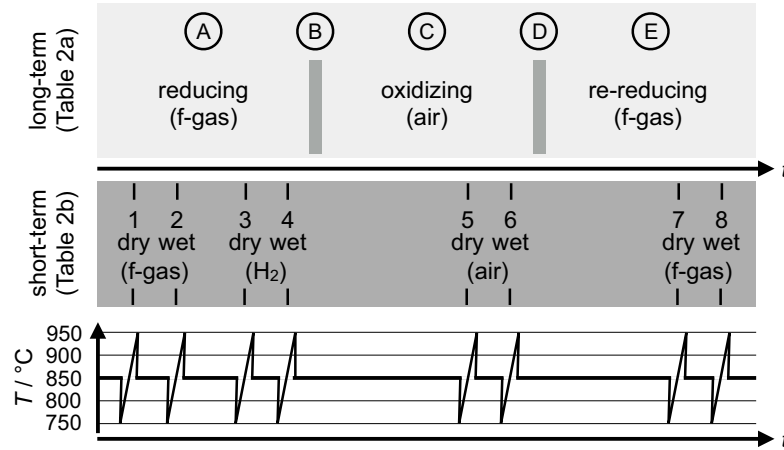
Fig. 5.37 Schematic illustration of the varying atmospheres during testing. The upper part represents the five different stages during isothermal long-term testing at 850 °C. In particular, stages B and D denote the points in time of shifting from reducing to oxidizing atmospheres and vice versa. The middle part illustrates the short-term testing with applied temperature variations between 750 and 950 °C to extract the thermal activation energy E_A. The lower part illustrate the corresponding temperature profiles for both long- and short-term testing.

σ_{eff} characterization was done in two batches (cf. Table 5.6).

The testing procedure included long-term measurements at a fixed temperature of 850 °C and additional short-term temperature variations in the range of 750–950 °C to extract the corresponding thermal activation energies at selected points of time. The upper part in Fig. 5.37 schematically illustrates the different stages in varying atmospheres during long-term testing and the middle part shows the short-term temperature variation to determine E_A at different times. Fig. 5.37 shows in addition the corresponding temperature profile during the test procedure. More specific details about the applied gas compositions and temperatures during long- and short-term testing are given in Tables 5.7a and 5.7b, respectively.

Table 5.7a Summery of long-term pellet test conditions with different atmospheres and specific gas compositions as illustrated in the upper part of Fig. 5.37.

stage	atmosphere	$T\,/\,°C$	gas label	gas composition	flow rate $\mathrm{Nml\,min^{-1}}$
A	reducing	850	f-gas	$5\,\%\,H_2$; $95\,\%\,N_2$	200
B	transition	850			
C	oxidizing	850	air	$21\,\%\,O_2$; $79\,\%\,N_2$	200
D	transition	850			
E	reducing	850	f-gas	$5\,\%\,H_2$; $95\,\%\,N_2$	200

Table 5.7b Summery of short-term pellet test conditions with different atmospheres and temperature variation ranges as illustrated in the middle part of Fig. 5.37.

T var no.	atmosphere	T / °C	gas label	humidity	gas composition	flow rate / Nml min^{-1}
1			f-gas	dry	$5\,\%\,H_2; 95\,\%\,N_2$	
2	reducing	750–950		wet	$4.8\,\%\,H_2; 91.7\,\%\,N_2; 3.5\,\%\,H_2O$	200
3			H$_2$	dry	$100\,\%\,H_2$	
4				wet	$96.1\,\%\,H_2; 3.9\,\%\,H_2O$	50
5	oxidizing	750–950	air	dry	$21\,\%\,O_2; 79\,\%\,N_2$	
6				wet	$20.3\,\%\,O_2; 76.2\,\%\,N_2; 3.5\,\%\,H_2O$	200
7	reducing	750–950	f-gas	dry	$5\,\%\,H_2; 95\,\%\,N_2$	
8				wet	$4.8\,\%\,H_2; 91.7\,\%\,N_2; 3.5\,\%\,H_2O$	200

Long-term measurement   The long term testing is done under isothermal conditions at 850 °C without additional humidification. σ_{eff} measurements were started in reduced forming gas (f-gas) atmosphere as denoted in the upper part in Fig. 5.37 by stage A. Note that details about all gas compositions and flow rates are given in Table 5.7a. Since the short time ranges during switching the gas compositions are also relevant for the interpretation of the results the shift from reducing to oxidizing conditions is denoted with stage B. The period where the samples were exposed to air for about 900 h is labeled as stage C and the transition from oxidizing back to reducing conditions as stage D. Finally, in stage E, the samples were again exposed to f-gas for about 900 h.

Short-term measurements, determination of activation energy   The thermal E_A was determined by temperature variation (T var) at different time steps as shown in the lower part of Fig. 5.37. For this purpose, the temperature was increased in steps of 25 °C from 750 to 950 °C. To reach steady-state short-term conditions for the relevant thermal activation process the dwelling time for each temperature level was 45 min. The thermal E_A was investigated in different gas atmospheres including humidification. Humidification is realized by rerouting the gas through a Perma Pure MH-110-12F-2 humidifier downstream to the furnace. With this equipment a humidification of 3–4 vol.% $H_2O(g)$ is reached. During stage A, i. e. in reducing atmosphere, thermal E_A was determined in f-gas (T var 1), in humidified f-gas (T var 2), in hydrogen (T var 3) as well as in humidified hydrogen (T var 4). In oxidizing atmosphere (stage C) the temperature variations was performed in dry (T var 5) and humidified air (T var 6). Activation energies were again determined at the end of the test (stage E), i. e. after re-reduction using f-gas (T var 7), again without and with humidification (T var 8). All details about the applied gas compositions and corresponding flow rates during temperature variation are given in Table 5.7b.

Atomic force microscopy

AFM measurements were performed with a Bruker Multimode 8 (Karlsruhe) in Peak-Force quantitative nano mechanical mode (QNM™). The nanomechanical properties were obtained by evaluation of a force distance curve performed at every contact point. Simultaneously to the topography, the electrical current was recorded using a PeakForce TUNA™ application module in tapping mode at an applied voltage of 1 V between tip and sample holder (tip at ground) and averaged by a lock-in amplifier. Further details on the measurement can be found in [195]. Furthermore, conductive PtIr-coated AFM probes (PPP-NCHPt (42 N m⁻¹; 330 kHz), Nanosensors™) were used. The investigated Cr_2O_3-20 pellet was glued onto a metallic AFM sample holder discs with conductive adhesive tape (Leit-C-Adhesive Tape, Plano).

Post test analysis

After the pellets have been cut out of the tablets the remaining materials were exposed to oxidizing and reducing conditions just as the pellets. At each sample removing point a small piece of these left overs was cut with a diamond disk for post test microstructure analysis.

In order to avoid artifacts from mechanical polishing [114], high quality cross sections were produced by broad ion beam (BIB) polishing. For this purpose the samples were fixed with resin on a 130 μm thick silica glass and polished with a Hitachi IM4000 BIB milling system. The parameters used for polishing are 1.5 kV accelerating voltage, 6 kV discharge, 30° swing angle and 2.5 h milling time. SEM images were taken with a Zeiss Gemini 1530 FEG with BSE detector.

X-ray diffraction (XRD) patterns were obtained on the cut surface of the Cr_2O_3-pellets with a Bruker D8 Advance. For this analyses Bragg-Brentano geometry with Ni-filtered Cu K_α radiation, constant illuminated sample-area, and a LynxEye position sensitive detector were used. The phases were identified by comparison with the ICDD database. For the figures presented in this thesis, the contributions of the $K_{\alpha2}$ radiation and the background were removed using the EVA (Bruker).

5.4.2 Results

The results section is structured as follows: First, the results from the long-term σ_{eff} measurements of the Cr_2O_3 pellets (with varying Ni contents) at 850 °C in various gas atmospheres are presented. Then, special focus is put on the changes of σ_{eff} during atmo-

sphere switches, i. e. during stages B and D according to Fig. 5.37. The next subsection shows the results of the microstructure analysis for the Cr_2O_3 pellets with 10 and 20 vol.% Ni followed by the XRD patterns and the AFM data. A comprehensive compilation of σ_{eff} values obtained at temperatures between 800 and 900 °C are summarized in Table 5.8. Finally, the effect of temperature variation in various gas atmospheres and the corresponding thermal E_A are presented in Table 5.9.

Long-term electrical conductivity of Cr_2O_3-pellets

Fig. 5.38 shows σ_{eff} data of the first batch of Cr_2O_3 pellets admixed with 0.5 vol.%, 5 vol.% and 10 vol.% Ni. Fig. 5.39 shows the corresponding results of the second batch for pure Cr_2O_3 pellets and those with 20 vol.% Ni. Note that σ_{eff} data for the initial reduction stage A have been omitted in both Figs. 5.38 and 5.39 because of the large scattering of the data during the temperature variations (T var 1–4) performed under this stage.

It can be observed that σ_{eff} of all samples shows a steep increase during stage B, i. e. when switching from reducing to oxidizing conditions. This increase takes place over a period of only a few hours. While exposed to air, i. e. during stage C, all Ni containing Cr_2O_3 pellets exhibit a further, but much slower increase in their σ_{eff} than during stage B. This is different, however, for the pure Cr_2O_3 samples, where σ_{eff} is constant in air. Switching back to reducing conditions, i. e. stage D, results in a "fast" decrease followed by an unexpected "fast" increase in σ_{eff} for the Cr_2O_3 pellets with Ni contents of 0.5 vol.% and higher. Both "fast" periods of decrease and increase last approximately 1–3 h. Again, the behavior of pure Cr_2O_3 without nickel is different in the sense that there is no increase of conductivity in the transition period at stage D. During the subsequent stage E in reducing atmosphere, all samples show a slow decrease in σ_{eff}. It is also important to note that the different responses of the sample properties (i. e. σ_{eff}) on the changing atmospheres (i. e. switching from reduced to oxidized and back) occur on different temporal lengths scales: some take place within few hours, others expand over hundreds of hours. This behavior is explained in section 5.4.3. These measurements clearly demonstrate that the addition of Ni has a strong effect on σ_{eff} when compared with the results of the pure Cr_2O_3 pellets.

Stage E shows the re-reduction in f-gas. The Cr_2O_3-10 and Cr_2O_3-20 pellets show a sharp increase of σ_{eff} after changing the atmosphere from air to f-gas (stage D). Subsequently to this temporary increase σ_{eff} is continuously decreasing. In summary, the total decrease of σ_{eff} upon re-reduction in stage E is less pronounced compared to the increase upon oxidation (stages B, C) and the fast increase upon reduction (stage D). This leads to an overall increase of σ_{eff} by up to one order of magnitude. The sample without Ni
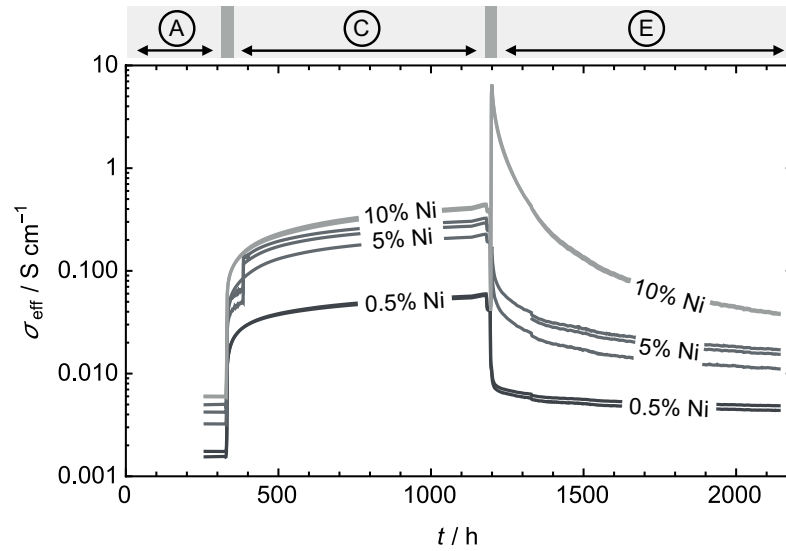
Fig. 5.38 Electrical conductivity evolution of Cr_2O_3-0.5, Cr_2O_3-5 and Cr_2O_3-10 pellets measured at 850 °C in reducing f-gas and air. Data points for other temperatures (used for thermal activation energy E_A determination) were removed.
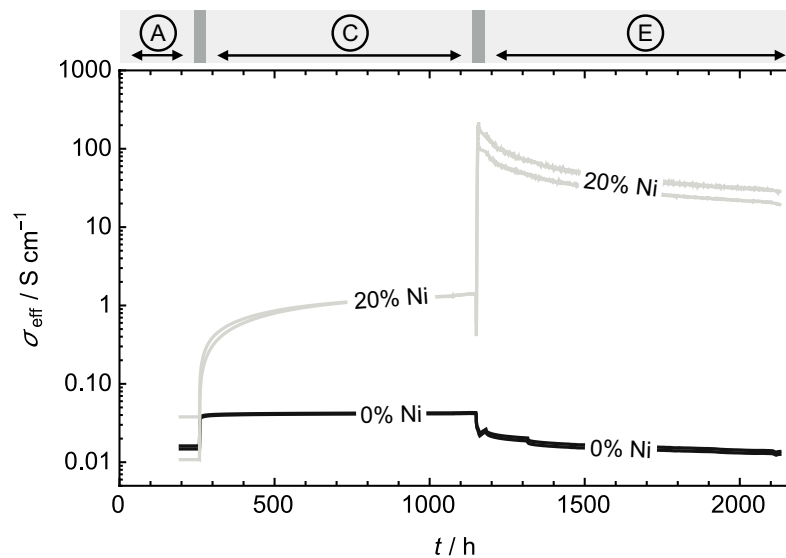
Fig. 5.39 Electrical conductivity evolution of Cr_2O_3-0 and Cr_2O_3-20 pellets measured at 850 °C in reducing f-gas and air. Data points for other temperatures (used for thermal activation energy E_A determination) were removed.

does not show this improvement and its conductivity turns back to the initial level after re-reduction.
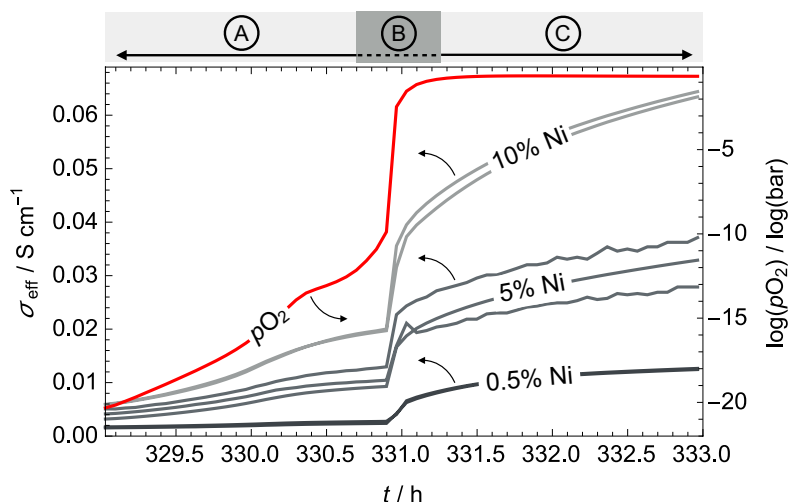
Fig. 5.40 Electrical conductivity data of the first batch with Cr_2O_3-0.5, Cr_2O_3-5 and Cr_2O_3-10 pellets during change from reducing forming gas (95 % N_2, 5 % H_2) atmosphere to air at 850 °C. The red curve shows the corresponding oxygen partial pressure based on the measured Nernst potential. Note, the tentative p_{O_2} increase after atmosphere change is related to some technical issues with the applied mass flow controller.
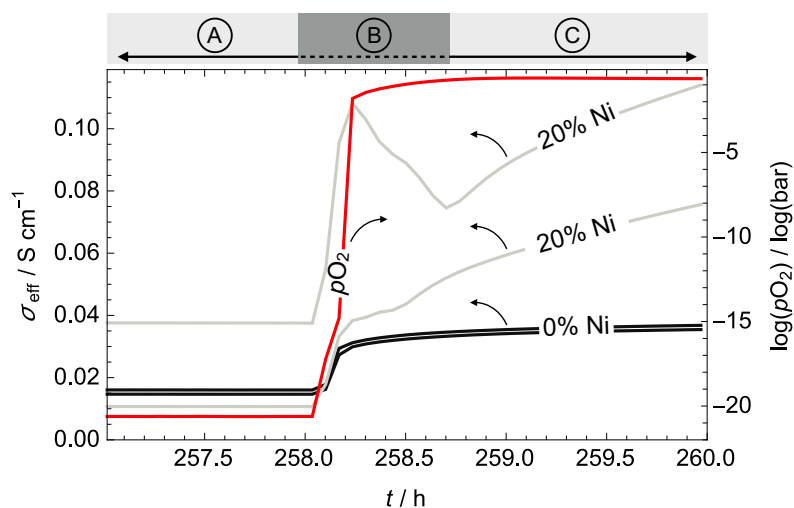
Fig. 5.41 Electrical conductivity data of the second batch with Cr_2O_3-0 and Cr_2O_3-20 pellets during change from reducing forming gas (95 % N_2, 5 % H_2) atmosphere to air at 850 °C. The red curve shows the corresponding oxygen partial pressure based on the measured Nernst potential.

Electrical conductivity behavior during atmosphere change

As pointed out above, changing the gas atmosphere from reducing to oxidizing conditions and back again has a profound impact on σ_{eff} of the Cr_2O_3 pellets. These changes in σ_{eff} become more pronounced with increasing Ni contents. To further highlight the conductivity behavior during the transitions from one gas atmosphere to another, Figs. 5.40–5.43
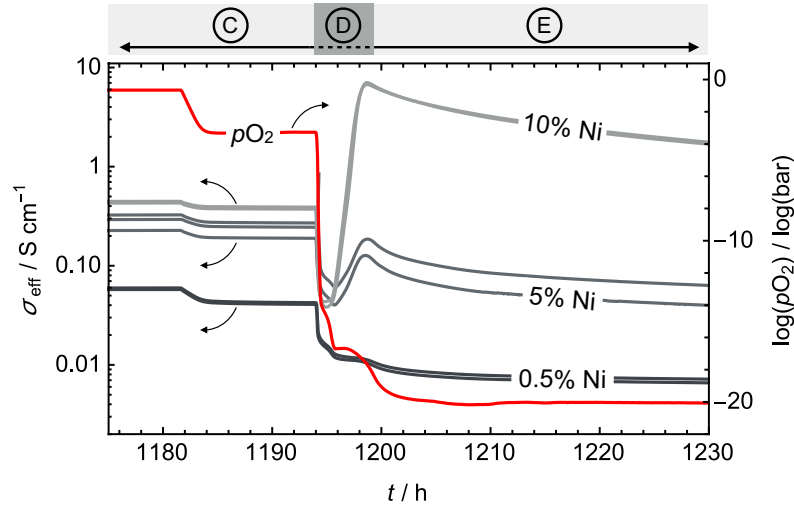
Fig. 5.42 Change from air to reducing forming gas (95 % N$_2$, 5 % H$_2$) atmosphere and corresponding electrical conductivity σ_{eff} behavior of Cr$_2$O$_3$ pellets admixed with Ni particles measured within the first batch. The red curve shows the corresponding oxygen partial pressure based on the measured Nernst potential. Note, the p_{O_2} plateau at 10^{-4} bar is related to technical issues with the applied mass flow controller during atmosphere switch form air to f-gas.
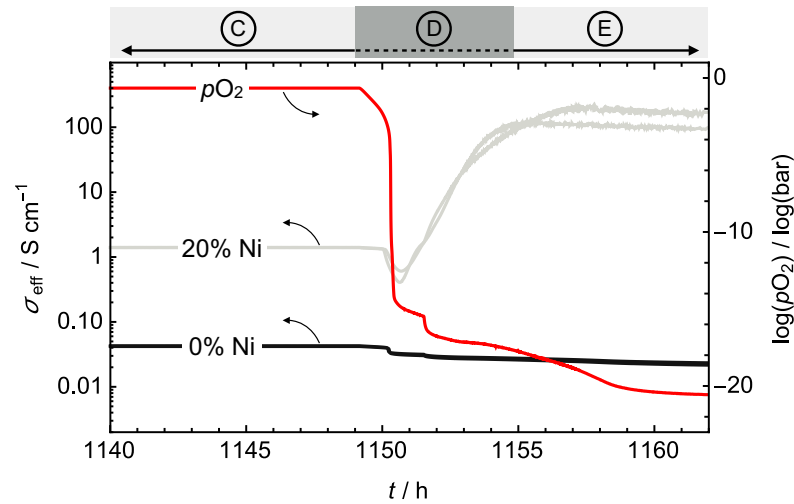
Fig. 5.43 Change from air to reducing forming gas (95 % N$_2$, 5 % H$_2$) atmosphere and corresponding electrical conductivity σ_{eff} behavior of Cr$_2$O$_3$ pellets admixed with Ni particles measured within the second batch. The red curve shows the corresponding oxygen partial pressure based on the measured Nernst potential.

provide further details. Figs. 5.40 and 5.41 provide details of the changes in σ_{eff} when going from reducing f-gas to air. Similarly, changing from air back to f-gas is shown in detail in Figs. 5.42 and 5.43. In addition to the provided σ_{eff}, all diagrams show the corresponding oxygen partial pressures as obtained from measuring the Nernst potential. Figs. 5.40 and 5.41 provide a clear trend: σ_{eff} shows an abrupt rise within few minutes

after switching from f-gas to air. This is followed by a much slower, continuous increase. This behavior is more pronounced at higher Ni content. Note also that one of the samples with 20 vol.% Ni deviates from the behavior described above. There, right after switching the gas composition, the steep increase is followed by a short decrease (over about half an hour), followed again by a slow increase in σ_{eff}. Moreover the oxygen partial pressure follows the behavior observed for σ_{eff}. However, after stage B, it reaches a constant value much more quickly.

Figs. 5.42 and 5.43 highlight the changes in σ_{eff} when switching back from air to f-gas. During the transition (stage D) the evolution of the p_{O_2} is discontinuous. Obviously the reduction of the samples influences or buffers somehow the p_{O_2} in the furnace. This is accompanied by a decrease in the oxygen partial pressure. After reaching a $p_{\text{O}_2} < 10^{-17}$ bar, σ_{eff} increases significantly for Cr_2O_3 pellets containing ≥ 5 vol.% Ni. After reaching a maximum at $p_{\text{O}_2} \approx 10^{-18}$ bar σ_{eff} decreases again. Note also that the Cr_2O_3-0.5 pellets show a stagnation in σ_{eff} at a p_{O_2} of around 10^{-17} bar, which is also visible in the p_{O_2} curve. A similar trend in the p_{O_2} behavior can be observed in Fig. 5.43.

Microstructure analysis of Cr_2O_3 pellets

SEM images of a Cr_2O_3-10 pellet polished with BIB are shown in Fig. 5.44. The horizontal direction gives the microstructure evolution at three different instants of time, i.e. at 300 h (stage A, f-gas), at 1200 h (stage C, air), and at 2150 h (stage E, f-gas). In the vertical direction, the magnification level increases from the top to the bottom line. Figs. 5.44a, 5.44d and 5.44g show the initial microstructure in f-gas atmosphere for three different magnification levels. The admixed Ni particles are evenly distributed within the Cr_2O_3-matrix. Sharp transitions between the two solid phases can be observed. The Ni particle sizes are still similar to the original particle sizes ($r_{50} = 5.5\,\mu$m) as admixed to the Cr_2O_3 powder.

After being exposed to air for 550 h the microstructure significantly differs from the original one. At the lowest magnification the Ni particles appear to be blurred, compare Figs. 5.44b with 5.44a. At higher magnifications shown in Figs. 5.44e and 5.44h the Ni particles were as expected oxidized and they fill up additional pore space due to the associated volume increase. Furthermore, the formation of a $NiCr_2O_4$ spinel took place, as confirmed by XRD patterns presented in section 5.4.2. Note that the different oxide phases (NiO, Cr_2O_3, $NiCr_2O_4$) have similar backscatter coefficients and hence the contrast in SEM is poor for the oxidized samples.

Re-reducing, i.e. exposing the samples again to the low p_{O_2} f-gas, leads to further
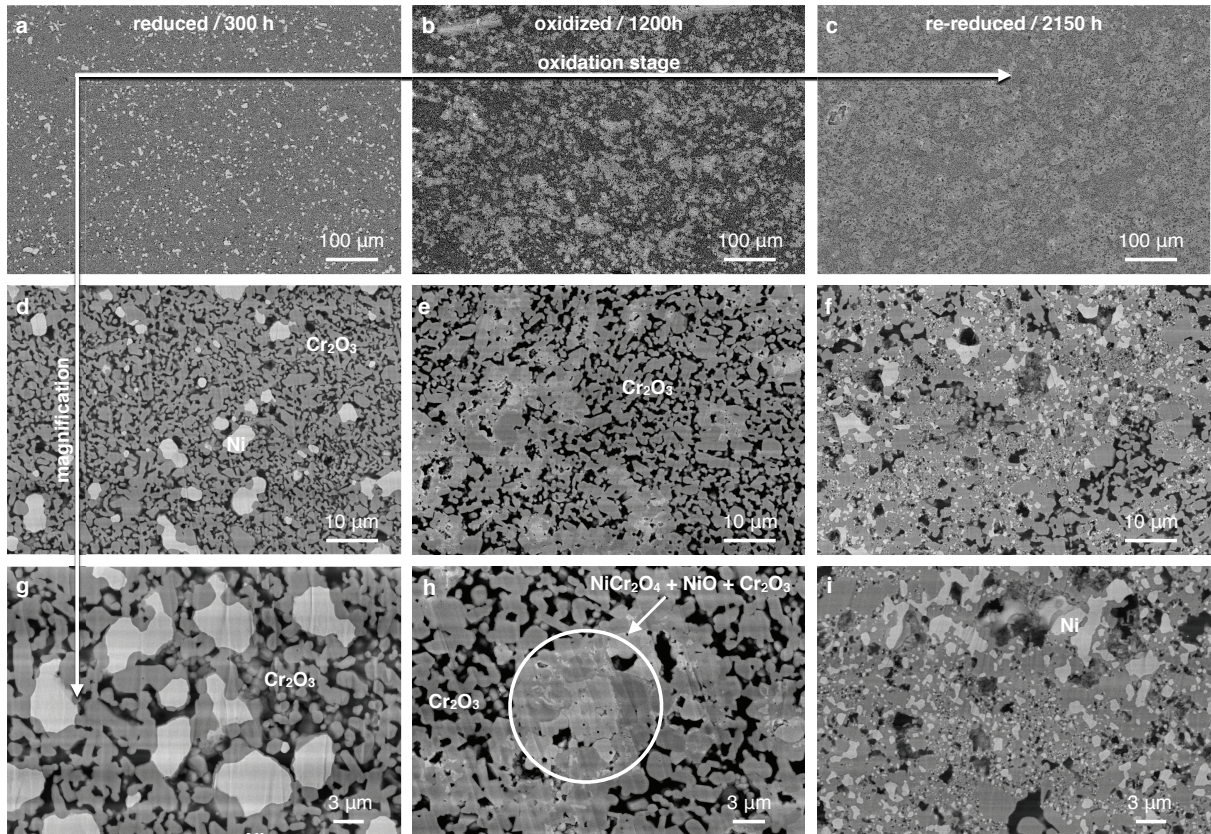
Fig. 5.44 Microstructures of Cr_2O_3 pellets with 10 vol.% Ni prepared by BIB after different test steps in reduced and oxidized atmosphere at 850 °C are shown in the columns. The time specification denotes the approximated furnace removal corresponding to Fig. 5.38. Increasing magnifications of Cr_2O_3 pellets section are shown from top to bottom. In reduced state in g) and i) two clearly separated solid phases i. e. Cr_2O_3 and Ni can be observed. In oxidized state the contrast between different phases including Cr_2O_3, NiO and $NiCr_2O_4$-spinel is very low. The black phase represents the pore.

microstructure transformations as shown in Figs. 5.44c, 5.44f and 5.44i. Under these conditions NiO and $NiCr_2O_4$ spinel are completely dissolved. Interestingly, the resulting Ni shown in Figs. 5.44f and 5.44i is finely dispersed into smaller particles with diameters of less than 1 μm. In addition the small black dots of similar sizes, which can be observed in these domains represent micro pores.

Fig. 5.45 provides examples of the microstructures of the Cr_2O_3-20 pellets at the beginning and at the end of stage E, i. e. after being again reduced in f-gas for 12 h and 900 h, respectively. Comparing Fig. 5.45a with Fig. 5.45b a general smoothing of the contours of the Ni particles can be observed.

The porosity of the samples was determined after sintering based on the weights and volumes of the pellets. The Cr_2O_3-5, Cr_2O_3-10 and Cr_2O_3-20 samples showed a porosity
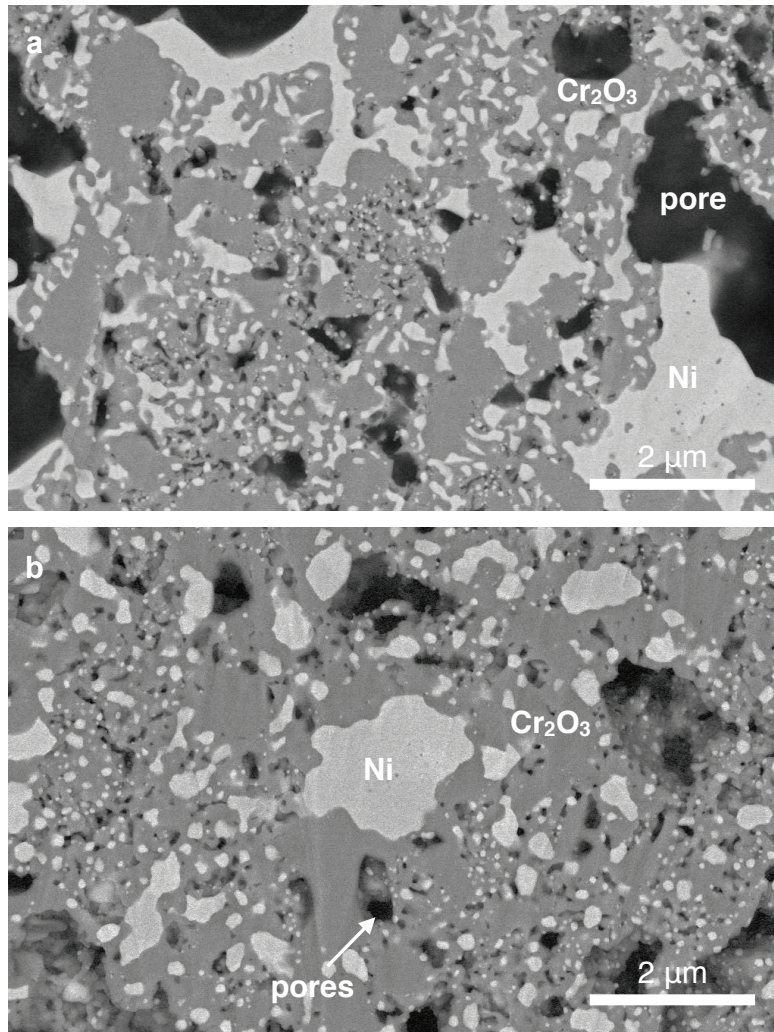
Fig. 5.45 a) Microstructure of Cr_2O_3 pellet with 20 vol.% Ni immediately (12 h) after atmosphere change from air to re-reduction in f-gas at 850 °C and b) after re-reduction in f-gas for about 900 h.

of around 36 %. The Cr_2O_3-0.5 samples exhibited a porosity of 44 %. The porosity of the Cr_2O_3-0 pellets was 27 %, as obtained from post test SEM images analysis. Note, that the rather large porosity of the analyzed pellets has a significant effect on the obtained σ_{eff}. Consequently, the obtained σ_{eff} will be generally lower than those for oxide scales thermally grown on metallic interconnects under typical SOFC stack operation conditions. Note also that the obtained σ_{eff} data and corresponding thermal E_A were not corrected to eliminate the effect of the pores. The reason is that the Cr_2O_3 pellets admixed with Ni contain two different electron conducting phases that cannot be simply corrected for pore effects, e. g. by Archie's law or by other recently published methods [196–198].
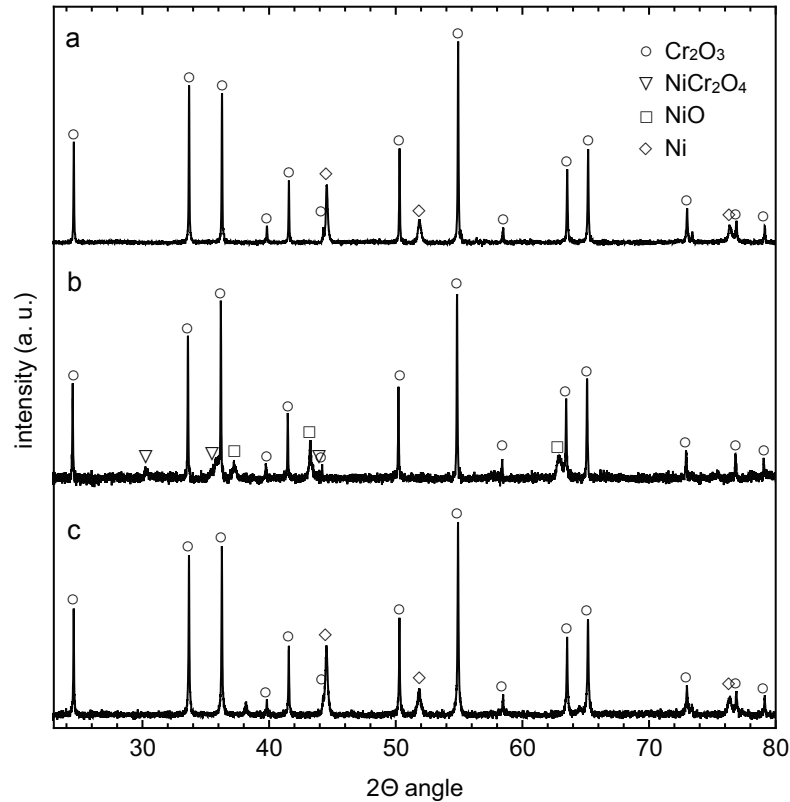
Fig. 5.46 XRD patterns of Cr_2O_3 pellets with 10 vol.% Ni after heat exposure in different atmospheres at 850 °C. a) after exposure to reduced forming gas (95 % N_2, 5 % H_2) removed after 320 h, b) after exposure to air for 550 h and c) after re-reduction in forming gas for another 900 h.

XRD data

XRD of sintered Cr_2O_3 pellets with 10 and 20 vol.% Ni were studied at different stages of the long-term experiments. Fig. 5.46 shows the results for the Cr_2O_3-10 pellets at the end of stage A in f-gas, during stage C in air and at the end of stage E in f-gas. Note that Cr_2O_3 diffraction peaks were present in all analyzed samples. Furthermore, from the pattern in Fig. 5.46a Cr_2O_3 and Ni can be identified after being exposed to f-gas for 320 h. As shown in Fig. 5.46b being exposed to in air for 550 h NiO and $NiCr_2O_4$ spinel can be identified. Finally, after re-reduction in f-gas for 900 h the previously formed NiO and $NiCr_2O_4$ spinel cannot be retrieved anymore in the XRD pattern shown in Fig. 5.46c.

Fig. 5.47 shows the XRD patterns for the Cr_2O_3-20 pellets after oxidation in air at the end of stage C and after re-reduction in forming gas for ca. 12 h i.e. at the end of stage D, respectively. The XRD pattern in Fig. 5.47a shows that the $NiCr_2O_4$ spinel and NiO phases are present after being exposed to air. These two phases cannot be detected anymore in Fig. 5.47b after short re-reduction using f-gas. However, metallic Ni could be
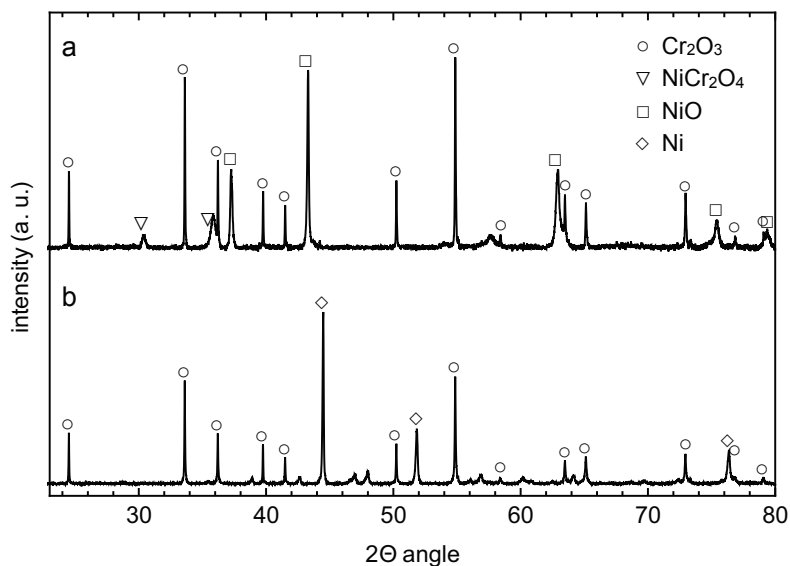
Fig. 5.47 XRD patterns of Cr_2O_3 pellets with 20 vol.% Ni after heat exposure in different atmospheres at 850 °C. a) after exposure to air for 850 h and b) after re-reduction in forming gas for 12 h. Note that the non-marked peaks in b) originate from the sample holder ($CaCO_3$).

verified in this XRD pattern.

AFM data

In Fig. 5.48 AFM images of a Cr_2O_3-20 pellet as sintered in reducing atmosphere are shown with a) surface topography, b) feedback signal, c) electrical current transition (bright spots) and d) the electrical current profile along the marked red line in c) are shown. The height image in Fig. 5.48a shows the topography of the sample. In the feedback regulation signal in Fig. 5.48b sharp height changes are recorded to enhance the surface structures. The current is measured during contact of the tip with the sample and averaged using a lock-in-amplifier. Numerous grains with an area from approximately $0.065\,\mu m^2$ up to approximately $11.561\,\mu m^2$ are visible. The large grain in the center is locally electrically conductive at room temperature as shown in Fig. 5.48c. This indicates that the admixed Ni forms some percolating paths across the pellets. In the current profile in Fig. 5.48d single conductive spots with a maximum current of approximately 80 pA were measured. Note, the scale in Fig. 5.48c is purposely limited to 2 pA to visualize electrical conductive spots i. e. to display it as a binarized electrical conductivity map. Thus the most part of the sample is not electrically conductive at room temperature. 3D-topography overlaid with adhesion force and electrical current data, respectively from a different sample location are shown in the appendix A.2 in Fig. A.6.
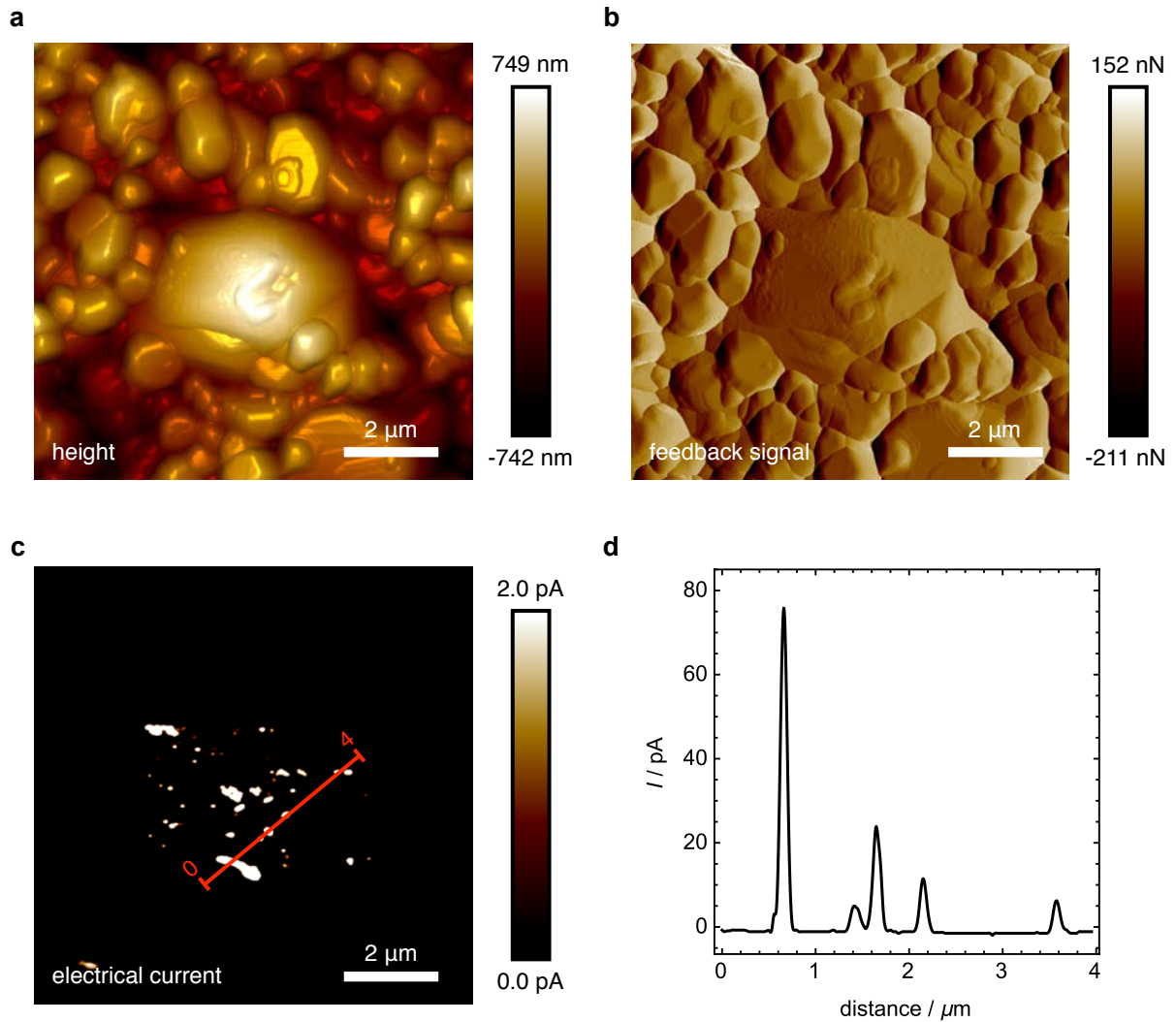
Fig. 5.48 AFM images of a Cr_2O_3-20 pellet after sintering with a) topography information, b) feedback signal, c) binarized electrical current flux (bright spots) and d) section of the effective electrical current along the red line in image c).

Temperature dependence of electrical conductivities

Temperature variations between 750–950 °C were applied to determine the thermal E_A based on σ_{eff} of the various Ni containing Cr_2O_3 pellets at different stages of the long-term experiments. The scatter of the experimentally determined σ_{eff} for the pellets with the same Ni amount is in general small i. e. 0–30 %. It is suggested that the observed deviations are related to some variances in the pellet dimension and measured distance between the voltage taps. Stage A included measurements T var 1–4 to determine the thermal E_A in f-gas and pure hydrogen, both either dry or additionally humidified with 3–4 vol.% water. σ_{eff} determined in stage A at 850 °C are in the range of 0.0012–0.0715 S cm^{-2}. σ_{eff} data
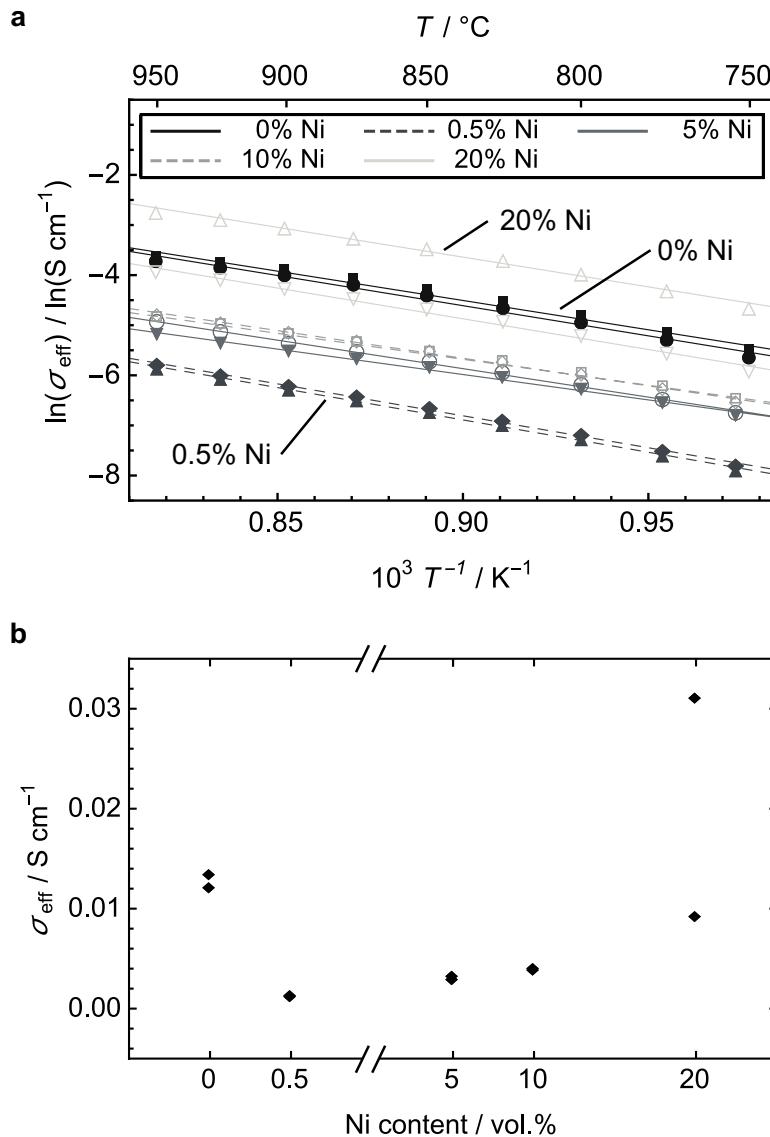
Fig. 5.49 a) Arrhenius plot of the electrical conductivities σ_{eff} of the investigated Ni containing Cr_2O_3 pellets in reducing f-gas atmosphere without humidification. The temperature variation was done within the first 100 h after startup. The corresponding E_A values are given in Table 5.9. b) Corresponding σ_{eff} plotted as a function of Ni content obtained at 850 °C.

from measurement T var 1 in dry f-gas are shown as an Arrhenius plot in Fig. 5.49a. All samples follow in good approximation a straight line in Arrhenius form with similar slopes resulting in thermal E_A between 0.873–1.112 eV. Samples with a higher amount of Ni generally have an increased σ_{eff} except for the Cr_2O_3-0 pellets, which are in the range of the Cr_2O_3-20 pellets. This behavior is attributed to different sintering conditions as will be discussed in section 5.4.3.

The data in Table 5.8 show that humidification of both f-gas and hydrogen leads to

Table 5.8 Electrical conductivity σ_{eff} of sintered Cr_2O_3 pellets with different amounts of Ni determined under reduced and oxidized atmospheres. Details about the used gas compositions are given in Table 5.7b. Note, the reported electrical conductivity values were not corrected to eliminate the effect of nonzero porosities.

sample no.	Ni vol.%	T /°C	stage A[a]				stage C[a]		stage E[a]	
			f-gas dry	f-gas wet	H_2 dry	H_2 wet	air dry	air wet	f-gas dry	f-gas wet
			σ_{eff} / S cm^{-1}	σ_{eff} / S cm^{-1}	σ_{eff} / S cm^{-1}	σ_{eff} / S cm^{-1}	σ_{eff} / S cm^{-1}	σ_{eff} / S cm^{-1}	σ_{eff} / S cm^{-1}	σ_{eff} / S cm^{-1}
1	0	800	0.0070	0.0125	0.0073	0.0069	0.0362	0.0364	0.0082	0.0096
		850	0.0121	0.0181	0.0119	0.0121	0.0414	0.0416	0.0130	0.0151
		900	0.0181	0.0240	0.0169	0.0178	0.0461	0.0463	0.0182	0.0213
2	0	800	0.0079	0.0139	0.0082	0.0078	0.0374	0.0376	0.0090	0.0104
		850	0.0134	0.0199	0.0132	0.0133	0.0425	0.0427	0.0142	0.0162
		900	0.0198	0.0260	0.0184	0.0193	0.0471	0.0473	0.0195	0.0227
3	0.5	800	0.0008	0.0013	0.0006	0.0010	0.0503	0.0515	0.0030	0.0040
		850	0.0013	0.0022	0.0010	0.0017	0.0567	0.0579	0.0049	0.0061
		900	0.0020	0.0034	0.0017	0.0026	0.0632	0.0644	0.0071	0.0085
4	0.5	800	0.0007	0.0012	0.0006	0.0009	0.0487	0.0501	0.0027	0.0037
		850	0.0012	0.0020	0.0010	0.0015	0.0547	0.0558	0.0044	0.0055
		900	0.0019	0.0030	0.0016	0.0024	0.0607	0.0618	0.0064	0.0077
5	5	800	0.0019	0.0052	0.0013	0.0030	0.2499	0.2594	0.0093	0.0171
		850	0.0029	0.0072	0.0022	0.0042	0.2740	0.2837	0.0154	0.0249
		900	0.0040	0.0091	0.0033	0.0056	0.2963	0.3068	0.0224	0.0336
6a	5	800	-	-	-	-	0.1949	0.2013	0.0066	0.0123
		850	-	-	-	-	0.2131	0.2201	0.0111	0.0181
		900	-	-	-	-	0.2302	0.2384	0.0164	0.0244
6b	5	800	0.0020	0.0058	0.0014	0.0034	0.2758	0.2863	-	0.0186
		850	0.0032	0.0084	0.0025	0.0052	0.3038	0.3149	0.0170	0.0274
		900	0.0047	0.0110	0.0042	0.0076	0.3313	0.3468	0.0249	0.0371
7	10	800	0.0025	0.0081	0.0018	0.0044	0.3725	0.3891	0.0236	0.0445
		850	0.0038	0.0120	0.0030	0.0062	0.4131	0.4307	0.0384	0.0641
		900	0.0055	0.0165	0.0045	0.0089	0.4522	0.4711	0.0554	0.0857
8	10	800	0.0025	0.0079	0.0018	0.0043	0.3572	0.3730	0.0226	0.0433
		850	0.0040	0.0121	0.0030	0.0063	0.3972	0.4143	0.0372	0.0634
		900	0.0058	0.0167	0.0046	0.0089	0.4357	0.4542	0.0545	0.0859
9	20	800	0.0187	0.0501	0.0151	0.0214	1.1971	1.2345	31.0576	29.6620
		850	0.0311	0.0715	0.0244	0.0373	1.3094	1.3487	29.6119	28.3176
		900	0.0470	0.0937	0.0370	0.0544	1.4200	1.4582	28.2604	28.2377
10	20	800	0.0054	0.0145	0.0043	0.0059	1.2009	1.2360	21.2173	20.4143
		850	0.0092	0.0211	0.0071	0.0107	1.3216	1.3618	20.6691	19.6699
		900	0.0138	0.0279	0.0111	0.0160	1.4441	1.4830	19.9695	19.3832

[a] details about the different stages are given in Fig. 5.37 and section 5.4.1, respectively.

an increase of σ_{eff} compared to the results in dry reducing atmospheres. Note that the influence of humidity is less pronounced in H_2 than in f-gas where compared to dry f-gas the thermal E_A is reduced by humidification (cf. Table 5.9). However, in pure hydrogen no clear trend could be observed for the thermal E_A resulting from dry and humidified atmospheres. At the end of stage C the thermal E_A was determined in T var 5 for dry and at T var 6 for humidified air. The corresponding data in Table 5.8 shows that σ_{eff} is not really affected by humidification of air. Furthermore, the thermal E_A for dry (0.187–0.265 eV) and humidified air (0.188–0.264 eV) are similar. The temperature dependence of σ_{eff} at the end of stage E in dry f-gas atmosphere are shown in Fig. 5.50 (T var 7). In addition, the results of the corresponding data in wet f-gas are given in Table 5.8 and Table 5.9, respectively. Finally, Arrhenius plots for all performed temperature variations are given in the appendix in Figs. A.7–A.10. It can be seen in Fig. 5.50 that σ_{eff} is increased in

Table 5.9 Thermal activation energy E_A data of sintered Cr_2O_3 pellets with different amounts of Ni determined under reduced and oxidized atmospheres. E_A were determined within a temperature range from 750 to 950 °C as shown in Figs. 5.49a and 5.50. Details about the used gas compositions are given in Table 5.7b. Note, the corresponding electrical conductivity values reported in Table 5.8 were not corrected to eliminate the effect of nonzero porosities.

| sample no. | Ni vol.% | stage A[a] | | | | stage C[a] | | stage E[a] | |
| | | f-gas dry | f-gas wet | H_2 dry | H_2 wet | air dry | air wet | f-gas dry | f-gas wet |
		E_A / eV	E_A / eV	E_A / eV	E_A / eV	E_A / eV	E_A / eV	E_A / eV	E_A / eV
1	0	1.038	0.744	0.937	1.051	0.264	0.265	0.882	0.888
2	0	1.008	0.709	0.904	1.016	0.253	0.253	0.854	0.866
3	0.5	1.099	1.056	1.110	1.037	0.252	0.247	0.945	0.818
4	0.5	1.112	1.065	1.135	1.072	0.243	0.235	0.953	0.809
5	5	0.874	0.640	0.957	0.695	0.188	0.187	0.799	0.755
6a	5	-	-	-	-	0.188	0.190	0.990	0.761
6b	5	0.980	0.755	1.058	0.867	0.202	0.204	0.861	0.654
7	10	0.893	0.797	0.971	0.794	0.214	0.211	0.933	0.723
8	10	0.951	0.838	1.005	0.818	0.219	0.217	0.958	0.755
9	20	1.024	0.717	1.012	1.093	0.190	0.187	−0.080	−0.052
10	20	1.057	0.748	1.066	1.155	0.204	0.203	−0.064	−0.058

[a] details about the different stages are given in Fig. 5.37 and section 5.4.1, respectively.

humidified atmosphere compared with dry. Except for the Cr_2O_3-20 pellets, which show a decreased σ_{eff} in humidified atmosphere after stage E resulting in thermal E_A value of −0.079 eV and −0.064 eV, respectively. Also, the thermal E_A in humidified f-gas is smaller compared to that in dry f-gas. The two Cr_2O_3-20 pellets show again a diametrically opposed behavior. A general comparison of the thermal E_A energies show that those in oxidizing atmosphere (T var 5 and 6) are four to five times higher compared to those in reducing atmosphere (T var 1–4, 7 and 8). Humidification and variation in the gas composition, i. e. f-gas versus pure H_2 do not influence the thermal activation significantly.

5.4.3 Discussion

This section is structured according to stages A–E of the performed long-term conductivity measurements, see Fig. 5.37. The measured σ_{eff} are discussed in detail, taking into account the applied gas atmospheres and the additional SEM, XRD and AFM data. Based on these experimental results, several microscopic mechanisms are proposed to explain the observed complex and partly counterintuitive time-dependencies of the obtained σ_{eff} data. Furthermore, the presented subsections are further subdivided into i) changes in the microsturcture of the Ni containing Cr_2O_3 pellets that affect the overall electrical conductivity and ii) effects related to the extrinsic electrical conductivities of the Cr_2O_3 phase. The temperature dependencies of the obtained σ_{eff} data and associated thermal
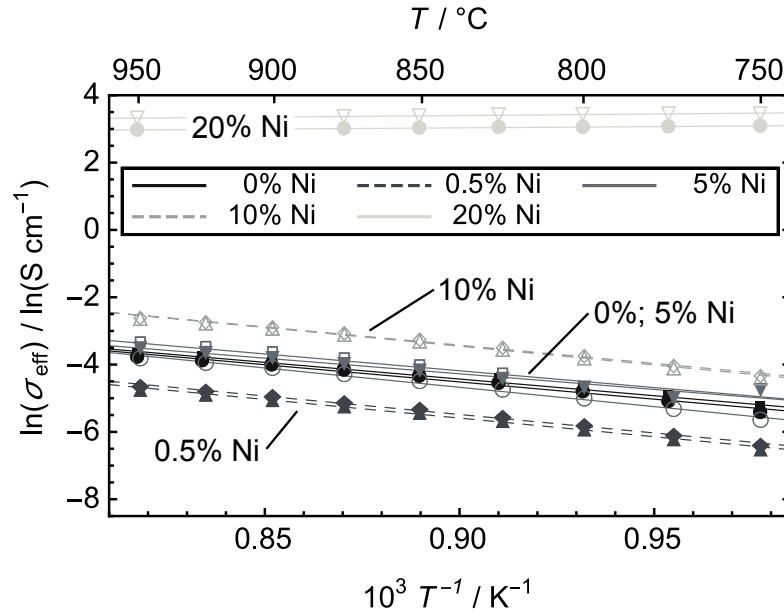
Fig. 5.50 Arrhenius plot of the electrical conductivities σ_{eff} of the investigated Ni containing Cr_2O_3 pellets at the end of stage E in dry f-gas atmosphere. The corresponding E_A values are given in Table 5.9.

E_A are discussed at the end of this section.

Electrical conductivities at stage A in reducing atmosphere

σ_{eff} behavior during stage A is shown in Figs. 5.38 and 5.39. After sintering and equilibration at constant reducing atmospheres the σ_{eff} of all samples is also constant, but it depends greatly on the Ni content of the samples. Explanations of the underlying mechanisms are provided in the following subsections.

Microstructure effects σ_{eff} of the Cr_2O_3 pellets with admixed Ni particles is significantly influenced by the amount of Ni as shown in Fig. 5.49 and Table 5.8. In general the electrical conductivity increases with the Ni content.

Representative microstructures of a Cr_2O_3-10 pellet after sintering and exposure to f-gas are shown in Figs. 5.44a, 5.44d and 5.44g. Note that the metallic Ni particles are in contact with the Cr_2O_3 and with additional pores, see Fig. 5.44d and 5.44g. Since at the considered temperatures the electrical conductivity of Ni [192] is several orders of magnitudes higher than that of Cr_2O_3 [87, 91, 164, 168, 194, 199] it is obvious that electrical current paths within the Ni particles are preferred over those within the Cr_2O_3 phase. This behavior is schematically illustrated in Fig. 5.51a. The arrows indicate preferred electrical current paths across the Ni particles. Since the Ni particles generally

do not percolate especially for pellets with low Ni contents, the electrical properties of the Cr_2O_3 matrix still limits the overall electrical behavior within the compacts.

Ni percolation can be expected starting roughly from about 20 vol.%. This might explain the rather large difference by a factor of three between σ_{eff} of the two considered Cr_2O_3-20 pellets. This deviation might be related to some partly percolated Ni paths within the two samples since the deviation for the Cr_2O_3 pellets with less Ni is determined in the range of 0–30 %. AFM data in Fig. 5.48 provides additional evidence for this type of behavior. It shows such percolating Ni paths in through plane direction obtained at room temperature by electrical potential measurements.

An additional microstructure effect is associated to the differences in the sinter conditions for the Cr_2O_3-0 pellets, as mentioned in section 5.4.1. The Cr_2O_3-0 pellets were sintered at higher temperature of 1585 °C compared to the Cr_2O_3 pellets with Ni ≥ 0.5 vol.% that were sintered at 1400 °C. As a result of the higher sinter temperature the Cr_2O_3-0 pellets exhibits a lower porosity, which improves σ_{eff} compared with that over the higher porosity Ni containing pellets.

Electrical conductivity of Cr_2O_3 phase In samples where the Ni content is below the percolation threshold all transport pathways lead partially or fully through the matrix of Cr_2O_3. The conductivity of Cr_2O_3 is thus the limiting phase for charge transport in these samples. From literature it is known that the conductivity of Cr_2O_3 varies greatly between 0.001 and 0.2 S cm^{-1} [91, 164]. Its conductivity is greatly dependent on the defect density. In the following the most important mechanisms of defect formation in Cr_2O_3 and the relationship with p_{O_2} are briefly discussed.

It is widely accepted that Cr_2O_3 is a p-type semiconductor. It has been suggested that the relevant defects for p-type conductivity are related to Cr vacancies, formulated by the Kröger-Vink notation, according to [188, 189, 202–204]

$$^3/_2\, O_2 \;=\; 3\,O_O + 2\,V_{Cr}''' + 6\,h^\bullet. \tag{5.12}$$
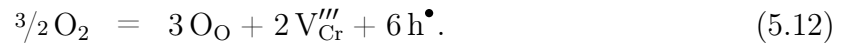
Note that Eq. (5.12) introduces a p_{O_2} dependency of the vacancies and of the associated electrical conductivity, which will be considered again in the discussion of the later stages. It has also been reported in the literature that the defect structure of a Cr_2O_3 phase can change at low oxygen partial pressures [169, 205]. Consequently, the electrical conductivity behavior can change from p-type to a n-type. Such a process was observed for Cr_2O_3 by Matsui and Naito [169] for pressures between 10^{-8} and 10^{-13} bar in a H_2/CO_2 atmosphere. Since the oxygen pressure is even lower in the applied f-gas atmosphere ($p_{O_2} \approx 10^{-20}$ bar)
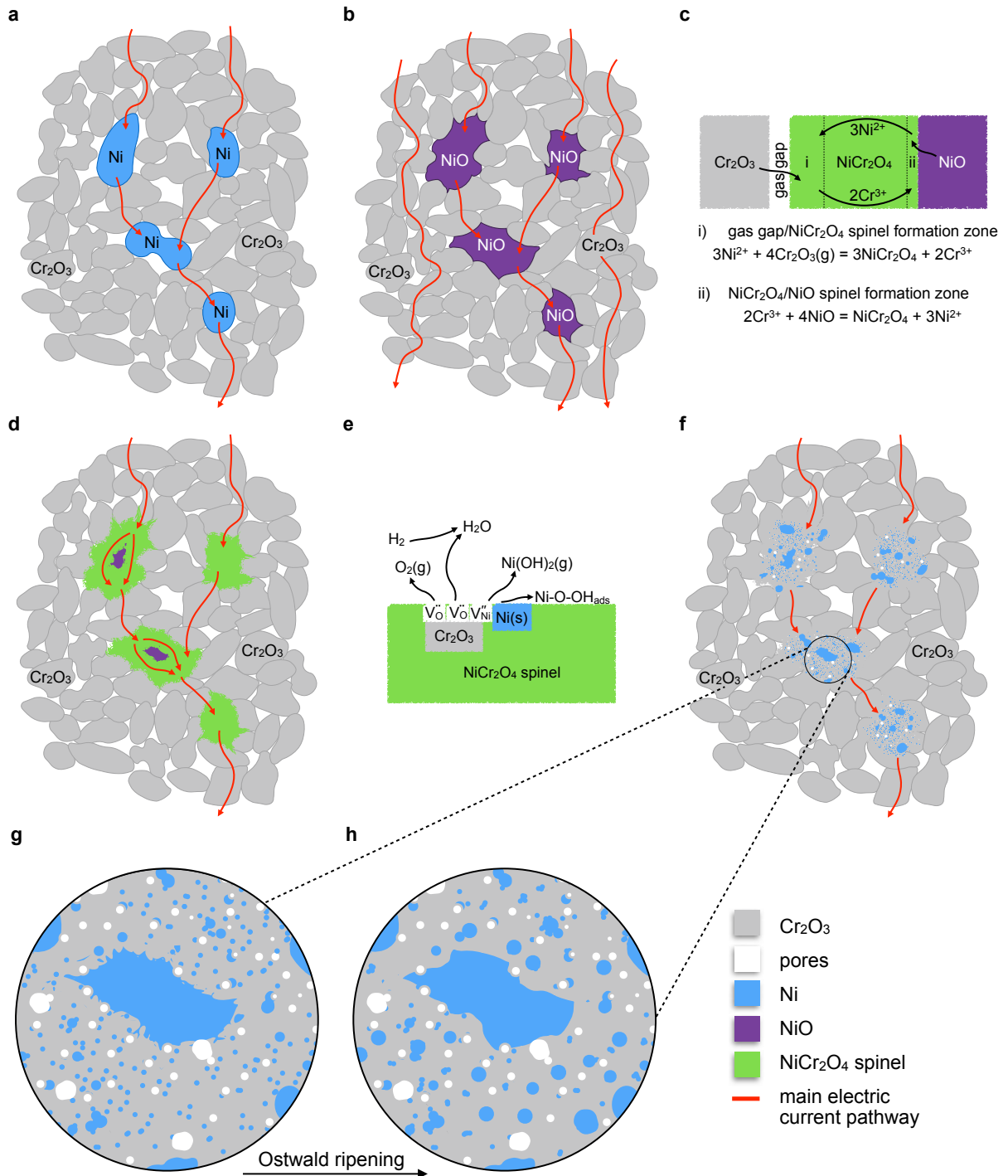
Fig. 5.51 Schematic illustration of microstructure changes during the evolution of the Ni containing Cr_2O_3 pellets under reducing, oxidizing and re-reducing conditions. a) initial microstructure at stage A with metallic Ni. b) NiO formed during change from f-gas to air at stage B. c) $NiCr_2O_4$ spinel formation mechanism [200, 201] during oxidation in air at stage C. d) Cr_2O_3 matrix with formed spinel and remaining NiO at the end of stage C. e) $NiCr_2O_4$ spinel decomposition mechanism during change from air again to f-gas at stage D. f) finely dispersed Ni after spinel decomposition at the beginning of stage E. g) and h) show the rearrangement and smoothing of small Ni particles during stage E by Ostwald ripening.

the defect mechanism might be related to an oxygen release accompanied by the formation of oxygen vacancies [87, 203, 206]

$$O_O \;=\; V_O^{\bullet\bullet} + 2\,e' + {}^1\!/_2\,O_2. \tag{5.13}$$
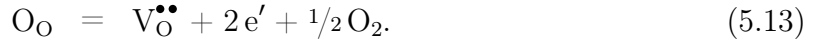
These very low p_{O_2} can also be observed under typical SOFC stack operation conditions on the anode side ($p_{O_2} < 10^{-14}$ bar, see Fig. 4.14). Park and Natesan [87] investigated the electrical conductivity of thermally grown Cr_2O_3 for temperatures below 1000 °C and for p_{O_2} near the decomposition pressure of Cr_2O_3 ($p_{O_2} < 10^{-24}$ bar) in a gas-tight cell. They only found a gradual decrease of electrical conductivity with decreasing oxygen partial pressure.

At the investigated temperatures below 950 °C the electronic defect concentration is assumed to be small, which indicates that the electrical conductivity of Cr_2O_3 is essentially influenced by impurities [88, 140, 164, 168, 188, 194, 202, 203, 206]. Impurities are side effects, which cannot be prevented neither in compacts produced in the laboratory nor in thermally grown oxide scales. A proposed defect mechanism for impurities is given by [88, 203]

$$2\,AO + {}^1\!/_2\,O_2 \;=\; 2\,A'_{Cr} + 3\,O_O + 2\,h^{\bullet} \tag{5.14}$$
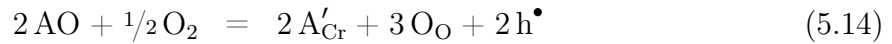
where A represents an impurity atom. However, for oxide layers formed on metallic interconnects during SOFC stack operation, such impurities are highly beneficial since they decrease the ohmic resistances. Overall, it must be emphasized that the defect structure of Cr_2O_3 is difficult to determine experimentally [204] and is only considered on a theoretical basis in this discussion.

The relatively high σ_{eff} of the Cr_2O_3-0 pellets (see Fig. 5.49) is on the one hand related to the microstructure as discussed above and on the other hand to the incorporation of different types of defects, which result in different defect densities in the Cr_2O_3 matrix. This defect incorporation can be associated to the sinter condition due the fact that the Cr_2O_3-0 pellets were sintered in air at 1585 °C whereas the Cr_2O_3 pellets with Ni ≥ 0.5 vol.% were sintered in reducing hydrogen atmosphere at 1400 °C. Dependencies of the electrical properties of Cr_2O_3 compacts on the sintering conditions also have been reported by Young et al. [205]. Note that σ_{eff} most probably is affected by a superposition of both microstructure and defect effects. Since the influence of varying sinter conditions and its effect on the porosity and hence electrical conductivity is not specifically addressed in this work the absolute deviations of σ_{eff} between the Cr_2O_3-0 and the Ni containing pellets are not discussed. Instead the observed behavior for the Cr_2O_3-0 pellets is used

as a reference to explain the response in the electrical conductivity during atmosphere changes.

Electrical conductivities at stage B during change from reducing to oxidizing atmosphere

Microstructure effects   Another aspect that influences σ_{eff} of the Cr_2O_3 pellets is related to the oxidation of metallic Ni into NiO at a given temperature in air. Ni reacts with gaseous oxygen to form NiO on the surface of the original Ni particles. A high defect concentration in the NiO crystal lattice promotes a fast and complete oxidation of Ni at 850 °C [37]. This transformation of Ni to NiO leads to an alteration of the microstructure, which is schematically illustrated in Fig. 5.51b. The oxide tends to fill the pores in the vicinity of the original Ni particles, since the formation of NiO comes along with a significant volume increase of 69.9 % [207].

The electrical conductivity of NiO is significantly smaller compared to that of metallic Ni [192, 208, 209] (cf. Table 5.10). Therefore, it can be ruled out that the observed fast increase in σ_{eff} during stage B is related to the formation of NiO. As pointed out above, NiO has a much lower electrical conductivity than Ni which results in a decrease of the overall conductivity of the pellet, if the effective conductivity is dominated by charge transport in the Ni phase. Such a decrease in σ_{eff} can be clearly identified in Fig. 5.41 for one of the Cr_2O_3-20 pellets. This pellet already showed in f-gas a more than three times higher σ_{eff} compared to the other one with the same Ni amount. The decreasing conductivity during stage B/beginning of stage C for one sample with 20 vol.% Ni can thus be attributed to a loss of percolation in the Ni phase upon transformation of Ni into NiO.

This transformation results in well pronounced transitions of σ_{eff} within 0.5 h after switching to air. However, this identified Ni oxidation time differs from those given in literature [214, 215] for the following reasons: the admixed Ni with $r_{50} = 5.5\,\mu m$ contains

Table 5.10 Summary of electrical conductivities of the various phases.

material	$\sigma\ /\ \text{S\,cm}^{-1}$
CFY [191]	7900
Cr_2N [210, 211]	> 11 000
Cr_2O_3 at 850 °C [87, 91, 164, 168, 194, 199]	< 0.1
Ni at 0 °C [192]	> 100 000
$NiCr_2O_4$ at 850 °C [212]	0.63
NiO at 850 °C [208, 213] and at 1000 °C [209]	0.1

also some smaller Ni particles, which results in faster complete oxidation. The observed behavior for the Cr_2O_3-20 pellet can be related to a superposition of Ni oxidation and the initial $NiCr_2O_4$ spinel formation, which provides new preferred electrical current pathways along the spinel phase, see Fig. 5.51d.

Electrical conductivity of Cr_2O_3 matrix σ_{eff} behavior during switching from f-gas to air is shown in Figs. 5.40 and 5.41. This change of gas atmosphere results in a fast and significant increase of σ_{eff} during stage B followed by a slower, exponential increase in stage C (discussed in the following section). The degree of conductivity change in stage C clearly correlates with the Ni content, whereas in stage B this correlation is not clear. The sharp increase of σ_{eff} in stage B can be assigned to the increase of the extrinsic electrical conductivity of the Cr_2O_3 matrix at higher oxygen partial pressure [87, 169]. This effect should be largely independent from the Ni content. Suppose the defect structure is described according to Eq. (5.12) thermodynamic equilibrium then yields to the relation

$$\sigma \propto p_{O_2}^{3/16} \tag{5.15}$$

i. e. the electrical conductivity σ is proportional to the oxygen pressure by the power of $3/16$ [87, 164, 188, 189, 216]. If impurities are involved thermodynamic equilibrium for Eq. (5.14) would yield to [88]

$$\sigma \propto p_{O_2}^{1/8}. \tag{5.16}$$

For n-type defects in low p_{O_2} atmospheres as described in Eq. (5.13) the following pressure dependence is obtained [204]

$$\sigma \propto p_{O_2}^{-1/6}. \tag{5.17}$$

In this case the electrical conductivity decreases due to the negative exponent. In this study, the p_{O_2} dependency was not established on a quantitative level, since conductivity measurements were not performed under systematic p_{O_2} variations, but only at two levels (either air or f-gas).

Electrical conductivities at stage C in oxidizing atmosphere

A continuous increase of σ_{eff} can be observed for the Ni containing pellets in the oxidizing air environment from Figs. 5.38 and 5.39. This is even more pronounced in Fig. 5.52 where the relative increase of σ_{eff} is plotted as a function of time. This demonstrates that the relative increase of σ_{eff} is increasing with the Ni amount. The strong deviations between the two Cr_2O_3-20 samples can be explained by the fact that at 20 vol.% Ni the
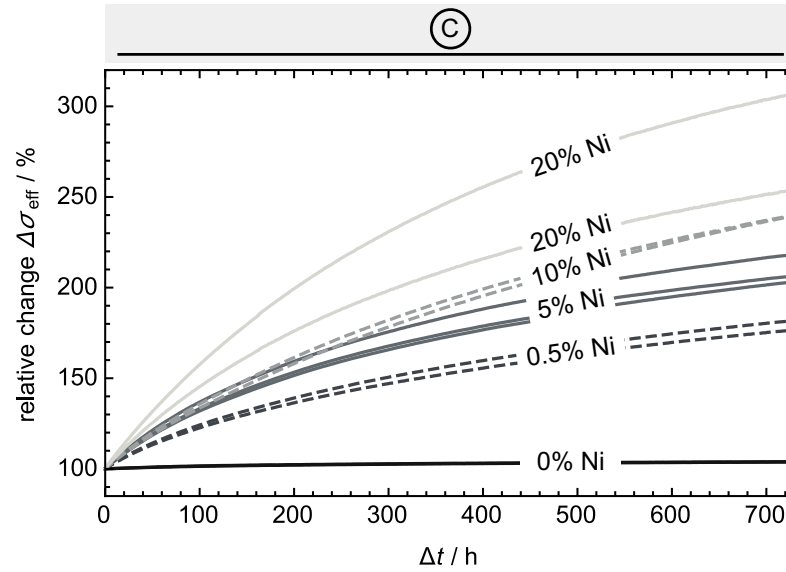
Fig. 5.52 Relative increase of electrical conductivity σ_{eff} during oxidation in air at 850 °C for all tested samples. For better comparison of the relative changes in σ_{eff} the starting point was defined several hours after the switch to oxidizing atmosphere.

percolation limit is reached.

Microstructure effects The improvement of σ_{eff} for the Ni containing pellets can be related to the formation of $NiCr_2O_4$ spinel as shown in Fig. 5.51d. The electrical conductivity of $NiCr_2O_4$ is higher compared to those of Cr_2O_3 and NiO [212, 213] (cf. Table 5.10). As a consequence a higher Ni content leads to more pronounced formation of $NiCr_2O_4$ spinel and therefore also to a stronger increase of σ_{eff}. Electrical conductivity in the spinel phase is generally explained by electron hopping and by the associated changes in the valence state of Cr. The formation of $NiCr_2O_4$ spinel at the expense of metalic Ni could be verified by XRD as shown in Figs. 5.46b and 5.47a. In the same XRD patterns some remnants of NiO could also be identified. Based on this observation it becomes evident that the spinel formation is not completed within the investigated period of about 900 h. However, based on the available data it can be estimated that the asymptotic behavior for σ_{eff} would be achieved within additional 500 h of exposure to air.

Fig. 5.51c illustrates the mechanism of spinel formation, which is initiated at the interface beween Cr_2O_3 and NiO phase according to

$$Cr_2O_3 + NiO = NiCr_2O_4. \tag{5.18}$$

After the initial formation of a first spinel phase between Cr_2O_3 and NiO the subse-

quent spinel formation takes place at the two new interfaces (i.e. $Cr_2O_3/NiCr_2O_4$ and $NiCr_2O_4/NiO$). As a consequence, further spinel formation depends on ionic counter diffusion within the spinel. A schematic illustration of the spinel formation mechanism within the Cr_2O_3 matrix is given in Fig. 5.51c [200, 217]. Cr_2O_3 is transported via the gas phase (e.g. by $CrO_3(g)$ and/or $CrO_2(OH)_2(g)$ [218]) to the reaction zone at the $NiCr_2O_4$ spinel interface [200, 201, 219]. Gas phase transport is more likely since the contact between Cr_2O_3 and $NiCr_2O_4$ is imperfect, i.e. at best there exist some isolated contact areas [219]. The reaction at the $Cr_2O_3/NiCr_2O_4$ interface can be written as

$$3\,Ni^{2+} + 4\,Cr_2O_3(g) \;=\; 3\,NiCr_2O_4 + 2\,Cr^{3+}. \tag{5.19}$$
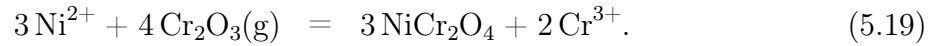
A similar reaction occurs at the opposing $NiCr_2O_4/NiO$ interface where the spinel is formed by

$$2\,Cr^{3+} + 4\,NiO \;=\; NiCr_2O_4 + 3\,Ni^{2+}. \tag{5.20}$$
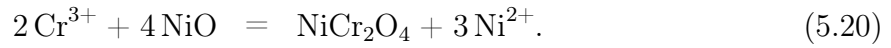
Based on the ionic counter diffusion that follows from the reaction mechanism given by Eqs. (5.19) and (5.20) it is expected that the spinel formation at the $Cr_2O_3/NiCr_2O_4$ interface is about three times higher compared to that at the $NiCr_2O_4/NiO$ interface [201]. Note also that the replacement of NiO by Ni can lead to local pore formation, as shown in Fig. 5.44h.

The increase of σ_{eff} during stage C in Figs. 5.38 and 5.39 shows an exponential behavior for the Ni containing pellets. This phenomenological observation is related to the diffusion controlled $NiCr_2O_4$ spinel formation where the increase in the length of ionic pathways correlates with the degree of spinel formation and associated grain size as illustrated in Fig. 5.51c. As a consequence of this increased transport length it is proposed that spinel formation exhibit a parabolic behavior [200, 219–221], which is in good agreement with the slightly sub-parabolic behavior of σ_{eff} observed in Figs. 5.38 and 5.39.

Electrical conductivity of Cr_2O_3 matrix   The experimental results for the evolution of σ_{eff} of Ni containing Cr_2O_3 pellets are presented in Figs. 5.38 and 5.39. In addition, Fig. 5.52 shows the relative increase of σ_{eff} upon exposure to air for all investigated samples. The figure illustrates that the increase is more pronounced for samples with higher Ni contents. For Ni free pellets the increase of conductivity during stage C is rather small but steady. This conductivity gain might be related to the fact that the equilibrium state of vacancies in Cr_2O_3 according to Eq. (5.12) was not yet reached until this stage.

Electrical conductivities at stage D during change from oxidizing to reducing atmosphere

Microstructure effects During stage D, the initial decrease in σ_{eff} of the Cr_2O_3 pellets with Ni content ≥ 5 vol.% is followed by a significant increase in σ_{eff} over a short period of about 5 h. After reaching a maximum electrical conductivity at the end of stage D it follows again a slow decrease during stage E. The required time span of about 5 h to reach the maximum is identical in both batches. Note that the temporary maximum in σ_{eff} correlates with the amount of Ni, i.e. a higher amount of Ni leads to a more pronounced increase of σ_{eff} by up to two orders of magnitudes. This increase of σ_{eff} is attributed to the formation of metallic Ni due to the decomposition of $NiCr_2O_4$ under reducing atmospheres for $p_{O_2} < 10^{-14}$ bar at 850 °C [129, 222]. The $NiCr_2O_4$ spinel decomposition in the applied f-gas atmosphere is given by

$$NiCr_2O_4 + H_2 = V_{Ni}'' + V_O^{\bullet\bullet} + 2\,Cr_{Cr} + 3\,O_O + Ni + H_2O. \qquad (5.21)$$
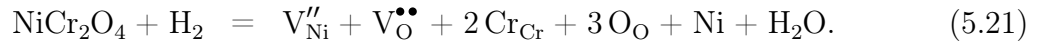
An illustration of the possible $NiCr_2O_4$ spinel decomposition mechanisms is shown in Fig 5.51e. Note that NiO formation as an interim stage is unlikely since the equilibrium partial pressure for NiO at 850 °C is in the order of 10^{-13} bar, which is above the $NiCr_2O_4$ spinel decomposition pressure [222]. However, based on the available experimental data the spinel decomposition mechanism is plausible but can not be proven to be correct. It is also possible that Ni is transported by evaporation and condensation of volatile nickel(II)-hydroxide ($Ni(OH)_2$), adsorption, surface diffusion or a combination of these mechanisms [57, 223]. Independent from those mechanisms, the complete reduction of Ni could be proven by XRD analysis, as shown in Fig. 5.47b. The XRD pattern in Fig. 5.47b originates from the Cr_2O_3-20 sample removed after 12 h, re-reduction in f-gas atmosphere, i.e. after reaching the maximal σ_{eff} (cf. Fig. 5.43).

In summary, it is proposed that the observed increase of σ_{eff} during stage D is related to the release of Ni during $NiCr_2O_4$ spinel decomposition. Thereby the released Ni builds a, at least partly, percolating metallic network that promotes the transport of electrons within the Cr_2O_3 pellets as illustrated in Figs. 5.51f and 5.51g. Further evidence for Ni percolation was found for the Cr_2O_3-20 pellets during cool down. Thereby, a further increase in σ_{eff} could be observed with decreasing temperature and vice versa during re-heating. Such a behavior is typical for metallic conductors. Note also that, temperature variations in air (i, e. T var 5 and 6 at stage C) did not show an increase in σ_{eff} with decreasing temperature (cf. Table 5.8).

Electrical conductivity of Cr$_2$O$_3$ matrix The results for the evolution of σ_{eff} during the transition from air to f-gas are shown in Figs. 5.42 and 5.43 for the first and second batch, respectively. Note that all Cr$_2$O$_3$ pellets show an instant decrease of their σ_{eff}. This can be well explained by the extrinsic p_{O_2} dependency of the electrical conductivity of the Cr$_2$O$_3$ matrix as discussed above. This means that lowering the p_{O_2} also leads to lower electrical conductivity.

Electrical conductivities at stage E during re-reduction in forming gas atmosphere

Microstructure effects Superimposed on the re-equilibration of the Cr$_2$O$_3$, there is a more pronounced effect on conductivity, which largely correlates with the Ni content. It can be assumed that for the Ni containing pellets the decrease in σ_{eff} is influenced by changes in the microstructure of the metallic Ni phase. The post test analyses in Figs. 5.44f and 5.44i illustrate that Ni is more finely dispersed after oxidation and re-reduction compared to the initial particle distribution shown in Figs. 5.44d and 5.44g. Furthermore the Cr$_2$O$_3$-20 pellets removed after the spinel decomposition in stage E confirm that the metallic Ni forms a partly percolating matrix that dominates the observed σ_{eff} of the pellet. Hence the continuous decrease of σ_{eff} during stage E is probably related to the disconnection of the Ni network. The reason is that the well dispersed Ni after spinel decomposition as shown in Fig. 5.45a tends to minimize its surface free energy known as the Ostwald ripening [37, 224]. Thereby enlarged Ni agglomerates are formed by a condensation-evaporation mechanism [224], which decreases the connectivity of the Ni network. This process goes along with a smoothing of the edges of the Ni particles as seen in Fig. 5.45b compared with Fig. 5.45a. The mechanism of Ostwald ripening is schematically illustrated in Figs. 5.51g to 5.51h.

The corresponding relative decrease of σ_{eff} is shown in Fig. 5.53. Interestingly there is a clear correlation between the Ni content and the relative decrease of σ_{eff}. As expected, Cr$_2$O$_3$-0 and Cr$_2$O$_3$-0.5 pellets show similar behaviors with the lowest relative decrease followed by the Cr$_2$O$_3$-5 and Cr$_2$O$_3$-10 pellets. The Cr$_2$O$_3$-20 pellets shows a relative decrease similar to the Cr$_2$O$_3$-5 pellets. Obviously the percolating network of this Cr$_2$O$_3$-20 pellets is still intact and only sparsely effected by the Ostwald ripening, respectively.

Electrical conductivity of Cr$_2$O$_3$ matrix During re-reduction in f-gas atmosphere a continuous decrease in σ_{eff} can be observed in Figs. 5.38, 5.39 and 5.53 for all samples. The continuous decrease of σ_{eff} for the Cr$_2$O$_3$ pellets without Ni can be explained by
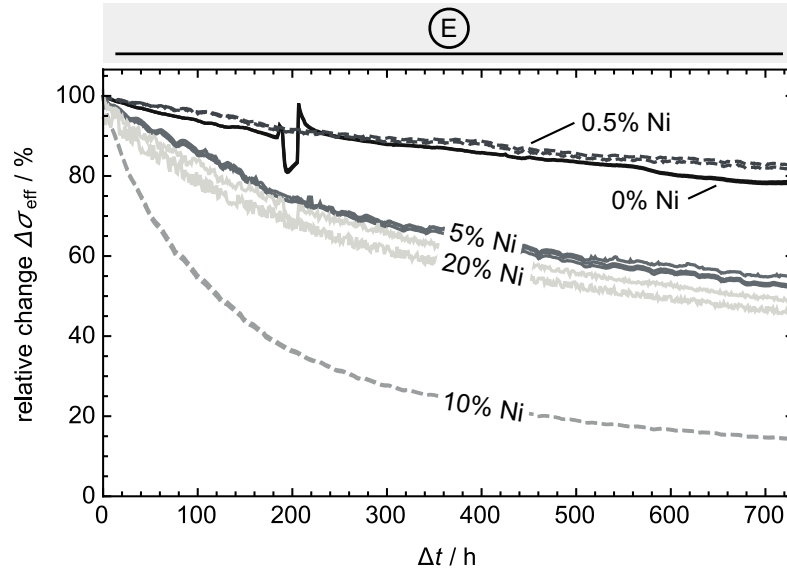
Fig. 5.53 Relative decrease of electrical conductivities σ_{eff} of Ni containing Cr_2O_3 pellets during re-reduction in f-gas at 850 °C.

a successive approximation to the equilibrium state. This is confirmed by the Cr_2O_3-0 pellets, which at the end of stage E return to σ_{eff} values that are close to the initial values.

Effect of humidity on electrical conductivity

σ_{eff} is further affected by the humidification of the atmosphere. The results in Table 5.8 show that σ_{eff} is increased when 3–4 vol.% of water are added to f-gas and H_2 compared to the respective dry conditions. This behavior can be observed for all Cr_2O_3 pellets except for those without Ni in H_2 where humidification does not affect σ_{eff}. The mechanisms behind this behavior is not completely clear [117]. It is assumed that this behavior is simply related to variations of p_{O_2} and its influence on the conductivity of Cr_2O_3. From the measured Nernst potential it can be concluded that for dry forming gas atmosphere the oxygen partial pressure is about three orders of magnitudes lower compared to humidified atmosphere. In hydrogen the p_{O_2} is increased by nearly 2 orders of magnitudes when 3–4 vol.% of water are added. Based on these differences, it is likely that the Cr_2O_3 pellets feature a p-type behavior under tested conditions, where increasing oxygen pressure increases σ_{eff}. This increase of σ_{eff} can be associated to the defect structure or more precisely to the concentration of electron holes, see Eq. (5.12).

Note however that σ_{eff} of the Cr_2O_3-20 pellets after stage E shows a deviating behavior since the electron transport is dominated by the partly percolating Ni network. Consequently σ_{eff} is decreased with increasing temperature and vice versa. Interestingly, for

samples with 20 vol.% Ni, σ_{eff} in humidified f-gas is lower than in dry f-gas. However, with increasing temperature this difference becomes smaller. This behavior can be attributed to an increased volatility of $Ni(OH)_2$ in humidified atmospheres, which leads to agglomeration and de-percolation of Ni and associated loss of σ_{eff}. The fact that this difference of σ_{eff} becomes smaller with increasing temperature can be attributed to the semi-conductive behavior of the Cr_2O_3 matrix, which increases with temperature and hence becomes more dominant. To prove this hypothesis however further dedicated experimental work is required.

Thermal activation energy E_A

For dry f-gas, the thermal E_A was determined from the Arrhenius plot as shown in Fig. 5.49a. For all other conditions they are summarized in Table 5.9 and in Figs. A.7 to A.10 in A.3. Inspection of the thermal E_A reveals that it is reduced with increasing p_{O_2}. In particular the thermal E_A is reduced in humidified atmospheres, since the water content increases the oxygen partial pressure. Note also that the obtained values for the thermal E_A of Cr_2O_3 in air (0.187–0.264 eV) are in good agreement with data available from the literature [206, 225].

The thermal E_A of the Cr_2O_3-20 pellets at the end of stage E is dominated by the percolating Ni network. As a consequence the determined thermal E_A become negative with values of −0.064 eV and −0.078 eV, which is characteristic for metallic conductors. The extracted E_A values in dry f-gas atmosphere are smaller compared to those determined under humidified conditions. This might also be attributed to the progressive dis-percolation of the Ni network as described in the previous section.

5.4.4 Conclusions

This section focuses on the interaction between Cr_2O_3 and Ni and on the associated variation of the electrical conductivity. These issues are related to long-term degradation phenomena, which occur on the anode side in SOFC stacks. Thereby Cr_2O_3 scales with enclosed Ni are typically formed on the metallic interconnects. Such a mixed oxide scale is shown by a representative SEM cross section image obtained after 40 000 h stack operation in Fig. 5.35.

Under reducing anode conditions (f-gas, stage A) the conductivity is mainly dominated by the properties of Cr_2O_3 (i.e. defect concentration and impurities). However, in samples with a Ni content of 20 vol.%, local percolation pathways are formed within the Ni

phase, which leads to elevated conductivities and a metallic behavior of conductivity upon temperature variations.

When changing to oxidizing conditions (air, stage B) there is first a fast response of the Cr_2O_3 material, which can be attributed to a thermodynamic re-equilibration including adaptations in the vacancy concentrations. This re-equilibration with the p_{O_2} leads to a fast and significant increase of the conductivity. In a second step, there is also a more sluggish response (stage C), which is related to spinel formation ($NiCr_2O_4$) at the expense of Ni and Cr_2O_3. The sluggish spinel formation leads to a exponential evolution of the electric conductivity. The conductivity that is finally reached upon complete transformation of Ni into $NiCr_2O_4$ spinel correlates with the total Ni content of the sample.

When changing back to reducing conditions (stages D and E), there are three main processes observed. First, a fast thermodynamic re-equilibration (with p_{O_2} dependent vacancy concentrations) leads to a drop in conductivity (at the beginning of stage D). Second, the decay of spinel and the associated formation of Ni is somewhat slower than the thermodynamic equilibration. It leads again to a temporary increase of the conductivity. The maximum conductivity that is temporarily reached correlates with the Ni content (end of stage D). Third, on a longer term, the newly formed Ni particles are reorganized during an extended period of up to $1000\,\mathrm{h}$ (stage E). The coarsening and the associated loss of percolation lead to a slow decrease in conductivity. Nevertheless, even at long reduction times (in stage E) the conductivity remains above the initial values (in stage A). This can be explained by the fact the Ni is now more finely dispersed due to a microstructure reorganization that is associated with the formation and decay of $NiCr_2O_4$ spinel.

The present investigation is considered as a basis for better interpretations of ohmic resistances occurring in SOFC stacks with metallic interconnects and with Ni containing anodes. In particular, the results indicate that at least $10\,\mathrm{vol.\%}$ of Ni is required within the Cr_2O_3-scales, in order to change the electrical properties from semi-conductive Cr_2O_3 into a metallic behavior of a (partially) percolating Ni network. Based on these findings further studies should focus on methods to increase the amount of metallic particles in thermally grown oxide scales to decrease ohmic losses at the metallic interconnect interfaces.

<div align="right">

Chapter **6**

</div>

Summary and Outlook

6.1 Summary

SOFCs are able to convert chemical energy into electrical current. This direct fuel conversion hopefully will be a relevant technology within the forward-looking energy strategies in Europe and other parts of the world. However the fuel cell stack degradation is still one of the most relevant technical issues specially for a successful commercialization of stationary fuel cell applications e. g. to continuously provide heat and power to single-family homes. Therefore, this work focused on the establishment of new methods to combine stack and laboratory experimental data with models to assess and subsequently reduce the degradation behavior of SOFC stacks. In particular, the developed methods and models allow one to:

- quantify and understand the complex degradation behavior of metallic interconnects (as major contribution to the overall SOFC stack degradation) caused by oxide scale growth under reducing and oxidizing conditions

- more reliable assess SOFC stack degradation based on current-voltage data

- extract internal stack resistances from current-voltage data to allow for direct comparisons with dedicated laboratory experiments of single degradation phenomena

As pointed out, one important degradation mechanism in SOFC stacks deals with the oxide scale formation on metallic interconnects under both reducing and oxidizing conditions. For an in-depth investigation of their behavior oxide scales were quantified based on a large amount of SEM image data and subsequently correlated with the resistances obtained from measuring effective electrical conductivities of the investigated MIC samples.

Chapter 6. Summary and Outlook

This study includes unique samples obtained from a Hexis SOFC stack that was operated for 40 000 h with CPOx reformed natural gas at about 900 °C. It turns out that the oxide scale formation in particular on the anode side follows rather a time depending sub-parabolic behavior instead of the widely accepted parabolic behavior according to Wagner's law. In contrast the increase of ohmic resistance obtained from electrical conductivity measurements on LSM coated CFY samples exposed to air follows an over-parabolic function. This observed non-linear relation between oxide scale formation and resulting ohmic resistances can be associated with the morphology of the thermally grown oxide scales. For a quantitative investigation of how the scale morphology influences the overall resistance FE simulations of the local electrical currents were performed using the scale morphologies as input. With this combined experimental-modeling approach a time dependent morphology factor could be extracted, which convincingly explains the relation between mean oxide scale formation and resulting overall resistance.

The developed methodical approach could be successfully transfered to the specific scale formation conditions on the anode side i. e. under reducing conditions and in the presence of Ni. It turned out that Ni particles incorporated into the oxide scale originally released from Ni-mesh and/or applied metallic coatings have a significant influence on the electrical current pathways. In particular, the Ni particle promote transversal electrical currents that reduce the overall ohmic losses. This behavior is even more pronounced at locations with inadequate contacts between the employed current collector mesh and the oxide scale and between the oxide scale and the interconnect, respectively. Such inadequate contacts can originate from pores, cracks and from the unavoidable cavities in the Ni-mesh. Additional FE simulations of local electrical currents allowed us to quantify the impact of metallic bridges across the oxide scale as they typically occur on spot welded Ni-meshes. The influence of such metallic bridges is limited to a small surrounding and depends on the scale thickness and bridge diameter. The result of these simulations were summarized in diagrams to provide design guidelines for stack developers.

To further investigate the influence of the size and arrangement of Ni particles located within the oxide scale a comprehensive test series was realized with sintered Cr_2O_3 pellets admixed with different amounts of Ni. Electrical conductivity were performed using a four point probe setup in reducing and oxidizing atmospheres at 850 °C. In addition, comprehensive post test analyses were realized using BIB sample preparation for SEM, XRD and AFM measurements. Based on these profound data set it was possible to identify the responsible phenomenological processes and phenomena on a microscopic level. It turned out that the observed conductivity behavior is related to $NiCr_2O_4$ spinel formation during

oxidation and to the $NiCr_2O_4$ spinel decomposition during reduction in atmospheres with low oxygen partial pressures, respectively. These proven phase conversions lead to an finer dispersion of Ni particles within the Cr_2O_3 phase and consequently to improved electrical conductivity behavior.

Furthermore, the model introduced in chapter 4 allows a reliable quantification and interpretation of the degradation of SOFC stacks based on (V,I)-data. Such interpretations are crucial for SOFC stacks operating in the field where more comprehensive testing methods such as EIS are usually not available. In this cases the degradation behavior is usually analyzed by computing the slopes of (V,I)-curves as a function of time. These slopes correspond with the overall ASR of one or several stack repeat units (RUs). However, the proposed model permits a reliable extraction of the true internal RU resistances from (V,I)-data considering often unavoidable fluctuations in the fuel gas amount and composition. Compared with the overall resistances, ASR_{RU} is more meaningful measure of the "true" stack degradation behavior. ASR_{RU} extracted by the model at different time steps can further be compared with the sum of the time-dependent ASRs of the electrolyte, the electrodes, the interconnect and their mutual interfaces. Since the degradation behavior of single components are usually obtained under accurately defined laboratory conditions the presented method allows one to make a direct link between laboratory degradation experiments and the related behavior of SOFC stacks under field operation conditions.

6.2 Outlook

The presented work focused on the establishment of new methods to combine stack and laboratory experimental data with models to assess and subsequently reduce the main sources for SOFC stack degradation. In particular, further insight into degradation phenomena, which are related to the oxide scale formation onto metallic interconnects was provided. The improvement of applied materials and therewith associated operation reliability is imported for the intended commercialization of SOFC systems. The following list provides recommendations for future research activities, which I believe will be useful for both, bringing forward the understanding of degradation phenomena and appropriate measure for their avoidance.

- Electrical current should be supplied during heat exposure experiments with MIC samples. It has been demonstrated that oxide scale formation is influenced by electrical current and even by its direction [157, 158]. The later one should be taken into account for any post test analyses.

- Heat exposure experiments with MIC samples should be carried out in furnaces, which provide dual gas atmospheres. Recently published results confirm that hydrogen permeability through the interconnect material from the fuel to the air side influences the oxide scale formation and growth rate on the cathode side [151, 226, 227].

- A comprehensive investigation of the impact of metallic coatings applied to Cr based interconnect materials such as CFY would be useful. Such an investigation should also clarify if metallic coatings are able to form a sufficient amount of metallic bridges as reported by Mikkelsen et al. [185]. Beside Ni containing coatings other potentially suitable materials such as ceria based coatings should be considered in further investigations [181].

- In the presented image data a large number of pores and cracks can be observed along the oxide scales. Since pores provides a infinite high ohmic resistance it is obvious that they should be avoided. As a consequence, further insight about the applied material combination and their interaction during oxide scale formation in SOFC stacks are crucial for further durability improvement. This must also include the stack operating conditions and strategies, as for example humidified air improves the scale adherence [115, 228].

- Analogous to the investigated interaction of Ni particles with Cr_2O_3 it would be interesting to investigate the interaction of the formed oxide scale with other metallic particles as for example with Mn. The results in section 5.1 demonstrate that interaction between the LSM coating and the adjacent Cr_2O_3 scale lead to $(Mn,Cr)_3O_4$ spinel formation. $(Mn,Cr)_3O_4$ spinel provides an electrical conductivity that is an order of magnitude higher compared to Cr_2O_3 [164, 229].

- Since Cr_2O_3 adjacent to NiO forms $NiCr_2O_4$ in oxidizing atmosphere it seemed obvious that this mechanism also would have a positive impact on the MIC resistance on the cathode side. This can also be implied from the results reported by Nagai et al. [164] where already small amounts of NiO dissolved in Cr_2O_3 show a significant improved electrical conductivity.

- In addition to the classic DC measurements of metallic interconnect resistances analyzing the formed oxide scales by electrical impedance spectroscopy could provide further insights into the responsible mechanism [230, 231].

- It would be of further interest to validate the reliability of the model introduced in chapter 4 with experimental data from SOFC stacks made of anode supported cells operated with steam reformed natrual gas.

List of Figures

List of Figures

List of Figures

156

List of Tables

Bibliography

[1] S. Selosse, O. Ricci, and N. Maïzi. "Fukushima's impact on the European power sector: The key role of CCS technologies." In: *Energy Econ.* 39 (2013), pp. 305–312.

[2] Bundesrat, Swiss Federal Office of Energy SFOE, and U. Generalsekretariat. *Bundesrat legt Energiestrategie 2050 als indirekten Gegenvorschlag zur Atomausstiegsinitiative vor.* 2013. URL: http://www.uvek.admin.ch/dokumentation/00474/00492/index.html?lang=de%5C&msg-id=48168 (visited on 01/23/2015).

[3] C. Kost et al. *Stromgestehungskosten Erneuerbare Energien.* Tech. rep. Frauenhofer ISE, 2013.

[4] M. Lehner, R. Tichler, and M. Koppe. *Power-to-Gas: Technology and Business Models.* Springer, 2014.

[5] Viessmann Werke GmbH & Co. KG. *Storing excess power in the gas grid.* 2013.

[6] O. Z. Sharaf and M. F. Orhan. "An overview of fuel cell technology: Fundamentals and applications." In: *Renew. Sustain. Energy Rev.* 32 (2014), pp. 810–853.

[7] R. Frischknecht et al. *Strommix und Stromnetz.* Tech. rep. 6. Swiss Centre for Life Cycle Inventories, 2007.

[8] A. Mai et al. "Hexis' SOFC System Galileo 1000 N – Lab and Field Test Experiences." In: *ECS Trans.* 57.1 (2013), pp. 73–80.

[9] A. Weber and E. Ivers-Tiffée. "Materials and concepts for solid oxide fuel cells (SOFCs) in stationary and mobile applications." In: *J. Power Sources* 127.1-2 (Mar. 2004), pp. 273–283.

[10] V. Sauchuk et al. "Influence of protective layers on SOFC operation." In: *Russ. J. Electrochem.* 47.5 (May 2011), pp. 522–530.

[11] K. Föger. "BlueGen for Europe – Commercialisation of Ceramic Fuel Cells ' residential SOFC Product." In: *Proc. 10th Eur. SOFC Forum.* Vol. A0503. June. 2012, A0518–A0524.

Bibliography

[12] A. Mai et al. "Progress in the Development of the Hexis' SOFC Stack and the Galileo 1000 N Micro-CHP System." In: *Proc. 10ᵗʰ Eur. SOFC Forum*. Vol. A0403. 2012, A0420–A0427.

[13] A. Nanjou. "Commercialization of SOFC micro-CHP in the Japanese market." In: *Proc. 10ᵗʰ Eur. SOFC Forum*. Vol. A0202. 2012, A028.

[14] Q. Ma et al. "Anode-supported planar SOFC with high performance and redox stability." In: *Electrochem. Commun.* 12.10 (Oct. 2010), pp. 1326–1328.

[15] A. Buyukaksoy, V. Petrovksy, and F. Dogan. "Redox Stability of Ni-YSZ Cermets Prepared by Polymeric Precursor Infiltration." In: *ECS Trans.* 45.1 (Apr. 2012), pp. 509–514.

[16] T. J. Armstrong, M. Smith, and A. V. Virkar. "Oxidation Kinetics of Metallic Interconnects for Intermediate Temperature SOFC." In: *ECS Meet. Abstr.* #1155 (Feb. 2005).

[17] S. Benhaddad et al. "Evaluation of Selected Interconnect Alloys at Versa Power Systems: Laboratory Screening and In-Stack Testing Sofiane." In: *ECS Trans.* 7 (2007), pp. 2125–2133.

[18] A. A. Kulikovsky. *Analytical Modelling of Fuel Cells*. Elsevier, 2010.

[19] T. Hocker. *Brennstoffzellen*. Lecture Notes. 2007.

[20] *NIST Chemistry WebBook*.

[21] C. Rayment and S. Sherwin. *Introduction to Fuel Cell Technology*. Lecture Notes. 2003.

[22] R. O'Hayre et al. *Fuel Cell Fundamentals*. Wiley, 2009.

[23] J. Larminie and A. Dicks. *Fuel Cell Systems Explained*. J. Wiley, 2003.

[24] Y. Wang et al. "A review of polymer electrolyte membrane fuel cells: Technology, applications, and needs on fundamental research." In: *Appl. Energy* 88.4 (2011), pp. 981–1007.

[25] S. Mekhilef, R. Saidur, and A. Safari. "Comparative study of different fuel cell technologies." In: *Renew. Sustain. Energy Rev.* 16.1 (2012), pp. 981–989.

[26] S. C. Singhal and K. Kendall. *High-temperature Solid Oxide Fuel Cells: Fundamentals, Design and Applications*. 1ˢᵗ. Elsevier Science, 2003.

[27] M. R. Walluk et al. "Diesel auto-thermal reforming for solid oxide fuel cell systems: Anode off-gas recycle simulation." In: *Appl. Energy* 130 (2014), pp. 94–102.

[28] W. G. Bessler et al. "Model anodes and anode models for understanding the mechanism of hydrogen oxidation in solid oxide fuel cells." In: *Phys Chem Chem Phys* 12.42 (2010), pp. 13888–13903.

[29] S. Munira et al. "Recent fabrication techniques for micro-tubular solid oxide fuel cell support : A review." In: 35 (2015), pp. 1–22.

[30] T. Wen. "Material research for planar SOFC stack." In: *Solid State Ionics* 148 (2002), pp. 513–519.

[31] C. Yuan et al. "Fabrication of composite cathode by a new process for anode-supported tubular solid oxide fuel cells." In: *Electrochim. Acta* 149 (2014), pp. 212–217.

[32] *KERAFOL Keramische Folien GmbH*. 2015. URL: http://www.kerafol.com/sofc/komponenten-fuer-brennstoffzellentechnologie/elektrolytgetragene-zellen-esc.html (visited on 05/04/2015).

[33] *Shanghai Institute of Ceramics, Chinese Academy of Sciences (SICCAS)*. URL: http://www.siccas.com/SOFCTube1.htm (visited on 02/02/2015).

[34] Fraunhofer Institute for Ceramic Technologies and Systems IKTS. *Metallgetragene Zellen für die SOFC*.

[35] L. Blum et al. "Worldwide SOFC technology overview and benchmark." In: *Int. J. Appl. Ceram. Technol.* 2 (2005), pp. 482–492.

[36] F. Fleischhauer et al. "Failure analysis of electrolyte-supported solid oxide fuel cells." In: *J. Power Sources* 258 (2014), pp. 382–390.

[37] B. Iwanschitz. "Degradation von Ni-Cermet-Anoden in keramischen Hochtemperaturbrennstoffzellen." PhD thesis. Rheinisch -Westfälischen Technische Hochschule Aachen, 2012.

[38] M. C. Tucker. "Progress in metal-supported solid oxide fuel cells: A review." In: *J. Power Sources* 195.15 (2010), pp. 4570–4582.

[39] B. J. McKenna et al. "Advances in metal supported cells in the METSOFC EU consortium." In: *Fuel Cells* 13.4 (2013), pp. 592–597.

[40] S. P. Jiang and Y. Yan. *Materials for High-Temperature Fuel Cells*. 1st. Wiley-VCH Verlag GmbH & Co., 2013.

[41] R. Fernández-González et al. "A novel microstructured metal-supported solid oxide fuel cell." In: *J. Power Sources* 272 (2014), pp. 233–238.

Bibliography

[42] E. Ivers-Tiffée, A. Weber, and D. Herbstritt. "Materials and technologies for SOFC-components." In: *J. Eur. Ceram. Soc.* 21 (2001), pp. 1805–1811.

[43] D. Mason, K. Taylor, and D. G. Löffler. "Bench-Scale Propane Reformer." In: *Abstr. Pap. Am. Chem. Soc.* Vol. 224. 2002, U565–U565.

[44] M. Linder et al. "Automated, Model-Based Analysis of Uj-Data for Electrolyte-Supported SOFC Short-Stacks." In: *Fuel Cells* 11.4 (Aug. 2011), pp. 573–580.

[45] S. P. Simner et al. "SOFC Performance with Fe-Cr-Mn Alloy Interconnect." In: *J. Electrochem. Soc* 152 (2005), pp. 740–745.

[46] R. S. Gemmen, M. C. Williams, and K. Gerdes. "Degradation measurement and analysis for cells and stacks." In: *J. Power Sources* 184.1 (Sept. 2008), pp. 251–259.

[47] L. G. J. de Haart et al. "Stack Degradation in Dependence of Operation Parameters; the Real-SOFC Sensitivity Analysis." In: *Fuel Cells* 9.6 (Dec. 2009), pp. 794–804.

[48] J. Malzbender, R. W. Steinbrech, and L. Singheiser. "A review of advanced techniques for characterising SOFC behaviour." In: *Fuel Cells* 9.6 (Dec. 2009), pp. 785–793.

[49] C. Comminges et al. "Monitoring the degradation of a solid oxide fuel cell stack during 10,000 h via electrochemical impedance spectroscopy." In: *Electrochim Acta* 59 (Jan. 2012), pp. 367–375.

[50] E. Barsoukov and J. R. Macdonald. *Impedance Spectroscopy: Theory, Experiment, and Applications*. Wiley, 2005, pp. 1–595.

[51] Hexis AG. *Hexis AG*. URL: http://www.hexis.com (visited on 01/28/2015).

[52] A. Mai et al. "Hexis and the SOFC System Galileo 1000 N – past , present , future." In: *Proc. 11th Eur. SOFC SOE Forum* A0501 (2014), pp. 3–11.

[53] A. Mai et al. "Hexis and the SOFC System Galileo 1000 N: Experiences from Lab and Field Testing." In: *ECS Trans.* 68.1 (July 2015), pp. 109–116.

[54] M. Dold. "Modellbasierte Interpretation von elektrochemischen Impedanzspektren von Festoxid-Brennstoffzellen." MA thesis. Zurich University of Applied Sciences - ZHAW, 2015.

[55] R. Steinberger-Wilckens and L. Blum. "Overview of the development of solid oxide fuel cells at Forschungszentrum Juelich." In: *Int. J. Appl. Ceram. Technol.* 476.6 (Nov. 2006), pp. 470–476.

[56] O. M. Pecho et al. "3D Microstructure of Ni-YSZ anodes: Prediction of effective transport properties and optimization of redox stability." Manuscript submitted for publication to J. Am. Ceram. Soc. 2015.

[57] H. Yokokawa et al. "Fundamental mechanisms limiting solid oxide fuel cell durability." In: *J. Power Sources* 182.2 (Aug. 2008), pp. 400–412.

[58] J. W. Fergus. "Effect of cathode and electrolyte transport properties on chromium poisoning in solid oxide fuel cells." In: *Int. J. Hydrogen Energy* 32.16 (Nov. 2007), pp. 3664–3671.

[59] Forschungszentrum Jülich. *Degradation von SOFCs – Chromvergiftung.* URL: http://www.fz-juelich.de/iek/iek-1/DE/Forschung/Brennstoffzellen/Degradation_SOFC_Chromvergiftung.html (visited on 02/09/2015).

[60] F. Fleischhauer et al. "High temperature mechanical properties of zirconia tapes used for electrolyte supported solid oxide fuel cells." In: *J. Power Sources* 273 (Jan. 2015), pp. 237–243.

[61] J. W. Fergus. "Electrolytes for solid oxide fuel cells." In: *J. Power Sources* 162.1 (2006), pp. 30–40.

[62] S. (Hui et al. "A brief review of the ionic conductivity enhancement for selected oxide electrolytes." In: *J. Power Sources* 172 (2007), pp. 493–502.

[63] M. R. Terner et al. "On the conductivity degradation and phase stability of solid oxide fuel cell (SOFC) zirconia electrolytes analysed via XRD." In: *Solid State Ionics* 263 (2014), pp. 180–189.

[64] Y. Suzuki, A. Shimada, and S. Senda. "Time-dependent change in electrical resistivity of polycrystalline YSZ and CSZ." In: *Solid State Ionics* 42 (1990), pp. 121–125.

[65] Z. Yang et al. "Electrical contacts between cathodes and metallic interconnects in solid oxide fuel cells." In: *J. Power Sources* 155.2 (Apr. 2006), pp. 246–252.

[66] J. Wu and X. Liu. "Recent Development of SOFC Metallic Interconnect." In: *J. Mater. Sci.* 26.4 (2010), pp. 293–305.

[67] A. Mai. *Abschlussbericht, SOF-CH ESC.* Tech. rep. 2014.

[68] P. E. Gannon et al. "High-temperature oxidation resistance and surface electrical conductivity of stainless steels with filtered arc Cr-Al-N multilayer and/or superlattice coatings." In: *Surf. Coat. Tech.* 188-189 (Nov. 2004), pp. 55–61.

[69] S. Megel et al. "Area specific resistance of oxide scales grown on ferritic alloys for solid oxide fuel cell interconnects." In: *J. Power Sources* 196.17 (Sept. 2011), pp. 7136–7143.

[70] L. Kaufmann. "Thermo-mechanisches Verhalten von Brennstoffzellen." MA thesis. Zurich University of Applied Sciences - ZHAW, 2013.

[71] C. Wagner. In: *Z. phys. Chem.* 21.B (1933), p. 25.

[72] R. Steinberger-Wilckens. "European SOFC Technology – Status and Trends." In: *Proc. 12th Int. Symp. Solid Oxide Fuel Cells XII* 35.1 (2011), pp. 19–29.

[73] R. R. Mosbæk et al. "Electrochemical Characterization and Degradation Analysis of Large SOFC Stacks by Impedance Spectroscopy." In: *Fuel Cells* 13.4 (Aug. 2013), pp. 605–611.

[74] M. Lang et al. "Characterization of SOFC Short Stacks and Stacks for Mobile Applications." In: *ECS Trans.* 7.1 (2007), pp. 85–94.

[75] D. Perednis. "Solid oxide fuel cells with electrolytes prepared via spray pyrolysis." In: *Solid State Ionics* 166.3-4 (Jan. 2004), pp. 229–239.

[76] Y.-S. Chou, J. W. Stevenson, and J.-P. Choi. "Long-term evaluation of solid oxide fuel cell candidate materials in a 3-cell generic short stack fixture, part I: Test fixture, sealing, and electrochemical performance." In: *J. Power Sources* 255 (June 2014), pp. 1–8.

[77] J. F. B. Rasmussen, P. V. Hendriksen, and A. Hagen. "Study of Internal and External Leaks in Tests of Anode-Supported SOFCs." In: *Fuel Cells* 8.6 (Dec. 2008), pp. 385–393.

[78] L. D. Hinkle and C. F. Mariano. "Toward understanding the fundamental mechanisms and properties of the thermal mass flow controller." In: *J. Vac. Sci. Technol.* A 9.May/Jun (1991), pp. 2043–2047.

[79] C. Westner, M. Lang, and R. Geieregger. "Electrochemical Impedance Spectroscopy (EIS) of SOFC Short Stacks." In: *Proc. 9h Eur. SOFC Forum* B1015 (2010), pp. 114–120.

[80] B. Shaffer and J. Brouwer. "Dynamic Model for Understanding Spatial Temperature and Species Distributions in Internal-Reforming Solid Oxide Fuel Cells." In: *J. Fuel Cell Sci. Technol.* 9.4 (2012), p. 041012.

[81] M. Lang et al. "Investigation of solid oxide fuel cell short stacks for mobile applications by electrochemical impedance spectroscopy." In: *Electrochim. Acta* 53 (2008), pp. 7509–7513.

[82] R. R. Mosbæk et al. "A0902 Fuel flow distribution in SOFC stacks revealed by impedance spectroscopy." In: *Proc. 11th Eur. SOFC SOE Forum* A0902 (2014), pp. 14–22.

[83] S. Primdahl and M. Mogensen. "Gas Conversion Impedance: A Test Geometry Effect in Characterization of Solid Oxide Fuel Cell Anodes." In: *J. Electrochem. Soc.* 145.7 (1998), p. 2431.

[84] S. Primdahl and M. Mogensen. "Gas Conversion Impedance: SOFC Anodes in H_2/H_2O Atmosphers." In: *Proc. 5th Int. Symp. Solid Oxide Fuel Cells V (SOFC-V)* 97.18 (1997), pp. 530–537.

[85] A. Momma et al. "AC impedance behavior of a practical-size single-cell SOFC under DC current." In: *Solid State Ionics* 174.1-4 (Oct. 2004), pp. 87–95.

[86] B. Liu et al. "Electrical conductivity and molten salt corrosion behavior of spinel nickel ferrite." In: *Solid State Sci.* 13.8 (Aug. 2011), pp. 1483–1487.

[87] J. H. Park and K. Natesan. "Electronic transport in thermally grown Cr_2O_3." In: *Oxid. Met.* 33.1-2 (Feb. 1990), pp. 31–54.

[88] A. Holt and P. Kofstad. "Electrical conductivity and defect structure of Cr_2O_3. II. Reduced temperatures ($< 1000\,°C$)." In: *Solid State Ionics* 69 (1994), pp. 137–143.

[89] ThyssenKrupp VDM GmbH. *Crofer 22 H, Material Data Sheet No. 4050, June Edition*. 2010.

[90] Plansee SE. *Plansee SE*. 2014. URL: http://plansee.com/en/CFY-1484.htm (visited on 07/07/2014).

[91] P. Huczkowski et al. "Growth Mechanisms and Electrical Conductivity of Oxide Scales on Ferritic Steels Proposed as Interconnect Materials for SOFC's." In: *Fuel Cells* 6.2 (Apr. 2006), pp. 93–99.

[92] M. Stanislowski et al. "Reduction of chromium vaporization from SOFC interconnectors by highly effective coatings." In: *J. Power Sources* 164.2 (Feb. 2007), pp. 578–589.

[93] T. F. Petersen. "A Zero-Dimensional Model of a 2nd Generation Planar SOFC Using Calibrated Parameters." In: *Int. J. Thermodyn.* 9.4 (2006), pp. 147–159.

Bibliography

[94]   W. C. Chueh and S. M. Haile. "Electrochemistry of mixed oxygen ion and electron conducting electrodes in solid electrolyte cells." In: *Annu Rev Chem Biomol Eng* 3 (Jan. 2012), pp. 313–41.

[95]   *Cantera*. 2014. URL: https://code.google.com/p/cantera/ (visited on 04/07/2014).

[96]   J. P. Neidhardt and W. G. Bessler. "Oxidation of nickel in solid oxide fuel cell anodes : A 2D kinetic modeling approach." In: *Proc. 10th Eur. SOFC Forum* B0502.June (2012), pp. 17–24.

[97]   A. Momma et al. "Simultaneous impedance measurement of 46 cells in 1 kW SOFC stack: Evaluation of the fuel flow rate distribution among the cells." In: *Proc. - Electrochem. Soc.* 7.2 (2005), pp. 554–563.

[98]   P. Metzger et al. "SOFC characteristics along the flow path." In: *Solid State Ionics* 177 (2006), pp. 2045–2051.

[99]   P. Kofstad. *High Temperature Corrosion*. Springer, 1988.

[100] Y. Larring and T. Norby. "Spinel and Perovskite Functional Layer Between Plansee Metallic Interconnect (Cr-5 wt% Fe-1 wt% Y_2O_3) and Ceramic $(La_{0.85}Sr_{0.15})_{0.91}MnO_3$." In: *J. Electrochem. Soc* 147.9 (2000), pp. 3251–3256.

[101] Z. Yang et al. "Evaluation of Perovskite Overlay Coatings on Ferritic Stainless Steels for SOFC Interconnect Applications." In: *J. Electrochem. Soc.* 153.10 (2006), A1852–A1858.

[102] J. A. Schuler et al. "Stroboscopic Ni Growth / Volatilization Picture." In: *Proc. 10th Eur. SOFC Forum* B0501 (2012), B0506–B0516.

[103] M. Linder et al. "Cr_2O_3 scale growth rates on metallic interconnectors derived from 40,000 h solid oxide fuel cell stack operation." In: *J. Power Sources* 243 (Dec. 2013), pp. 508–518.

[104] L. C. Baqué et al. "Long-term Stability of LSM-YSZ Based Cathodes." In: *ECS Trans.* 57.1 (2013), pp. 2027–2036.

[105] L. Jin et al. "Quantitative contribution of resistance sources of components to stack performance for planar solid oxide fuel cells." In: *J. Power Sources* 253 (May 2014), pp. 305–314.

[106] W. Y. Lee, J. Hanna, and A. F. Ghoniem. "On the Predictions of Carbon Deposition on the Nickel Anode of a SOFC and Its Impact on Open-Circuit Conditions." In: *J. Electrochem. Soc.* 160.2 (2012), F94–F105.

[107] A. Hagen. "Sulfur Poisoning of the Water Gas Shift Reaction on Anode Supported Solid Oxide Fuel Cells." In: *J. Electrochem. Soc.* 160.2 (2013), F111–F118.

[108] S. Campanari and P. Iora. "Definition and sensitivity analysis of a finite volume SOFC model for a tubular cell geometry." In: *J. Power Sources* 132.1-2 (May 2004), pp. 113–126.

[109] K. Takano et al. "Numerical simulation of a disk-type SOFC for impedance analysis under power generation." In: *J. Power Sources* 132.1-2 (May 2004), pp. 42–51.

[110] W. G. Bessler and S. Gewies. "Gas Concentration Impedance of Solid Oxide Fuel Cell Anodes." In: *J. Electrochem. Soc.* 154.6 (2007), B548.

[111] R. J. Kee et al. "Solid Oxide Fuel Cells: Operating Principles, Current Challenges, and the Role of Syngas." In: *Combust Sci Technol* 180.6 (May 2008), pp. 1207–1244.

[112] M. Hänsel, W. J. Quadakkers, and D. J. Young. "Role of water vapor in chromia-scale growth at low oxygen partial pressure." In: *Oxid. Met.* 59.3-4 (2003), pp. 285–301.

[113] A. Hagen et al. "Degradation of Anode Supported SOFCs as a Function of Temperature and Current Load." In: *J. Electrochem. Soc.* (2006), pp. 1165–1171.

[114] L. Holzer et al. "Microstructure degradation of cermet anodes for solid oxide fuel cells: Quantification of nickel grain growth in dry and in humid atmospheres." In: *J. Power Sources* 196.3 (Feb. 2011), pp. 1279–1294.

[115] W. J. Quadakkers et al. "Metallic interconnectors for solid oxide fuel cells - a review." In: *Mater. High. Temp.* 20.2 (May 2003), pp. 115–127.

[116] Z. Yang. "Recent advances in metallic interconnects for solid oxide fuel cells." In: *Int. Mater. Rev.* 53.1 (Jan. 2008), pp. 39–54.

[117] Y. Larring, R. Haugsrud, and T. Norby. "HT Corrosion of a Cr-5 wt.% Fe-1 wt.% Y_2O_3 Alloy and Conductivity of the Oxide Scale." In: *J. Electrochem. Soc.* 150.8 (2003), B374.

[118] P. Y. Hou and J. Stringer. "The effect of reactive element additions on the selective oxidation, growth and adhesion of chromia scales." In: *Mater. Sci. Eng., A* 202 (1995), pp. 1–10.

[119] H.-P. Martinz, W. Köck, and T. Sakaki. "Ducropur, Ducrolloy - New chromium materials." In: *J. Phys. IV Fr.* 03.C9 (Dec. 1993), pp. 205–213.

[120] ThyssenKrupp VDM GmbH. *Crofer 22 APU, Material Data Sheet No. 4046, May Edition*. 2010.

[121] P. Huczkowski. "Effect of geometry and composition of Cr steels on oxide scale properties relevant for interconnector applications in Solid Oxide Fuel Cells (SOFCs)." PhD thesis. RWTH Aachen, 2005.

[122] J. H. Froitzheim. "Ferritic steel interconnectors and their interactions with Ni base anodes in solid oxide fuel cells (SOFC)." PhD thesis. RWTH Aachen, 2008.

[123] W. Z. Zhu and S. C. Deevi. "Development of interconnect materials for solid oxide fuel cells." In: *Mater. Sci. Eng.* A348.1-2 (2003), pp. 227–243.

[124] S. Fontana et al. "Metallic interconnects for SOFC: Characterisation of corrosion resistance and conductivity evaluation at operating temperature of differently coated alloys." In: *J. Power Sources* 171.2 (Sept. 2007), pp. 652–662.

[125] Z. Lu et al. "Electrical Conductivity of the Manganese Chromite Spinel Solid Solution." In: *J. Am. Ceram. Soc.* 88.4 (Apr. 2005), pp. 1050–1053.

[126] M. Stanislowski et al. "Chromium vaporization from high-temperature alloys." In: *J. Electrochem. Soc.* 154 (2007), A295.

[127] S. Taniguchi et al. "Degradation phenomena in the cathode of a solid oxide fuel cell with an alloy separator." In: *J. Power Sources* 55.1 (May 1995), pp. 73–79.

[128] J. A. Schuler et al. "Cathode thickness-dependent tolerance to Cr-poisoning in solid oxide fuel cells." In: *Electrochem. Commun.* 12.12 (Dec. 2010), pp. 1682–1685.

[129] W. Z. Zhu and S. C. Deevi. "Opportunity of metallic interconnects for solid oxide fuel cells: a status on contact resistance." In: *Mater. Res. Bull.* 38.6 (May 2003), pp. 957–972.

[130] N. Shaigan et al. "A review of recent progress in coatings, surface modifications and alloy developments for solid oxide fuel cell ferritic stainless steel interconnects." In: *J. Power Sources* 195.6 (Mar. 2010), pp. 1529–1542.

[131] W. J. Quadakkers. "Growth mechanisms of oxide scales on ODS alloys in the temperature range 1000-1100 °C." In: *Mater. Corros.* 41 (1990), pp. 659–668.

[132] M. Michalik et al. "Effect of water vapour on growth and adherence of chromia scales formed on Cr in high and low p_{O_2}-environments at 1000 and 1050 °C." In: *Mater. High. Temp.* 22 (2005), pp. 213–221.

[133] M. Palcut et al. "Corrosion stability of ferritic stainless steels for solid oxide electrolyser cell interconnects." In: *Corros. Sci.* 52.10 (Oct. 2010), pp. 3309–3320.

[134] W. J. Quadakkers and D. Naumenko. "Growth rates of alumina scales on Fe–Cr–Al alloys." In: *Oxid. Met.* 61.February (2004), pp. 17–37.

[135] D. Naumenko et al. "Correlation between the Microstructure, Growth Mechanism, and Growth Kinetics of Alumina Scales on a FeCrAlY Alloy." In: *Met. Mater. Trans. A* 38.12 (Nov. 2007), pp. 2974–2983.

[136] X. H. Wang et al. "Insights into high temperature oxidation of Al_2O_3-forming Ti_3AlC_2." In: *Corros. Sci.* 58 (May 2012), pp. 95–103.

[137] H. Greiner, T. Grogler, and W. Kock. "Chromium based alloys for high temperature SOFC applications." In: *Proc. 4th Int. Symp. SOFC* (1995), pp. 879–888.

[138] J. W. Fergus. "Metallic interconnects for solid oxide fuel cells." In: *Mater. Sci. Eng., A* 397.1-2 (Apr. 2005), pp. 271–283.

[139] K. P. Lillerud and P. Kofstad. "On High Temperature Oxidation of Chromium I. Oxidation of Annealed, Thermally Etched Chromium at 800-1100 °C." In: *J. Electrochem. Soc.* 127.11 (1980), p. 2397.

[140] P. Kofstad. "High temperature oxidation of chromium." In: *Proc. 2nd Eur. SOFC Forum* (1996), pp. 479–490.

[141] D. M. Bastidas. "High temperature corrosion of metallic interconnects in solid oxide fuel cells." In: *Rev. Met. Madrid* 42.6 (2006), pp. 425–443.

[142] H. Nickel et al. "The effect of water vapor on the oxidation behavior of 9%Cr steels in simulated combustion gases." In: *Anal. Bioanal. Chem.* 361.6-7 (Aug. 1998), pp. 540–544.

[143] J. W. Fergus. "Materials challenges for solid-oxide fuel cells." In: *Jom-Us* 59.12 (2007), pp. 56–62.

[144] N. Birks, G. H. Meier, and F. S. Pettit. *Introduction to the High Temperature Oxidation of Metals*. Cambridge University Press, 2006.

[145] W. J. Quadakkers, H. Greiner, and M. Hänsel. "Compatibility of perovskite contact layers between cathode and metallic interconnector plates of SOFCs." In: *Solid State Ionics* 91.1-2 (1996), pp. 55–67.

[146] E. Konysheva et al. "Chromium vaporization of the ferritic steel Crofer22APU and ODS $Cr5Fe1Y_2O_3$ alloy." In: *J. Mater. Sci.* 42.14 (Apr. 2007), pp. 5778–5784.

[147] J. P. Pirón Abellan et al. "Ferritic steel interconnect for reduced temperature SOFC." In: *Proc. 7th Int. Symp. Solid Oxide Fuel Cells VII* 16 (2001), pp. 811–819.

Bibliography

[148] E. Batawi et al. "The Selection and Optimisation of Thermally Sprayed Perovskite-Based Coatings for Improved Long-Term Electrochemical Performance." In: *Proc. 2nd Eur. SOFC Forum* 1 (1996). Ed. by B. Thorstensen, pp. 307–314.

[149] Z. Yang and M. S. Walker. "Anomalous Corrosion Behavior of Stainless Steels under SOFC Interconnect Exposure Conditions." In: *Electrochem. Solid. St.* 6.10 (2003), pp. 35–37.

[150] Z. Yang et al. "Structure and Conductivity of Thermally Grown Scales on Ferritic Fe-Cr-Mn Steel for SOFC Interconnect Applications." In: *J. Electrochem. Soc.* 151.11 (2004), A1825.

[151] P. Gannon and R. Amendola. "High-Temperature, Dual-Atmosphere Corrosion of Solid-Oxide Fuel Cell Interconnects." In: *Jom-Us* 64.12 (Oct. 2012), pp. 1470–1476.

[152] K. Nakagawa, Y. Matsunaga, and T. Yanagisawa. "Corrosion behavior of ferritic steels on the air sides of boiler tubes in a steam/air dual environment." In: *Mater. High. Temp.* 20.1 (2003), p. 7.

[153] H. Kurokawa et al. "Hydrogen Permeation Through Fe-16Cr Alloy Interconnect in Atmosphere Simulating SOFC at 1073 K." In: *J. Electrochem. Soc.* 151.8 (2004), A1264.

[154] D. J. Young. *High Temperature Oxidation and Corrosion of Metals, Volume 1 (Corrosion Series).* Elsevier Science, 2008.

[155] K. Taneichi et al. "Oxidation or Nitridation Behavior of Pure Chromium and Chromium Alloys Containing 10 mass%Ni or Fe in Atmospheric Heating." In: *Mater. Trans.* 47.10 (2006), pp. 2540–2546.

[156] Å. H. Persson et al. "Interaction mechanisms between slurry coatings and solid oxide fuel cell interconnect alloys during high temperature oxidation." In: *J. Alloy. Compd.* 521 (Apr. 2012), pp. 16–29.

[157] K. Kawamura et al. "Effect of Electric Current on Growth of Oxide Scale on Fe-25Cr Alloy for SOFC Interconnect at 1073 K." In: *J. Electrochem. Soc.* 159.3 (Jan. 2012), B259–B264.

[158] P. Kodjamanova, Q. Fu, and L. Gautier. "Electric Current Effects on the Corrosion Behaviour of High Chromium Ferritic Steels." In: *Oxid. Met.* 79.1-2 (Dec. 2012), pp. 53–64.

[159] S. Fontana, S. Chevalier, and G. Caboche. "Metallic Interconnects for Solid Oxide Fuel Cell: Performance of Reactive Element Oxide Coating During 10, 20 and 30 Months Exposure." In: *Oxid. Met.* 78.5-6 (July 2012), pp. 307–328.

[160] A. Atkinson, R. I. Taylor, and A. E. Hughes. "A quantitative demonstration of the grain boundary diffusion mechanism for the oxidation of metals." In: *Philos. Mag. A* 45.5 (1982), pp. 823–833.

[161] L. Chen et al. "Strontium transport and conductivity of $Mn_{1.5}Co_{1.5}O_4$ coated Haynes 230 and Crofer 22 APU under simulated solid oxide fuel cell condition." In: *Solid State Ionics* 204-205 (Dec. 2011), pp. 111–119.

[162] V. I. Gorokhovsky et al. "Evaluation of SOFC Interconnects Made of Ferritic Steels with Nano-Structured Oxi-Ceramic Protective Coatings Deposited by the LAFAD Process." In: *J. Electrochem. Soc.* 158.5 (2011), B526.

[163] D. M. England and A. V. Virkar. "Oxidation Kinetics of Some Nickel-Based Superalloy Foils and Electronic Resistance of the Oxide Scale Formed in Air Part I." In: *J. Electrochem. Soc.* 146.9 (1999), pp. 3196–3202.

[164] H. Nagai, T. Fujikawa, and K.-i. Shoji. "Electrical Conductivity of Cr_2O_3 Doped with La_2O_3, Y_2O_3 and NiO." In: *T. Jpn. I. Met.* 24.8 (1983), pp. 581–588.

[165] G. Sartoris. *NM-SESES*. 2013. URL: http://icp.zhaw.ch/en/engineering/institutes-centres/institute-of-computational-physics/research-and-development/multiphysics-software-development/nm-seses.html (visited on 05/18/2015).

[166] H. Ebrahimifar and M. Zandrahimi. "Oxidation and electrical behavior of AISI 430 coated with cobalt spinels for SOFC interconnect applications." In: *Surf. Coat. Tech.* 206.1 (Oct. 2011), pp. 75–81.

[167] S. Shim and D. Mumm. "Stability Analysis of the Interface Between Electrical Contact Layers and Metal Interconnects in Solid Oxide Fuel Cells." In: *ECS Trans.* 7.1 (2007), pp. 795–804.

[168] H. Nagai, S. Ishikawa, and K.-i. Shoji. "Electrical Conductivity of Sintered Cr_2O_3 with Fe_2O_3." In: *T. Jpn. I. Met.* 26.1 (1985), pp. 44–51.

[169] T. Matsui and K. Naito. "Electrical conductivity anomaly of nonstoichiometric chromium sesquioxide." In: *J. Nucl. Mater.* 120 (1984), pp. 115–118.

[170] S. Henry et al. "Characterization of Chromia Scales Grown on Pure Chromium in Different Oxidizing Atmospheres." In: *Mater. High. Temp.* 17.2 (May 2000), pp. 231–235.

Bibliography

[171] V. I. Gorokhovsky et al. "Deposition and Evaluation of Protective PVD Coatings on Ferritic Stainless Steel SOFC Interconnects." In: *J. Electrochem. Soc.* 153.10 (2006), A1886.

[172] J. G. Grolig, J.-e. Svensson, and J. Froitzheim. "Coated Stainless Steel 441 as Interconnect Material for Solid Oxide Fuel Cells: Evolution of Electrical Properties." In: *Proc. 11th Eur. SOFC SOE Forum* B0508 (2014), pp. 25–36.

[173] F. C. Nix and D. MacNair. "The thermal expansion of pure metals. II: molybdenum, palladium, silver, tantalum, tungsten, platinum, and lead." In: *Phys. Rev.* 61 (1942), pp. 74–78.

[174] S. D. Bagdade. *ASM Ready Reference: Thermal Properties of Metals (Materials Data Series)*. ASM International, 2003.

[175] F. Tietz. "Thermal expansion of SOFC materials." In: *Ionics (Kiel).* 5 (1999), pp. 129–139.

[176] D. Stöver et al. "Recent developments in anode supported thin film SOFC at research center Julich." In: *Proc. 6th Int. Symp. Solid Oxide Fuel Cells VI (SOFC-VI)* 99.19 (1999), pp. 812–821.

[177] I. Kapralik. "Thermal Expansion of Spinels $MgCr_2O_4$, $MgAl_2O_4$ and $MgFe_2O_4$." In: *Chem. zvesti* 23 (1969), pp. 665–670.

[178] G. Samsonov. *The Oxide Handbook.* 2nd. Springer, 1982.

[179] W. Z. Zhu and S. C. Deevi. "A review on the status of anode materials for solid oxide fuel cells." In: *Mater. Sci. Eng., A* 362.1-2 (Dec. 2003), pp. 228–239.

[180] A. Weber. "Oxidation of H_2, CO and methane in SOFCs with Ni/YSZ-cermet anodes." In: *Solid State Ionics* 152-153 (Dec. 2002), pp. 543–550.

[181] J. Froitzheim et al. "Anode Side Diffusion Barrier Coating for Solid Oxide Fuel Cells Interconnects." In: *J. Fuel Cell Sci. Tech.* 7.3 (2010), p. 031020.

[182] M. Canavar and Y. Kaplan. "Effects of mesh and interconnector design on solid oxide fuel cell performance." In: *Int. J. Hydrog. Energ.* (Dec. 2014), pp. 4–9.

[183] K. A. Nielsen et al. "Testing of Ni-Plated Ferritic Steel Interconnect in SOFC Stacks." In: *Fuel Cells* 6.2 (Apr. 2006), pp. 100–106.

[184] C. Fu et al. "Effects of the nickel-coated ferritic stainless steel for solid oxide fuel cells interconnects." In: *Corros. Sci.* 50.7 (July 2008), pp. 1926–1931.

[185] L. Mikkelsen, J. Høgh, and P. V. Hendriksen. "Interface resistance between FeCr interconnects and Ni/YSZ." In: *Proc. 8th Eur. SOFC Forum* A0905 (2008), pp. 1–10.

[186] V. Sarda et al. "Long Term Resistivity Behavior of SOFC Interconnect/Ni-Mesh/Anode Interfaces." In: *ECS Trans.* 57.1 (2013), pp. 2279–2288.

[187] L. Garcia-Fresnillo et al. "Long-term behaviour of solid oxide fuel cell interconnect materials in contact with Ni-mesh during exposure in simulated anode gas at 700 and 800 °C." In: *J. Power Sources* 271 (Dec. 2014), pp. 213–222.

[188] J. A. Crawford and R. W. Vest. "Electrical Conductivity of Single-Crystal Cr_2O_3." In: *J. Appl. Phys.* 34.1959 (1964), pp. 2413–2418.

[189] A. Holt and P. Kofstad. "Electrical conductivity and defect structure of Cr_2O_3. I. High temperatures (> 1000 °C)." In: *Solid State Ionics* 69 (1994), pp. 127–136.

[190] A. Holt. "Electrical conductivity and defect structure of Mg-doped Cr_2O_3." In: *Solid State Ionics* 100.3-4 (Oct. 1997), pp. 201–209.

[191] Plansee SE. *Plansee SE.* 2015. URL: http://plansee.com/en/Materials-Chromium-939.htm (visited on 01/08/2015).

[192] T. Farrell and D. Greig. "The electrical resistivity of nickel and its alloys." In: *J. Phys. C* 1.5 (Oct. 1968), pp. 1359–1369.

[193] A. Ul-Hamid. "TEM Study of the Effect of Y on the Scale Microstructures of Cr_2O_3- and Al_2O_3-Forming Alloys." In: *Oxid. Met.* 58.August (2002), pp. 23–40.

[194] H. Nagai, S. Ishikawa, and N. Amano. "Electrical Conductivity of Sintered Cr_2O_3 Simultaneously Doped with NiO and Rare Earth Oxide at Low Oxygen Potential." In: *T. Jpn. I. Met.* 26.10 (1985), pp. 753–762.

[195] R. Hiesgen et al. "Insight into the Structure and Nanoscale Conductivity of Fluorinated Ionomer Membranes." In: *J. Electrochem. Soc.* 161.12 (Aug. 2014), F1214–F1223.

[196] G. E. Archie. "The Electrical Resistivity Log as an Aid in Determining Some Reservoir Characteristics." In: *Soci. Pet. Eng.* Vol. 146. 01. Apr. 1942, pp. 54–62.

[197] G. Gaiselmann et al. "Stochastic 3D modeling of $La_{0.6}Sr_{0.4}CoO_{3-\delta}$ cathodes based on structural segmentation of FIB-SEM images." In: *Comp. Mater. Sci.* 67 (Feb. 2013), pp. 48–62.

[198] D. Wiedenmann et al. "Three-dimensional pore structure and ion conductivity of porous ceramic diaphragms." In: *AlChE J.* 59.5 (May 2013), pp. 1446–1457.

Bibliography

[199] M. Linder et al. "Model-based prediction of the ohmic resistance of metallic interconnects from oxide scale growth based on scanning electron microscopy." In: *J. Power Sources* 272 (Dec. 2014), pp. 595–605.

[200] C. Greskovich. "Kinetics of $NiCr_2O_4$ Formation and Diffusion of Cr^{3+} Ions in NiO." In: *J. Am. Ceram. Soc.* 53.9 (Sept. 1970), pp. 498–502.

[201] J. S. Armijo, D. L. Douglass, and R. A. Huggins. "Mechanism and Kinetics of Nickel Chromite Formation." In: *J. Electrochem. Soc.* 120.6 (1973), p. 825.

[202] P. Kofstad. *Nonstoichiometry, Diffusion and Electrical Conductivity in Binary Metal Oxides*. Reprint Ed. Wiley, 1983, p. 207.

[203] J. S. Park and H. G. Kim. "Electrical Conductivity and Defect Models of MgO-Doped Cr_2O_3." In: *J. Am. Ceram. Soc.* 71.3 (Mar. 1988), pp. 173–176.

[204] H. Nagai and K. Ohbayashi. "Effect of TiO_2 on the Sintering and the Electrical Conductivity of Cr_2O_3." In: *J. Am. Ceram. Soc.* 72 (1989), pp. 400–403.

[205] E. W. A. Young, P. C. M. Stiphout, and J. H. W. de Wit. "n-Type Behavior of Chromium (III) Oxide." In: *J. Electrochem. Soc.* 132.4 (1985), p. 884.

[206] P. Kofstad and K. P. Lillerud. "On High Temperature Oxidation of Chromium II. Properties of Cr_2O_3 and the Oxidation Mechanism of Chromium." In: *J. Electrochem. Soc.* 127.11 (1980), pp. 2410–2419.

[207] D. Sarantaridis and A. Atkinson. "Redox Cycling of Ni-Based Solid Oxide Fuel Cell Anodes: A Review." In: *Fuel Cells* 7.3 (June 2007), pp. 246–258.

[208] N. G. Eror and J. B. Wagner. "Electrical Conductivity of Single Crystalline Nickel Oxide." In: *Phys. Status Solidi (B)* 35.2 (1969), pp. 641–651.

[209] M. C. Pope and N. Birks. "The electrical conductivity of NiO at 1000 °C." In: *Corros. Sci.* 17.9 (Jan. 1977), pp. 747–752.

[210] D.-G. Nam and H.-C. Lee. "Thermal nitridation of chromium electroplated AISI316L stainless steel for polymer electrolyte membrane fuel cell bipolar plate." In: *J. Power Sources* 170.2 (July 2007), pp. 268–274.

[211] L. Japan New Metals Co. *Japan New Metals Co., LTD.* 2014. URL: http://www.jnm.co.jp/en/data/electrical_conductivity.html (visited on 09/30/2014).

[212] W. Qu et al. "Electrical and microstructural characterization of spinel phases as potential coatings for SOFC metallic interconnects." In: *J. Power Sources* 153.1 (Jan. 2006), pp. 114–124.

[213] C. M. Osburn and R. W. Vest. "Defect structure and electrical properties of Nio—II. Temperatures below equilibration." In: *J. Phys. Chem. Solids* 32.6 (Jan. 1971), pp. 1343–1354.

[214] F. N. Rhines. "Role of Grain Growth in the Oxidation of Nickel." In: *J. Electrochem. Soc.* 124.7 (1977), p. 1122.

[215] R. Peraldi, D. Monceau, and B. Pieraggi. "Correlations between growth kinetics and microstructure for scales formed by high-temperature oxidation of pure nickel. II. Growth kinetics." In: *Oxid. Met.* 58.3/4 (2002), pp. 275–295.

[216] C. Greskovich. "Deviation from Stoichiometry in Cr_2O_3 at High Oxygen Partial Pressures." In: *J. Am. Ceram. Soc.* 67.6 (June 1984), pp. 111–112.

[217] R. J. D. Tilley. *Principles and Applications of Chemical Defects*. 1st. CRC Press, 1998.

[218] J. A. Schuler et al. "Air side contamination in Solid Oxide Fuel Cell stack testing." In: *J. Power Sources* 196.17 (2011), pp. 7225–7231.

[219] H. SchmaIzried. "Reaktionen im festen Zustand." In: *Ber. Dtsch. Keram. Ges.* 42 (1965), pp. 11–22.

[220] H. Schmalzried. "Solid-State Reactions." In: *Angew. Chem. Int. Ed.* 2.5 (1963), pp. 251–254.

[221] F. S. Pettit, E. H. Randklev, and E. J. Felten. "Formation of $NiAl_2O_4$ by solid state reaction." In: *J. Am. Ceram. Soc.* 49.April (1966), pp. 199–203.

[222] S. C. Schaefer. *Electrochemical Determination of Thermodynamic Properties of $NiCr_2O_4$ and $CoCr_2O_4$*. Tech. rep. US Bureau of Mines, 1986.

[223] B. Iwanschitz et al. "Nickel agglomeration in Solid Oxide Fuel Cells under different operating conditions." In: *Proc. 10th Eur. SOFC Forum*. June. 2012, A1005–A1015.

[224] J. A. Marqusee and J. Ross. "Theory of Ostwald ripening: Competitive growth and its dependence on volume fraction." In: *J. Chem. Phys.* 80.1 (1984), p. 536.

[225] R. C. Ku and W. L. Winterbottom. "Electrical Conductivity in Sputter-Deposited Chromium Oxide Coatings." In: *Thin Solid Films* 127 (1985), pp. 241–256.

[226] T. Horita et al. "Oxide Scale Formation and Stability of Fe–Cr Alloy Interconnects under Dual Atmospheres and Current Flow Conditions for SOFCs." In: *J. Electrochem. Soc.* 153.11 (2006), A2007.

Bibliography

[227] R. Amendola et al. "Oxidation behavior of coated and preoxidized ferritic steel in single and dual atmosphere exposures at 800 °C." In: *Surf. Coatings Technol.* 206.8-9 (Jan. 2012), pp. 2173–2180.

[228] Y. Jacob et al. "The effect of gas composition on the isothermal oxidation behaviour of PM chromium." In: *Corros. Sci.* 44.9 (Sept. 2002), pp. 2027–2039.

[229] Z. Yang et al. "$(Mn,Co)_3O_4$ spinel coatings on ferritic stainless steels for SOFC interconnect applications." In: *Int. J. Hydrogen Energy* 32.16 (2007), pp. 3648–3654.

[230] J. J. Senkevich, D. A. Jones, and I. Chatterjee. "Measuring the growth of oxide films on low carbon steel at 500 °C by impedance spectroscopy." In: *Corros. Sci.* 42.2 (2000), pp. 201–210.

[231] L. Hamadou, A. Kadri, and N. Benbrahim. "Impedance investigation of thermally formed oxide films on AISI 304L stainless steel." In: *Corros. Sci.* 52.3 (2010), pp. 859–864.

Appendix

A.1 Visualization of streamlines from FE simulation
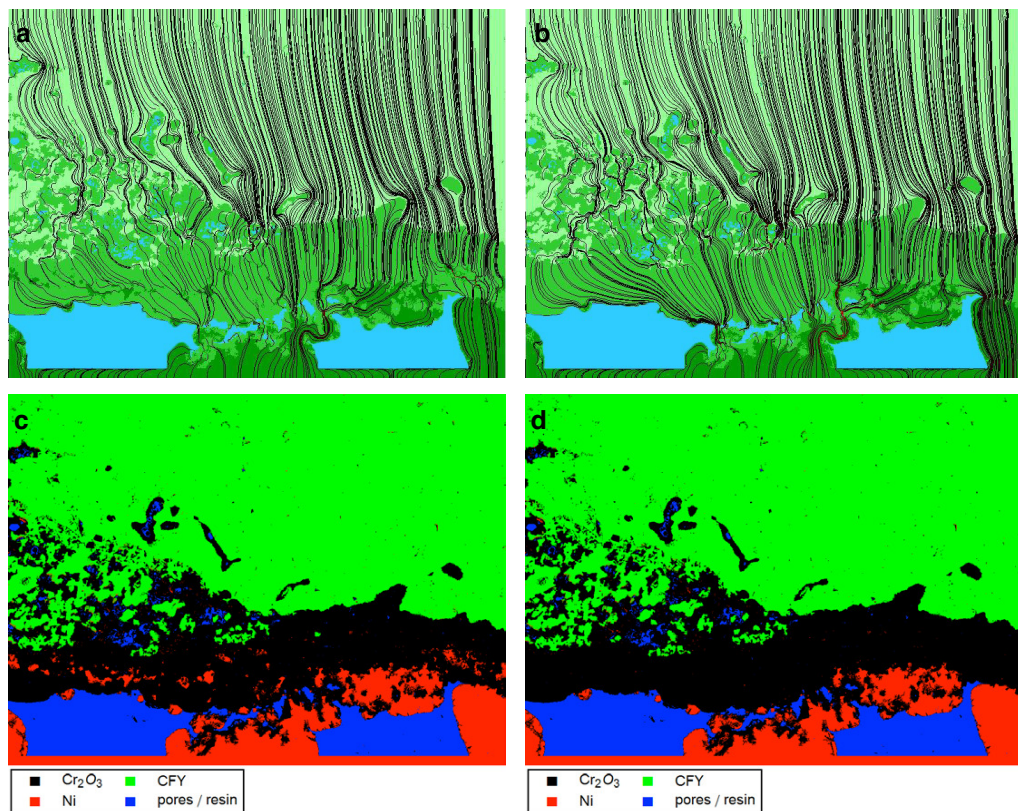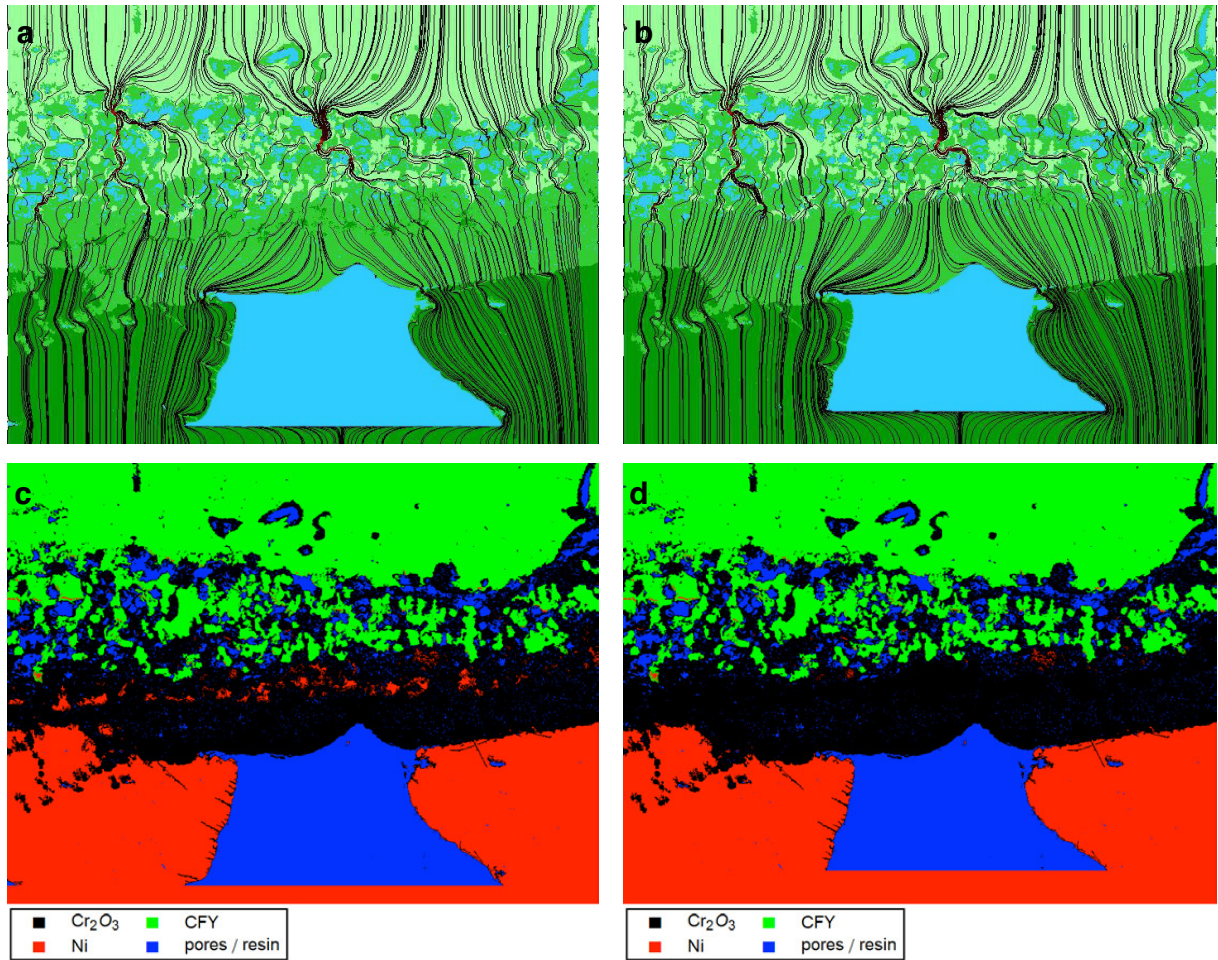

Fig. A.1 Preferred pathways of local electrical current densities obtained from FE simulations a) after 10 700 h stack operation with CPOx reformed natural gas at 900 °C with Ni particles and b) without Ni particles, i. e. the latter artificially replaced by Cr_2O_3 by image processing (SEM image label as used in Fig. 5.31 and Table 5.5: #120323). c) and d) shows the corresponding SEM image as segmented for the simulations.
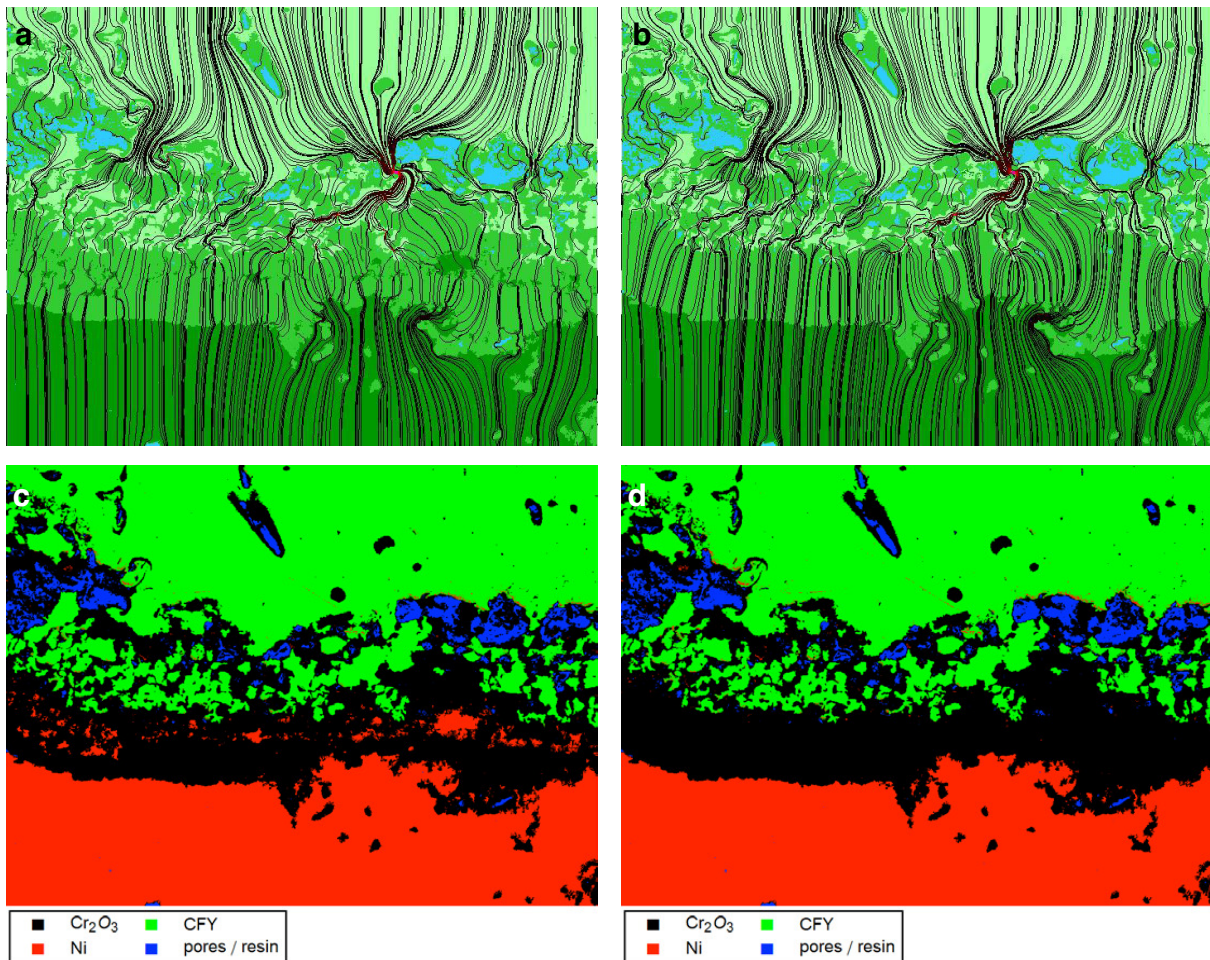
Fig. A.2 Preferred pathways of local electrical current densities obtained from FE simulations a) after 10 700 h stack operation with CPOx reformed natural gas at 900 °C with Ni particles and b) without Ni particles, i. e. the latter artificially replaced by Cr_2O_3 by image processing (SEM image label as used in Fig. 5.31 and Table 5.5: #120325). c) and d) shows the corresponding SEM image as segmented for the simulations.
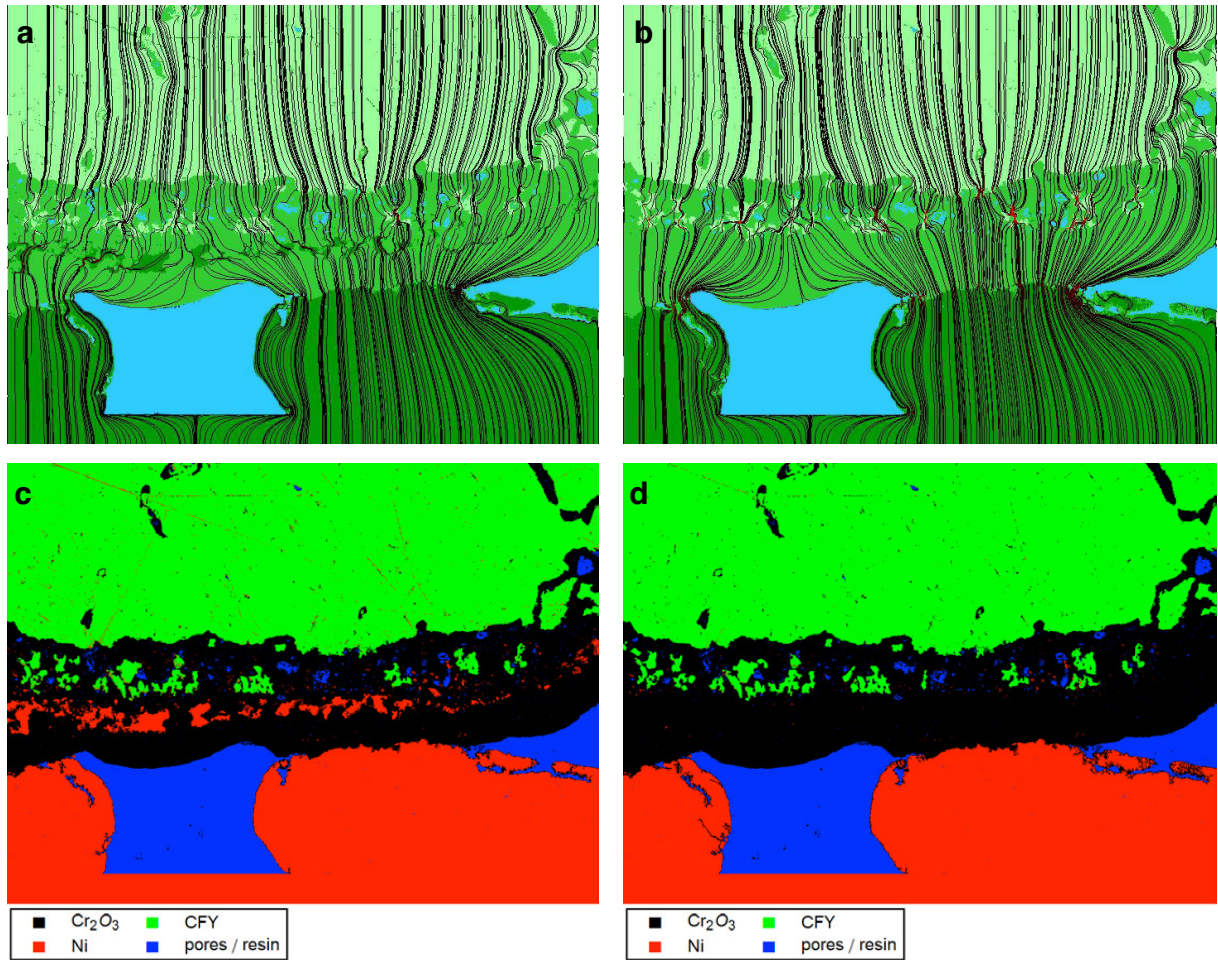
Fig. A.3 Preferred pathways of local electrical current densities obtained from FE simulations a) after 10 700 h stack operation with CPOx reformed natural gas at 900 ℃ with Ni particles and b) without Ni particles, i. e. the latter artificially replaced by Cr_2O_3 by image processing (SEM image label as used in Fig. 5.31 and Table 5.5: #120360). c) and d) shows the corresponding SEM image as segmented for the simulations.
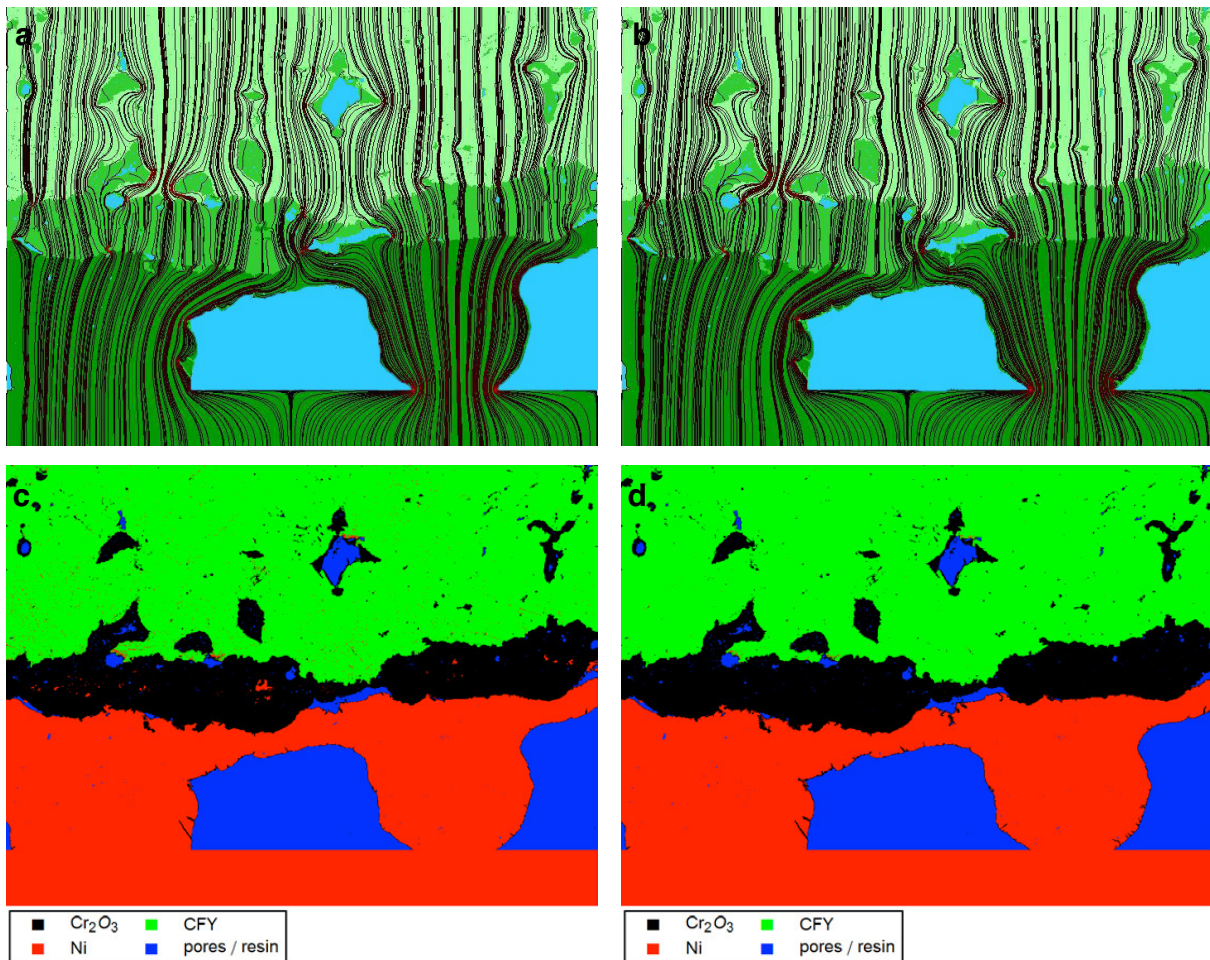
Fig. A.4 Preferred pathways of local electrical current densities obtained from FE simulations a) after 10 700 h stack operation with CPOx reformed natural gas at 900 °C with Ni particles and b) without Ni particles, i. e. the latter artificially replaced by Cr_2O_3 by image processing (SEM image label as used in Fig. 5.31 and Table 5.5: #120479). c) and d) shows the corresponding SEM image as segmented for the simulations.

Fig. A.5 Preferred pathways of local electrical current densities obtained from FE simulations a) after 10 700 h stack operation with CPOx reformed natural gas at 900 °C with Ni particles and b) without Ni particles, i. e. the latter artificially replaced by Cr_2O_3 by image processing (SEM image label as used in Fig. 5.31 and Table 5.5: #120534). c) and d) shows the corresponding SEM image as segmented for the simulations.

A.2   AFM results

In Figs. A.6a and A.6b the 3D-topography overlaid with the adhesion force data is displayed, with a higher resolution in Fig. A.6b. In the adhesion image areas with different adhesion force that indicate different surface properties or different material can be discerned. The 3D-topography overlaid with the electrical current data is shown in Fig. A.6c and at higher resolution in Fig. A.6d, where a lamellar structure is visible in the electrical current. Electrical current flow coincides with the low adhesion areas. In topography, this area is completely flat, and the lamellar structures can be assigned to a lamellar stacking of the material.
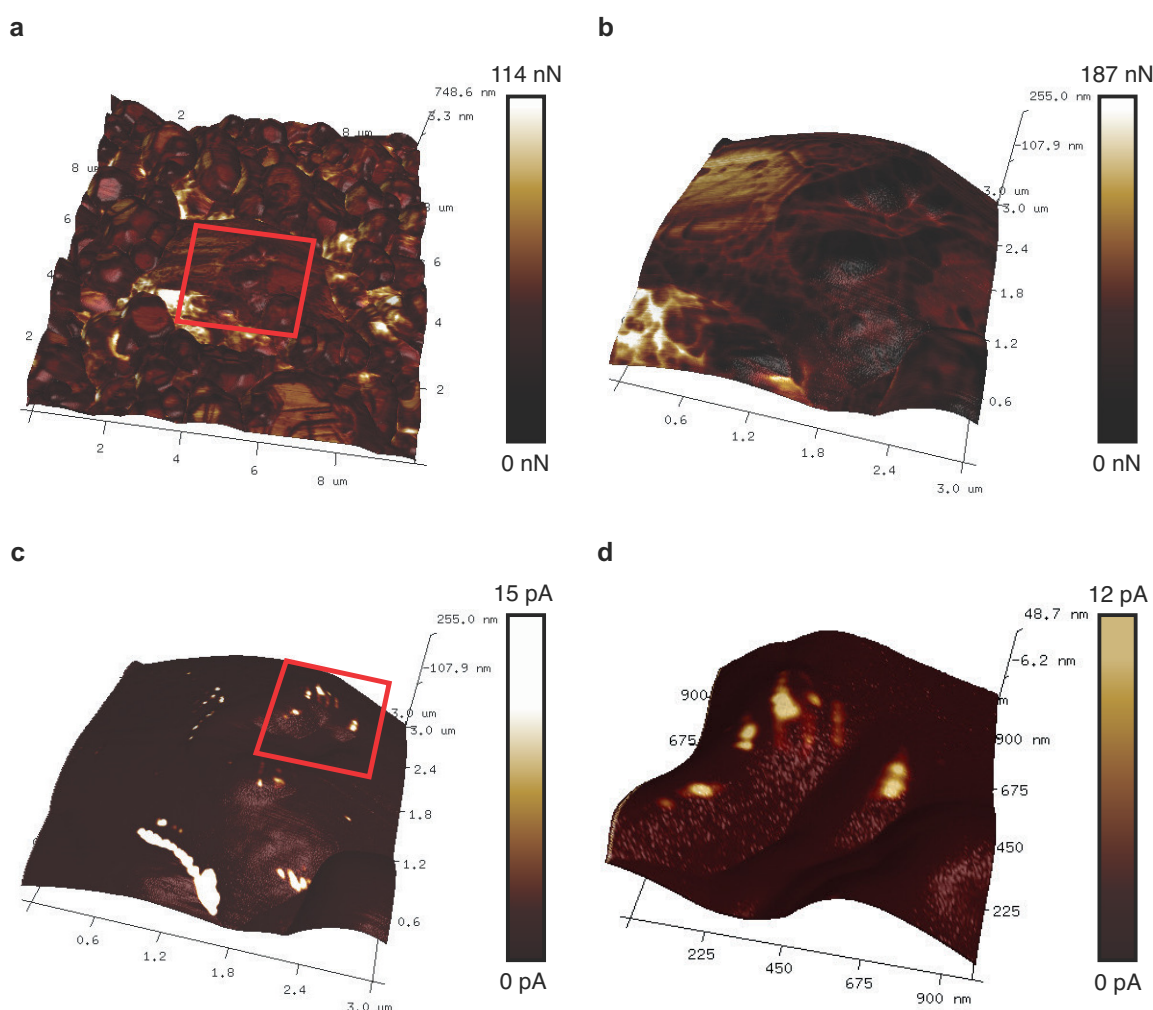
Fig. A.6 AFM images of a Cr_2O_3-20 pellet a) topography overlaid with adhesion data, the red rectangle marks the section of b) zoomed-in image of topography overlaid with adhesion data, c) topography overlaid with the current data, and d) the corresponding zoomed-in image of topography overlaid with the current data (section marked by the red rectangle in c)).

A.3 Temperature variation plots
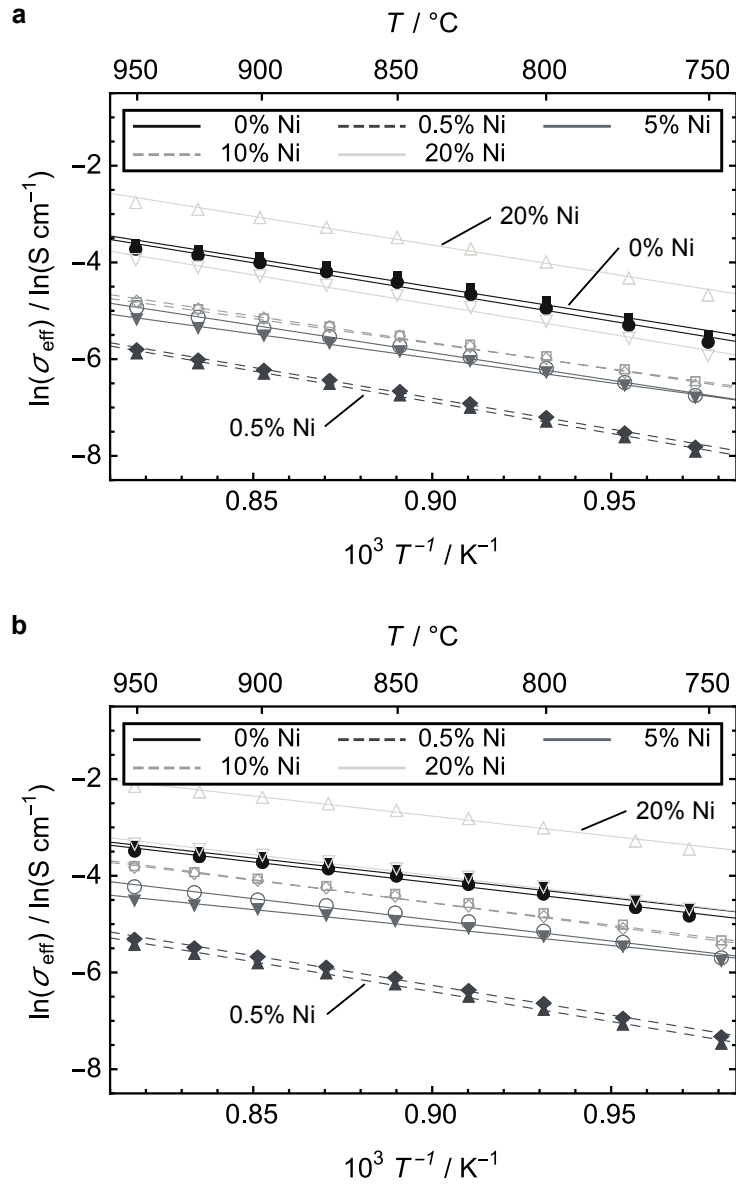
Fig. A.7 Temperature variation at the begin of stage A in dry (T var 1) a) and wet (T var 2) b) f-gas atmosphere.
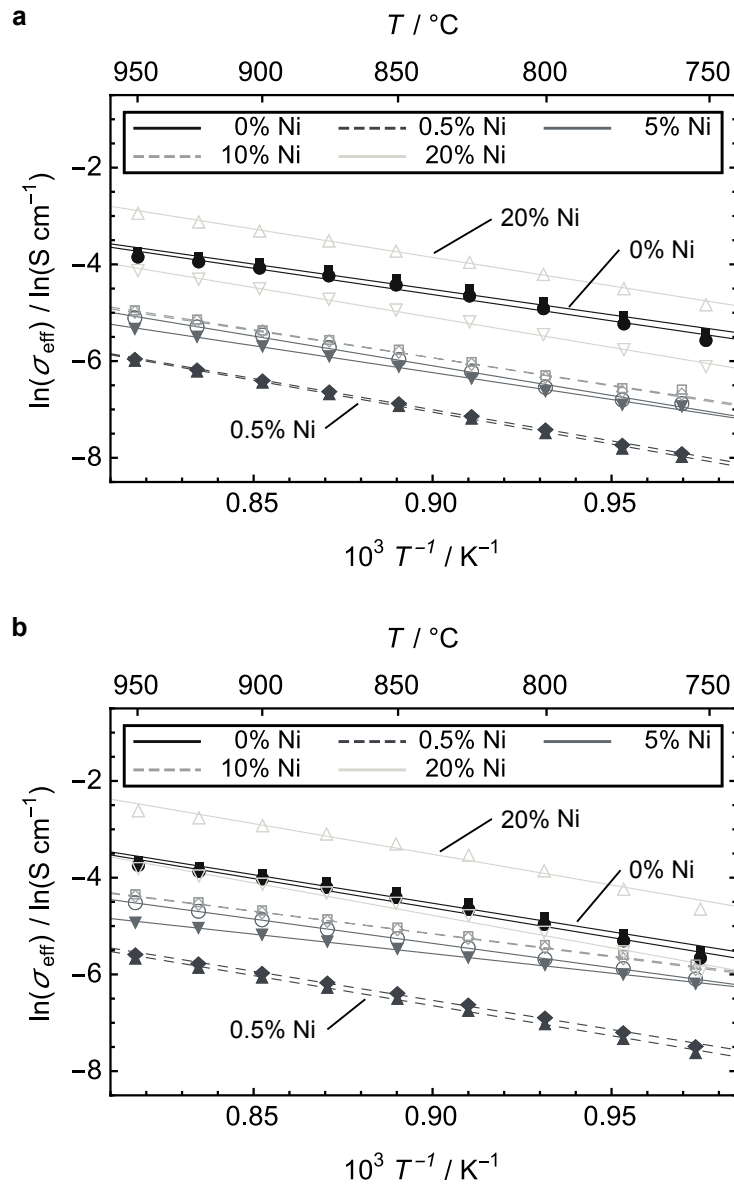
Fig. A.8 Temperature variation at the end of stage A in dry (T var 3) a) and wet (T var 4) b) hydrogen atmosphere.
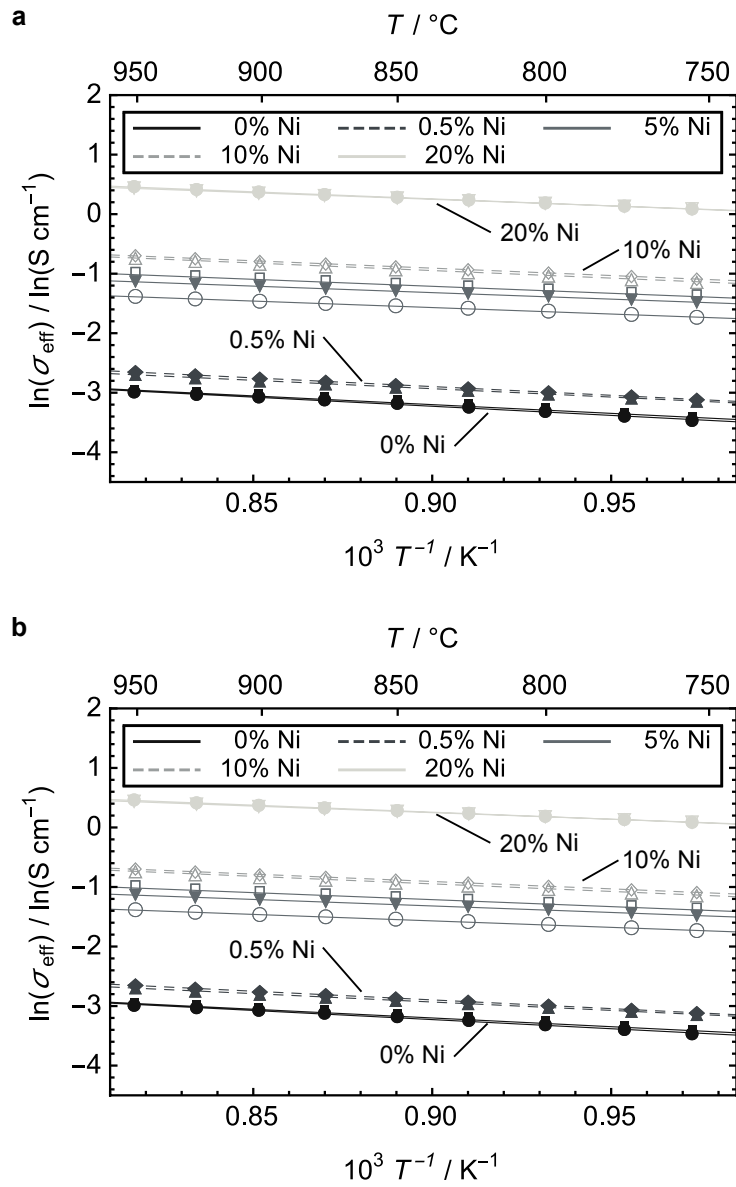
Fig. A.9 Temperature variation at the end of stage C in dry (T var 5) a) and wet (T var 6) b) air atmosphere.
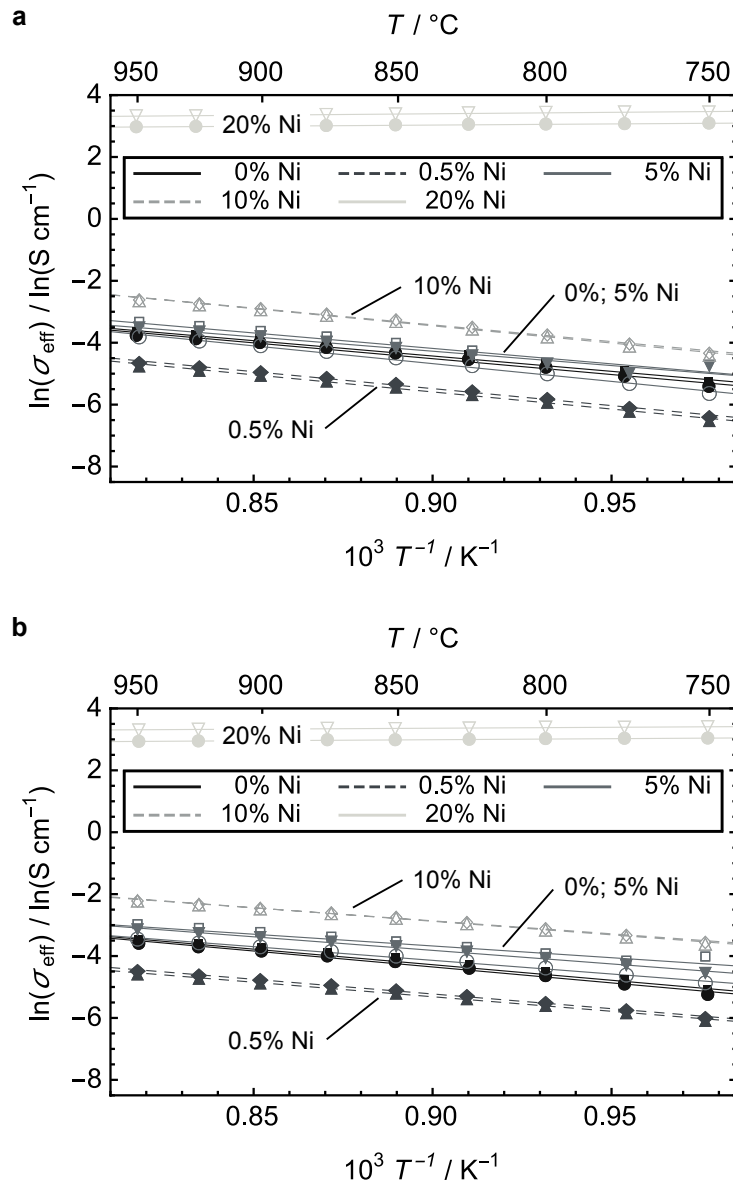
Fig. A.10 Temperature variation at the end of stage E in dry (T var 7) a) and wet (T var 8) b) f-gas atmosphere.

Acknowledgement

Acknowledgement

support in the experimental fields.

I thank Tobias Morawietz and Prof. Renate Hiesgen from the University of Applied Sciences Esslingen for giving me an insight in the attractive field of atomic force microscopy and providing me with experimental data derived from my samples.

I am deeply grateful to "swisselectric research" and Swiss Federal Office of Energy (SFOE) for their financial support within the SOF-CH ESC project. Additionally I would like to thank all project partners for the personal exchange during the regular project meetings and expanding my horizons in terms of other relevant topics in the domain of SOFC. Likewise I appreciated the frequent discussions with Felix Fleischhauer who too was a PhD student in the SOF-CH ESC project. I also thank him for organizing and performing the sintering of samples at EMPA in Dübendorf. In addition I thank Dr. Andre Heel for the interesting discussion about the not intuitively comprehensible ASR increase coupled to temperature variation and Dr. Roman Kontic for doing the X-ray diffraction and his competent data interpretation.

I would also like to thank all the others PhD students for the great time and enjoyable discussions during the annual meetings in Stuttgart.

A very special thank you goes to Regula. Thank you for your all your passion, understanding and unconditional support during the past years, which has not always been easy. I love you.

List of publications

Peer reviewed papers

Markus Linder[†], Thomas Hocker, Lorenz Holzer, Omar Pecho, K. Andreas Friedrich, Tobias Morawietz, Renate Hiesgen, Roman Kontic, Boris Iwanschitz, Andreas Mai, J. Andreas Schuler. "Ohmic resistance of nickel infiltrated chromium oxide scales in solid oxide fuel cell metallic interconnects." *Solid States Ionics* 283 (2015) pp. 38-51

Markus Linder[†], Thomas Hocker, Christoph Meier, Lorenz Holzer, K. Andreas Friedrich, Boris Iwanschitz, Andreas Mai, J. Andreas Schuler. "A model-based approach for current voltage analyses to quantify degradation and fuel distribution in solid oxide fuel cell stacks." *Journal of Power Sources* 288 (2015) pp. 409-418

Markus Linder[†], Thomas Hocker, Lorenz Holzer, K. Andreas Friedrich, Boris Iwanschitz, Andreas Mai, J. Andreas Schuler. "Model-based prediction of the ohmic resistance of metallic interconnects from oxide scale growth based on scanning electron microscopy image data." *Journal of Power Sources* 272 (2014) pp. 595-605

Markus Linder[†], Thomas Hocker, Lorenz Holzer, K. Andreas Friedrich, Boris Iwanschitz, Andreas Mai, J. Andreas Schuler. "Cr_2O_3 scale growth rates on metallic interconnectors derived from 40,000 h solid oxide fuel cell stack operation." *Journal of Power Sources* 243 (2013) pp. 508-518

Markus Linder, Thomas Hocker, Roland Denzler, Andreas Mai, Boris Iwanschitz. "Automated, Model-Based Analysis of Uj-Data for Electrolyte-Supported SOFC Short-Stacks." *Fuel Cells* 11.4 (2011), pp. 573-580

[†] Text have been partially used within this thesis.

Conference contributions

Markus Linder, Thomas Hocker, Christoph Meier, Lorenz Holzer, K. Andreas Friedrich, Boris Iwanschitz, Andreas Mai, J. Andreas Schuler. "Quantification of SOFC stack degradation and fuel distribution based on current voltage data." Oral presentation at 12th Symposium for Fuel Cell and Battery Modeling and Experimental Validation – ModVal 12, at Freiburg, Germany (2015).

Michael Dold, Thomas Hocker, **Markus Linder**, Lorenz Holzer, Andreas Mai, J. Andreas Schuler. "Model-based analysis of electrochemical impedance spectra of solid oxide fuel cells." Poster presentation at 12th Symposium for Fuel Cell and Battery Modeling and Experimental Validation – ModVal 12, at Freiburg, Germany (2015).

Markus Linder, Thomas Hocker, Lorenz Holzer, K. Andreas Friedrich, Boris Iwanschitz, Andreas Mai, J. Andreas Schuler. "Oxide (Cr_2O_3) scale growth on metallic interconnects and its impact on ohmic resistance: Combined study of image analysis and modeling." Oral presentation at 11th European SOFC & SOE Forum, at Lucerne, Switzerland (2014).

Markus Linder, Thomas Hocker, Lorenz Holzer, K. Andreas Friedrich, Boris Iwanschitz, Andreas Mai, J. Andreas Schuler. "Effects of Cr_2O_3 layer morphology on SOFC-interconnect resistance." Oral presentation at 12th Symposium for Fuel Cell and Battery Modeling and Experimental Validation – ModVal 11, at Winterthur, Switzerland (2014)

Markus Linder, Thomas Hocker, Lorenz Holzer, K. Andreas Friedrich, Boris Iwanschitz, Andreas Mai, J. Andreas Schuler, Alexander Schuler. "Quantifizierung und Charakterisierung der Stromsammler Degradation im Brennstoffzellenstapel." Poster at Jahrestreffen der ProcessNet-Fachgruppe Energieverfahrenstechnik; at Karlsruhe, Germany (2014)

Markus Linder, Thomas Hocker, Lorenz Holzer, Boris Iwanschitz, Andreas Mai, and J. Andreas Schuler. "Cr_2O_3 scale growth rates on metallic interconnectors derived from 40'000 hours solid oxide fuel cell stack operation." Oral presentation at 10th Symposium for Fuel Cell and Battery Modeling and Experimental Validation – ModVal 10, at Bad Boll/Stuttgart, Germany, (2013)

Markus Linder, Thomas Hocker, Roland Denzler, Andreas Mai, Boris Iwanschitz. "Automated, model-based analysis of Uj-data for Hexis SOFC short-stacks that run on CPO-reformed natural gas." Poster presentation at 7th Symposium for Fuel Cell and Battery

Modeling and Experimental Validation – ModVal 7, at Lausanne, Switzerland, (2010)

Patents

Andreas Mai, Boris Iwanschitz, **Markus Linder**, Hanspeter Kuratli; "Verfahren und Regelvorrichtung zur Regelung einer Brennstoffzelle oder eines Brennstoffzellenstapels" Hexis AG; EP 2658021 A1, EP 2658021 B1

Andreas Mai, Boris Iwanschitz, **Markus Linder**, Hanspeter Kuratli; "Method and regulation apparatus for regulating a fuel cell or a fuel cell stack" Hexis AG; US 20130288147 A1

Declaration of authorship

I hereby certify that the dissertation entitled

"Characterization and Quantification of Metallic Interconnect Degradation in Solid Oxide Fuel Cell Stacks"

is entirely my own work except where otherwise indicated. Passages and ideas from other sources have been clearly indicated.

Ich versichere, dass ich die vorliegende Dissertation mit dem Titel

"Characterization and Quantification of Metallic Interconnect Degradation in Solid Oxide Fuel Cell Stacks"

selbständig verfasst und keine anderen als die angegebenen Quellen und Hilfsmittel benutzt habe. Aus fremden Quellen entnommene Passagen und Gedanken sind als solche gekennzeichnet.

Name / Name: _____

Place, date / Ort, Datum: _____

Signature / Unterschrift: _____